



**UNIVERSITY** *of the*  
**WESTERN CAPE**

**FACIES, DEPOSITIONAL ENVIRONMENTS AND RESERVOIR  
PROPERTIES OF THE ALBIAN AGE GAS BEARING  
SANDSTONE OF THE IBHUBESI OIL FIELD, ORANGE BASIN,  
SOUTH AFRICA.**

**A Thesis in Applied Geology (Petroleum Geology Option)**



**BY**

**OLUWASEUN ADEJUWON FADIPE**

*UNIVERSITY of the*  
**WESTERN CAPE**

**Submitted in Fulfillment of the Requirements for the Degree of Magister  
Scientiae in the Department of Earth Sciences,  
University of the Western Cape,  
Cape town, South Africa.**

**Supervisor: Prof. Paul Carey**  
**Co- Supervisor: Dr. Akinsehinwa Akinlua**

**November, 2009**

## ABSTRACT

The Orange Basin was formed during the late Jurassic to early Cretaceous periods due to Gondwana breakup and rifting and later drifting apart of the African and South American plates. The basin consists of siliciclastic sandstone which took its sediment supply from river system with a rivalling delta to the north of the basin. Geological and petrophysical studies were carried out to evaluate the reservoir potential of the wells in the study area.

This study considered five wells (A-G1, A-W1, A-K1, A-K2 and A-Y1) in the Orange Basin with attention to the Albian age sandstone. Only three of the studied wells (A-G1, A-W1 and A-K1) have core samples for analysis. The methods used for the execution of this study include the description and calibration of spot cores with conventional standard logging record responses, wireline log interpretation using sequence stratigraphy approach, detailed petrographic (SEM, HR-TEM, XRD and thin section) and geochemical (pore water geochemistry, FTIR and XRF) analyses, and petrophysical analysis to unravel the complexities with regard to facies association, depositional environment and diagenesis. Linking diagenesis to depositional facies and sequence stratigraphy has given a clearer picture to the spatial and temporal distribution of diagenetic alterations and thus of evolution of reservoir quality in the studied wells.

Three depositional lithofacies were identified based on a detailed core description [fine grained sandstone (F1), very fine grained sandstone (F2) and mudstone (F3)]. Fluvio-deltaic and shallow marine environments were also interpreted from the core description based on the sedimentary structures and mineral assemblage while the log interpretation shows that the different reservoir units range between LST, TST and HST but mostly of LST. Mineralogical predictions were made possible in the wells without core samples (A-K2 and A-Y1) through the use of density-neutron cross plot, these reveal that the two wells contain some considerable amount of clay minerals like kaolinite, chlorite and illite.

Petrophysical evaluation of the different reservoir bodies show a relatively fair to good porosity and permeability ( $> 15\%$ ) with most of the reservoir interval highly water saturated ( $> 70\%$ ) except for the first two delineated reservoir in A-G1 having water saturation of  $34\%$  and  $8\%$  respectively. The integration of petrographic analysis with pore water data explains cements succession in the sandstones mixing with acid water derived from dewatering of interbedded organic rich mudstones

which probably added  $Mg^{2+}$  and  $Fe^{2+}$  to partially buffer the loss of these cations to chlorite. The acid produced during the breakdown of this organic matters are presumed to have mixed with sandstone pore fluid due to further compaction of muds leading to reduction of initial alkalinity in some of the studied wells. The changes in the chemical characteristics of the pore fluid leads to a more complex distribution of reservoir porosity at different depths than that of the secondary porosity formed by classical acidic water.

The results obtained from geochemical analysis indicate that the sandstones are Fe-rich belonging to the terrigenous class of sands (greywacke for A-W1 sand and litharenite for A-K1 and A-G1 well) while chemical index of alteration (CIA) in the various wells with average CIA values of 62.23 %, 57.01 % and 61.65 % in the wells A-G1, A-K1 & A-W1, respectively reveals that the sandstone samples have undergone a moderate to high degree of weathering.

The lithologic-diagenetic model of the study area rocks reflects that these clay minerals have an influence on the effective porosity and consequently on the fluid saturation. Kaolinite, chlorite and illite and mixed clay are the principal clay minerals, which strongly affected the percentage of effective porosity and hydrocarbon saturation. This study demonstrates that deploying this approach is useful because depositional facies and sequence stratigraphy has provided useful information on parameters controlling the near surface diagenesis such as changes in (i) influence of organic matters on pore water geochemistry, (ii) residence time of sediment under certain geochemical conditions, (iii) detrital composition and proportion of extra and intra-basinal grains.

**Keywords: Facies, Diagenesis, Depositional environments, Sequence stratigraphy, Reservoir sand, Petrophysics, Hydrocarbon potential, and Orange Basin.**

## DECLARATION

I declare that my research work titled “Facies, Depositional Environments and Reservoir Properties of the Albian Age Gas bearing Sandstone of the Ibhuesi Oil Field, Orange Basin, South Africa” is my own work, that it has not been submitted before for any degree or examination in any other university, and that all the sources I have used or quoted have been indicated and acknowledged by means of complete references

**Oluwaseun A. FADIPE**

November, 2009



.....  
Signature



## ACKNOWLEDGEMENT

I am highly indebted to Dr. A. Akinlua who created time out of his tight schedule to attend to me without much delay. Special thanks go to Petroleum Agency, SA for providing core samples and digital wireline log data for this research work, iThemba Labs, University of the Western Cape Physics and Chemistry departments for HRTEM and Pore water analysis study respectively.

I am also deeply grateful to Petroleum Oil and Gas Corporation of South Africa (PetroSA) for financing the first phase of this research work, Gustavus E. Achie for chosen me in Africa region as the only benefactor of the 2009 AAPG grant-in-aid award.

My immense gratitude is due to Anthony Van-zyl and Libert Mombo of Schlumberger Information solutions for their kind assistance with respect to Petrel software. Their friendly response and timely training program on Petrel 2008 version added speed to the execution of this research. Without mincing words, I would also like to thank Dr. Daniel Mikes (Stellenbosch University) for going through my chapter five, the members of staff of Earth Science Department for their support and most especially Prof. Jan Van Bever Donker (Dean of Science) whom God has really used for me to complete this study. Special thanks go to my fellow post graduate students (Mr. S.A. Adekola, Mr. S.A. Akinyemi and others) for creating an enabling environment that contributed to the success of this study.

Finally, I am particularly grateful to my parents (Mr. & Mrs L.O Fadipe) and immediate family (O.T. Adetoba, Bola & Dupe Fadipe) for their continuous support during my studies.

# TABLE OF CONTENTS

	<b>PAGES</b>
<b>ABSTRACT</b>	<b>ii</b>
<b>DECLARATION</b>	<b>iv</b>
<b>ACKNOWLEDGEMENT</b>	<b>v</b>
<b>TABLE OF CONTENTS</b>	<b>vi</b>
<b>LIST OF FIGURES</b>	<b>x</b>
<b>LIST OF TABLES</b>	<b>xiii</b>
<b>LIST OF APPENDICES</b>	<b>xiv</b>
<b>CHAPTER ONE</b>	<b>1</b>
Introduction	1
1.2 Aims and Objectives of Study	2
1.3 Scope of Work	3
1.4 Study Area	3
1.5 Previous Work on Orange Basin	5
1.5 General Overview of Subsurface Studies	7
<b>CHAPTER TWO</b>	<b>7</b>
2.0 Literature Review	8
2.1 Core Analysis	8
2.2 Well Logs	10
2.3 Classification of Geophysical Wireline Logs	12
2.3.1 Classification Based on Usage	12
2.4 Characteristics of Selected Wireline Logs	12
2.4.1 Radioactive Logs	12
2.4.2 Gamma Ray Logs	13
2.4.3 Neutron Logs	14
2.4.4 Density Log	15
2.4.5 Sonic Log	17
2.4.6 Spontaneous Potential Logs	18
2.4.7 Resistivity Logs	20
2.5 Systems tracts, Sequence boundary and Parasequence sets	20
2.5.1 Falling stage Systems tract	20
2.5.2 Lowstand Systems tract	21



2.5.3	Transgressive Systems tract	21
2.5.4	Highstand Systems tract	21
2.5.5	Regressive Systems tract	22
2.5.6	Sequence Boundary	22
2.5.7	Maximum Flood Surface	23
2.6	Depositional Environment and Facies	25
2.7	Reservoir Quality and Facies Discrimination	25
2.8	Diagenetic Studies	26
2.9	Hydrocarbon Recovery	26
2.10	Quantitative Mineralogy Techniques	27
2.11	Geochemistry of Pore Water	30
<b>CHAPTER THREE</b>		<b>31</b>
3.1	Geological Background of the Orange Basin	31
3.2	Offshore Basin	32
3.3	Regional Geology of the Orange Basin	33
3.4	Sequence Stratigraphic and Chronostratigraphic Framework	35
3.5	Tectonic Setting of the Orange Basin	36
3.6	Stratigraphy and Brief History of Albian Age Reservoir	38
<b>CHAPTER FOUR</b>		<b>40</b>
4.0	Materials and Analytical Methods	40
4.1	Wireline Log Loading	41
4.2	Core Description	42
4.3	Petrophysical Calculation Procedures	43
4.3.1	Volume of shale	43
4.3.2	Porosity	43
4.3.3	Formation Water resistivity	44
4.3.4	Water Saturation ( $S_w$ ) and Hydrocarbon Saturation ( $S_{hc}$ )	45
4.3.5	Bulk Volume of Water ( $V_b$ )	45
4.3.6	Irreducible Water Saturation ( $S_{wir}$ )	45
4.3.7	Permeability (K)	45
4.4	Thin Section	46
4.5	Scanning Electron Microscopy	46
4.6	X-ray Diffractometry (XRD)	47
4.7	Fourier Transform Infrared Spectrometry (FTIR)	48

4.8	High Resolution Transmission Electron Microscopy (HRTEM)	48
4.9	Pore Water Geochemistry	49
4.10	X-ray Fluorescence Spectrometry (XRF)	49
<b>CHAPTER FIVE</b>		<b>50</b>
5.0	Core Description Results and Interpretation	50
5.1	Lithofacies of A-G1 Core # 1	53
5.1.1	Facies 1: Fine grained sandstone	53
5.1.2	Facies 2: Very fine grained sandstone	53
5.1.3	Facies 3: Mudstone	54
5.2	Lithofacies of A-K1 Core # 1 & Core # 2	55
5.2.1	Facies 1: Fine grained sandstone	56
5.2.2	Facies 2: Very fine grained sandstone	56
5.2.3	Facies 3: Mudstone	57
5.3	Lithofacies of A-W1 Core	59
5.3.1	Facies 1: Fine grained sandstone	59
5.3.2	Facies 2: Very fine grained sandstone	59
5.3.3	Facies 3: Mudstone	60
5.4	Mineralogical Prediction from Core Description	62
5.5	Well Log Interpretation Correlation	64
5.5.0	Geological Interpretation of Wireline Logs	65
5.5.1	Reservoir unit geophysical log interpretation of A-G1	66
5.5.2	Reservoir unit geophysical log interpretation of A-K1	70
5.5.3	Reservoir unit geophysical log interpretation of A-K2	73
5.5.4	Reservoir unit geophysical log interpretation of A-Y1	75
5.5.5	Reservoir unit geophysical log interpretation of A-W1	77
5.6	Mineralogical Predictions from Well Logs	80
5.6.1	A-G1 Well	81
5.6.2	A-K2 Well	84
5.6.3	A-W1 Well	85
5.6.4	A-K1 Well	87
5.6.5	A-Y1 Well	87
5.7	Well Correlation and Stratigraphic Analysis	90
5.7.1	Log Correlation	90
5.7.2	Description of Correlated Section	90



5.8	Petrophysical Analyses	92
5.8.1	Petrophysical Evaluation of the Wells	97
<b>CHAPTER SIX</b>		<b>99</b>
6.0	Petrography and Geochemistry	99
6.1	Results and Discussion	99
6.1.1	Thin section petrography for well A-G1	99
6.1.2	Thin section petrography for well A-K1	102
6.1.3	Thin section petrography for well A-W1	106
6.2.1	SEM results and discussion for A-G1 well	112
6.2.2	SEM results and discussion for A-K1 well	114
6.2.3	SEM results and discussion for A-W1 well	119
6.3	XRD Results	123
6.3.0	XRD results of A-G1 well	123
6.3.1	XRD results of A-K1 well	124
6.3.2	XRD results of A-W1 well	127
6.4	FTIR Results	129
6.4.1	FT-IR results of A-G1 well	129
6.4.2	FT-IR results of A-K1 well	130
6.4.3	FT-IR results of A-W1 well	131
6.5	High Resolution Transmission Electron Microscopy	134
6.5.1	HR-TEM Results of A-G1 well Reservoir zone	134
6.5.2	HR-TEM Results of A-K1 well Reservoir zone	137
6.5.3	HR-TEM Results of A-W1 well Reservoir zone	139
6.5.4	Semi-quantitative x-ray diffraction (XRD) results	142
6.6	Pore Water Geochemistry	143
6.6.1	Pore water geochemistry of A-G1 well	143
6.6.2	Pore water geochemistry of A-K1 well	145
6.6.3	Pore water geochemistry of A-W1 well	147
6.7	Bulk Rock Geochemistry	149
6.7.1	Geochemical classification of sandstones	150
6.7.2	Weathering and paleo-environmental conditions during deposition	154
6.7.2.1	Sediment maturity	154
6.7.2.2	Paleo-weathering	156
6.7.2.3	Climate	157

6.7.3	Tectonic setting and source rock lithology of the source area.	158
6.8	General diagenetic sequence for the studied wells	159
<b>CHAPTER SEVEN</b>		<b>164</b>
7.0	Conclusions and Suggestions for future work	164
7.1	Core and Well Log	164
7.2	Petrography and geochemical characteristics	165
7.3	Pore water geochemistry	166
7.4	Suggestions for future work	166
<b>REFERENCES</b>		<b>167</b>

## LIST OF FIGURES

Figure 1.0	Frame work diagram of the thesis	2
Figure 1.1	Location map showing Orange basin, offshore South African coast	4
Figure 1.2	Location map showing study well distribution across block 2A Orange Basin.	5
Figure 2.1	Sidewall-Coring scheme	10
Figure 2.2	Gamma Ray Tool	14
Figure 2.3	Schematic of Compensate neutron tool	16
Figure 2.4	Schematic of dual-spacing density logging device	15
Figure 2.5	Sonic Logging tool showing Receiver	18
Figure 2.6	Spontaneous Potential Logging tools	19
Figure 2.7	illustrating the different depositional system tracts	24
Figure 2.8	Model of the different System Tract	24
Figure 3.0	South Africa continental Margin and Oceanic crust	31
Figure 3.1	Topography derived from satellite image showing sea floor and continental margin surrounding South Africa	32
Figure 3.2	Western, eastern and southern offshore zones of South Africa	33
Figure 3.3	Topographic and Bathymetric Map of the Orange River Basin	35
Figure 3.4	Sequence Chronostratigraphic framework of the Orange Basin	36
Figure 3.5	Generalized W-E Cross-sections through the Orange River Basin	38
Figure 4.1	The flow chart of the research methodology	41
Figure 4.2	Scanning and detection system in scanning electron microscope	47
Figure 5.0	Core Representations for the Three Cored Wells Showing	

& 5.1	Different Sedimentary Structures	51
Figure 5.2	Core graph showing the summary of the core description for A-G1 results.	55
Figure 5.3	Core graph showing the summary of the core description for A-K1 results.	58
Figure 5.4	Core graph showing the summary of the core description for A-W1 results.	61
Figure 5.5	Wireline Log delineating reservoir sand A and B of A-G1 well	68
Figure 5.5.1	Wireline Log delineating reservoir sand C and D of A-G1 well	69
Figure 5.5.2	Wireline Log delineating reservoir sand A and B of A-K1 well	71
Figure 5.5.3	Wireline Log delineating reservoir sand C of A-K1 well	72
Figure 5.5.4	Wireline Log delineating reservoir sand A and B of A-K2 well	74
Figure 5.5.5	Wireline Log delineating reservoir sand A and B of A-Y1 well	76
Figure 5.5.6	Wireline Log delineating reservoir sand A and B of A-W1 well	78
Figure 5.5.7	Wireline Log delineating reservoir sand C of A-W1 well	79
Figure 5.6.1	Crossplots of Density (RHOB) against Neutron (NPHI) for Mineralogical predictions in A-G1 well.	83
Figure 5.6.2	Crossplots of Density (RHOB) against Neutron (NPHI) for Mineralogical predictions in A-K2 well.	84
Figure 5.6.3	Crossplots of Density (RHOB) against Neutron (NPHI) for Mineralogical predictions in A-W1 well.	86
Figure 5.6.4	Crossplots of Density (RHOB) against Neutron (NPHI) for Mineralogical predictions in A-K1 well.	88
Figure 5.6.5	Crossplots of Density (RHOB) against Neutron (NPHI) for mineralogical predictions in A-Y1 well.	89
Figure 5.7.1	Stratigraphic cross-section across the studied wells.	91
Figure 5.7.2	Environmental correction chart for neutron porosity (NPHI) log to compensated neutron Log (CNL).	95
Figure 6.1.1	Thin section photomicrographs of the reservoir zone in A-G1 well.	101
Figure 6.1.2	Thin section photomicrographs of the reservoir zone in A-K1 Core # 1 well.	104
Figure 6.1.3	Thin section photomicrographs of the reservoir zone in A-K1 Core # 2 well.	105
Figure 6.1.4	Thin section photomicrographs of the reservoir zone in A-W1 well.	107

Figure 6.1.5	General Cartoon Line drawings of different diagenetic features and altered mineral constituents observed in thin sections.	108
Figure 6.1.6	Thin section photomicrographs of the remaining reservoir zone in A-W1 well.	110
Figure 6.2.0	Scanning Electron Microscopy photograph of A-G1 well.	113
Figure 6.2.1	Scanning Electron Microscopy photograph of A-K1 well.	115
Figure 6.2.2	Scanning Electron Microscopy photograph of the remaining A-K1 Well.	117
Figure 6.2.3	Scanning Electron Microscopy photograph for A-W1 well.	120
Figure 6.2.4	Scanning Electron Microscopy photograph for the remaining A-W1 well.	122
Figure 6.3.1	XRD spectra of A-G1 well.	124
Figure 6.3.2	XRD spectra of A-K1 Core # 1 well.	125
Figure 6.3.3	XRD spectra of A-K1 Core # 2 well.	126
Figure 6.3.4	XRD spectra of A-W1 well.	128
Figure 6.4	Representative FTIR spectra of A-G1 well.	130
Figure 6.4.1	Representative FTIR spectra of A-K1 well.	131
Figure 6.4.2	Representative FTIR spectra of A-W1 well.	132
Figure 6.5.1	High Resolution Transmission Electron Microscopy photograph of A-G1.	136
Figure 6.5.2	High Resolution Transmission Electron Microscopy photograph of A-K1.	138
Figure 6.6.1	Pore water plot result of A-G1 well.	144
Figure 6.6.2	Pore water plot result of A-K1 well.	146
Figure 6.6.3	Pore water plot result of A-W1 well.	148
Figure 6.7.1	Analysis of alkali content of the Albian age sandstones based on major element geochemistry.	152
Figure 6.7.2	Classification of terrigenous sandstone using Log (Na <sub>2</sub> O/K <sub>2</sub> O) Versus Log (SiO <sub>2</sub> /Al <sub>2</sub> O <sub>3</sub> ) from Pettijohn et al., (1972), modified by Herron (1988).	155
Figure 6.7.3	Geochemical classification of samples from Albian age sandstone based on Log (SiO <sub>2</sub> /Al <sub>2</sub> O <sub>3</sub> ) vs. Log (Fe <sub>2</sub> O <sub>3</sub> /K <sub>2</sub> O) diagram (after Herron, 1988).	156
Figure 6.7.4	SiO <sub>2</sub> vs. CIA (Chemical alteration index) of the studied Albian	

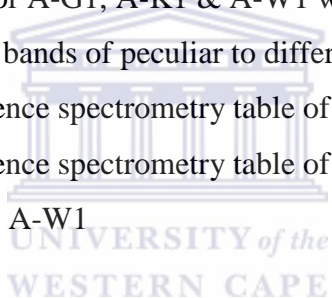
	age sandstones.	157
Figure 6.8.1	Paragenetic Sequence of reservoir sandstone of the Albian formation of well A-G1.	161
Figure 6.8.2	Paragenetic Sequence of reservoir sandstone of the Albian formation of well A-K1.	162
Figure 6.8.3	Paragenetic Sequence of reservoir sandstone of the Albian formation of well A-W1.	163

### LIST OF TABLES

Table 1.0	Names and Location of Wells.	4
Table 5.0	Summary of core findings.	63
Table 5.1	Summary of the Geophysical Well Logs Interpretation of the Reservoir Units of the Wells in this Study.	80
Table 5.2	Log responses of Major Groups.	82
Table 5.8.1	Well information used for petrophysical evaluation in the studied Wells.	94
Table 5.8.2	Summary for the sampled data of Log derived petrophysical Properties of the Albian age sandstone of the five wells.	96
Table 6.2	Energy dispersive spectrometry (EDS) results of A-G1 well.	113
Table 6.2.1	Energy dispersive spectrometry (EDS) results for A-K1 well.	118
Table 6.2.2	Energy dispersive spectrometry (EDS) results for A-W1 well.	122
Table 6.4	Key peaks used in identifying clay minerals in FTIR.	129
Table 6.4.1	showing the wave numbers ( $\text{cm}^{-1}$ ) of different minerals in studied Well.	133
Table 6.5.1	HR-TEM/EDS data of A-G1 well sandstone samples.	135
Table 6.5.2	HR-TEM/EDS data of A-K1 well sandstone samples.	141
Table 6.5.3	HR-TEM/EDS data of A-W1 well sandstone samples.	141
Table 6.5.4	XRD semi-quantitative estimate of the phase abundance (% weight) for selected samples across the wells in the study area.	142
Table 6.7.1	Mean composition of principal sandstone classes and average Albian age sandstone for the studied wells.	150
Table 6.7.2	Major oxides (wt %) of the selected sandstone samples of the Albian age gas bearing formation along with their calculated Chemical index of alteration (CIA).	153

## LIST OF APPENDIX

Appendix A	Table of raw data obtained from core examination of A-G1 well	182
Appendix B	Table of raw data obtained from core examination of A-K1 well	183
Appendix C	Table of raw data obtained from core examination of A-W1 well	184
Appendix D	Photomicrograph of A-G1 under PPL	185
Appendix E	Photomicrograph of A-K1 under PPL	186
Appendix F	Photomicrograph of A-W1 under PPL	187
Appendix G	Energy dispersive spectrometry plot of A-G1 well	188
Appendix G	Energy dispersive spectrometry plot of A-W1 well	190
Appendix G	Energy dispersive spectrometry plot of A-K1 well	191
Appendix H	XRD raw spectra for A-G1 well	192
Appendix I	XRD raw spectra for A-K1 well	193
Appendix J	XRD raw spectra for A-W1 well	194
Appendix K	FTIR spectra for A-G1, A-K1 & A-W1 wells	195
Appendix L	Table showing bands of peculiar to different functional groups	201
Appendix M	X-ray fluorescence spectrometry table of A-G1, A-K1 & A-W1	202
Appendix N	X-ray fluorescence spectrometry table of trace elements for A-G1, A-K1 & A-W1	203



## CHAPTER ONE

### 1.1 **Introduction**

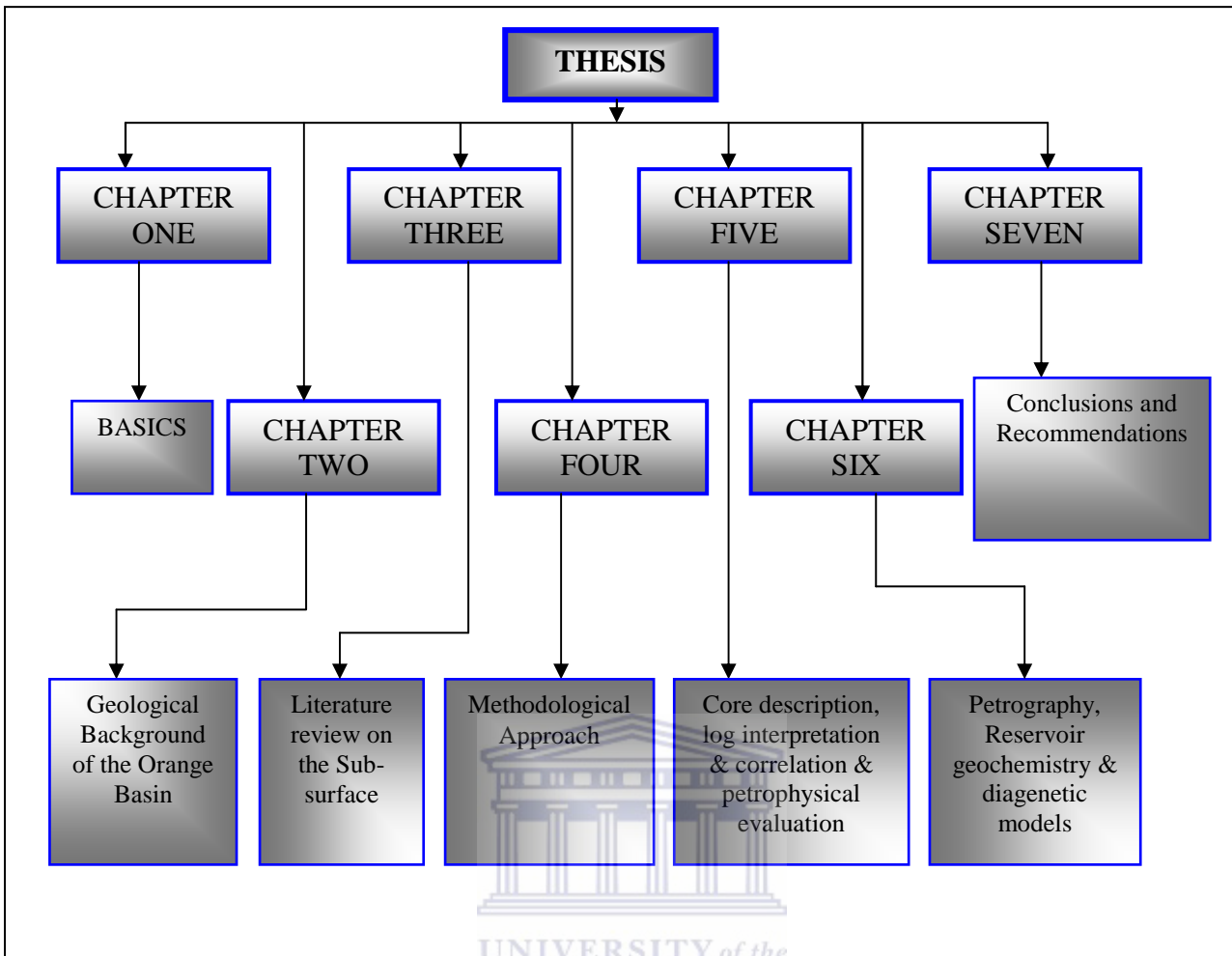
---

The search for hydrocarbon in the Orange basin, South West of South Africa continental margin has been intensive due to its economic importance to the country. Therefore, there is a need for special attention in order to increase the economic viability of the basin. A successful evaluation of petrophysical properties is vital in assessing the hydrocarbon accumulation potential of reservoir rocks before major decisions are taken. This study will involve reservoir quality assessment and the estimation of petrophysical properties such as porosity, permeability and water saturation deduced from core analysis and well log. The principle of measurement involved in core analysis and geophysical logs are well understood and the techniques have made continuous sophisticated advancement.

Reservoir properties are derived from the individual characteristics of mineral constituents forming the rock (Serra, 1986) but the minerals themselves are seldom considered in the evaluation of rock properties. The study of sandstones in the laboratory reveals that various reservoir properties such as density, porosity, radioactivity, resistivity, magnetic susceptibility and sonic velocity may vary depending on the presence of clay and heavy minerals, rock fabric and carbonaceous materials (Emerson, 2000).

In petroleum reservoir evaluation, mineralogical studies have demonstrated to be crucial in the Northern North Sea when porosity evaluation from logs was complicated by radioactive and heavy minerals and the evaluation had to resort to an integrated approach which includes mineralogical studies with the core and log analyses (Nyberg et al., 1978). However, mineralogical input in geophysical log analysis has also provided porosity evaluation results that are more comparable with direct measurements carried out on core samples (Guest, 1990).

The existence of a reservoir rock (typically sandstones and fractured limestones) is based on evaluation of petrophysical properties of the rock; this could provide a more valuable basis for further reservoir development studies. The importance of mineralogical studies in the evaluation of reservoir rock properties is premised on the need to understand the influence of those minerals or rock properties on the geophysical log responses which are often the tools available for evaluating those parameters.



**Figure 1.0:** Frame work diagram of the thesis

## 1.2 Aims and Objectives of Study

This study is aimed at evaluating the reservoir potential of sandstone intervals of wells in Ibhubesi field of the Orange Basin through the interpretation, integration and critically juxtaposing the results from core analysis, mineralogical studies, sedimentological analysis to correct the key petrophysical parameters obtained from the wire line logs in order to predict an effective reservoir quality and to construct a diagenetic model. The physical rock characteristics such as fluid type, lithology and hydrocarbon bearing zones will be qualitatively defined while parameters such as porosity, permeability, resistivity of formation water, water saturation and hydrocarbon saturation will be estimated using Interactive Petrophysics and Petrel calculator function for selected reservoir intervals in all the wells. Wire line log data will be further used to identify productive zones to determine depth, thickness of



zones, to distinguish between oil, gas or water in a reservoir and to estimate the hydrocarbon reserves.

The main objective of this study is to investigate the effect of mineralogy on the petrophysical properties of sandstone. The research approach shall be:

To determine the mineralogy of a range of core samples from a selected reservoir interval in the five wells.

- (i) Establish the correlation between mineralogy, geophysical log response and key rock properties.
- (ii) Use these correlations to refine the methods of petrophysical interpretations from logs based on specific mineralogical characteristics.
- (iii) Present petrophysical characteristics of selected reservoir sands from petrophysical analysis.

### **1.3 Scope of Work**

The scope of work is as follows:

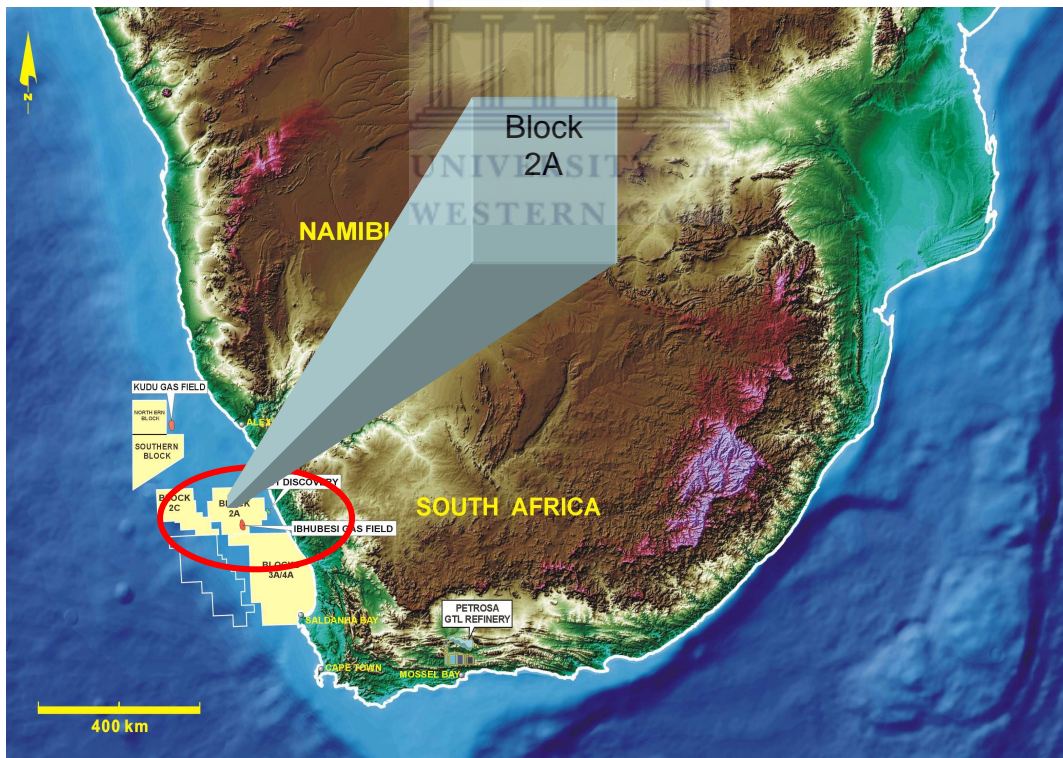
- Characterization of the different sand units within the reservoir zones
- Assessment of the impact of clay and cement composition on porosity and permeability distribution.
- The stratigraphic correlation of wells under study, to understand the distribution of sands across the wells.
- X-ray diffraction for bulk mineralogy quantification and phase identification.
- Analysis of pore systems in cores through the use of thin section petrography and Scanning electron microscopy
- Establishment of the diagenetic history through the interpretation of the petrographic and geochemical analysis results

### **1.4 Study Area**

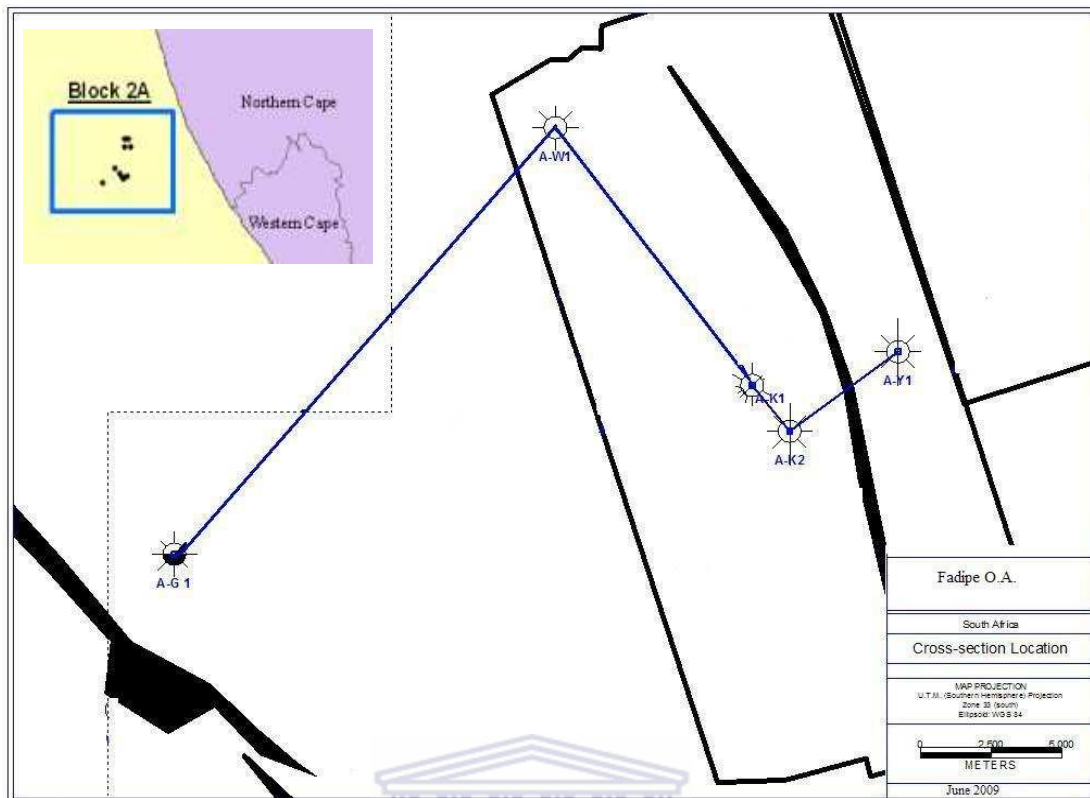
Orange Basin, South Africa underlies the Atlantic Ocean, offshore west coast and it extends 50km in length between Cape Town and the South African-Namibian border with water depth that ranges between 250m at the continental shelf and 2500m in deepwater environment. The study area is bounded in the west and east by geographical co-ordinates (Table 1.0) of each studied well which are located within Block 2A. The study is focused on reservoir zones encountered by the five wells in the Block 2A of the basin which include: AW-1, AK-1, AK-2, AY-1, and AG-1. Figure 1.1 below shows the distribution of the wells across the block within the basin.

**Table 1.0: Names and Location of Wells**

Well Name	Location	UTM Format	Depth (MD)
AW-1	Lat: 30° 46' 31.096"S Long: 16° 37' 24.65"E	Lat: 655362.68 Long: 6594173.09	3511
AK-1	Lat: 32° 41' 21.88"S Long: 17° 13' 59.27"E	Lat: 6381240.88m N Long: 709440.66m E	3681
AK-2	Lat: 30° 52' 24.144"S Long: 16° 36' 41.520"E	Lat: 6583620.92m N Long: 654146.26m E	3430
AY-1	Lat: 30° 50' 48.94"S Long: 16° 39' 3.812"E	Lat: 657881.740N Long: 6586195.316E	3407
AG-1	Lat: 16° 23' 06.27"E Long: 30° 54' 58.23"S	Lat: 6579168.30m N Long: 632436.07m E	4100



**Figure 1.1:** Location map showing Orange Basin, offshore South African coast (PASA 2003).



**Figure 1.2:** Location map showing distribution of wells in this study across Block 2A Orange Basin.

### 1.5 Previous Work on Orange Basin

The Orange Basin has been relatively less explored in terms of the geology, stratigraphy, paleo-geography, structural features and hydrocarbon potential of reservoir rocks. This is one of the reasons why the academics need to collaborate with the oil companies so as to carry out a comprehensive research to bridge the gap for a better understanding of the basin.

Previous works have looked into the uses of seismic sections in calibrating the fluid flow predictions against observed gas chimneys (Kuhlmann et al., 2007). Recently gas seepage events have been mapped from seismic section in the Orange Basin (Ben Avraham et al., 2002). Natural gas leakage is a common phenomenon observed along most continental margins of the world. These gases are in form of methane and carbon dioxide which are major contributors to green house gases (Kuhlman et al., 2007),

Jikelo (1999), worked on the “Petroleum Prospectivity of the deepwater Orange Basin, South Africa”, using new 2D seismic data which allows a more complete understanding of the hydrocarbon potential of the deepwater Orange Basin, and therefore predicted sandstone reservoirs in the Lower Cretaceous.

Stevenson and McMillan (2004) worked on the Upper Cretaceous succession of the proximal Orange Basin, using seismic stratigraphic analysis of shallow seismic Sleevegun data, as well as cores obtained from sea-bed samples. The paleo-environment of the incised valley was looked at in details. Results from the studies conducted shows fluvial incision, which is dominant within the Lower Turonian and Upper Coniacian. Fluvial flood plain facies reflects a waterlogged, highly reduced environment, which favours the formation of groundwater ferricretes.

Van der spur (1999) looked into the prospectivity of the Northern Orange Basin by interpreting the seismic of 3 wells in the area. He discovered the phases of sedimentation and in-turn used this valuable information to determine the depositional environment. These methods were used to predict the petroleum plays (rift and drift). The rift plays are represented by possible lacustrine sandstone, trapping oil from organic rich claystone as encountered in A-J graben of the south. He concluded that the northern-most sectors of the South African territory have proven discovery of huge gas reserve.

Paton et al. (2007) investigated the petroleum systems within the southern Orange Basin. The model created was used to predict the present day gas seepage at the sea floor and calibrated it with observed seepage events. Basin modeling results obtained from the study of the southern Orange Basin indicates that the main period for hydrocarbon generation occurred in the late Cretaceous. This event was then followed by erosion at the end of the Cretaceous, deposition altered during the shelf-break and sediment volumes prograded into the deep basin. This led to a second period of maturation which was mainly focused on prograding Tertiary wedges. The model predicts that the kitchen area is active up until the present day and is the source of hydrocarbons that are observed seeping from the sea-floor at present.

Hirsch et al. (2007) investigated the Orange Basin located on the south-west African continental margin in an attempt to proffer solution to some pending challenges as regard how the mantle and crustal dynamics interact to generate the observed margin geometries. It was noted that the basin fill is considered to consist of classic rift-drift passive margin sequence (which recorded the break-up of Gondwana and later opening of the South Atlantic Ocean). The study concluded that the best-fit model requires dense, presumably mafic material (in middle and lower crust of the basin) an abrupt change to less dense material near the coast to reproduce the observed results.

## 1.6 General Overview of Subsurface Studies

The study of the subsurface has improved tremendously over the years with the use of geophysical methods. Measurements within a geographical restricted area are used to establish the distribution of physical properties that reflect the distinguishing characteristics of the local subsurface geology. Once these methods especially seismic have been used to locate favourable geological features for likely hydrocarbon accumulation and subsequently a possible reservoir position identified, an exploratory well will be drilled through the prospective structure to open way for various techniques of evaluating the resources. Hydrocarbon accumulation is mostly found in the pore spaces of reservoir rocks such as sandstone, limestone and dolomites. In order to have an idea of how viable economically a reservoir is, some basic petrophysical parameters need to be generated and the reservoir quality needs to be evaluated. These include porosity, permeability, hydrocarbon saturation, thickness and extent of reservoir formation and the depositional environments.

Well logging is the process of recording various physical, chemical, electrical and other properties of the rock/fluid mixture penetrated by drilling a well into the earth's crust (Crain, 2004). Petrophysics encompasses standard log analysis and various techniques of characterizing reservoir rocks through derivation of conventional reservoir parameters. It is by far one of the most important and useful field of science available to petroleum geologists. However, for a clearer and better understanding of any reservoir performance, the integration of sedimentological studies with reservoir analysis is very imperative.

In the early stages of planning exploration and development in a new area, the surface seismic survey is used to delineate prospective structural or stratigraphic traps. Improvement in digital filtering has led to high quality results under favourable conditions. Reservoir characterization and evaluation has progressed beyond the conventional manual petrophysical analysis and their use in estimating recoverable hydrocarbons in reservoir rocks. Several windows based softwares packages for petrophysical analysis are available. Where available, well and seismic data are input in the correct format, they can be used to carry out petrophysical analysis and visualize the distribution of reservoirs parameters within a framework of 3D reservoir model. Good examples are PETREL, Interactive Petrophysics and Fast Tracker (FugroJason).

## CHAPTER TWO

### **2.0 Literature Review**

---

The topics included in this review focused on core description, geophysical logs, depositional environments, facies and diagenetic studies. The discussion on core analysis concentrates on the possible source of errors that may arise during the analysis. Attention is also paid to the principle of various geophysical logging measurements and to the effect of different minerals on the logs and the procedures used in the evaluation of the rock properties. The review of various mineralogical techniques is limited to those most commonly used for sedimentary rocks and the discussion is based on the applicability of each technique in reservoir evaluation. An overview of the various application of mineralogy in reservoir assessment is also included.

### **2.1 Core Description**

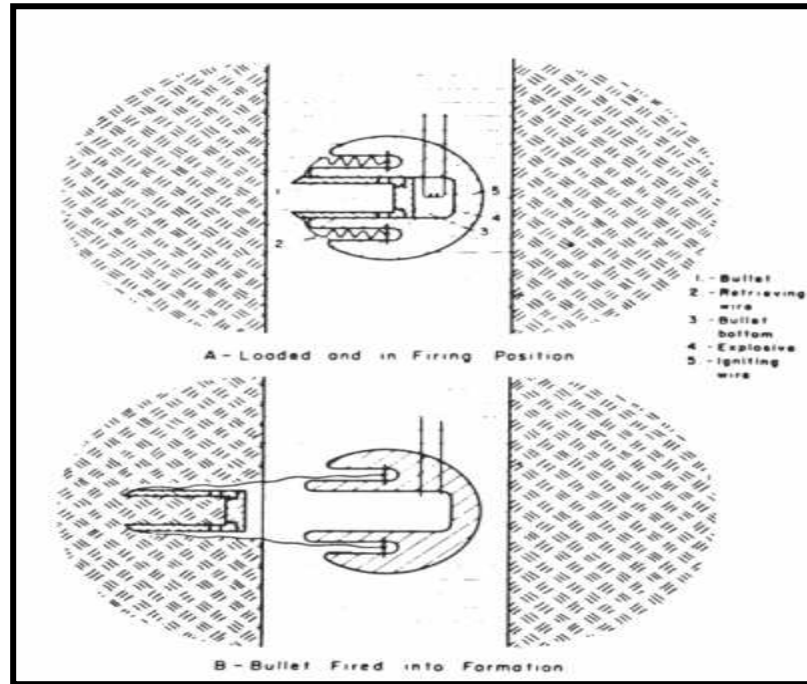
Core analysis is the starting point for a wide range of geologic and engineering studies; it's the only tool in the reservoir assessment that directly measures many important formation properties. The analysis may aim to determine among other things porosity, permeability, grain size distribution, grain density, and mineral composition, effect of overburden stress and sensitivity of fluid (Bateman, 1985).

Laboratory core analysis could provide very accurate measurements. Laboratory test procedure, core handling and sample preparation may introduce damage to the core if incorrectly performed (Sinclair and Duguid, 1990). Destructive processes, such as plugging may cause partial disintegration of formation and thus significantly modify the results of petrophysical property measurement. Partial disintegration of cores, due to aforementioned process (plugging) has been noted to cause highly optimistic permeability measurements (Hurst 1987b). Unnecessary breakage may also be introduced when removing the cores from the core barrel, transporting them, and laying them out in the laboratory. Laboratory procedures such as drying of the sample may drive off all the water in the clay particles (Sinclair and Duguid 1990). This may cause misidentification of minerals on the petrophysical properties (e.g. swelling).

Core analysis has evolved from qualitative geological description to the use of sophisticated analytical tools, such as scanning electron microscope (SEM), x-ray diffraction (XRD), yet there are no uniform accepted experimental procedures or calibration standard (Juhasz, 1990). There may be significant discrepancies in the analysis of a particular reservoir by different laboratories and the results may be valid

only within set of procedures followed by each individual laboratory. For example, porosity measured in core plugs dried using humidity controlled methods has been noted to be consistently lower than those measured from oven dried core plugs (Penney and Looi, 1996). Analysis of similar set of core samples by different laboratories according to their respective procedures may thus result in considerable differences in the assessment of potential reservoir sequence. The manner of drying core samples, for examples was shown to be critical in preserving the in-situ morphology of some minerals (illite) and in understanding the differences in permeability measurements obtained by core analysis and well test data (Pallat et al., 1984). A similar observation has been noted by McHardy et al. (1982) in comparing the morphology of illite contained in samples that have undergone different drying processes. Due to lack of standards, the validity of rock properties evaluated based on particular core analysis procedures may not always be considered, and estimation of the magnitude of errors that may arise during the analysis is not possible. Thus, the errors are most likely to carry on to where core analysis results are applied. One of the serious consequence is that core analysis results may be seriously different from geophysical log data, and, in such cases, predictions from geophysical logs are sometimes doubtful without consideration of laboratory analytical procedures.

Other coring methods such as sidewall coring could be carried out when additional rock samples are required after the well has been drilled and before it has been cased. Sidewall cores are obtained with wireline tool from which a hollow cylindrical bullet is fired into the formation and retrieved after each bullet has been fired into the formation wall by free pull by wires connecting the barrel to the gun (Fig. 2.1). Core barrels are available for penetrating formations of different hardness. The type of barrel and size of charges are varied to optimize recovery in different formations. The problem with coring lies in the tendency of formation samples to undergo physical changes on its journey from the bottom of the well to the surface. More sophisticated coring mechanism that can preserve the orientation, pressure and original fluid saturations of the core samples have been developed.



**Figure 2.1:** Sidewall-Coring Scheme (modified from Schlumberger, 1972)

## 2.2 Well Logs

Well logs are class of the most useful and important tools available to petroleum geologists. They are products of survey operations consisting of one or more set of digitized datas. It involves lowering a suite of petrophysical instruments down the hole. Data from the formation are transmitted to the surface and are recorded as continuous log as instrument is being pulled from the bottom of the hole to the surface. They are used to identify and correlate their physical properties and the nature of the fluids they contain. While drilling a well, little can be learned about the potential of the penetrated formation. The analyses of the returned cuttings sometimes referred to as measurement while drilling (MWD) reveals the lithology. This is already one step towards giving petrophysical information as the rock bit penetrates the formations and indeed a primitive lithological log.

Geophysical logs however are not direct measures of the petrophysical properties of the formation. Instead, the logs record different formation parameters which are then translated into properties of geological significance during log interpretation. The formation parameters measured by the logs may be inherited to the formation itself, such as natural radioactivity, or may be induced parameters such as formation's resistance to an electrical current. Logs also record mechanical parameters in the borehole, such as the hole diameter and the down-hole temperature.



Geological sampling during drilling leaves a very imprecise record of formation encountered. Mechanical coring is slow and expensive even though, geophysical logs need interpretation to bring it to the level of geological or petrophysical experience, the strong points are their precision and ability to bridge the gap between well cuttings and core samples.

The petrophysical properties determined from core and logs are not always directly comparable. The difference may be attributed, among other things, to the scale of individual measurements. Core analysis especially when done on core plugs provides point data taken from segments of a continuous but heterogeneous sequence of rocks, while log measurements can be taken over a large interval of well and cover more of variation within the rock sequence. Considerable core therefore has to be observed when comparing data from core log analysis. The conditions under which core and log measurements are obtainable also differ considerably. Well logs measure in-situ parameters and these cannot always be directly attributed to geological factors. Logging devices are also affected by the environment, temperature, overburden pressure, casing and other factors (Rider, 1996).

Although, laboratory measurements can be made under simulated reservoir conditions, restoring cores to the original confining pressure is not always successful due to irreversible expansion when cores are drilled and brought to the surface. The difference between properties derived from core measurement and geophysical log complicate reservoir assessment and there is no basis from which to estimate the validity of determinations and the degree of error in each techniques. Important information can still be obtained by comparing core and log data pertaining to some properties. The most important information is probably correcting the depth of core against the depths recorded by well logs. This can be done for example, by comparing lithology from core descriptions and from neutron-density logs. Laboratory core measurement can also be used to calibrate log values, so that the logs can be interpreted more confidently in zones where no core samples are available. Core data can also be used to extrapolate micro-scale geological information, such as mineralogy data, so that it can be integrate at a reservoir scale.

After drilling, samples are obtained by sidewall sampling; samples of fluid are also taken with formation tester for identification and measurement of their properties to aid interpretation of some of the geophysical measurements. The first log to be obtained is the drilling time logs which records the rate of drilling progress because

this depends on the nature of the formation. The chips carried to the surface are filtered from the mud examined to provide the mud log. This gives an imperfect record of the formations penetrated by the drill; this is because chips travel to the surface at rates that depend on their size and density.

### **2.3 Classification of Geophysical Wireline Logs**

Wireline logs can be classified on either the principle of operation of logging tools or their usage i.e. measurable physical parameters and deductions that can be made from them.

Based on operational principle: wireline logs can be classified as:

1. Electrical logs: Spontaneous Potential (SP) and Resistivity logs.
2. Nuclear or Radioactive logs: Gamma ray (GR), Density and Neutron logs.
3. Acoustics log: Sonic logs.

#### **2.3.1 Classification Based on Usage**

1. Resistivity logs: Induction, Laterolog, Deep-resistivity logs.
2. Lithology logs: Gamma ray and Spontaneous potential.
3. Porosity logs: Sonic, Density and Neutron logs.
4. Auxiliary logs: Caliper, Dip meter, Bit Size logs e.t.c

### **2.4 Characteristics of Selected Wireline Logs**

#### **2.4.1 Radioactive Logs**

This log involves the use of radioactivity and is mainly to identify lithologies and help deduce the density and porosity particularly when a hole is cased, they will function with steel casing in place. Radioactivity logs belong to two groups which are:

- (i) Those that passively measure the natural gamma ray radioactivity of the formation
- (ii) Those that measure the induced radioactivity from strong radioactive sources in the Sonde.

The first group which uses a natural radioactive phenomenon is due mainly to potassium, thorium and Uranium of lithologies commonly present. Shale usually has the highest radioactivity, sands are intermediate, dolomite, limestone and quartz are very low. Occasionally, potash beds, ash bands and radioactive ores with higher activity than shale may be encountered. As shale is most radioactive, common sediment like shale log tool was first used primarily for identifying them. However, radioactive logs should be interpreted with utmost care for not all shales are radioactive, and not all radioactive formations are shale. Although the gamma ray

activity of shales varies widely on a world wide basis, it tends to be constant in a particular field.

This kind of log can be used in monitoring the injection of cement, depth by incorporating radioactive bullet into the collars at joints in the casing to produce sharp signals in the logs in combination tools. The spectral gamma ray is the borehole equivalent of gamma ray spectrometer. It differs from the simple gamma ray in recording separately the activities of potassium, thorium and uranium which can be used to depict the depositional environment of formations. Uranium is concentrated in marine sediments and thorium is in terrestrial sediments.

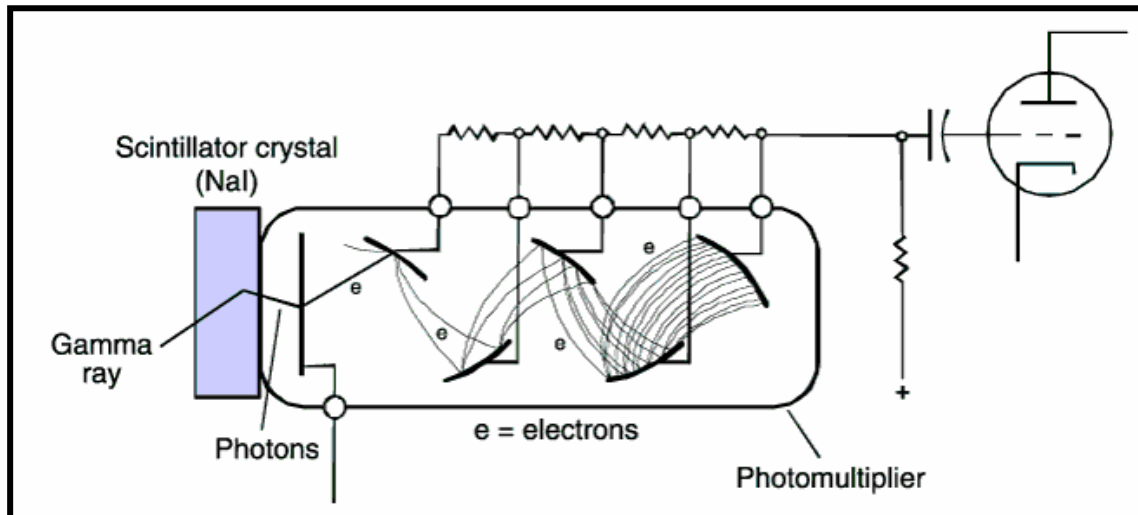
There are two types of these radioactive logs which are:

- (i) The Gamma-Gamma or formation density log which deals with densities
- (ii) The neutron or porosity logs

#### **2.4.2 Gamma Ray Logs**

A gamma ray log measures the natural gamma emission from sub-surface formations. Gamma rays originate from the radioactive elements in the minerals of the rock which can be effectively divided into potassium, uranium and thorium groups. When these elements decay into stable isotopes, they emit gamma ray energy in a specific frequency pattern. Potassium feldspar, volcanic ash, granite wash and some salt rich deposits containing potassium (e.g. Potash) may also give low gamma ray readings.

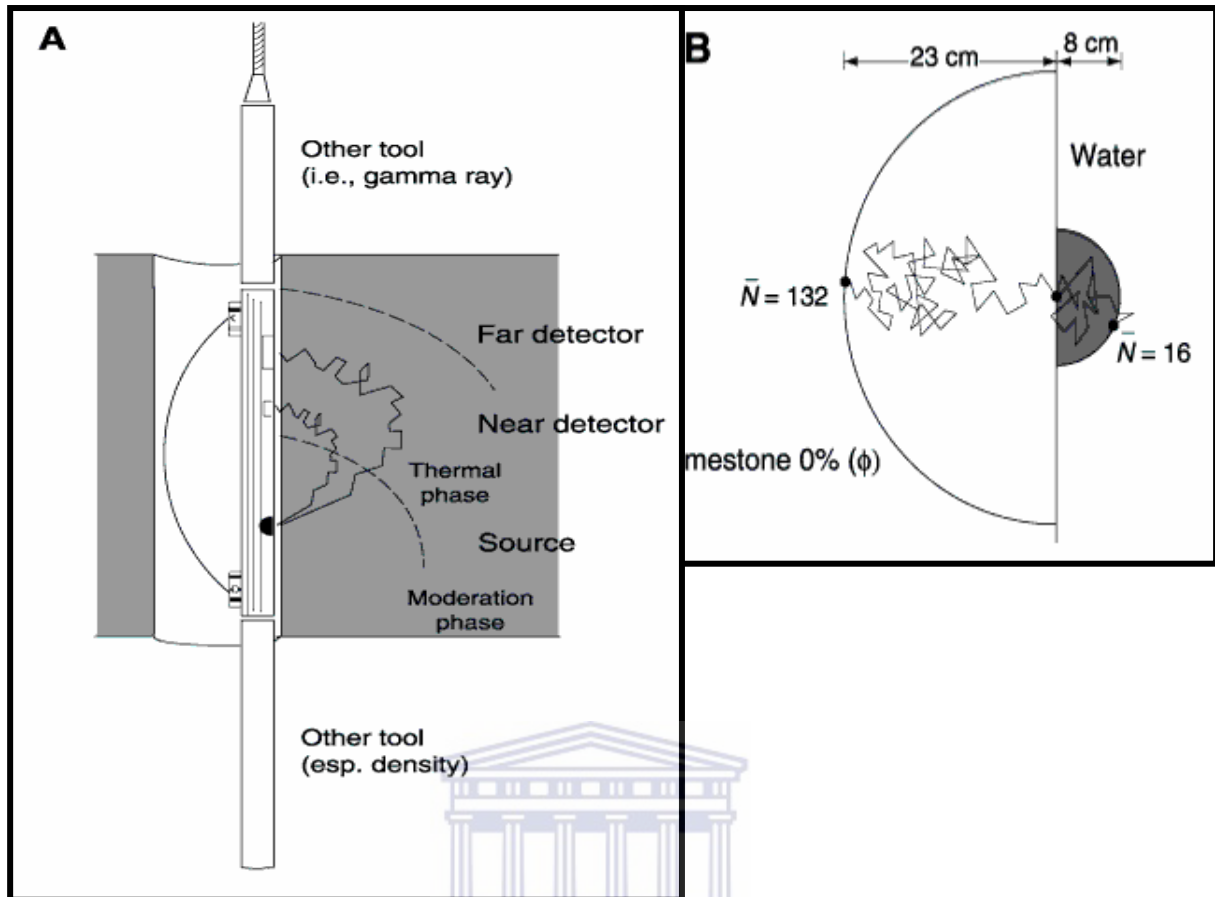
The standard unit of measurement is API (America Petroleum Institute). High gamma ray may not imply shaliness, but a reflection of radioactive sands such as potassium rich feldspar, glauconitic or micaceous sandstone. Gamma ray log is usually preferred to spontaneous potential logs for correlation purposes in open holes non-conductive borehole fluids, for thick carbonate intervals and to correlate cased hole logs with open logs.



**Figure 2.2:** Gamma ray tool (modified from Serra, 1984)

### 2.4.3 Neutron Log

Neutron logs are a porosity log that measures primarily the hydrogen ion concentration in a formation. In neutron, there is radioactive source from where formations are bombarded with radioactive (fast neutron rather than gamma rays. These neutrons traveling through formations only slow down significantly when they collide with atoms of similar mass i.e. Hydrogen atoms. Once they have been slowed by repeated collision, they are absorbed into the nuclei of heavier atoms present and cause them to emit gamma rays which are being recorded by counter. The number of neutron that reach the detector (neutron count) is affected by a number of factors in the borehole environment, such as hole size, mud weight and casing size (Bateman, 1985). An example of neutron tool designed to compensate environmental effects is illustrated in figure 2.3 A & B. The far detector is affected by both borehole and formation, while the near detector records signals from borehole. The ratio of the counting rates from the two detectors leaves only information from the formation, and is used to produce a record of neutron porosity index. The neutron tool however is also affected by clay minerals. Bound lattice water in the clay minerals may cause high porosity to be indicated by neutron log, but the effective porosity in such rocks may be zero due to the presence of fine clay particles in the pore spaces.



**Figure 2.3:** (A) Schematic of Compensate neutron tool (B) Schematic trajectories of neutron in limestone with no porosity and pure water (modified Rider, 1996).

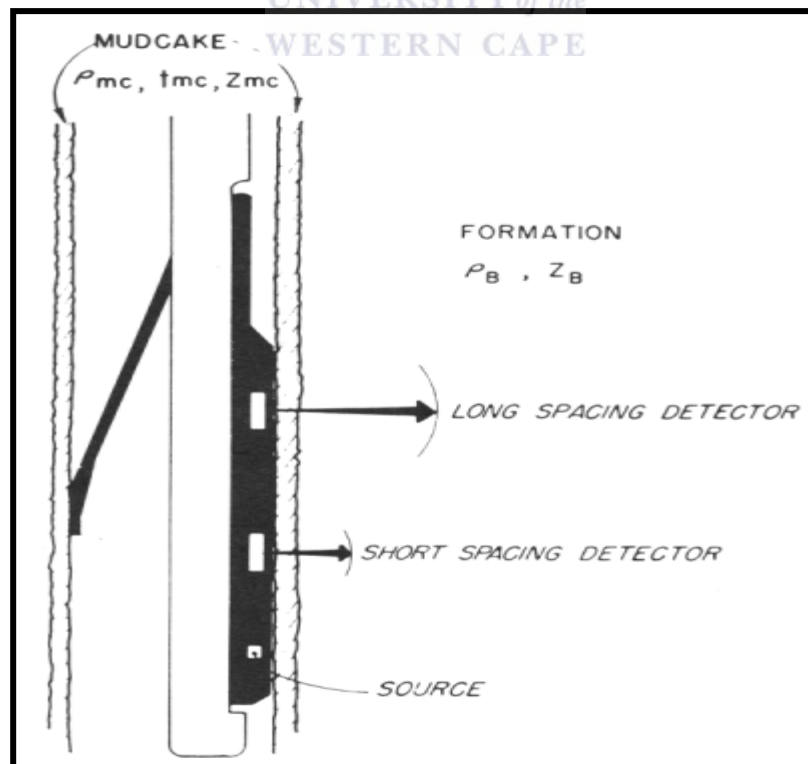
The more rapid the neutron slows down, the nearer to the counter the gamma rays are produced resulting in stronger signal since hydrogen is an important component of both water and oil. In clean formations, where the porosity is filled with water or oil, the neutron log measures liquid-filled porosity. Whenever pores are filled with gas rather than oil and water, neutron reads low values. This occurs as a result of less concentration of hydrogen in gas compared to oil or water. The lowering of neutron porosity by gas is called Gas effect. As the two tools, gamma-gamma and neutron respond to permeability and fluid in a similar way to SP and resistivity respectively, they are used to replace them in cased holes.

#### 2.4.4 Density Log

The density log gives a record of the bulk density of the formation, which includes the density of the rock or matrix and the density of the fluid enclosed in the pores. The density log is primarily used to determine porosity, lithology and the type of fluid in the pores. The logging techniques involve exposing the formation to gamma rays, which are backscattered and absorbed by the materials in the formation. The rate of

absorption and the intensity of the backscattered rays depend on the number of electrons (electron density) that the formation contains, which in turn is closely related to the common density of the materials. Dense materials have more electrons per unit volume (electrons/cm<sup>3</sup>), with which the gamma particles can collide and lose energy. Hence, higher energy is absorbed and backscattering is lower, in dense materials. In less dense formations, which have lower electron density, more gamma particles reach the detector and more counts are recorded per unit time. The detector counts are then translated to bulk density as presented in the density log.

An illustration of a density tool is provided in Figure (2.4). The tool consists of a gamma ray source and two detectors (near or short spacing and far or long spacing). The counting rate recorded by the detector allows correction for the effects of mud cake density and thickness. The geometry of the logging tool itself is also designed to minimize the effects of the drilling mud. The source and the detectors are mounted in a plough-shaped skid and pressed against the wall of the borehole by an eccentric arm. The force exerted by the arm, and the shaped design of the skid, allows the tool to cut through the mud cake so that the tool and the formation are in perfect contact, minimizing the contribution of the drilling mud in the recorded signal. The depth of investigation is around 10cm (Rider, 1996).



**Figure 2.4:** Schematic of dual-spacing density logging device (Modified from SPWLA Library)

Variations in the bulk density indicate changes in porosity, as water and hydrocarbon have lower densities than the solid (mineral or rock) materials.

The accuracy of porosity estimate from the density log depends on the choice of density values used for the matrix and the fluid in the above equation. The most reliable source of these values is from actual laboratory analysis. There is, however, a tendency to use assumed values in log analysis, especially when the lithology of formation is not known or when cores are not available. A rock density of  $2.65 \text{ g/cm}^3$  is no longer valid. A study of Jurassic Brent group in the North Sea has shown that, for a sand of 20% porosity, the error associated with each 1 % increase in the proportion of siderite led porosity decreases around 0.8 of one porosity percent if not accounted for in the matrix density values (Guest, 1990). In another study, the use of more accurate matrix density parameters giving consideration to the presence of organic matter and dense minerals resulted in least a 10 % increase in porosity values than by using the assumed value of  $2.65 \text{ g/cm}^3$  (Herron and Herron, 2000). The error in the porosity values incurred with incorrect choice of matrix density is approximately 50 times the error in the matrix value (Granberry et al., 1968). For example, an error of  $0.01 \text{ g/cm}^3$  in grain density will produce error of 0.5 % in porosity. The implications are that errors in matrix density parameters may have profound effects in the evaluation of reservoirs. When cores are not available to verify the calculated density log porosity and if the matrix density value used is too low, the calculated porosity will also be low and the potential of the reservoir could be seriously under-estimated.

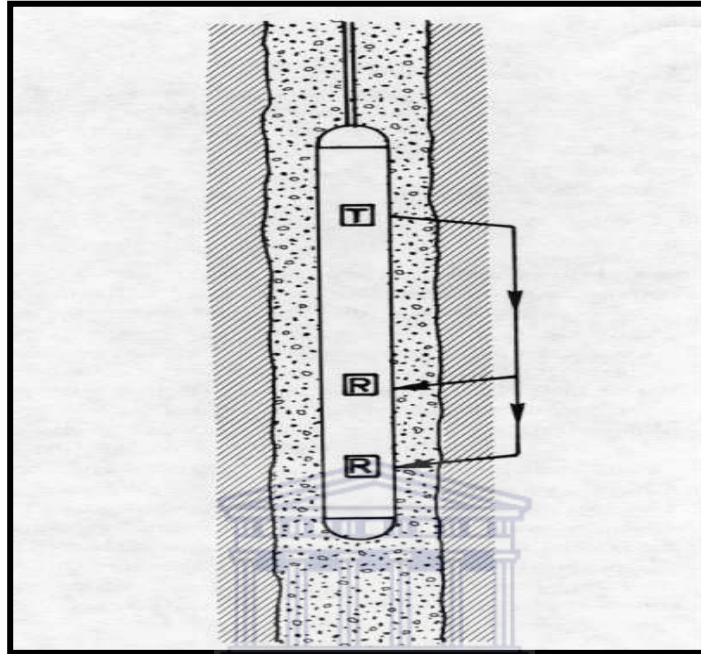
In similar argument, the fluid density values usually assumed in density log analysis is that of water ( $1 \text{ g/cm}^3$ ) but the actual fluid density may be lower when the reservoir is saturated with gas or light hydrocarbons. Evaluation from the density log may thus result in an excessively high porosity estimate.

#### **2.4.5 Sonic Log**

A sonic log measures the velocity at which the formation transmits sound waves. It is used primarily to estimate porosity and to identify the lithology and the type of fluid in the pores. The tool principally records the time (interval Transit time) it takes for sound waves to travel through one foot of the formation. Interval transit time is the reciprocal of velocity of the sound wave.

The sonic tool consist if transducers and receivers. The transducers translate electrical signal into ultrasonic vibrations while the receivers convert pressure waves into

electromagnetic pulses, which can be amplified to produce the logging signal. An example of sonic tool array is shown in Figure (2.5). It consists of a number of both transducer and receiver, which are separated by specific distances. Averaging the interval transit time recorded by each receiver reduces unwanted borehole effects such as the effect of Sonde tilt and borehole size.



**Figure 2.5:** Sonic Logging tool showing Receiver (R) and Transmitter (T) (modified from [http://www.spwla.org/library\\_info/glossary](http://www.spwla.org/library_info/glossary))

When the sonic log is being run, many acoustic waves interfere with the measurements. The first arrival or compressional wave is the one being amplified and measured by tool. It is the wave pulse that has traveled from the transducers to the formation, has been refracted at the borehole wall, traveled within the formation and then traveled back to the receivers as a fluid pressure wave (Schlumberger, 1989).

The sonic log is used in combination with other logs (e.g. density and neutron logs for porosity, shaliness and lithology interpretation). Integrating transit time is also helpful in interpreting seismic records.

#### **2.4.6 Spontaneous Potential Logs**

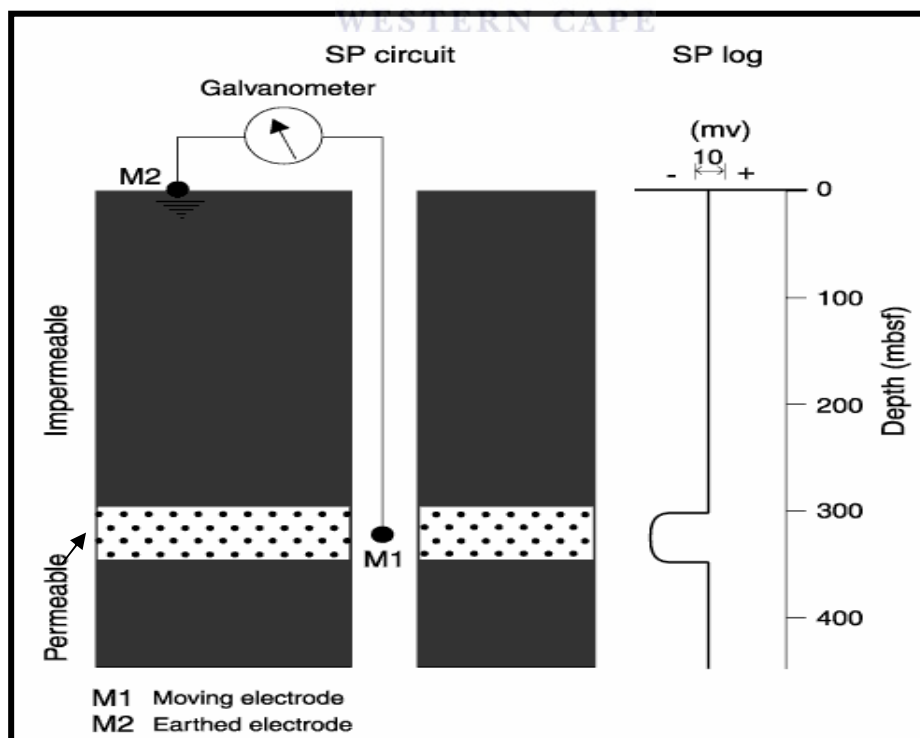
The SP log is a measurement of the natural potential difference or self potential between an electrode in borehole and a reference electrode at the surface: no artificial currents are applied in the measurements. The currents were actually called “potential spontanes” or spontaneous potentials by Conrad Schlumberger and H.G. Doll who discovered them. They originate from formation vertically (in electrical sense) when in nature they are isolated.



The principal use of SP log is to calculate formation water and to indicate permeability. It can also be used to estimate shale volume, to indicate facies and in some cases for correlation. Three factors are necessary to provoke an SP current:

1. Conductive fluid in the borehole
2. Porous and permeable bed surrounded by impermeable formation
3. Difference in salinity (or pressure) between the borehole fluid and the formation water.

SP current originate principally through the electrochemical effects of salinity differences between the borehole fluid (mud filtrate) and formation water. These differences create spontaneous currents either when the fluids themselves come into contact through a porous medium or when in contact through shale which acts as semi-permeable membrane (Rider, 1996). SP log was one of the first logs introduced for correlative purposes in sand-shale sequences, principally because certain intervals had typical log shapes. This shapes in sand-shale sequences, is related to shale abundance, the full SP occurring over clean intervals, a diminished SP over shaly zones. The relationship is considered as linear and so far shaliness is related to grain size, the SP is used to delineate both permeable and impermeable zones (Fig. 2.6) and also as good facies indicator.



**Figure 2.6:** Spontaneous Potential Logging tools (modified from Rider, 1996).

### **2.4.7 Resistivity Logs**

The resistivity log is a measurement of formation's resistivity, i.e. its resistance to passage of an electric current. Conductivity logs measure a formation's conductivity or its ability to conduct an electric current but this value is generally converted directly to resistivity. Most rock materials are essential insulators, while their enclosed fluids are conductors. Hydrocarbons are the exception to fluid conductivity and on the contrary, they are infinitely resistive. When a formation is porous and contains salty water the overall resistivity will be low. When this same formation contains hydrocarbon, its resistivity will be very high. It is this character that is exploited by the resistivity logs: high resistivity values may indicate a porous, hydrocarbon bearing formation.

The resistivity logs were developed to find hydrocarbons. This is still their principal quantitative use. To interpret the geological significance of resistivity logs, it is essential to realize that the same porous bed can have a multitude of resistivity responses, depending on the fluid content.

### **2.5 Systems tracts, Sequence Boundary and Parasequence sets**

Genetically associated stratigraphic units that were deposited during specific phases of relative sea level cycle (Posamentier et al., 1988) are represented in the rock records as three dimensional facies assemblages. They are defined on the basis of bounding surfaces, position within a sequence and parasequence stacking pattern (Van Wagoner et al., 1988). Three system tracts will be used in this study.

#### **2.5.1 Falling Stage Systems Tracts**

This includes all the regression deposit that accumulated after the onset of relative sea level fall and before the start of the next relative sea level rise. The falling stage system tract is the product of forced regression (this is however frequently confused with the sediments deposited during a normal regression). The FSST lies directly on the sequence boundary and is capped by the overlying Lowstand Systems Tract sediments. A variety of parasequence stacking patterns can be produced including: downward stepping prograding clinoforms, stranded parasequence, and mass flow deposited in distal areas. Each of these parasequence stacking patterns depends on the depositional profile, the rate of sediment supply and the rate of sea level fall. The FSST was firstly fully defined by Plint and Nummedal, (2000). This system tract has also been termed the Early Lowstand System Tract (ELST) (Posamentier and Allen, 1999). The fall is evidenced by erosion of sub-aerially

exposed sediment surface up-dip and the formation of diachronous sequence boundary that caps the Highstand system tract (HST). On seismic data, the upper boundary is the first definable horizon that onlaps the FSST, but when well logs are used; this boundary is instead recognised as the first marine flooding surface that overlies the FSST. Coincidentally it is often marked by time transgressive ravinement surface overlain by sediment lag.

Earlier papers that defined systems tract, including Vail (1987) and Posamentier and Vail (1988) placed part of the FSST within the Lowstand Systems Tract (LST). The sediments of this former LST definition included the deposits that accumulated just after the maximum rate of relative sea-level fall and were divided into three separate depositional units - basin-floor fan, slope fan, and Lowstand wedge, all of which overlies a so-called Type 1 sequence boundary.

### **2.5.2 Lowstand Systems Tract (LST)**

These include deposits that accumulate after the onset of relative sea-level rise. This systems tract lies directly on the upper surface of the Falling Stage Systems Tract and is capped by the transgressive surface formed when the sediments onlap onto the shelf margin. Stacking patterns exhibit (backstepping, onlapping, retrogradational, aggrading clinofolds that thicken up-dip). Lowstand Systems Tract sediments often fill or partially infill incised valleys that were cut into the Highstand Systems Tract, and other earlier deposits, during the FSST. This systems tract has also been termed the Late Lowstand Systems Tract (Posamentier and Allen, 1999).

### **2.5.3 Transgressive Systems Tract (TST)**

This comprises the deposits that accumulated from the onset of coastal transgression until the time of maximum transgression of the coast, just prior to the renewed regression of the HST. The TST lies directly on the transgressive surface (TS) formed when the sediments onlap the underlying LST and is overlain by the maximum flooding surface (MFS) formed when marine sediments reach their most landward position. Stacking patterns exhibit backstepping onlapping retrogradational clinofolds that thicken landward. In cases where there is a high sediment supply the parasequences may be aggradational.

### **2.5.4 Highstand Systems Tract (HST)**

This refers to the progradational deposits that form when sediment accumulation rates exceed the rate of increase in accommodation space. This HST constitutes the upper systems tract of a stratigraphic sequence, and lies directly on the

maximum flooding surface (MFS) formed when marine sediments reached their most landward position. This systems tract is capped by a sequence boundary. Stacking patterns exhibit prograding aggrading clinofolds that thin upward.

### **2.5.5 Regressive Systems Tracts (RST)**

The Regressive Systems Tract was defined by Embry and Johannessen, (1992). In this definition it lies above a Transgressive Systems Tract and is overlain by the initial transgressive surface of the overlying Transgressive Systems Tract. This complete sequence is known as a Transgressive-Regressive Sequence (T-R Sequence). The sediments of this systems tract include the Highstand System Tract of Posamentier and Allen, (1999), and the Falling Stage System Tract defined by Plint and Nummedal, (2000) and/or the systems tract termed the Early Lowstand Systems Tract (ELST) (Posamentier and Allen, 1999).

### **2.5.6 Sequence Boundary (SB)**

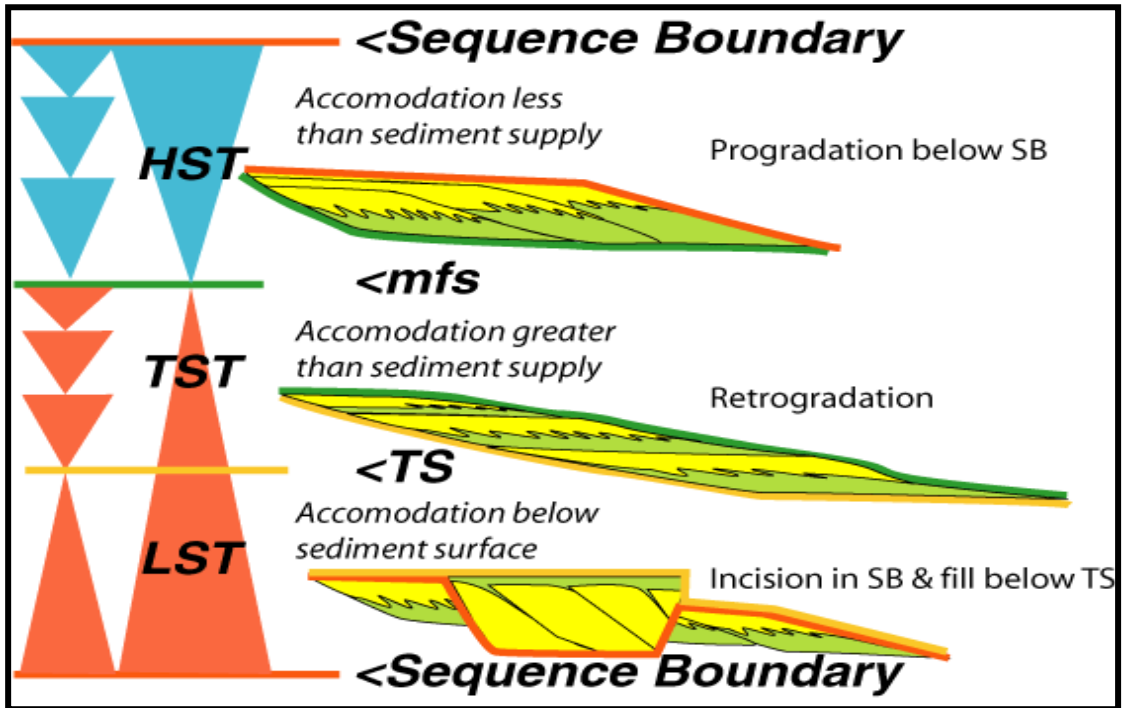
Sequences are enveloped by sequence boundaries (SB) that are identified as significant erosional unconformities and their correlative conformities. These boundaries are the product of a fall in sea level that erodes the sub-aerially exposed sediment surface of the earlier sequence or sequences. These boundaries are diachronous, capping the previous Highstand Systems Tract and eroding the surface of the downstepping sediments deposited during accompanying forced regression associated with the sea level fall (Catuneanu, 2002).

Hunt and Tucker (1992) emphasize how the upper surface of down-lapping and prograding shoreline of the forced regression is eroded and is expressed as a diachronous sub-aerial unconformity. Plint and Nummedal, (2000) name the sub-aerial unconformity that caps the forced regression as the "regressive surface of fluvial erosion". Hunt and Tucker (1992) match this unconformity to a down-dip surface they call the marine correlative conformity and relate to the end of base level fall and suggest that this "sequence boundary" over the forced regression does not match Mitchum's (1977) original definition of a sequence boundary or its time equivalent marine correlative conformity that was tied to the onset of a sea level fall.

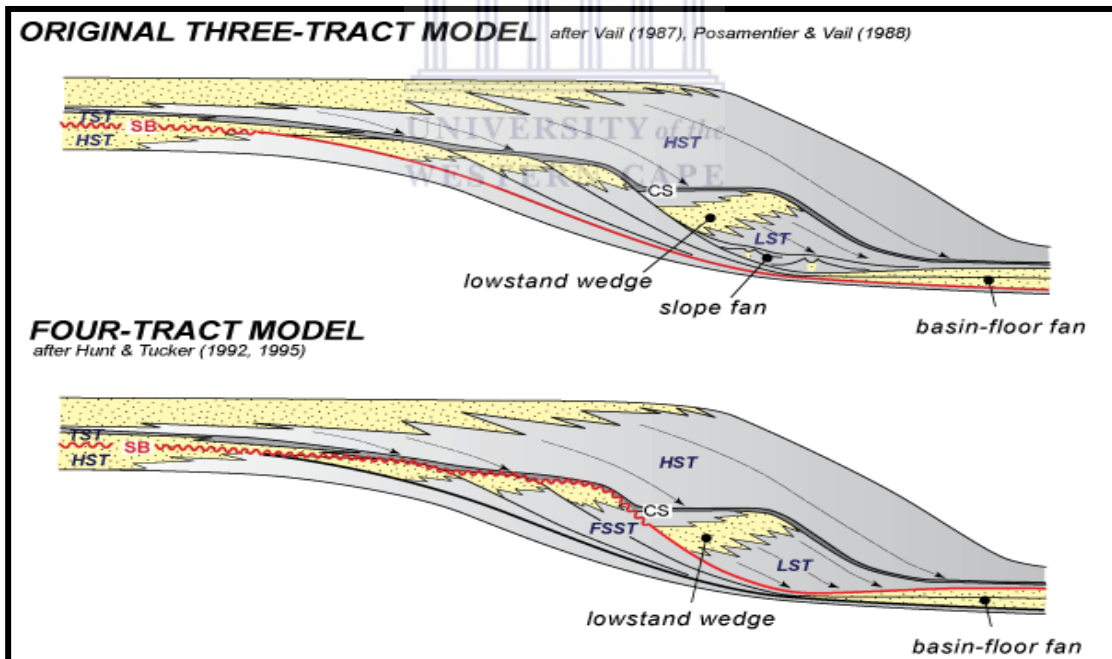
### 2.5.7 Maximum Flooding Surfaces

A surface of deposition at the time the shoreline is at its maximum landward position i.e. the time of maximum transgression (Posamentier and Allen, 1999). The surface mark the time of maximum flooding or transgression of the shelf and it separates the Transgressive and Highstand Systems Tract. Seismically, it is often expressed as a down-lap surface. Marine shelf and basinal sediments associated with this surface are the result of slow rates of deposition by pelagic-hemipelagic sediments and they are usually thin and fine grained. These fine sediments make up the condensed section (Mitchum, 1977).

An MFS is often characterized by the presence of radioactive and often organic rich shales, glauconite, and hard grounds. There are commonly widespread thin bedded concentrations of fauna (condensed sections) with high abundance and diversity. An MFS can often be the only portion of a sedimentary cycle which is rich in fauna. Often in a landward direction, the maximum flooding surface may match the underlying Transgressive surface formed during or just after the initial transgressive phase that immediately follows sea level Lowstands. In this case, glossifungite burrows may occur within this surface. The MFS is not commonly burrowed or bored. Any burrowing or boring are likely connected to the preceding transgressive surface before the water deepens and conditions become inimical for colonization but favour preservation. The MFS often mark the bounding surface between coarsening and/or fining upward cycles and are used to relate these cycles to deepening and shallowing in the geological section. It is synonymous with the Maximum transgressive surface (Helland-Hansen and Martinsen, 1996); final Transgressive surface at the top of retrogradational strata, down-lapped by highstand normal regressive strata (Catuneanu, 2006).



**Figure 2.7:** Illustration of different depositional systems tracts (modified from Kendall, 2003).



**Figure 2.8:** Models of the different Systems Tract (modified from Vail, 1987; Hunt and Tucker, 1992 and 1995).

## 2.6 Depositional Environment and Facies

Study on sufficiently broad scale clearly reveals that the basic primary control of oil occurrence can be summed up in two words, “depositional environment”. Environmental impact is the basic control for all the natural phenomena, whether it is the occurrence of oil or any other mineral. Our problem as oil finder is to establish what are the products of those all important environmental factors, their relationships in the original sedimentary basin and to recognize them in the present basin.

The only direct indicator of the past basin environments is the facies which can be compared with the environment of similar facies in modern basin. The advantage in the modern basins is that the various elements that determine environment can actually be observed and measured. They include such factors as the oxidation-reduction potential (Eh), alkalinity-acidity range (pH), the salinities and other electrometric and physico-chemical conditions, the bacterial and other biochemical activities, temperature, pressure and other physical factors (Reading, 1996).

The environment and the resulting facies are in turn controlled more than anything else by the basin bottom form at the time of deposition and by the deposition rate and type of sediments (Moody, 1961). The basin bottom form varies with the type of basin and its own peculiar individual development. Other things being equal, oil occurrence is related in sequence to:

- ✚ The mechanics of the basin subsidence, which varies in general way with basin type.
- ✚ The resulting basin form, which along with supply and current determine:
  - a. The sediment distribution which further modifies the basin forms.
  - b. The environment which is largely influenced by the basin form and the rate of deposition.

All this controls the facies distribution, alongside with the adequacy of reservoir, timeliness of traps and the efficacy of seal determines the incidence (volume and distribution) of oil (Moody, 1961).

## 2.7 Reservoir Quality and Facies Discrimination

Reservoir performance has been related to the variability in sedimentary facies with a reservoir sequence, where continuous sequence of rocks with similar geological characteristics possesses comparable petrophysical properties (Hearn et al., 1984). Porosity reduction in the study of Hearn et al, (1984) was associated with particular minerals occurring in the particular sedimentary facies. The applications of

mineralogy in that study were focused on two main aspects. Mineral identification was used in conjunction with other geological and well log data, to define different facies within the sedimentary sequence. Based on the facies sub-division, porosity reduction was then attributed to particular mineralogical components contained within a particular facies. Incorporation of mineralogical data in such a study is thus seen to be important, especially where the geophysical data do not provide sufficient information to describe the heterogeneity within the reservoir sequence.

## **2.8 Diagenetic Studies**

Diagenetic study is relevant to petroleum reservoir assessment because diagenesis modifies the original characteristics of the sediments through physical and chemical reactions. Diagenetic phenomena may alter rock properties such as porosity, pores size distribution and also cation-exchange capacity and also the relationship of these properties to the mineral composition of the reservoir sequence (Hurst 1984). Diagenetic study typically involves the use of x-ray diffraction, thin section petrography and scanning electron microscopy techniques (Hurst and Nadeau 1995) to determine the mineral content of the sediments. As the influence of clay mineral on reservoir characteristics are well known, study of diagenesis in reservoir sandstones often involves identifying, characterizing and quantifying the clay minerals present. A lot of substantial works are available that describe the effect of clay minerals on porosity and permeability (e.g. Ehrenberg, 2001; Howard, 1992; Hurst and Nadeau 1995; McHardy et al. 1982; Serra 1984; Wilson, 1992; Pittman et al. 1992).

The timing of development and the distribution of diagenetic minerals within a reservoir sequence also influence some of the variations in petrophysical characteristics (Al-Ramadan et al., 2005, BjØlykke, 1998). The implication of diagenetic studies in reservoirs is that they allow prediction of porosity and permeability, in this way they serve to proffer possible and lasting solutions as regards the appropriate well treatment methods to be adopted for the wells

## **2.9 Hydrocarbon Recovery**

Optical microscopy, x-ray diffraction and scanning electron microscopy have been applied in a study of clay mineral diagenesis in sandstone of the Niger Delta (Lambert – Aikhionbere and Shaw, 1982). In this study, possible problems that may arise in the recovery of hydrocarbons from the reservoirs because of the friable nature in the sandstone were that could have provided a source of silica cement, which in turn could have strengthen the sediment framework of sandstone clay mineralogy in



this study will be considered important not only because of the effect of clay minerals of permeability, but also for assessing the best means to enhance hydrocarbon recovery. The use of clay mineralogy has also been suggested in designing water injection facilities for friable reservoir sands, where the swelling capacities and fine kaolinite particles might reduce permeability and possibly cause irreversible formation damage (Morris and Shepperd 1982). Information provided by scanning electron microscope and x-ray diffraction was considered as useful addition to flow test data for predicting clay reactions during drilling and well completion (King, 1992).

### **2.10 Quantitative Mineralogy Techniques**

The choice of mineralogical evaluation as a complementary tool in the analysis of rock properties is constrained by the cost of the analysis and the time frame to meet the completion of the well. Among the quantitative mineral evaluation techniques used in some core laboratories are thin section, x-ray diffraction analysis, x-ray fluorescence spectrometry, infrared spectroscopy. Mineralogical analysis in reservoir description typically includes a combination of methods; thin section petrography and x-ray diffraction are the most common (Hurst and Nadeau, 1995).

Thin section petrography can provide much information on mineralogical composition, sediment provenance, petrofabric and diagenesis (Harwood, 1988). Quantitatively, the technique requires counting of at least 500 points to cover mineral components present in small proportions (Van der plas and Tobi, 1965). This increases the time and cost needed for analysis. The technique also does not provide a true evaluation of mineralogy, since it treats poly-mineralic particles, such as detrital rock fragments and matrix component as separate phases, rather than determining the percentages of individual minerals involved. With the limited resolution of the ordinary petrographic microscope, fine particles such as clay minerals and other closely inter-grown phases may be inadequately identified or even overlooked. Clay mineralogy however is of particular concern in evaluating reservoir properties. Electrical, radioactive and nuclear logging techniques, for example are all affected by different clay minerals. Significant proportions of these minerals may also provide drilling, completion and production problems in potential reservoir rocks (Frost and Fertl, 1981). Clay minerals however are difficult to quantify or even to identify by optical microscopy techniques. Hence, there is need for an alternative approach that could provide a detailed and quantitative evaluation of mineralogy including the clay

components. Point counting analysis may also be affected to some extent by three-dimensional heterogeneities in mineral distribution, due to limitations imposed by small area embraced in a thin section, thereby limiting the applicability of the technique to reservoir studies concerned with larger volumes of investigation or more heterogeneous lithological materials. Operator preferences during the analysis have been shown to produce consistent differences in point counting results performed on similar sets of samples (Swanson, 2001). Thus, point count analysis does not always yield accurate and reproducible results. The technique has nevertheless been used in reservoir description, mainly in research on diagenetic effects applied to porosity and permeability issues (e.g. Baker et al., 2002, Rossi et al., 2002).

The x-ray diffraction (XRD) technique is based on the diffraction of x-rays by atomic layers within the crystalline phases (minerals) of the rock sample. Because each crystalline material has distinct set of atomic layer spacing (d-spacings), all of the crystalline materials in a sample can be identified from XRD scan. The analysis requires finely powdered samples, packed in a sample holder and directly inserted into the XRD instrument. Powdered based techniques have advantage over thin section studies of being able to include a split from larger, more representative sample in the analysis, to cover any compositional variability. Such capability is important in studies of sedimentary rocks which may be very heterogeneous. In reservoir applications, the inclusion of more representative samples in the analysis is important to complement geophysical log data, which typically cover a larger volume of rock than single thin section. Identification and quantification of clay minerals can also be performed using XRD techniques, either by powder analysis or by preparation of oriented slides from the fine fraction of sample. A more detailed discussion of the XRD techniques and their interpretation, including the technique used in the present study is given in Chapter 4. X-ray diffraction has been applied in reservoir sandstone studies involving the assessment of effects of clay minerals on porosity (Ramm, 2000; Ramm and BjØlykke, 1994). The technique has also provided valuable information to facilitate log interpretation (e.g. Cannon and Coates, 1990). Understanding of the mineralogical factors affecting petrophysical properties is traditionally based on thin section petrography included as part of routine core analysis. However, this provides a petrographic rather than true mineralogical analysis (e.g. the mineralogy of poly-mineralic components such as rock fragments and matrix is not taken into account),

and thus does not always provide sufficient information to address the need for understanding of mineralogical influences on reservoir properties.

Traditionally, x-ray diffraction (XRD) is used to identify minerals of oil well core samples (Ruessink et al., 1992). The qualitative aspects of infrared spectroscopy are one of the most useful techniques to complement XRD technique. Over the years, much has been published in terms of fundamental absorption frequencies (also known as group frequencies) which are the key to unlocking the structure-spectral relationships of the associated molecular vibrations. Currently, bulk mineralogical analysis relies heavily on x-ray diffraction (XRD) which tends to be supported by data from infrared spectroscopy, chemical analysis and electron microscopy (Środoń, 2002) therefore, this technique will be used to complement the petrographic results (Thin section, SEM and XRD). Infrared spectroscopy has not been utilized significantly in the identification of minerals and in structural studies (Xu, 1999, Moore et al., 1989). Typical spectra of minerals display characteristic features which can be related qualitatively to variations in the constituent minerals. Infrared spectrometry (IR) is a standard analytical tool that based on the fact that chemical bonds between unlike atoms can absorb IR radiation and cause vibrations of the bonds. The absorbed IR wavelength is characteristic of a particular bond in a particular molecule or mineral which is measured by an FTIR spectrometer. The different functional groups ( $\text{SO}_4^{2-}$ ,  $\text{OH}^-$ ,  $\text{NO}_3^-$ , R-C-H, C-C and O-Si-O) can be identified in an unknown material by comparison with the literature and correlative charts. Most modern FTIR instruments produce plots with wave number (units:  $\text{cm}^{-1}$ ) on the abscissa and absorbance on the ordinate. FTIR spectroscopy has recently been receiving attention for its potential use in quantitative mineral analysis (Ruessink et al., 1992, Matteson, 1993). Infrared spectroscopy is another technique used in mineral identification and quantification, the principle of the technique is based on the fact that chemical bonds can be stretched, bent, or located by photons of infrared radiation (Lewis and McConchie, 1994). The infrared region of the electromagnetic spectrum used in mineralogy is usually between  $2.5\mu\text{m}$  to  $25\mu\text{m}$  (Lewis and McConchie, 1994). Photons with a particular wavelength are absorbed by chemical bonds that have the same natural vibration frequency. The natural vibration of the bond is increased in the process. A scan over a range of infrared wavelengths produces an absorption spectrum, which is used to identify the minerals that are not sufficiently crystalline to be studied by x-ray diffraction. Infrared techniques however cannot recognise all of

the clay minerals types due to similar and weak nature of the molecular bonding among the different mineral species (Guest, 1990). Mineral quantification may also not be fully achieved, especially in shaly lithologies and the application of the techniques is seen to be limited in instance when the assessment of reservoir properties is complicated by an abundance of clay minerals.

Analysis of rock chemistry by x-ray fluorescence (XRF) is based on the characteristic of radiation spectra emitted by the different elements on exposure to x-ray radiation. A wide range of elements can be identified with high precision. The technique however, cannot analyse elements with atomic weight less than that of fluorine, and there is also some difficulty in analysing some trace elements with high molecular weights (Lewis and McConchie, 1994).

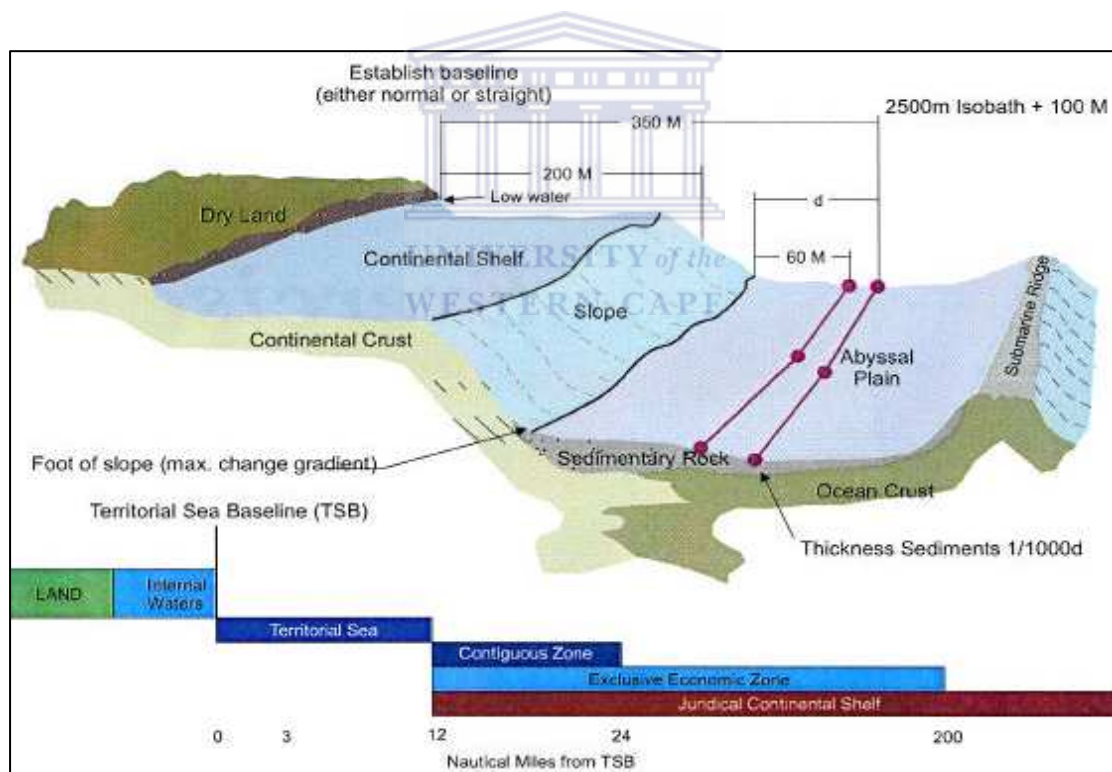
### **2.11 Geochemistry of Pore Water**

Deposited sediments also have high water content if accumulated under water. The sediments progressively lose water (with time) after burial and become lithified due to diagenetic changes (Gerhard, 2000). Mechanical diagenesis caused by overburden of younger sediments and tectonic stresses expel pore water and lead to a rearrangement of sediment particles. Chemical diagenesis involves dissolution and recrystallization of primary minerals, as well as precipitation of cement in pore space. Dissolution and cementation may take place at different depths within the sediments. The effects of mechanical and chemical diagenesis in various sediment types are quite complex but can be investigated using various proxies in which pore water is one of the most important proxy. pH is so important as it can drastically change equilibrium state and speed of many reactions (<http://www.chembuddy.com/?left=pH-claculation&right=pH-scale>). It is well established through field observations, experiments, and chemical models that (redox) reaction and pH exert a strong influence on the speciation of dissolved components and the solubility of minerals in hydrothermal fluids (<http://www.chembuddy.com/?left=pH-claculation&right=ionic-strength-activity-coefficients>).

## CHAPTER THREE

### 3.1 Geological Background of the Orange Basin.

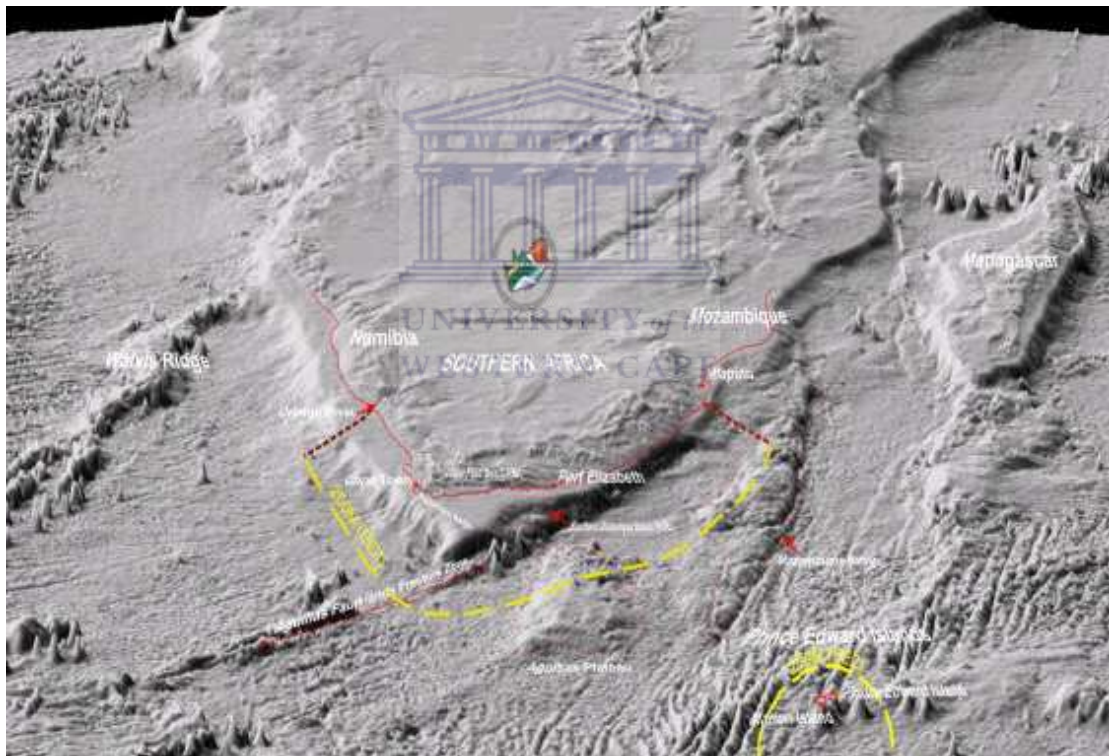
South Africa has a coastline of about 3000 km in length. This includes the West Coast, which is about 900 km starting from the Orange River to Cape point while more than 2000 km long moving from Cape point further round the southern coast up along the western coast through Cape Town to Namibian border (Petroleum Agency SA Brochure 2004/05). Beyond the coastline is the continental margin which constitutes the South African offshore environment. The immediate relatively shallower shelf area is about 20-160 km wide off the western coast, 50-200 km wide off the southern coast and averaging 30 km wide on the eastern coast. The continental slope connects the shelf area with the deep marine environment it follows a similar trend in width and fairly wide on the west and south coast but narrower to the eastern coast (Fig. 3.0; Olajide, 2005).



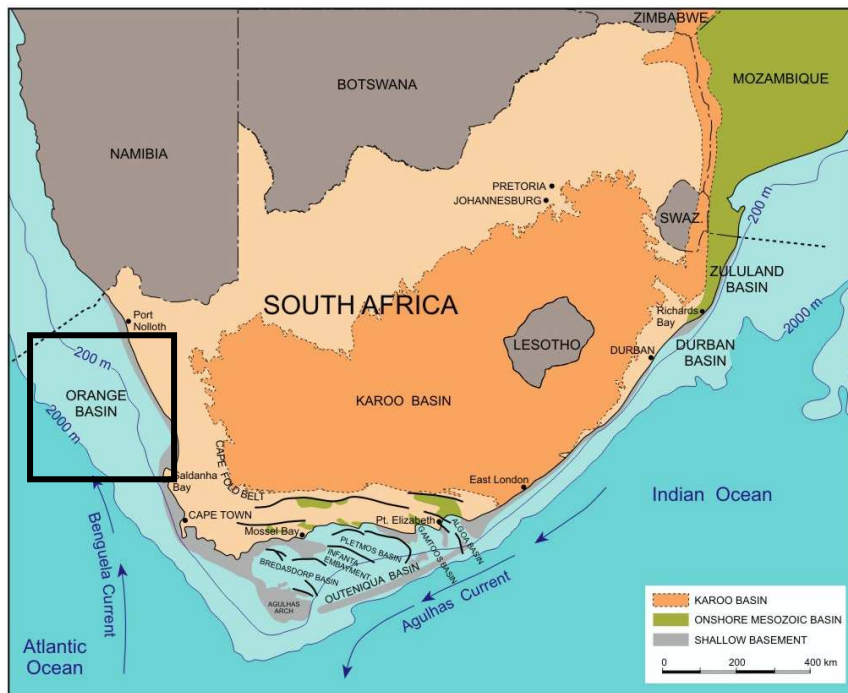
**Figure 3.0:** South Africa continental margin and oceanic crust (Modified from Broad 2004).

### 3.2 Offshore Basin

The offshore basins of South Africa have been divided into three distinct tectonostratigraphic zones: western, southern and eastern offshore (Petroleum Agency handbook 2004/05). These basins have developed in the Permo Triassic-Jurassic period or earlier. The western zone known as Orange Basin is a divergent plate margin with graben structures trending sub-parallel to coastline (Jikelo, 1999). It is related to the opening of south Atlantic in the early cretaceous. A narrower passive margin describes the eastern offshore which is part of the African rift system formed as a result of breakup of Africa, Madagascar and Antarctica in the Jurassic (Fig. 3.1). Unlike the western and southern margin, this zone has limited deposition with only the Durban and Zululand basins containing an appreciable sedimentary succession.



**Figure 3.1:** Topography derived from satellite image showing sea floor and continental margin surrounding South Africa (modified from Broad 2004).



**Figure 3.2:** Western, eastern and southern offshore zones of South Africa (Petroleum Agency SA brochure 2003)

### 3.3 Regional Geology of the Orange Basin

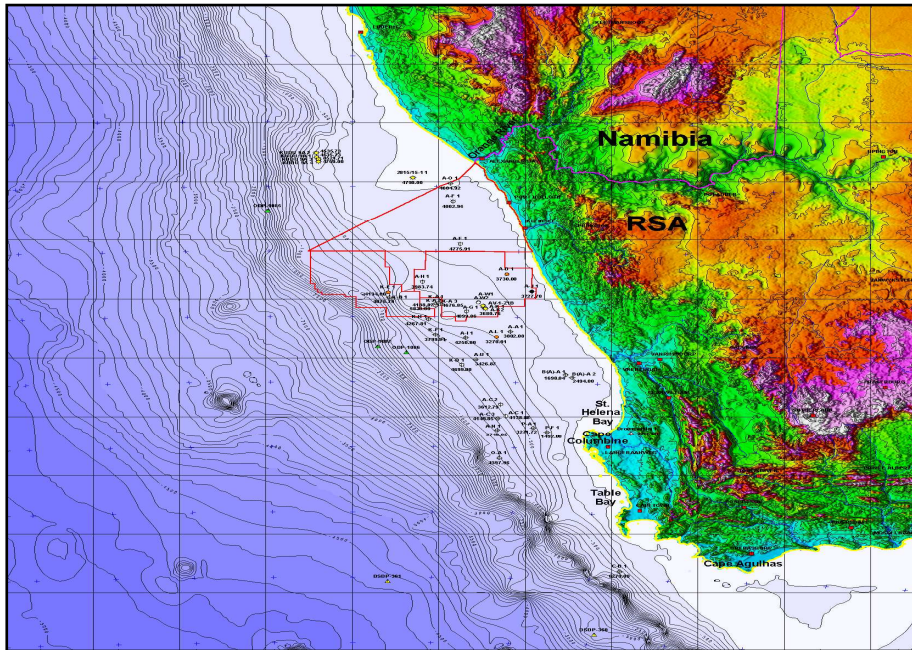
The Orange Basin which is relatively unexplored, with up to one well per 400 km<sup>2</sup> and South Africa's largest offshore basin (Petroleum Agency, 2006) and Africa's most southern west coast basin. The sedimentary supply to the basin was obtained from river system, with a rivaling delta to the north of the basin. The underlying rift succession of the basin comprises isolated remnants half grabens that occur east of medial hinge. The sediments within the Orange Basin may be as old as Jurassic, but oldest dated back to Hauterivian. The sediments within the basin are continental in origin and are deposited together with volcanic sediments (Fatti et al., 1994). These basalt interbeds are coeval with the sediments of Barremian transgressive succession, implying that the western margin was of a volcanic type. The western margin was segmented into a number of crustal segments with the southern part of the margin being of the rifted margin types (Visser, 1998) and the Cretaceous sediments of the basin range from continental in the east to deep marine in the west (Petroleum Agency SA, 2006). This basin which is situated off the south western coast of Africa, is bounded to the north by Kudu Arch and to the south west by Agulhas-Columbine arch. However, the basin is not strictly structurally confined, rather, it is defined by the extent and thickness of post-rift sedimentary succession deposited off the west coast of South Africa and the southern portion of the coast of Namibia (Petroleum Agency Handbook 2007).

Tertiary succession of the basin mainly comprises of calcareous oozes and chemical sediments, with the thick wedge of drift sediment undergone repeated deformation of the paleo-shelf edge and paleo-slopes due to sediment loading and slope instability during the Upper Cretaceous. This sedimentary tectonic event typically comprises of extensional gravity faults and fold up-dip a detachment glide plane in an over pressured shale (Petroleum Agency SA, 2006). The basin thus defined covers an area of around 160,000 km<sup>2</sup> to the 2000m isobaths (Olajide, 2005). Basin formation probably began with the separation of African and South American plates in the later part of the Jurassic, possible in the Oxfordian or Kimmeridgian, although the oldest penetrated sediments are from the ancestral Orange River drainage system. The Olifant and Berg River system have also contributed, although their influence is confined mostly to the South (Petroleum Agency 2007). The basin evolution can most easily be described in terms of the period of rift and drift.

The Orange Basin extends the coast along the coast of western Africa for 1500 km from the Aguilhas Arch in the south to the Walvis Ridge in the north (Figure 3.3). The basin is one of the most lightly explored passive margin systems in the world with the South African portion of the basin encompassing 130,000 km<sup>2</sup> with water depths ranging to greater than 3000 m. More than 75 % of the prospective area is in water depths shallower than 500m and half of the prospective region lies in water depths shallower than 250 m. Till date, only 47 wells have been drilled in the basin (PASA, 2004). These exploration efforts have led to the discovery of one gas field in Namibian waters (Kudu), with reserves estimated from 250 BCF to 1.5+ TCF, and some other gas field in South African waters (PASA, 2005).

Earliest sedimentation is dated as Pre-Hauterivian and likely began in the Kimmeridgian or Tithonian (~152-154 Ma), although fossil control in the older rocks is absent due to the lack of marine facies in wells drilled to date (Figure 3.4).



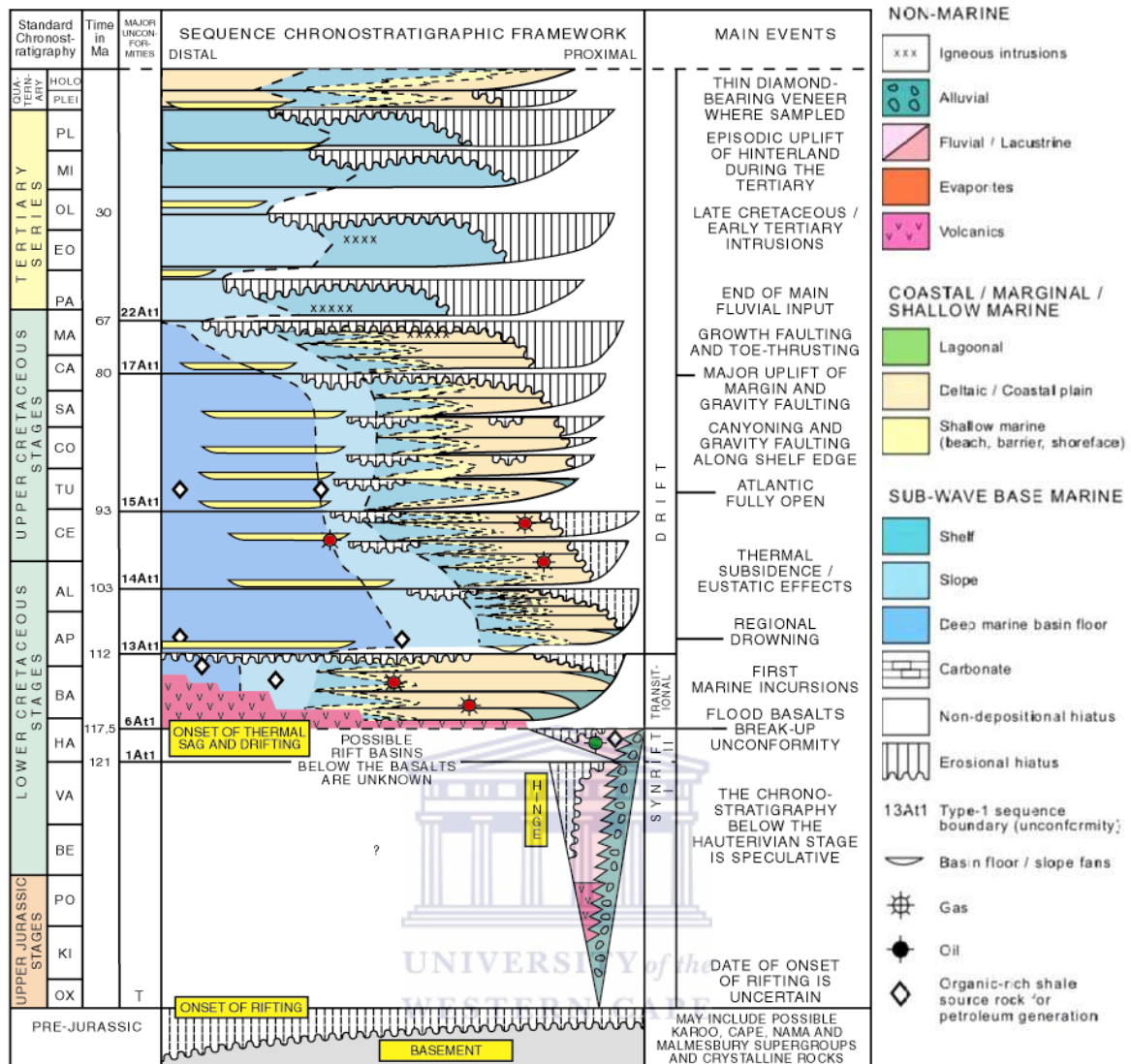


**Figure 3.3:** Topographic and Bathymetric Map of the Orange River Basin (PetroSA Report 2003).

### 3.4 Sequence Stratigraphic and Chronostratigraphic Framework

Utilizing the principles of sequence stratigraphy, the drift successions in South Africa's offshore basins have been divided into unconformity – bounded sedimentary sequences. Each sequence is interpreted to have been deposited in response to world wide (eustatic) relative changes of sea level and is defined at its base by type 1 unconformity, as defined by Van Wagoner et al. (1987). Each sequence is associated with a sea level Lowstand followed by Highstand flooding event. The methodology and principles of the sequence stratigraphic process and their application to the South African offshore are describe by Brown et al., (1996).

The chronostratigraphic correlation chart (Fig. 3.4) is based on these studies and utilizes the time scale of Haq et al. (1998) to provide a geological time framework, which is useful for understanding the distribution of lithofacies through space and time. The sequence stratigraphic approach has relevance for understanding and predicting the occurrence of petroleum source rocks and reservoirs.



**Figure 3.4:** Sequence Chronostratigraphic framework of the Orange Basin (Geol. Report PetroSA 2003).

### 3.5 Tectonic Setting of the Orange Basin

The Orange Basin was formed during the late Jurassic to early Cretaceous periods due to Gondwana breakup and the rifting and later drifting apart of the African and South American plates. During the late Jurassic, the initial fragmentation of west Gondwanaland into the South African plate and South American plate began; it was initiated by extensional forces that commenced in the early Mesozoic and separated by continental drifting that began in the early Cretaceous (Petroleum Agency Handbook 2006). The South African western plate is a divergent passive margin and the southern and eastern margins are transformed margin consisting of rift basin modified by strike-slip movement along transform faults. The breakup of Gondwanaland started along the eastern coastal margin of South Africa whilst the separation of Africa, the Falkland plateaus, Antarctica and South America. This

separation of the super-continent divided the South African offshore basins into three distinct tectonostratigraphic zones. The narrow passive margin that displays a protracted rift phase history (east coast) is a direct result of the separation of Madagascar and Antarctica (PASA brochure 2006) and due to limited influx, only the Durban and Zululand basins had contained hefty amounts of sedimentation. To the S-E, the African plate is bounded by the Agulhas marginal fracture zone (Visser, 1998), a dextral (right-lateral) transform margin that formed during the movement of the Falkland plateau, movement began in the early cretaceous at the onset of drifting and caused the truncation of structural trends such as Permo – Triassic Cape Fold belt on the Jurassic Early Cretaceous graben and half graben complexes of Outeniqua basin. Movement along this transform fracture zone had given rise to the offshore basin off the south coast of South Africa. This offshore region is called Outeniqua basin and consists of a series of en-echelon sub-basins that comprises a complex rift half graben overlain by variable thickness of sediments. The western offshore region of South Africa as described by Dingle, et al. (1983) as a tensional transverse marginal fractured zone that had undergone local displacement (Petroleum Agency Handbook 2006) and displays major structural attributes: the Columbine-Agulhas Arch and adjacent continental margins and Orange Basin. The Orange Basin initiated as series of North-South trending grabens during the lower Cretaceous (Fatii et al., 1994)

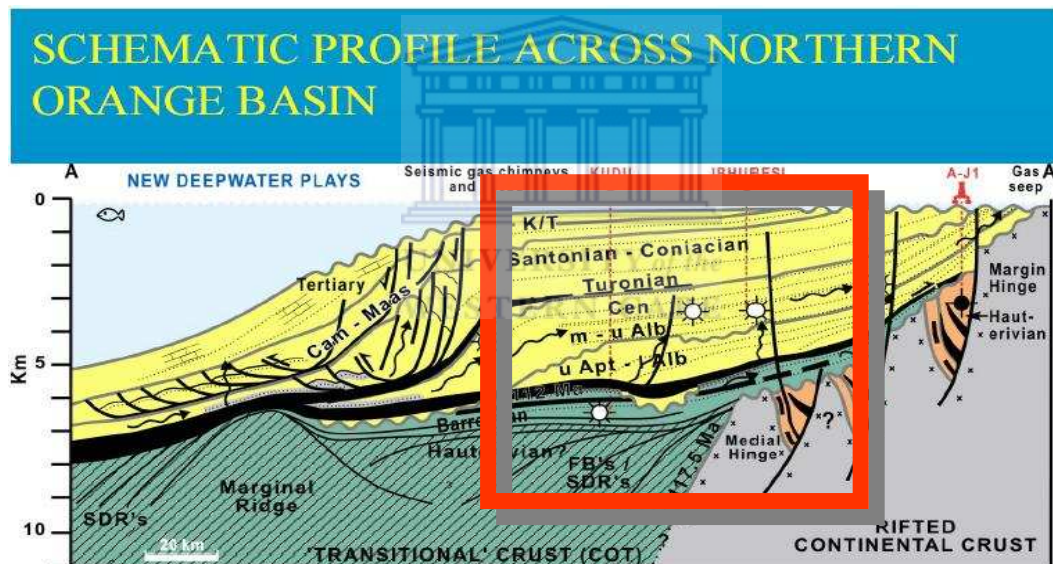
Two source rocks are present in the basin, (1) lacustrine shales restricted to the pre-Hauterivian section in rift phase half-graben sub-basins and, (2) terrigenous derived Type II kerogen in Upper Cretaceous shales of the drift section (Fig. 3.5) (Van der spur, 1999). Both source rock sequences are currently generative. Reservoir rocks in the rift section are fluvial and deltaic sandstones and conglomerates derived from the Paleozoic Karoo supergroup and underlying basement. Drift sequence reservoir facies on most of the broad shelf are primarily fluvial sandstones and floodplain deposits.

Two episodes of structural deformation are evident; the first one involves normal faulting during initial rifting of the Atlantic margin. These faults show progressive rotation and displacement through time and produce typical half graben structures, with the rift depositional section progressively on-lapping basement towards the rift hinge line. (Geol. report PetroSA 2003).

The second episode of deformation was modest extension of drift phase sediments across most of the shelf. Two types of drift deformation are recognized on seismic.

1. Basement involved normal faults predominantly active from the Aptian through the late Paleogene.
2. Neogene to recent gravity driven detachment faults are largely super-imposed on earlier rift faults, but also includes new higher angle faults not originally formed during rifting.

These faults result from thermal subsidence of the cold brittle transitional crust. Four-way closures are seldom associated with these faults and are of limited nature when they do occur. On dip oriented sections, the displacement on these younger extensional faults is relatively constant through the upper Mesozoic and lower Paleogene section with offset decreasing in the upper Paleogene section. In most cases, Neogene section overlaps these faults and shows no offset. However, faults associated with the western flank of the large main rift graben system show Neogene reactivation and displacement (PASA, 2008).



**Figure 3.5:** Generalized W-E Cross-sections through the Orange River Basin (PASA 2005).

### 3.6 Stratigraphy and Brief History of Albian Age Reservoir

The Albian successions of the Orange Basin typically consist of thick and thin-bedded clay-silt and sand sequences and occurrence of thin and shaly beds is common. It is shown that thin bedding effects cause limitations in detection of thin beds and evaluation of marginal reservoir (Derder, 2003). The Albian gas reservoir interval in the Orange Basin consist of an association of coarsening upward, laminated and bioturbated mudstone to massive planar cross-bedded sandstone with evidence of reducing conditions (Muntingh, 1993). The deposition took place in the

overall shallow marine shelf type environment (Muntingh, 1993). The reservoir in the studied area is heterogeneous consisting of massive sands with rare shale laminations and thinly bedded sand with abundant shaly/silty inter-lamination.

The Albian sequence is also composed of alternating siltstone and mudstone with minor sandstone. The average Albian sandstone reservoir thickness ranges from 3 m to 70 m. The sandstone is indistinctly greenish which shows the presence of glauconite (marine conditions). Overall grayish colors of sandstone indicate that the deposition condition was reducing. The greenish sandstone is generally well sorted ranging in grain size from very fine to medium. The lower and upper contacts of sandstone are characterized by abrupt lower contacts, gradual bioturbated upper contact. The siltstones are more heterolithic and are cm-dm bedded and often exhibit swaley lamination and cm to dm scale bioturbation. (Derder, 2003)



## CHAPTER FOUR

### 4.0 Materials and Analytical Methods.

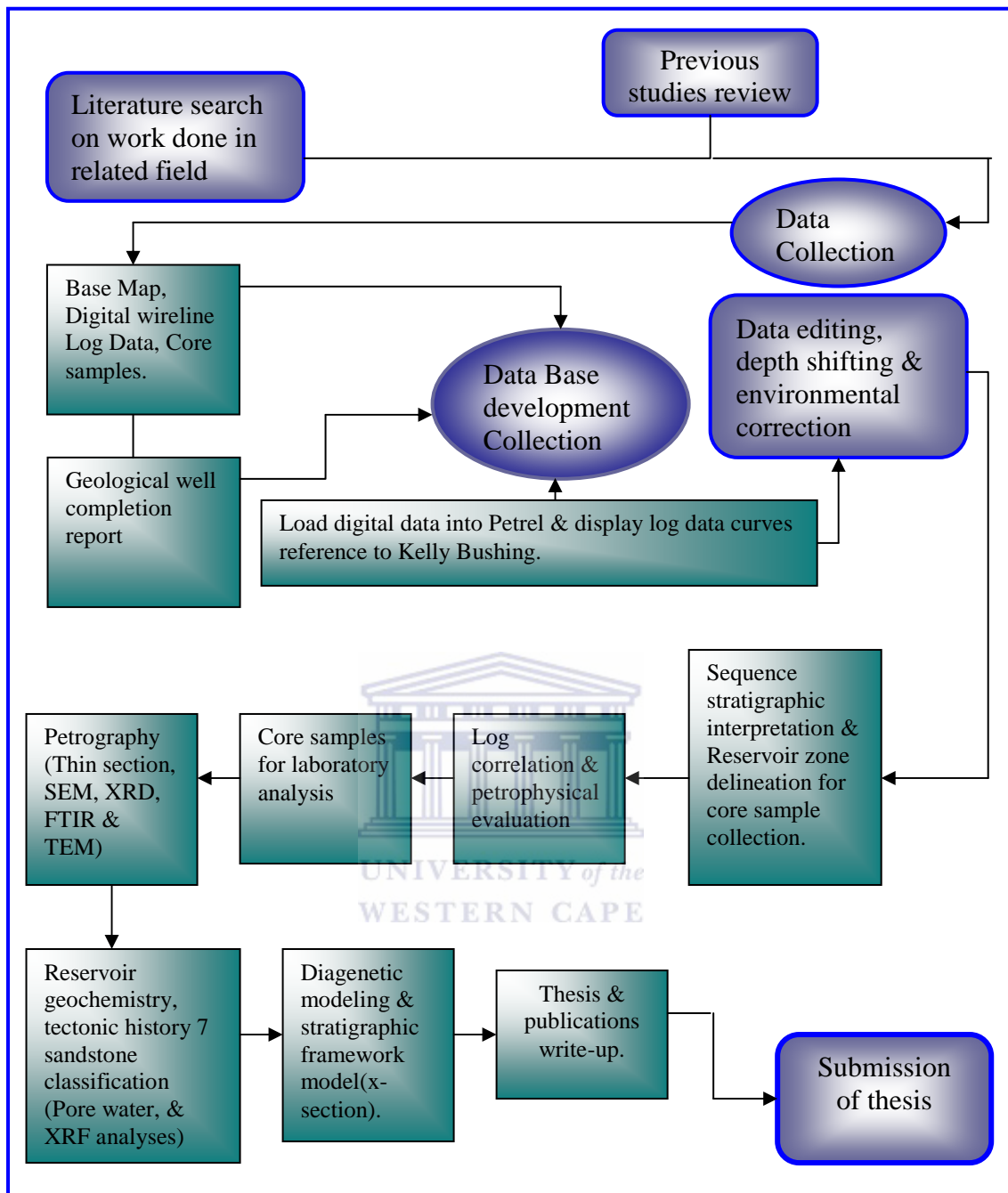
---

This chapter describes the techniques used for the study. The framework diagram in chapter one (Fig. 1.0) provides a quick look at the methodological approach while figure 4.1 presents the flow chart of the various methods that was used in this course of this study. Well logs and core samples were obtained from the Petroleum Agency, SA for this study. The softwares used for this study are (Fast Tracker, Petrel 2009 and Interactive Petrophysics).

The data sets include:

- ✚ Conceptual map for the block.
- ✚ Digitized wire line log data.
- ✚ Composite paper logs.
- ✚ Core data and sedimentological core logs.
- ✚ Well survey data.
- ✚ Well completion report.
- ✚ Core samples of selected depths for analysis.

The flow chat shown in figure 4.1 illustrates sequential steps taken in carrying out this study. The process starts with the review of previous studies and literature search in comparable oil and gas field so as to get familiar with the basin geometry, tectonic history sediment source, digenetic history, flow units and structural features. The discussion of the quantitative mineralogy techniques includes the principle of measurement, sample preparation and analytical programs used in the study. The textural similarities and elemental geochemistry of some interested depth and section are carried out. This is supported with the use of wire line logs to pick out the depths of interest for correlation purpose. The core mineralogy would be measured by whole rock x-ray diffraction (XRD) for the purpose of validating modeling result from the EDAX analysis. The multiminerall analysis study would create a geologic model which will used to enhance the characterization of the reservoir especially where clay is present. The internal architecture of reservoir rock of interested sections will be determined with SEM to reveal the diagenetic history of each well. The data collection segment has list of all the data collected from petroleum Agency SA, which is used in this thesis. They are being loaded into the softwares used to display the log curves reference to Kelly bushing (RKB).



**Figure 4.1:** The flow chart of the research methodology

#### 4.1 Wireline Log Loading

Interactive Petrophysics and Petrel were used for the loading and display of the log curves, the data were received in LAS format and were loaded directly into the Interactive Petrophysics workstation where depth shifting was done based on the core description and the necessary environmental corrections were also done. This data were exported from Interactive Petrophysics in “ASCOUT” format and converted into ASCII wordpad format which was the loadable format into Petrel. Proper quality

controls were performed and reservoir zones were identified using the appropriate well logs. Petrel was chosen to model this reservoir because it is window based software for 3D visualization with a user interface based on the windows Microsoft standards as well as shared earth modelling. A data base was created within petrel clearly delineating the different information and data needed to complete this project. The geophysical, geological and petrophysical data were imported to the Petrel within the main data base through this it was possible to generate and visualize the imported data in 2D as well as 3D.

#### **4.2 Core Description**

Core description comprises a combination of quantitative and qualitative data, which needs to be concisely recorded. The quantitative information varies continuously down hole and best displayed as some type graphic plot. The core description process started by identifying the depths of interest and then the laying out of the cores. The equipments used for effective core description are listed below:

- ❖ Digital Camera
- ❖ Tape rule
- ❖ Log sheet
- ❖ Microscope
- ❖ Sample bags
- ❖ Pyrex spot plate
- ❖ Hammer
- ❖ Water bottle and foam
- ❖ Small Clip board
- ❖ Hand lens
- ❖ Grain size standard chart



After the laying out of the core, the total depth was established as well as the log format. The samples were laid out in compartmentalized trays so that a sequence of five to ten samples could be observed in a single tray. The samples were laid in a stack of five-cell trays with the depths marked on the trays. Ten metres or more of the samples were scanned to observe the lithologic “breaks”. The samples were then re-examined for more detailed study and to identify other properties. Wetting the samples not only cleans off mud and other contaminants, but also brought out the rock characteristics that were not apparent in the dry samples.



Critical visualization was done by observing the following parameters: rock type, sedimentary structures and grain size variation, packing pattern, fossils assemblages, colour, textures, cement/matrix and the effect of HCL on the samples. During the description, the rock type was first established, after which the colour was determined using the standard geologic colour chart, then a proper examination was done to determine the grain size, texture and degree of sorting. The sedimentary structures were observed and recorded however, some of these structures cannot be seen by our naked eye, chips were taken out of the core samples using hammer, and examined under microscope in the laboratory. In the cause of the microscopic examination, the cement/matrix, fossil content, and some minerals were observed. The representative chips selected were etched lightly in dilute HCl (10ml) and placed in a clear pyrex spot plate and then quickly viewed under the microscope to observe the degree of effervescence, reaction and etching in order to the presence of calcareous materials and possibly to identify some other minerals and porosity estimation.

### 4.3 Petrophysical Calculation Procedures

The methodological approach used in arriving at the petrophysical results is as follows:

#### 4.3.1 Volume of shale ( $V_{sh}$ )

The values of shale volume ( $V_{sh}$ ) were derived from gamma ray log. Stieber method was used for the estimation as it has the advantage of suppressing likely initial high response of GR log to a small amount of shale (Olajide, 2005). It defines volume of shale as:

$$V_{sh} = \frac{I_{sh}}{(3 - 2I_{sh})}$$

Or

Clavier's model for Older rocks given as:  $0.33 (2^{2I_{sh}} - 1)$  or Stieber model  $I_{sh}/(3-2I_{sh})$ .

$I_{sh}$  is the gamma ray shale Index which varies from 0 – 1 and it is given as:

$$I_{sh} = \frac{Y_{log} - Y_{cl}}{Y_{sh} - Y_{cl}}$$

#### 4.3.2 Porosity

Porosity of the selected reservoir formation is determined from the recorded porosity logs. The logs used for this research work are density (RHOB) and neutron (NPHI) logs.

Porosity from density log ( $\Phi_D$ ) is given as:  $\frac{\rho_{ma} - \rho_{log}}{\rho_{ma} - \rho_{log}}$

$$\rho_{ma} - \rho_f$$

Table 5.2 below highlights the different parameters (fluid density) obtained from the well completion report used as input for the generated results

Note: The standard density for sandstone used in this calculation is  $2.65\text{g/cm}^3$  while that of shale is  $2.7\text{g/cm}^3$  (Rider, 1982).

Porosity from neutron log ( $\Phi_N$ ) was read and then corrected with the 1972 Schlumberger chart (Fig. 5.7.2) to generate a corrected porosity from neutron log ( $\Phi_{CNL}$ ).

Total Porosity ( $\Phi_T$ ) is given by: 
$$\frac{\Phi_D + \Phi_{CNL}}{2}$$

However for this research work total Porosity ( $\Phi_T$ ) for better estimation of gas zone was used which is given as:  $[0.5 * (\Phi_D^2 + \Phi_{CNL}^2)]^{0.5}$

Effective Porosity ( $\Phi_{eff}$ ) is given as:  $\Phi_T * (1 - V_{sh})$  provided  $V_{sh}$  is determined using Stieber method.

### 4.3.3 Formation Water Resistivity

Formation resistivities;  $R_t$  and  $R_s$  are taken directly from the resistivity record of deep and shallow resistivity measuring devices. Invaded zone resistivities  $R_s$  were deduced directly from: Spherically Focused Log (SFLU), Shallow Laterolog (LLS), and Microspherically Focused Log while uninvaded zones resistivities or true formation resistivities  $R_t$  were recorded by: Deep induction Log (ILD) and Deep Laterolog (LLD) Formation water resistivity ( $R_w$ ) was estimated from clean non shaly water filled reservoir using relationship between formation factor and shale free, water filled formation defined by Gus Archie in 1940 – 1941. In shale free, water filled formation, formation factor (F) is a constant defined by:  $F = R_0 / R_w$  where  $F = a / \Phi^m$

By rearranging the equation:  $R_w = (\Phi_D^{m/a} * R_0)$

Note:  $R_w$ , a, m and n used for this research work evaluation were  $0.09 \Omega\text{m}$  at  $200^\circ\text{F}$ , 1, 1.94 and 1.80 respectively. The a and m were obtained from the electrical properties measurement from special core analysis (SCAL) from A-K1 and A-G1 wells while the  $R_w$  was based on the pickett plot (A-Y1)  $R_w$  from SP and water gradient slope from RFT pressure data obtained from the well report. However,  $R_w$  for A-W1 well was reported to be  $0.08\Omega\text{m}$  at  $200^\circ\text{F}$  and it can also be calculated by locating water saturated sandstone and subsequently measuring its porosity ( $\Phi$ ) and

$R_0$ , formation water resistivity were estimated for selected reservoir intervals and corrected to their respective temperature.

#### 4.3.4 Water saturation ( $S_w$ ) and Hydrocarbon saturation ( $S_{hc}$ )

In a hydrocarbon bearing reservoir, the void spaces are partly occupied by formation water and remaining volume by hydrocarbon. The resistivity of hydrocarbon reservoir is function of formation factor (F), Resistivity of formation water ( $R_w$ ) and its water saturation ( $S_w$ ).

Using Archie's equation, water saturation ( $S_w$ ) for hydrocarbon bearing reservoir is defined as:  $S_w = [F * (R_w / R_t)]^{0.5}$

Where  $F = a / \Phi^m$

Hydrocarbon saturation ( $S_{hc}$ ) is the fraction of pore volume filled with hydrocarbon (oil and gas). It is given by:  $S_{hc} = 1 - S_w$

#### 4.3.5 Bulk Volume of Water ( $V_b$ )

This is the measure of the quantity of formation water present in a unit volume of rock. It is defined as the product of water saturation ( $S_w$ ) and porosity ( $\Phi$ )

$$V_b = S_w * \Phi$$

#### 4.3.6 Irreducible Water Saturation ( $S_{wir}$ )

This is the minimum saturation attainable by reservoir water when displaced from porous medium by immiscible hydrocarbons i.e. the fraction of pore volume occupied by water in the reservoir at maximum hydrocarbon saturation. It is normally used in preparation for permeability calculation.

$$\text{This is defined as: } S_{wir} = \frac{V_b}{\Phi_{eff} / (1 - V_{sh}^2)}$$

Note:  $S_w = S_{wir}$ : implies an obvious hydrocarbon bearing zone

$S_w > S_{wir}$  implies production hydrocarbon likely with some water cut

$S_w < S_{wir}$  implies error in calculation

#### 4.3.7 Permeability (K)

The values of permeability of selected reservoir rocks are calculated using Coates simplified method. This method works well in shaly sands (Crain, 2004). The generated values also correlate well with values estimated from core analysis.

Coates defines Permeability (K) in millidarcies as:

$$K = G \Phi_{eff}^4 \left[ \frac{[\Phi_T - (\Phi_{eff} * S_{wir})]}{\Phi_{eff} * S_{wir}} \right]^2$$

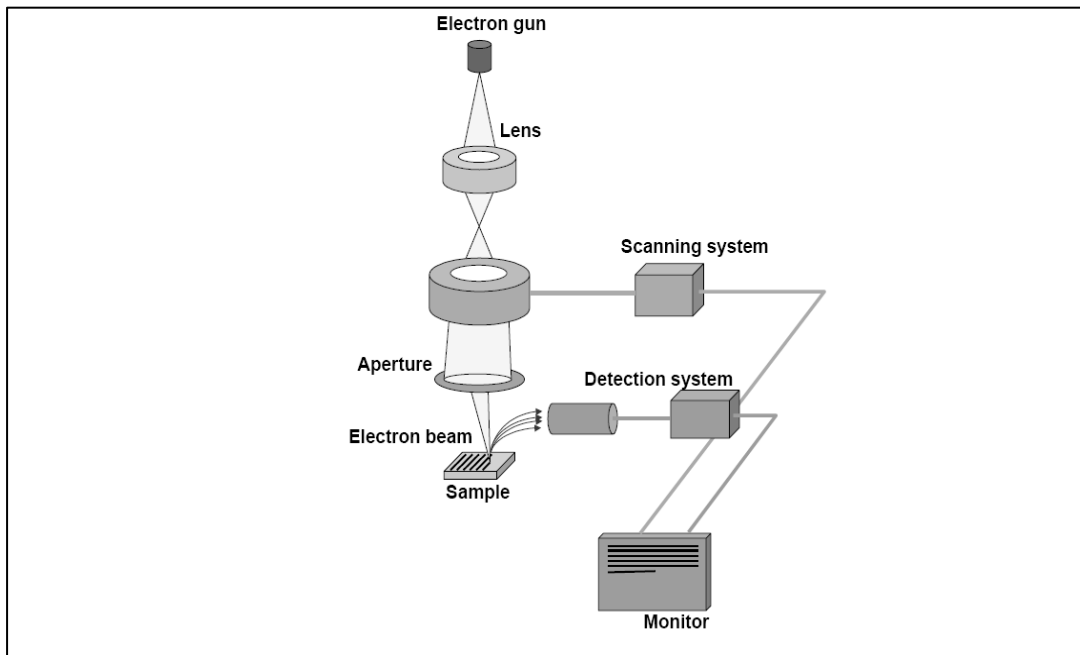
Note:  $G = 65,000$  to  $10,000$  for oil,  $650$  to  $1000$  for gas (Crain's Petrophysical Handbook). However  $G$  is taken to be  $1000$  in this study.

#### **4.4 Thin Section**

Thin section was prepared by making a thin slice of about a centimetre thick from the sample with a diamond saw. The slice glued to glass slide and further thinned with diamond saw. The slide was thinned further by grinding with progressively finer abrasives. When the thickness has been reduced to about  $0.03\text{mm}$ , a thin cover was glued to the top of the slice to complete the thin section. Thin sections were studied with a petrographic microscope that has a polarized light source. The effect of the passage of polarized light through individual mineral crystal was analysed and information about the arrangement of the atoms of the crystals were obtained.

#### **4.5 Scanning Electron Microscopy**

Scanning Electron Microscopy is a versatile and well-established complementary technique to light optical microscopy. By using a beam of electrons instead of photons, samples can be imaged at far higher magnifications. The Topcon Leo S440 at ITRI Innovation is capable of imaging up to  $100,000$  times magnification, although in practice magnifications of this magnitude are seldom required. The Leo S440 is also fitted with an energy-dispersive x-ray (EDX) spectrometer. This device measures the energy of x-rays that are generated by the atoms of the sample during interactions with the electron beam. The x-ray spectra formed are characteristic of the atoms that formed them, allowing the chemical composition of the sample to be determined. Pellets are prepared by using very little grams ( $> 0.3$  g) of the samples, the pellets were first selected and the surface was covered with adhesive, after some minutes this minute sample was spread on the pellet evenly, this process was repeated for all the samples. The pellets were inserted into a carbon sputter where they were coated with carbon. After coating the pellet with carbon, it was then inserted into the SEM machine for image/EDX analysis. The diagram below explains the workability of the SEM (Fig. 4.2), the focused electron beam was deflected in x and y direction by the scanning system. The deflection is controlled such that small rectangular frame was scanned on the system's surface. The scanning system synchronised the electron beam in the microscope with the electron beam inside the monitor that is used to display the image. The intensity of the monitor was modulated by the signal that was obtained from the electron detector in the SEM.



**Figure 4.2:** Scanning and detection system in scanning electron microscope (Theodoor, 2000).

In this way, the image was built point by point and line by line, with intensity in each point that is proportional to the signal from the electron detector. The signal from the electron detector in turn is dependent on the amount of electrons collected. The magnification is defined as the ratio of the size of the image on the monitor and the size of the frame that is scanned on the sample's surface. The magnification can be increased by reducing the size of the scanning frame, which is controlled by the scanning coils.

#### 4.6 X-ray Diffractometry (XRD)

Diffraction measurements for phase identification were done using BRUKER D8 ADVANCE diffractometer located at iThemba LABS x-ray facility. Measurements were done using the 8 KeV Cu radiations. The X-ray generator was operated at 40 kV and 40 mA. Experimental set-up included a 3 ° divergence slit on the primary side and 3 ° on the secondary side. The diffracted beam was collected with a 4° window position sensitive detector, Lynx eye. Samples were measured from 2-theta start of 10 ° to 2-theta stop 85°, with step size of 0.02 ° and step time of 0.3 s. The analysis of the data was carried out using BRUKER's Eva software

#### **4.7 Fourier Transform Infrared Spectroscopy (FTIR)**

FTIR (Fourier transform infrared spectroscopy) is a technique that provides information about the chemical bonding or molecular structure of materials, whether organic or inorganic. It is used in failure analysis to identify unknown materials present in a specimen, and is usually conducted to complement petrographic analysis. FTIR was used to determine the structure and composition of hydrocarbon. It provides a means of characterising the component within an organic matter concentrate. The method relies on the absorption of infrared waves from the electromagnetic spectrum by bonds within the organic matter, resulting in change in dipole moment of the bond as the bond vibrations change (Silverstein et al., 1974). The analysis of geological samples differs from that pure organic species in that signals produced by former are restricted to broad bands assigned to chemical groups, by reference to spectra of many pure compounds (Gize, 1985). The technique works on the fact that bonds and groups of bonds vibrate at characteristic frequencies. A molecule that is exposed to infrared rays absorbs infrared energy at frequencies which are characteristic to that molecule. During FTIR analysis, a spot on the specimen was subjected to a modulated IR beam. The specimen's transmittance and reflectance of the infrared rays at different frequencies is translated into an IR absorption plot consisting of reverse peaks. The resulting FTIR spectral pattern was then analyzed and matched with known signatures of identified materials in the FTIR library. FTIR was used to provide a broad characterization of the Albian age, sandstone samples. The obtained results were interpreted with reference to the literature. The FT-IR analysis of all core samples in this work was carried out on a Perkin Elmer 1600 series spectrophotometer.

#### **4.8 High Resolution Transmission Electron Microscopy (HRTEM)**

Pulverized sample (~1 - 2) g of the sandstone samples was poured into a small conical container while little amount of ethanol was added to the sample to serve as medium for solution. This solution is now placed inside the centrifuge for few minutes (5 mins), drops of the stirred solution is hereby placed on a labeled 200  $\mu\text{m}$  and 400  $\mu\text{m}$  of copper grid underlain by a filter paper with a hot lamp light focused directly on the samples to dry up the earlier added ethanol. The resultant was placed inside the air gun channel so as to project the beam on it for image analysis at a nanometric scale. The energy dispersive spectroscopy (EDS) was performed on the

zone of interest by adjusting the equipment to spot size 7 which is the standard for EDS quantification of the HRTEM machine. The HR-TEM analysis of study was carried out on TECHNAI G<sup>2</sup> F20 X-TWIN MAT 200Kv field emission transmission electron microscopy.

#### **4.9 Pore Water Geochemistry**

##### **pH, EC AND TDS PROFILE OF THE EXTRACTED INTERSTITIAL PORE WATER**

The pH, EC and TDS parameter of the extracted interstitial pore water were achieved using 1:10 core sample to water ratio by following the method of Eckert (1988). 5 grams of each of the core samples taken at depth of interest were weighed and put in a beaker and (50 ml) of ultra-water added. The mixture was then stirred thoroughly for 5 minutes, allowed to settle for 15 minutes and the pH, EC and TDS of the supernatant recorded. After every measurement the pH meter is preserved in potassium chloride (KCl). The procedure was duplicated for each sample at each depth.

#### **4.10 X-ray Fluorescence spectrometry**

The bulk chemical compositions of the reservoir core samples were determined with X-ray fluorescence spectrometry. Samples for XRF analysis were taken at an interval of interest along the depth of the drilled wells based on log interpretation and core description. The core samples were oven-dried at 100 °C for 12 hours to remove the adsorbed water and then crushed with a mortal and pestle to a fine powder. A PW1480 x-ray fluorescence spectrometer using a Rhodium Tube as the x-ray source was used. The technique reports concentration as % oxides for major elements and ppm for trace elements.

## CHAPTER FIVE

### 5.0 CORE DESCRIPTION RESULTS AND INTERPRETATION

---

---

Accurate core description is a basic work, the foundation upon which the entire structure of subsurface investigation rests. The study of cores from both field and wildcat wells offer the opportunity to interpret subsurface rock sequences and relate them to surface sections, to calibrate mechanical logs with observed lithologies and to use these data to enhance both field development drilling and wildcat exploration.

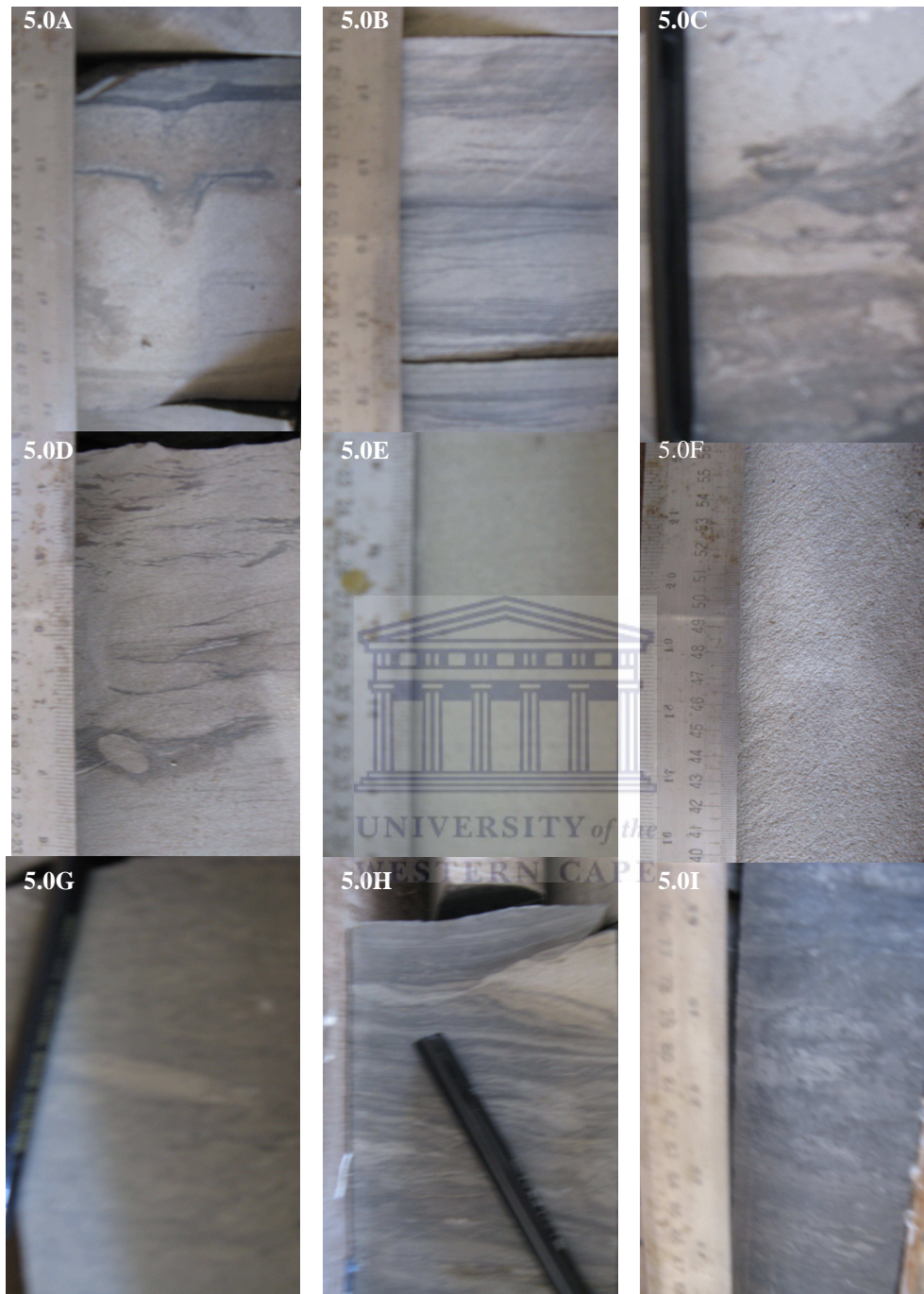
This chapter presents the results of core description and geophysical logs interpretation of three wells A-G1, A-K1, and A-W1 with core samples. The core sequences of the siliciclastic rocks described herein are organized on the basis of grain size variation, sedimentary structures, mineralogical constituents, facies distribution and depositional environments. These are presented sequentially from the depositional system through the continental environment to shoreline and finally shallow marine/offshore and deeper water environment. Albian age (start of the Lower Cretaceous) is the age of interest in this study, therefore the interpreted core intervals in this chapter are all within the Albian age for all the studied wells.

Three large-scale lithologic categories were delineated by this study. These lithofacies are based on distinguishable sedimentary structures, textures, grain size, primary mineralogy and environment as inferred from these characteristics. The list below shows the different lithofacies defined by this core examination.

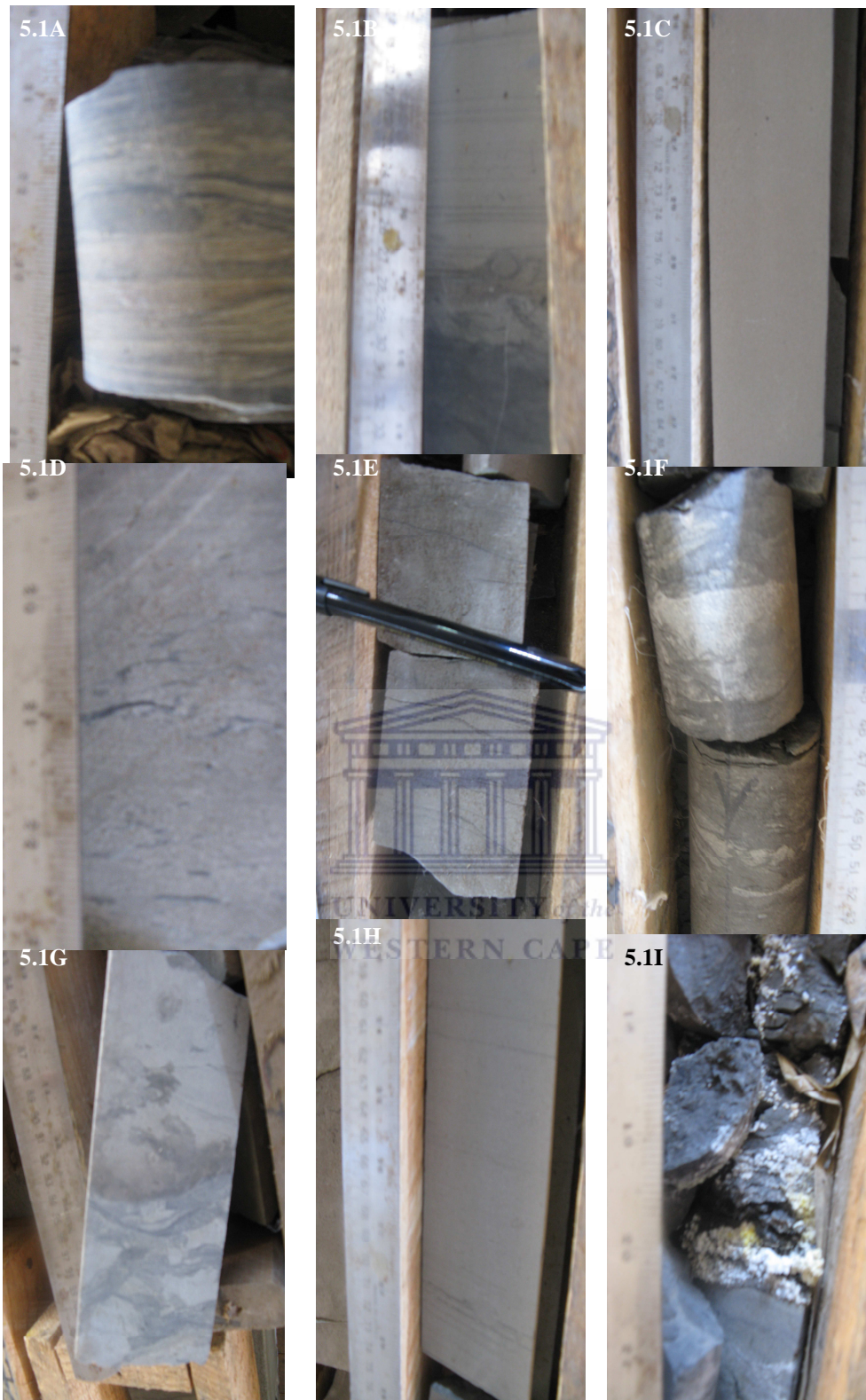
- ❖ F1: Fine grained sandstone
- ❖ F2: Very fine grained siltstone
- ❖ F3: Mudstone



**Core Representation for the Three Cored Wells Showing Different Sedimentary Structures**



**Figure 5.0: (A) Burrowing flaming water escapes structure. (B) Parallel lamination, clay stone drape over ripples. (C) Rip-up clasts at high energy sheet flow (D) Ball and pillow structure, mud drape and current ripple marks. (E) Massive sandstone with very faint lamination (F) Coarse sandstone with blurred cross bedding evidence (G) Leave shaped flaser lamination entrapment. (H) Two-directional bedding (Herring Bone cross bedding) planar nature of lamination suggest this is herringbone rather than festoon cross bedding. (I) Silty-shale unit with evidence of bioturbation.**



**Figure 5.1: (A) Flaser and lenticular lamination (B) Flat bedded sandstone with siltstone interlamination (planar bedding), rip-up clasts with shaly lithology showing bioturbation towards the base (C) Clean massive sandstone unit. (D) Mud drapes, trough cross bedding size suggest either ripple or small sand dune bedding (E) claystone lamination within the sandstone unit (F) Flaser lamination embedded within the shaly unit (G) Siltstone unit dominated by thick diameter claystone ripples (H) upward fining cycle with some claystone lamination within the massive sandstone. (I) Water reaction on the shattered shaly unit**

## **5.1 LITHOFACIES OF A-G1 CORE # 1**

### **5.1.1 FACIES 1: Fine grained sandstone**

After proper examination of A-G1 core 1, it was observed that facies 1 (fine grained sandstone) occurred in the upper 2.5m at depth ranging from (3372.5 - 3370) m and also re-occurred at (3377.8 - 3375) m which is about 2.2m thick. This sandstone is light gray and it shows a well sorted arrangement with grains ranging from sub-angular to sub-rounded. Mineral components deduced from microscopic study include glauconite, quartz and chlorite show while the accessory minerals within the facies are weathered chert, mica and siderites. Different sedimentary structures such as climbing ripples, parallel laminations, claystone drapes were observed in the upper 2.5 m thickness while load casts, soft sediment deformation, ball structures, flaser and streaky lamination and erosional surfaces were noted in the 2.2m depth range of the F1 section. The addition of dilute HCl to the samples generally shows no reaction except at depth 3376.57 m where there was a rapid effervescence confirming the presence of calcareous materials. Following the different mineralogical characteristics observed, the presence of chert within this environment was confirmed upon reaction of HCl with the sample. Lack of reaction always distinguish chert from carbonates, also the soft sediment deformation could be accrued to the presence of weathered chert observed within the facies. Siderite is known to be usually brownish in colour with a slow rate of effervescence upon addition of HCl. The sedimentary structures show that the thick sand (Fig. 5.2) is a distributary channel while the thin sands with shales are crevasse splays.

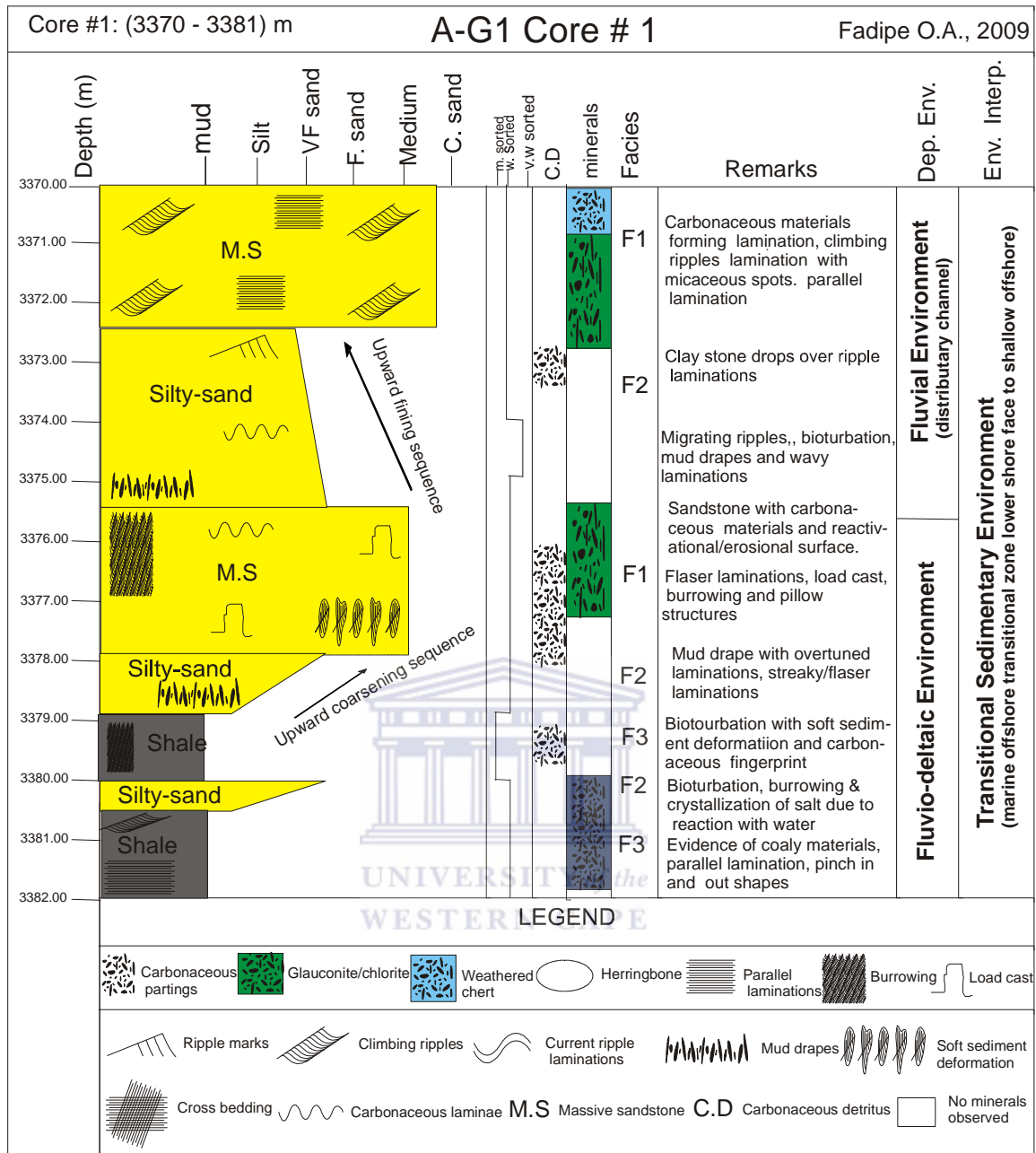
### **5.1.2 FACIES 2: Very Fine grained siltstone**

This facies was noticed in an interval between (3375.5 – 3372.8) m having about 2.7m thickness with an upward fining sequence. Also, Facie 2 was observed at depth range (3378.9 – 3377.8) m and (3380 – 3379.7) m having 1.1 m and 0.3 m thickness respectively with an upward coarsening sequence. The 2.7m thickness is generally ranging from light – medium – dark grayish colour with a rounded shape and averagely well sorted. Mineral components includes siderite, coaly material, spots of micaceous materials, chlorite shows and glauconite, sedimentary structures involved within this intervals are migrating ripples, bioturbation, wavy lamination, load cast, flaser and streaky lamination. Oxidation evidence is prominent at 3375.52 m while there was also little or no reaction upon the addition of dilute HCl. The 1.1m thickness also shows the same characteristics with the 2.7 m thickness with reference

to sedimentary structures and mineralogical compositions but the lithologic colour observed from the core is dark gray. The facies is assumed to be tight in terms of porosity evaluation due to the inability to absorb dilute HCl added to it. The presence of glauconite is attributed to a marine setting; it is usually associated with organic residues (Odin and Matter (1981), indicating that organic matter plays a role in formation of the mineral. Bacterial activity may promote glauconite formation by producing micro-reducing conditions in the sediment. However, the different sedimentary structures observed within this interval make it somehow complex for interpretation.

### **5.1.3 FACIES 3: Mudstone**

The shale beds are typically less than 1m thick (3379.8 – 3378.9) m and also grade into the underlying facies 2 beds. The dark colour of this shale is a function of their high organic carbon contents. The grain sizes are very fine with a sub-angular shape and well sorted grain arrangement, observed minerals include chlorite, glauconite, mica and some coaly materials. There was no reaction with dilute HCl signifying absence of calcareous material within that interval. Sedimentary structures like bioturbation, burrowing, overturned laminations, pillow structures, flaser laminations, finger print marks were observed during core examination. The shale sequence observed from this section is likely deposited in a crevasse splay environment although other analysis of the samples picked from this section would be used to confirm the inferred depositional environment.



**Figure 5.2:** Core graph showing the summary of the core description for A-G1 results.

## 5.2: LITHOFACIES OF A-K1 CORE 1 AND CORE 2

The A-K1 well consists of two cores namely core 1 and 2, these cores were examined in details, shown in figure (5.3) is the core description for both cores 1 & 2. Three large scale lithologic categories were delineated by this study. These lithofacies are based on distinguishable sedimentary structures, texture, grain size, primary mineralogy and environment as inferred from these characteristics.

### **5.2.1 FACIES 1: Fine grained sandstone**

These facies occurred in the upper 3.5 m and 4.8 m of core 1 and 2 respectively, these appear to be purely clean sands, the sandstone is light gray, very well sorted, and range in grain shape from sub-rounded to sub-angular but mostly sub-rounded with evidence of cross stratification and lithoclasts. Upon the addition of drops of dilute HCl, there was no serious effervescence. Mineral component observed during microscopic examination include quartz (dominating), glauconite (greenish bean shaped) and occasional traces of pyrite. Bi-directional bedding (herringbone) structure was observed at depth 3237.68 m with some evidence of carbonaceous materials while ripple marks are prominent across the facies. Some reddish brown laminations were observed which could be as a result of oxidation activity within the depth range.

The formation of ripples due to oscillation of waves and their morphology have been studied mainly in cases of silty or sandy bottoms (Baas, 2003), ripple forming deposits are commonly sorted by grain size and density, the material of largest size and least density is commonly found on ripple crests (Bucher, 1919; Reineck and Singh 1973, Allen, 1984). In this study, no clear trend was observed in grain size distribution for the ripple marks. The prominence of the ripples in this facies suggests wave-current origin.

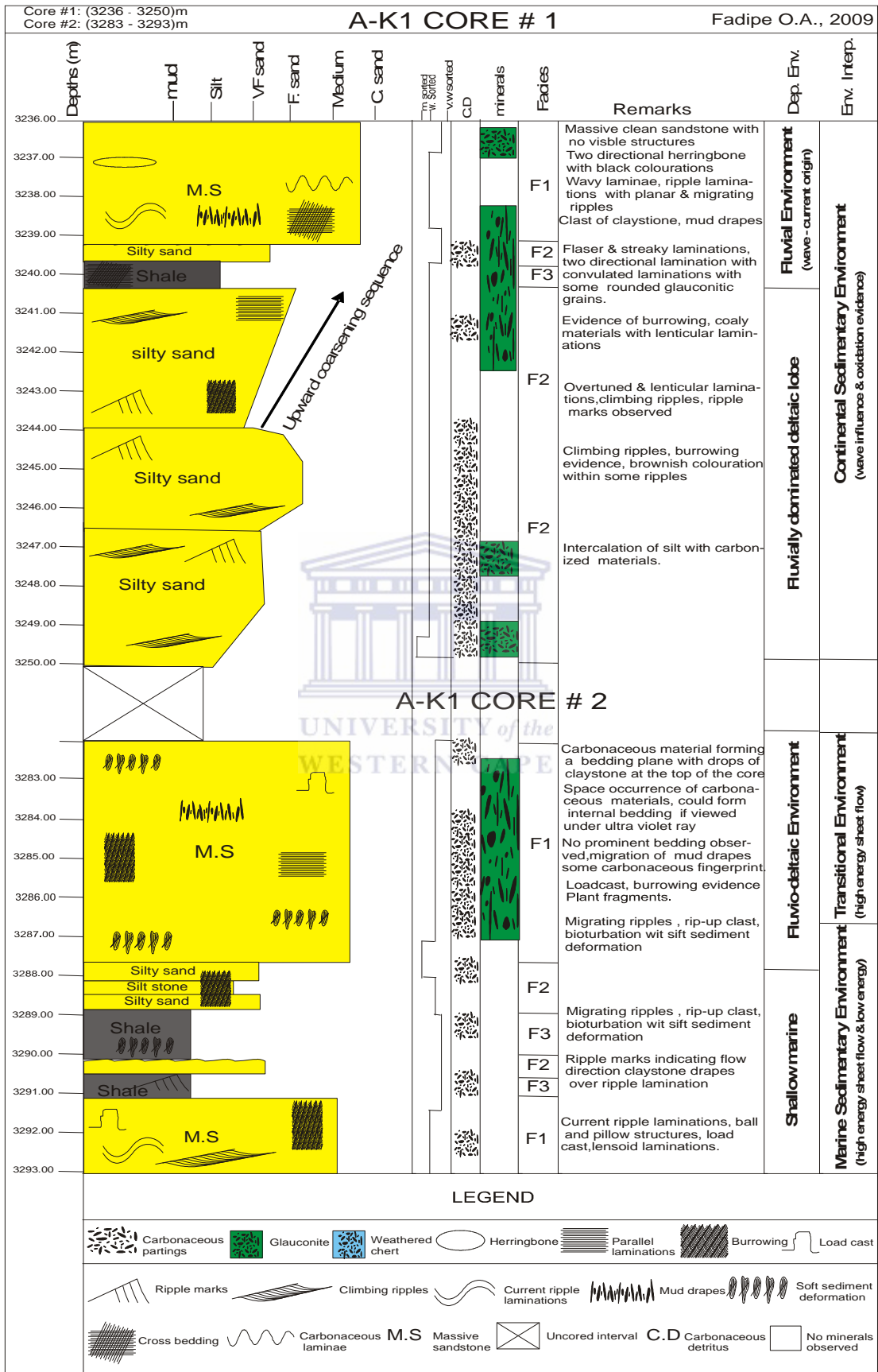
### **5.2.2 FACIES 2: Very Fine grained siltstone**

These facies occurred mainly as partings in core # 2 which range in thickness from 0.5 m – 0.7 m (Fig. 5.3) having a sharp/scoured basal contact which is graded into the underlying shale or mudstone. This siltstone ranges in colour from gray to medium gray while evidence of burrowing, vertically stacked invagination features which probably represent escape burrows (Fig. 5.0A) and lenticular and flaser bedding comparable to features observed and described from cores from A-G1 well. The sorting is very good while it possesses a sub-rounded grain size classification; the grain size is also very fine. The mineral constituents include traces of mica (probably muscovite), occasional laminated pyrite and carbonized plant remains. Among the sedimentary structures observed are the flaser and streaky lamination, two directional lamination suggesting wave influences. There was no rigorous reaction with dilute HCl showing that the presence of carbonates or calcareous materials can not be observed and also its ability to retain the dilute HCl added shows that the porosity could be assumed tight. The upward coarsening organization of this facies and the

presence of wave-formed structures indicate a marine origin. However, the interlamination of silt and clay with some ripple cross lamination sand has produced gradations between flaser and streaky laminations. The interbedded siltstone facies is hereby interpreted as forming in anaerobic conditions which are interdistributary bays, paralic between distributary channels.

### **5.2.3 FACIES 3: Mudstone**

The shale beds observed in core 1 ranged from 3239.20 m – 3250 m with a thickness of 10.8m while in core 2, it was intercalated with facies 2. These facies (3) are disrupted by small, horizontal burrows; thin isolated lenses of silt occur infrequently, the black colour of this shale could be a function of their high carbon content. Organics occur in association with locally abundant pyrite which was observed during microscopic examination. The grain size is very fine with a sub-rounded grain shape. This mudstone is very abundant in core 1 than core 2; bioturbation has destroyed original sedimentary structures. The intensity of bioturbation ranges from extreme to moderate, the degree of bioturbation is important as it introduces sand and silt and increases the vertical permeability (Cody, 2001). Fossil burrows from burrowing or feeding animals that leaves traces generally parallel to bedding were evident in the cores. This fossil might be an indicator of deep water deposition (slope to basin) settings (Basan et al., 1978). Pyrite ( $\text{FeS}_2$ ) is a common mineral product of early diagenesis in organic-rich sediments. It results from reaction of sulphide (produced via bacterial sulphate reduction (Berner, 1970) with either  $\text{Fe}^{3+}$  in sediment or  $\text{Fe}^{2+}$  produced by bacteria reduction (Lovely, 1991). The presence of bioturbation and pyrite is noted for delineating the condition of the environment (anoxic or oxic environment). The effect of bioturbation has washed away primary sedimentary structures like cross stratification and ripples, the period of storm events provides benthic organisms with plenty of opportunity to rework the sediment, sometimes even in the deeper areas of the shelf where life is usually sparse. The local presence of abundant preserved organics, probably marine kerogens (suggestive of very slow rates of deposition in poorly oxygenated or deoxygenated bottom waters).





**Figure 5.3:** Core graph showing the summary of the core description for A-K1 results.

### **5.3 LITHOFACIES OF A-W1 CORE**

The 24 m core of A-W1 was examined having three different lithofacies. These facies are discussed below:

#### **5.3.1 FACIES 1: Fine grained sandstone**

These facies occurred in the upper 19.5 m with some intercalation of other observed facies (parting form) between them (Fig. 5.4). This sandstone is light to medium olive gray in colour and shows fair to good sorting with grains being sub rounded and sub-angular. Mineral components observed from microscopic examination include quartz (estimated to be 85%) and dark mineral materials including authigenic minerals like glauconite and some coal fragments. Some quartz grain surfaces were frosted which could be attributed either to quartz grain overgrowth or aeolian sandblasting. Composite beds are often difficult to indentify due to relatively uniform grain size. The presence of cross bedding suggests deposition of these sands by active channel bars and the lower part of point bars. The cross bedding also suggest deposition by series of migrating dunes on mid-channel bars, and the lower part of point bars. The coaly shaly flaser drapes perhaps represent features similar to the “coffee grounds” observed on lower point bars of Mississippi river following flooding events as slack water depositional events occurred during falling river stage. These bars likely occurred in a meandering system dominated by lateral cuttings. The log characteristics in this section is expected to display a blocky signature given the uniform grain size distribution observed in the core and in few instances bell shaped signatures which will be consistent with the meandering interpretation. Environment of deposition for Facies 1 is the mid-channel bars in dominantly laterally-cutting meandering channel system.

#### **5.3.2 FACIES 2: Very Fine grained siltstone**

Very fine grained siltstone was observed in an interval between 3455.8 m – 3456.5 m bracketed by the fine grained sand and also at the depth range 3465.5 m and 3466.5 m (Fig. 5.4) which was embedded between facies 1 and facies 3. This very fine grained siltstone is light olive gray to dark gray, shows fair to good sorting with sub-angular to sub-rounded grains. Mineral components include quartz (85 %) and dark minerals including mafic minerals and coal fragments, glauconite with silica cement. Internally, facies 2 shows faint laminae and flaser bedding. In the lower part

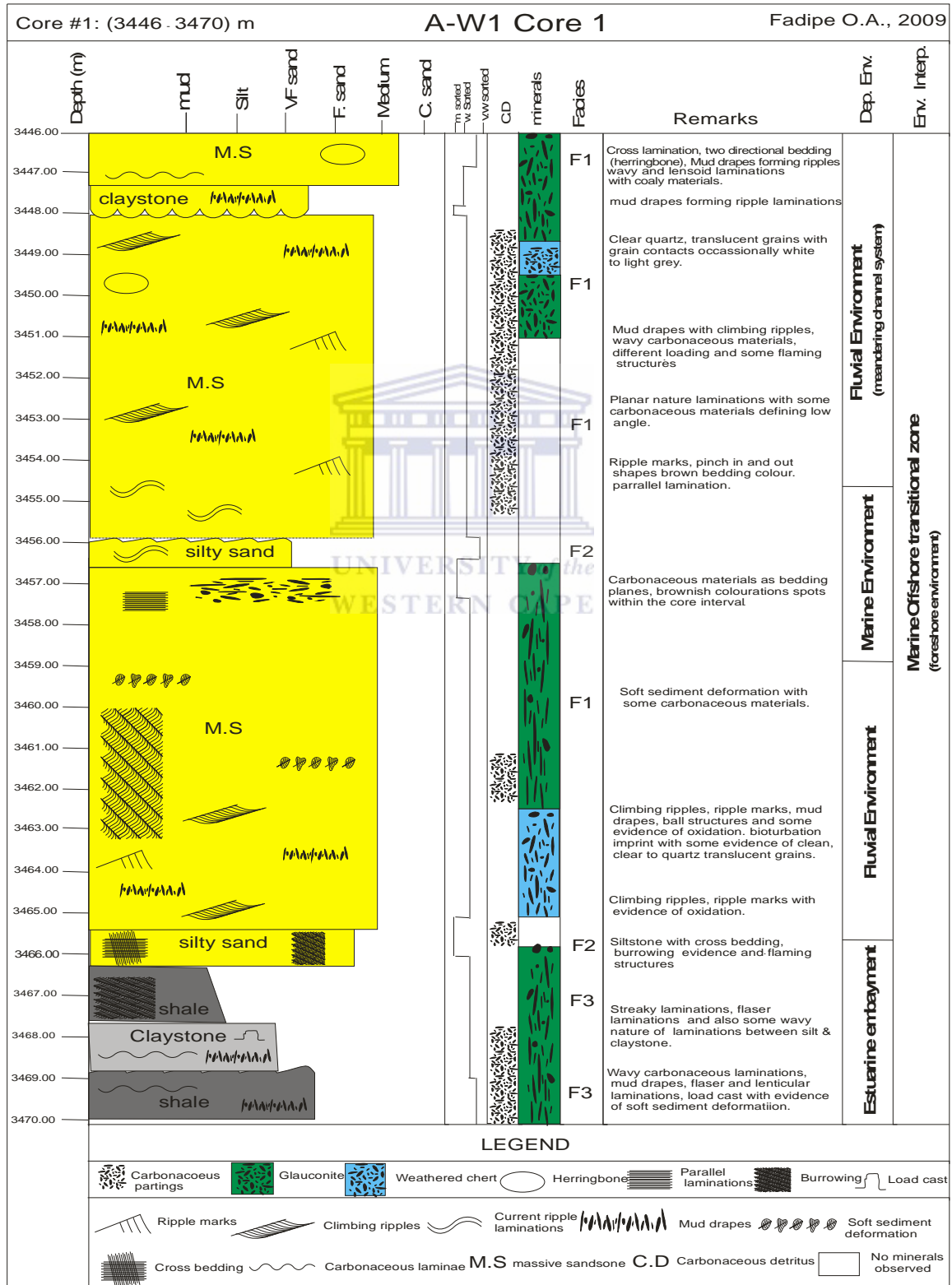
of the core, they show extensive micro-cross laminae with flaser clay drapes and parallel laminae. Intra-formational mud chips are common with internal mudstone partings, flame structures and fluid escape imprints. This sandstone shows some fining upward (3466.5-3465.5 m) and (3456.5-3455.9 m). These sandstones are also burrowed with non-specific animal burrows as described in figure 5.4. The presence of burrows is indicative of marine conditions ranging from estuarine settings, shoreline settings and shelf settings, especially storm dominated shelves. The fluid escape and flame structures observed in this facies is indicative of rapid deposition and subsequent dewatering. Also fluid escape structure may originate from local liquefaction and fluidization processes which are favoured by rapid sediment accumulation, presence of less permeable layers and immature sediment texture. The fining upward pattern shows it could be a progradational sequence; the finely parallel laminated siltstones were formed probably by suspension settling of silt and very fine particles from submarine density currents.

### **5.3.3 FACIES 3: Mudstone**

Mudstones were observed in the A-W1 core from 3466.5 m to the base with a small thin bed facies 4 embedded in between the mudstone facies (Fig. 5.4). Two types of mudstone were present, one mudstone type is gray laminated with animal burrows and contains interbedded thin (0.5 m) very fine – medium grained sands (Facies 4) with flaser and wavy bedding. The second mudstone type is black shale with thin parallel laminae black shale bedding and planes at 3469 m with evidence of bioturbation, pinch in and out shapes. These shales are organized between sands into two-fold sequences consisting of basal mudstones with interbedded fine grained sands and an upper zone of laminated burrowed black shale. Primary sedimentary structures (wave, ripples and hummocky cross stratification) are not prominent in this facies due to the effect of bioturbation; this has considerably obscured the internal structure of the bed thereby causing mixing of finer and coarser materials into a homogenous structure less units.

These shales represent part of an estuarine bay setting, an interdistributary bay or embayment is not unlikely. Such a setting is also influenced by estuarine overbank deposition, or even crevasses splay deposition. Both these processes may account for the thin fine grained sandstones. The mudstones with interbedded very fine grained siltstone were deposited near the outer part of the levee wedges caused by overbanks deposition or near the edges of crevasse splays. These were exposed periodically by

tidal exchange and plant rooting occurred. The two-fold sequence is interpreted as representing a basal estuarine embayment beyond (Tokar and Evans 1993), followed by perhaps a slight rise in sea level opening to more marine circulation followed by filling and additional deposition of estuarine embayment (black shale with laminae and burrows) sediments (PetroSA, 2003).



**Figure 5.4:** Core graph showing the summary of the core description for A-W1 results.

#### **5.4 Mineralogical Prediction from Core Description**

Glaucinite is a well-ordered K- and Fe-rich mica-structure clay mineral. It occurs as flakes or pellets, and may occur as infilling in foraminifera shells and sponge spicules (Odin and Matter, 1981). It may occur in fissures in feldspars, as crusts on phosphorite nodules, and as replacement mineral in coproliths. The colour is usually blue-green, but this depends on the original clay-type and chemical composition. For example, dark-green illitic clays alter to dark-green glauconite, while yellowish smectite clays alter to yellowish glauconite. It is usually associated with organic residues, indicating that organic matter plays a role in formation of the mineral. Bacterial activity may promote glauconite formation by producing micro-reducing conditions in the sediment. It forms from micaceous minerals or muds of high iron content where sedimentation rates are relatively low. Associated sediments are mainly calcareous, with a high proportion of fecal pellets. Most clay mineralogists have regarded glauconite as being formed under marine conditions (Odom, 1984, Odin and Matter 1981) (Fig. 5.4). Odom (1984) reviewed the various theories related to the mode or modes of glauconite formation. Odom (1984) refers to the theories of glauconite formation through potassium (K) uptake by a detrital smectite precursor as the “layer lattice theory”, in contrast to the “neof ormation theory” that does not require a detrital smectite or smectite-like precursor. Odom (1984) favours the neof ormation theory using evidence reported by Odin and Matter (1981), in which smectite might be a precursor of glauconite, but the smectite involved is apparently a neof ormation product.

Glaucinite abnormal occurrence in fluvial environment (Figs. 5.2, 5.3 &5.4) could be attributed to re-working of sediment which is allochthonous in nature (Odin and Matter 1981), its reworking attribute was also confirmed by the roundness in shape which shows that it has travelled a long distance from its origin (provenance). The chemistry of sea water favours the formation of glauconite (mica) (Fanning et al., 1989). Sea water contains about 380 mg L<sup>-1</sup> of K, 400 mg L<sup>-1</sup> of Ca and 3 mg L<sup>-1</sup> of Si. Although the exact pH for glauconite stability is not known, it seems that the formation of micas in sea water is possible because of the high K<sup>+</sup> activity and pH.

**Table 5.0:** Summary analysis of core findings.

<b>Well # Core #</b>	<b>Age</b>	<b>Lithologies</b>	<b>Depositional Facies</b>	<b>Environmental Interpretation</b>
A-W1	Albian	Thick sands, carbonaceous fragments, with mudstone partings, ripple, wave and cross stratification, bioturbation and water escape structure	F1 sands are channel and point bars (Meandering channel system). F2 is marine condition (estuarine, shoreline, shelf and storm settings), progradational sequence. F3 is estuarine bay settings and crevasse splay	Marine Offshore Transitional Zone (Foreshore environment)
A-K1, Core 1	Albian	Thick sands, carbonaceous fragments with ripple marks herringbone structure, flaser/streaky lamination. Shales are burrowed with intense bioturbation	F1 is wave-current origin while F2 is marine origin which could be interdistributary bay. F3 is marine kerogens (slow rate deposition)	Marine Offshore Transitional Zone (Shoreface environment)
Core 2	Albian			
A-G1, Core 1	Albian	Upper sandstone with erosional surfaces, claystone drape. Bioturbation, migrating ripples, load cast and burrowing within the shales	Thick sand (F1) is distributary channel, while F2 is complex (needs more data) F3 is related to A-W1 (crevasse splay).	Marine Offshore Transitional Zone (Lower shore face to shallow offshore)

## 5.5 Well Log Interpretation and Correlation

Well log analysis is one of the most important tasks for any well after drilling to determine the petrophysical parameters of reservoir rocks. Such analysis depends on the quality output needed. Lithologic identification can be considered as the most important information desired prior to any computations, especially those concerning fluid saturations. This is due to the relationship between the contained rocks and the occupied water, oil and gas contents. The mixed lithology possesses a particular problem for the log analyst because the difficulties arise from the mineralogical complexity reflected from varying rock associations, facies and depositional environments. By this way, the demand for appropriate methods and techniques to resolve the lithologic problems is advisable.

In this work, logging applications are primarily used to determine the lithologic components and reservoir zones through adequate assumptions and combinations of logging data. At first, the rock types can be easily identified through the various crossplots. A number of crossplots (GR- RHOB and RHOB-NPHI) were established for recognizing the rock types. These crossplots assist in defining the different lithologies: sandstones, shales and limestones e.t.c (Schlumberger, 1972). The qualitative interpretation of these crossplots is based on the transformation of the encountered log responses into the lithologic components and mineral constituents (Serra, 1986). The quantitative interpretation of this type of crossplots revealed the rock type and amount in addition to the effect of shaliness, secondary porosity and gas show (Schlumberger, 1974). Secondly, the effects of clay minerals (kaolinite, montmorillonite, illite, mixed clay layer, mica and glauconite) are determined by observing the geophysical log response to these clay minerals. The qualitative and quantitative interpretation of this type of crossplots helped in determining the clay type and amount in the evaluated rock unit (Schlumberger, 1982). Moreover, the presence of clay minerals within any reservoir interval normally complicates the problem for the log analyst when evaluating the potentials of this reservoir (i.e. shale volume, effective and total porosities, permeability and water and hydrocarbon saturations e.t.c). As a result, it is very essential to define their effects on both effective porosity and hydrocarbon saturation through clay minerals-saturation

crossplot and lithologic-geologic models. Thus, this study will give a brief insight on the mineralogical and lithologic evaluation of the studied core units and the effects of both on the fluid contents in the later chapter.

The development of geologic pattern displayed stratigraphic units that are equivalent in time, age, or stratigraphic position through the use of electric wireline logs is generally referred to as log correlation (Rider, 1996). It is a product of basic geological principles, which include sound understanding of depositional processes and environment, concepts of logging tools and measurements, reservoir engineering fundamentals, and qualitative and quantitative log analyses. Out of the five wells evaluated for hydrocarbon potentialities in the study area of the Orange Basin, three of the wells (A-G1, A-K1, A-W1) have core samples available which has been subjected to different analysis while the other two well (A-K2 and A-Y1) lacks core samples. The shapes of well log curves have long been interpreted in terms of depositional facies because of their resemblance to grain size succession (Selly, 1978).

Many published works used simplistic “pigeon-hole” approach for interpretation. An example is the classification of bell shaped gamma ray profile as fining upward meandering stream facies successions (Douglas, 1987). Although, there are problems associated with this approach which involved the most typical vertical patterns seen on gamma ray, SP and resistivity logs (Douglas, 1987). It is therefore emphasized that no pattern is unique to, or diagnostic of any particular depositional environment. It follows that interpretation based on log curves shape alone is a predictive method. In those particular wells where log-pattern has been calibrated to understand depositional environment succession in cores, the log pattern method can be applied successfully to the interpretation of correlative un-cored facies succession. The crossplots of different logs from each reservoir zone identified in each well will be used coupled with analysed core samples from the other three wells for a good understanding of the other two wells without core samples.

#### **5.5.0 Geological Interpretation of Wireline Logs.**

The Albian age of the A-G1 well falls within the range of (3050 – 3450) mRKB, through a quick look at the qualitative interpretation using gamma ray, the lithologic interpretation was built while within this lithologic interpretation, four reservoir zones were identified based on the integration of the available wireline log

(GR, RHOB, NPHI, SFLU, MSFL, ILD) as displayed in the PETREL 2009 software (Figs 5.5A & B, 5.5.1A & B). A summary of the different reservoir unit is presented in table 5.1. Stratigraphically, the core lies very close to the lower part of the horizon M2K1 (3416 m).

### **5.5.1 Reservoir unit geophysical logs interpretation of A-G1**

#### **SAND A OF A-G1 WELL:**

The well section (Fig. 5.5A) reveals the reservoir sand A reservoir zone ranging from (3181.50 – 3196.50) mRKB having a gross and net of 15m and 5.41m respectively. Sand A has a coarse sandstone of almost a uniform grain size as revealed from the log signature (delineated with a blue dotted line) having an average gamma ray reading of 32.34 API unit indicating a clean sand and probably a fluvial environment based on log shape (Rider, 1996). The low neutron porosity reading with corresponding high bulk density and resistivity log reading within the zone reveals the presence of hydrocarbon in sand A which also falls within the Lowstand system tracts. The unit directly on top of the reservoir zone could act as a possible seal for the hydrocarbon within this interval.

#### **SAND B OF A-G1 WELL:**

Reservoir sand B was observed at (3309.98 – 3331.04) mRKB having a gross and net thickness of 21 m and 8.38 m respectively with a similar trend of log signature as that of sand A but with an upward fining sequence (Fig. 5.5B). Though the average gamma ray reading within the zone is 54.20 API showing that sand B is not as clean as that of sand A, notwithstanding sand B could still be attributed to have similar characteristics as those of sand A (predicted fluvial environment which falls within a Lowstand system tract). However, the panel grouping of both the bulk density and neutron log gives the indication of the hydrocarbon prediction having a low neutron porosity reading with corresponding high bulk density and deep resistivity readings. The shaly/silt sand directly above the reservoir zone has an average gamma ray reading of 108 API with a gamma ray scale between 0-180 API showing that the rock type could also serve as a cap rock for hydrocarbon trapping.

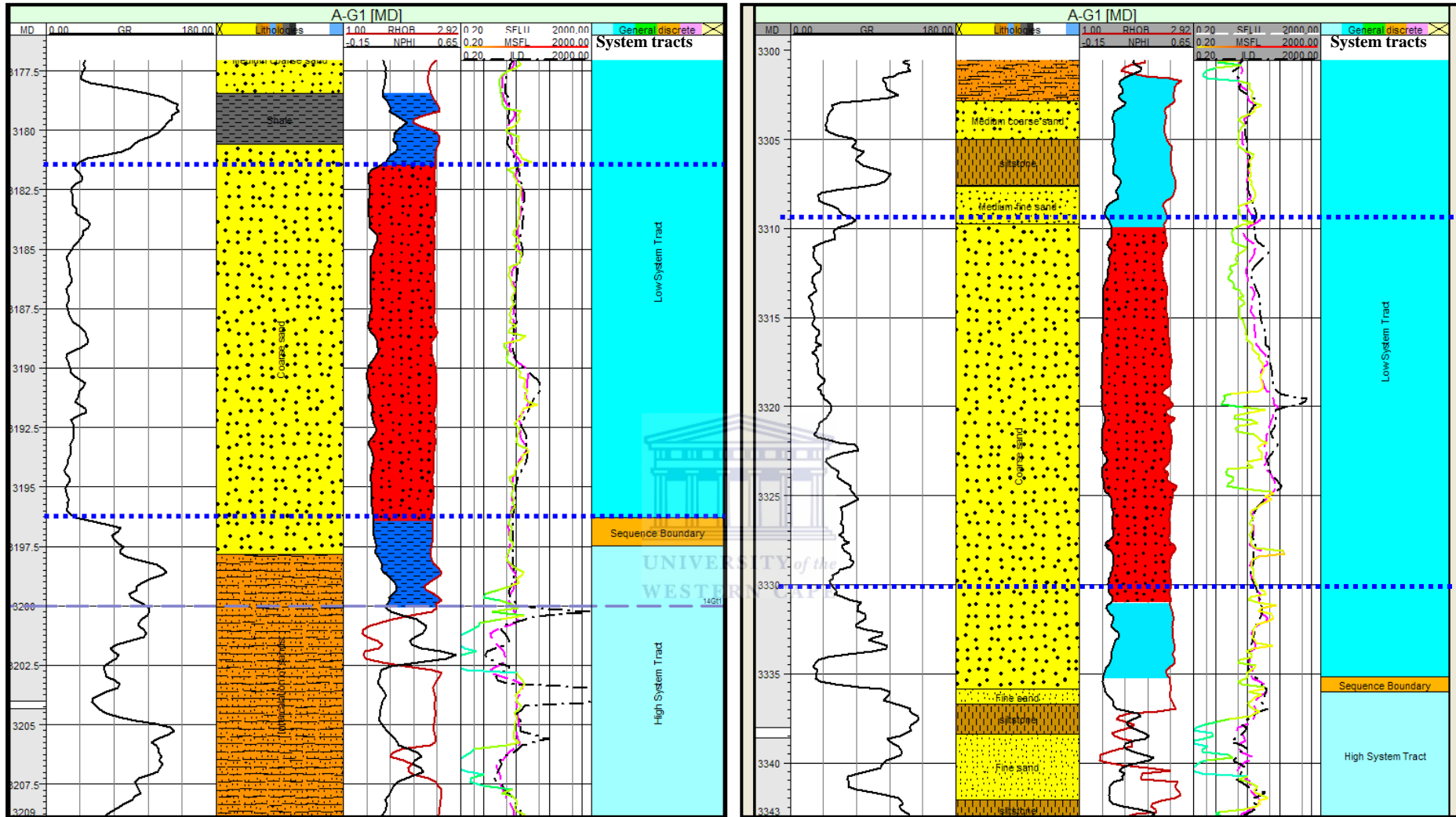


### **SAND C OF A-G1 WELL**

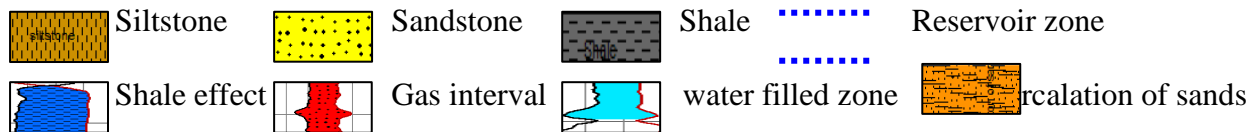
Reservoir sand C (3368.11 – 3375.75) mRKB is the only reservoir unit in this well that has core sample available for reservoir characterization. Figure 5.3 allows a quick look at core visualization in comparison with the wireline logs, it was observed that the driller's depth (Logs) and the core depth has a difference of about 1.18m signifying that for a proper correlation of both the core graph and the well log section, 1.18m should be added to the core depth to serve as a shift of the shale base line believing that the driller's depth is the actual depth (Schlumberger, 1972). The average gamma ray reading of 59.29 API confirms the sandy nature of the reservoir. However, a fluvial setting could be predicted within the reservoir zone due to the log shape having a blocky nature (Rider, 1996) as seen in figure C which agrees with the core description interpretation. The reservoir unit falls within the Highstand system tracts (HST) while the shaly unit directly below the reservoir zone was interpreted as the period of maximum flood surface (MFS) having a very fine grain size due to the low energy settling of the sediments during the peak of the rise in sea level.

### **SAND D OF A-G1 WELL**

Reservoir sand D (3391.40 – 3406.36) mRKB was interpreted as a medium coarse sandstone unit with an average gamma ray reading of 56.83 API delineating the sandy nature of the unit, however, a very high resistivity (MSFL = 1938  $\Omega$ m) reading was observed at depth 3404m – 3405m with a corresponding high density and low neutron log readings suggesting the presence of hydrocarbon in the environment. The gross and net thickness of the reservoir unit is 14.96m and 3.9m, respectively. An upward fining sequence with a Transgressive system tract (TST) was observed (Fig. 5.5.1B) at the reservoir zone based visualization. A fluvio-deltaic setting is suggested based on log signature in the absence of core examination (Rider, 1996).



**Figure 5.5: (A) Reservoir sand A (3181.50 – 3196.50) mbKB in the A-G1 well (B) Reservoir sand B (3309.98 – 3331.04) mbKB in A-G1 well.**



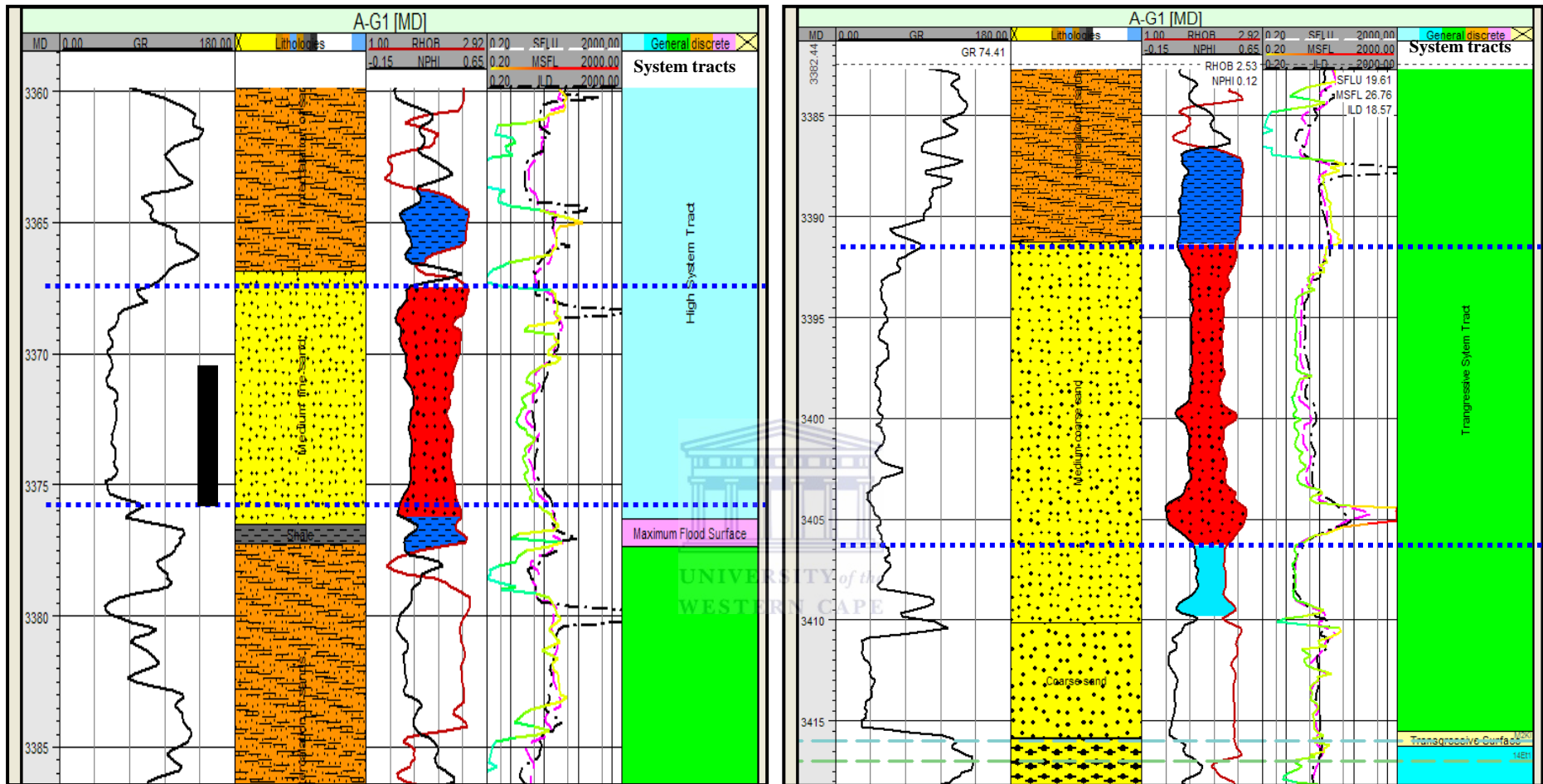
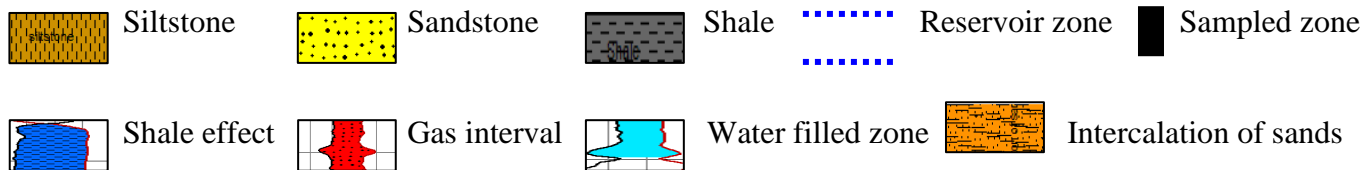


Figure 5.5.1: (A) showing Reservoir sand C (3368.11 – 3375.75) mbKB (B) showing Reservoir sand D (3391.40 – 3406.736) mbKB in A-G1 well.



## **5.5.2 Reservoir unit geophysical logs interpretation of A-K1**

### **SAND A OF A-K1 WELL**

The well section for A-K1 (Fig. 5.5.2A) reveals the reservoir sand A ranges from (3230.10 – 3240.00) mRKB having a gross and net of 9.9 m and 3.19 m respectively (Table 5.1). The average gamma ray reading (63.70 API) indicates medium-coarse sand unit as seen in figure 5.5.2A below. The high resistivity values in the resistivity log coupled with the low neutron porosity log and high density suggest hydrocarbon within the reservoir zone. The prominence of the ripple marks in the described core 1 as observed in the earlier discussed section (core description) suggest a wave-current origin, interdistributary bay and distributary channel, however, the log signature show the uniform distribution of grain size within the reservoir interval located within the lowstand systems tracts (LST) suggesting a fluvial environment (Per. Comm. Hugo Simon 2008).

### **SAND B OF A-K1 WELL**

The well section for A-K1 (Fig. 5.5.2B) reveals the reservoir sand A ranging from (3274.13 – 3287.10) mRKB with a gross and net of 12.97 m and 3.00 m (Table 5.1) respectively. The average gamma ray reading (43.54 API) explains the interpreted medium-coarse sand unit as seen in figure 5.5.2B below. The log signature shows a dirtying-up trend i.e. a gradual upward increase in the gamma ray response signifying a decrease in the depositional energy, the fining upward sequence as observed (Fig. 5.5.2B) could be attributed to a meandering or tidal channel deposits with an upward decrease in fluid velocity within the channel i.e. coarser sediments at the base of the channel (<http://strata.geol.sc.edu/log-char.html>) which falls within the transgressive system tract.

### **SAND C OF A-K1 WELL**

Sand C ranging from (3354 – 3270.7) mRKB with a gross and net reservoir thickness of 16.7 m and 2.04 m (Table 5.1) respectively falls within the transgressive systems tracts having a blocky shape (GR) with a sharp top and base within the reservoir zone. The boxcar trend of the gamma ray log (Fig. 5.5.3A) shows a very low reading having an average of 34.43 API with no significant internal change in the log trend. This trend indicates in a fluvial channel sands (<http://strata.geol.sc.edu/log-char.html>).

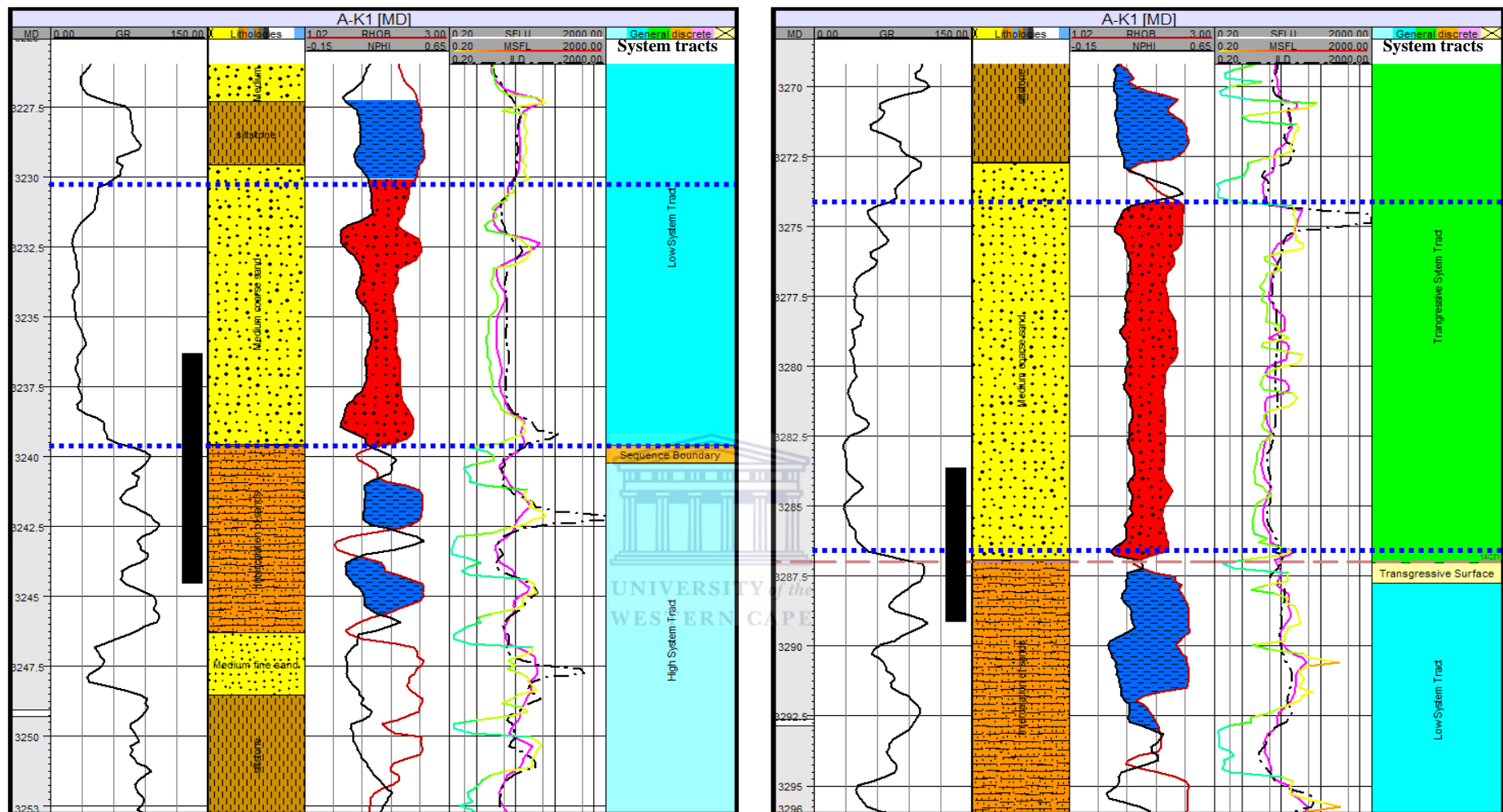
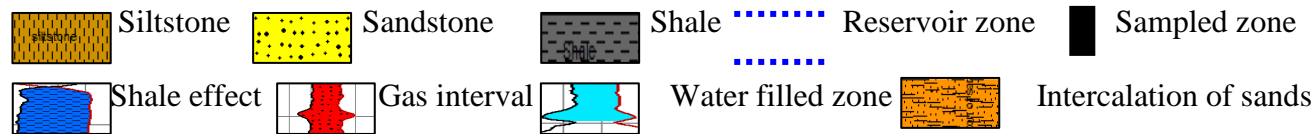


Figure 5.5.2: (A) showing Reservoir sand A (3230.10 – 3240.00 mRKB (B) Reservoir sand B (3274.13 – 3287.10 mRKB in A-K1 well



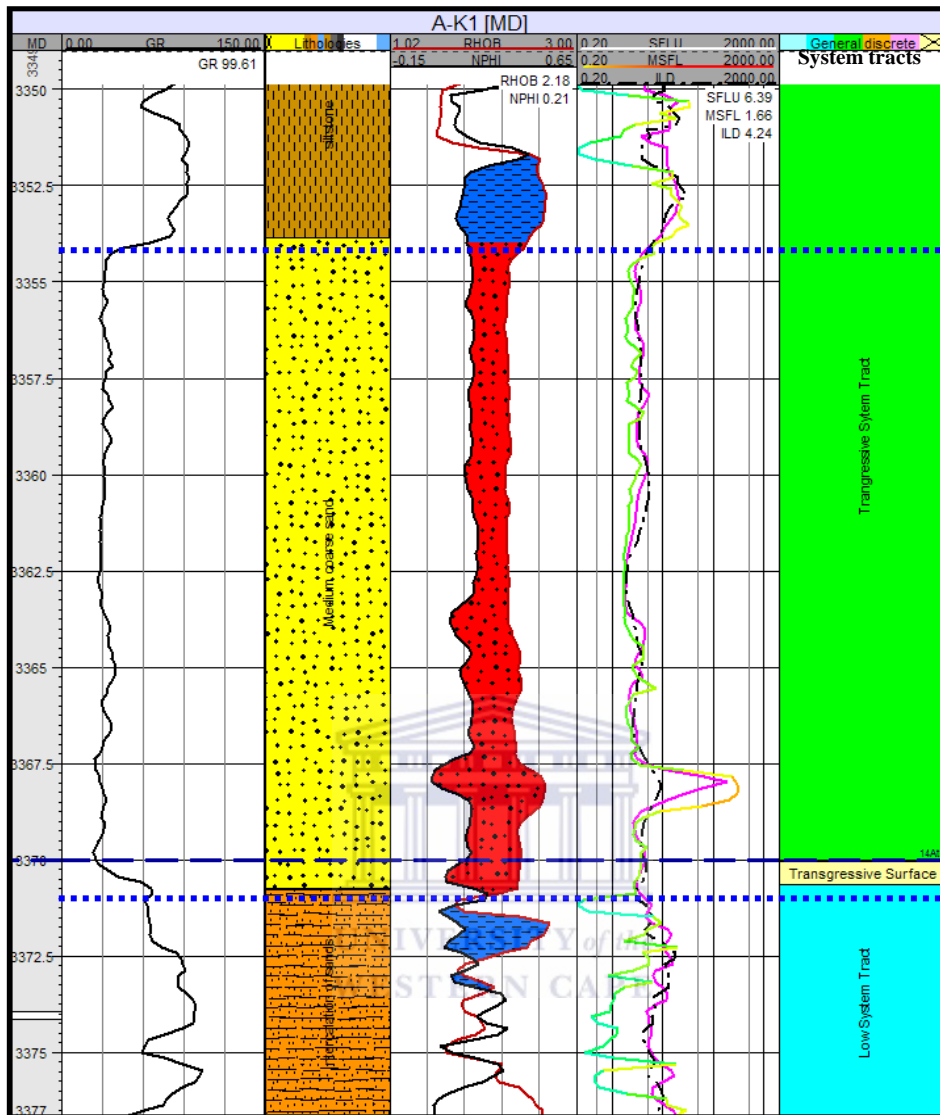
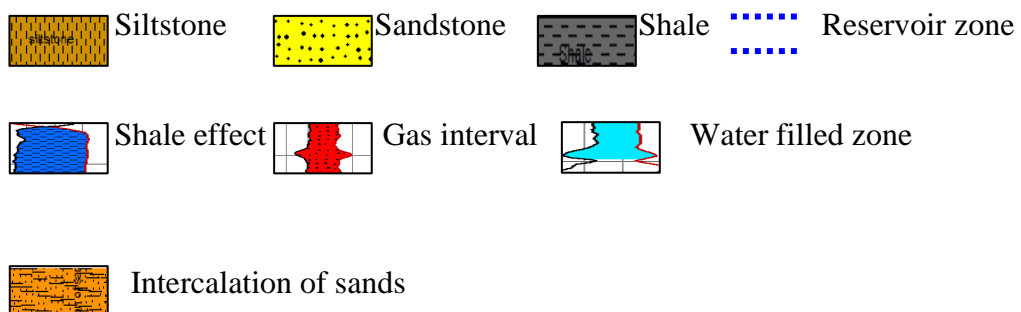


Figure 5.5.3: (A) showing Reservoir sand C (3354 – 3370.70 mRKB in A-K1 well.



### **5.5.3 Reservoir unit geophysical logs interpretation of A-K2**

#### **SAND A OF A-K2 WELL**

A-K2 well reservoir sand A thickness falls within the range of (3107.73 – 3122.87) mRKB with a gross and net thickness of 15.4 m and 10.64 m respectively (Table 5.1). The net thickness shows a promising reservoir potential with very good average neutron porosity (NPHI) and high resistivity readings (0.055 and about 1000  $\Omega$ m). The gamma ray log shape is also similar to that of reservoir sand C of the A-K1 well (Fig. 5.5.3) having a blocky shape with sharp base and top of the reservoir interval. The blocky signature of the gamma ray log also could also be linked to the aggradational sequence of the sand sediment within the reservoir zone which could be linked to either a braided fluvial or distributary channel fill environment.

#### **SAND B OF A-K2 WELL**

Reservoir sand B falls within the range of (3236.33 – 3257.46) mRKB having a gross and net thickness of 21.13 m and 11.67 m respectively (Table 5.1). The reservoir sand could be as a result of the continental sand deposit shortly after the maximum flood surface (MFS) thereby given rise to the interpreted high system tract (HST) in which the reservoir was located (Catuneanu, 2006). Heterogeneity of the reservoir interval is observed based on the 0.78 m siltstone unit, also noted was the high resistivity readings observed shortly beneath the silty unit, this could be attributed to a heterogeneous facies as well as vertical stratigraphic trend associated with depositional cycles (Keumsuk, 2007). The heterogeneity of the interval also buttresses the characteristics of an HST consisting of an aggradational to progradational set of parasequence that overlies the maximum flooding surface (Fig. 5.5.4B) and overlain by the next sequence boundary (Emery 1996). The environment of deposition could also be interpreted based on log signatures as an inner fan channel deep sea settings (<http://strata.geol.sc.edu/log-char.html>).

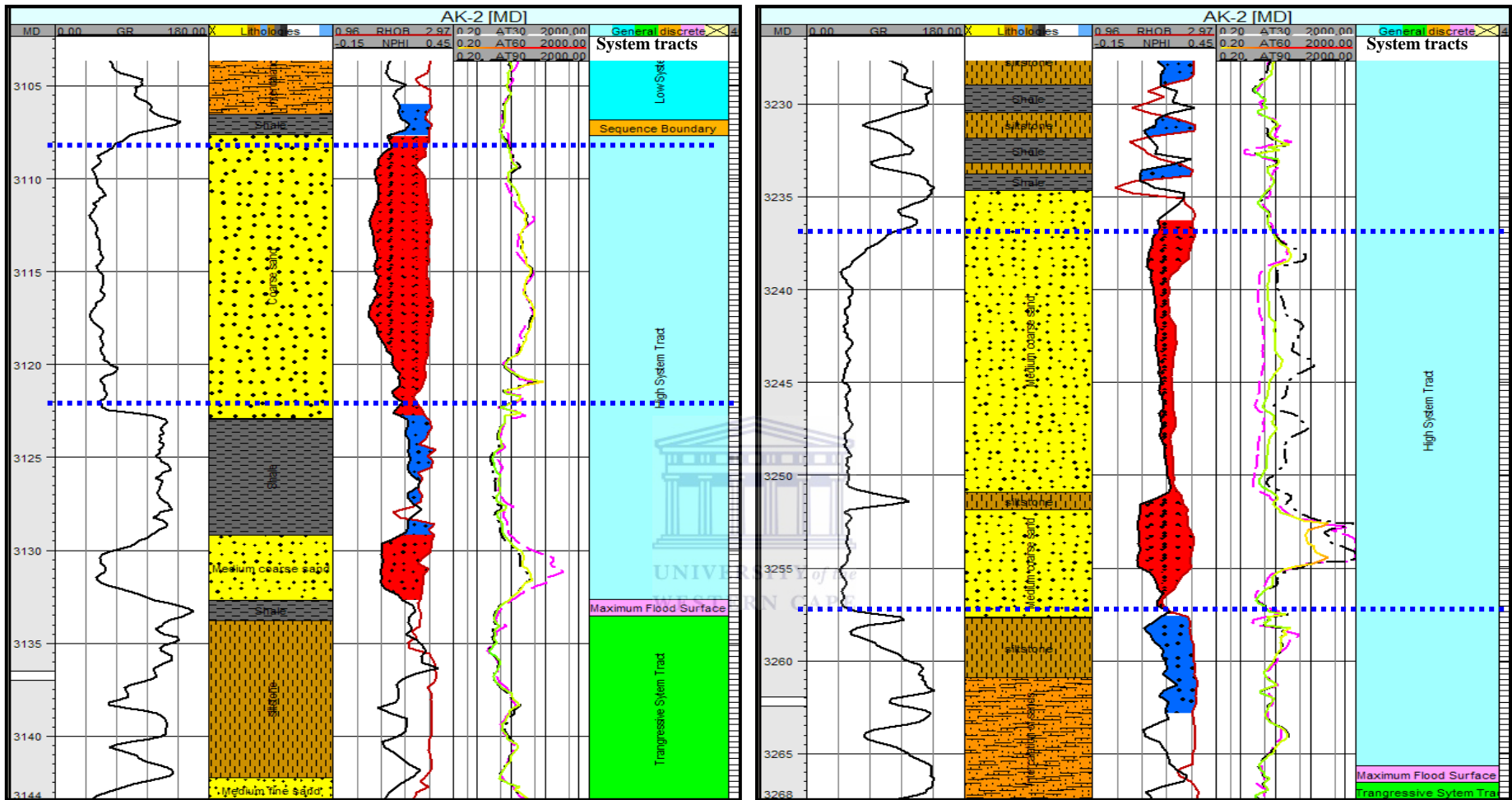
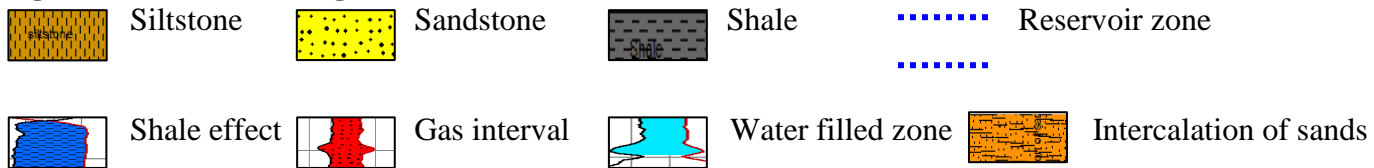


Figure 5.5.4: (A) showing Reservoir sand A (3107.73 – 3122.87) mRKB (B) Reservoir sand B (3236.33 – 3257.46) mRKB in A-K2 well.





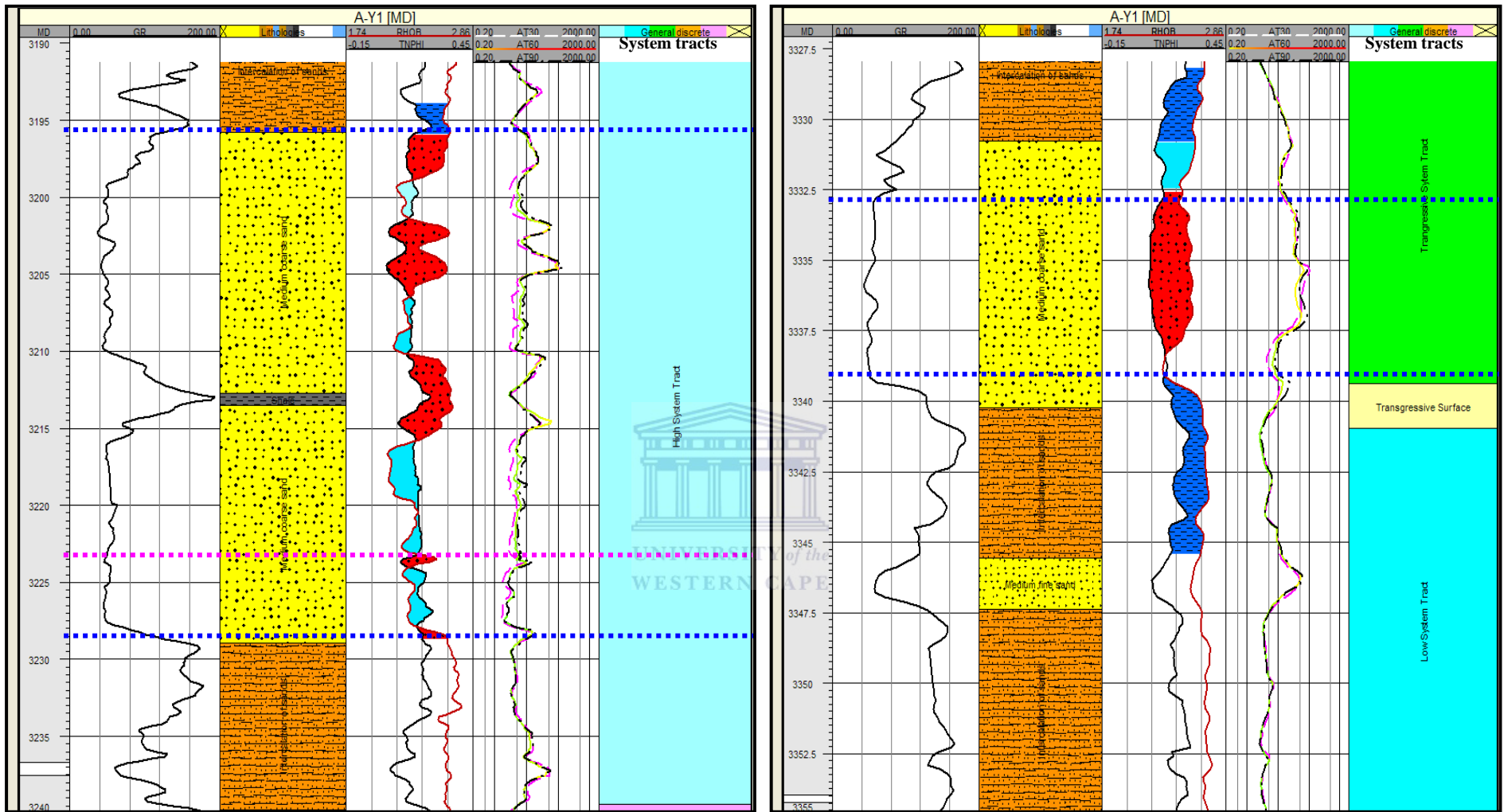
#### **5.5.4 Reservoir unit geophysical logs interpretation of A-Y1**

##### **SAND A OF A-Y1 WELL**

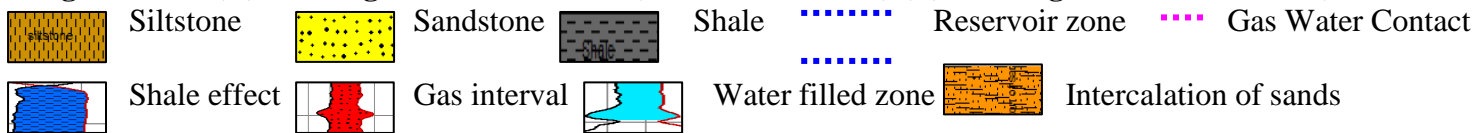
The first reservoir sand A encountered in A-Y1 well was located at the interval ranging from (3195.95 – 3228.77) mRKB with a gross and net thickness of 32.82 m and 13.42 m respectively (Table 5.1). The gamma ray signature of the reservoir unit is similar compared to that of A-K2 reservoir unit B. However, the thin shaly unit observed within the reservoir interval could be attributed to the compartmentalization of the reservoir unit. Well report (DST) of reservoir unit indicate separate pressure compartment with possible GAS/WATER contact to be found at 3,223 m (denoted with purple dotted line). This reservoir sand also falls within the Highstand systems tracts. In siliciclastic system, estuaries are either filled with sediment by the beginning of highstand system tract or finally filled in the earliest phases, nevertheless, figure 5.5.5A shows that progradational stacking is increasingly favoured over aggradational stacking (Emery 1996). Therefore, this reservoir sand unit could be a product of continental sand deposit shortly after a period of falling of the sea level rise (MFS). The depositional environment could be attributed to a fluvial settings distributary channel fills based on the aggradational sequence at each compartment of the reservoir unit.

##### **SAND B OF A-Y1 WELL**

Reservoir sand B which falls within the Transgressive system tracts (TST) and has a gross and net thickness of 6.51 m and 4.06 m respectively (Table 5.1). The sharp base and upward fining sequence toward the top of the reservoir sand B based on the gamma ray log signature suggest the depositional environment could possibly be a channel-point bar or fluvial system (<http://strata.geol.sc.edu/log-char.html>). Transgressive system tract usually consist of a retrogradational set of parasequence underlain by a transgressive surface (Fig. 5.5.5B) and overlain by the maximum flooding surface, this situation are unusually prominent and display strong facies contrasts with a pronounced deepening (Emery, 1996).



**Figure 5.5.5: (A) showing Reservoir sand A (3195.95 – 3228.77) (B) showing Reservoir sand B (3332.59 – 3339.16) mRKB in A-Y1 well.**



### **5.5.5 Reservoir unit geophysical logs interpretation of A-W1 SAND A OF A-W1 WELL**

Reservoir sand A (3185.20 – 3202.78) mRKB falls within the Lowstand system tract with a gross and net thickness of 17.50 m and 2.86 m respectively (Table 5.1). The high resistivity and corresponding high and low bulk density (RHOB) and neutron porosity (NPHI) logs respectively could be attributed to the presence of hydrocarbon within the reservoir unit, petrophysical evaluation should confirm the nature of the hydrocarbon (oil, gas or condensate). The gamma ray log signature shows the interval probably has even distribution of grain size with no visible internal changes with an average gamma ray readings of 71.24 API on the gamma ray log scale range of (0 – 300) API indicating that both the shale and sandstone in this well could possibly contain high radioactive elements within it.

### **SAND B OF A-W1 WELL**

The reservoir sand B (3306.03 – 3322.85) mRKB in the well falls within the lowstand systems tracts with a gross and net thickness of 16.82 m and 4.65 m respectively (Table 5.1). Gamma ray signature within the reservoir interval reflects a boxcar trend; this trend is usual in fluvial channel sands typically with considerable range of thickness (<http://strata.geol.sc.edu/log-char.html>). Also observed is the high gamma ray range (0 – 300 API) in the A-W1 well showing that the amount of radioactive element within the reservoir unit is high with average gamma ray reading of 55.07 API in the cleanest zones as observed from gamma ray signature and a corresponding relatively low bulk density log reading (Fig. 5.5.6B) which could be attributed to a very less abundance of clays minerals within the zone.

### **SAND C OF A-W1 WELL**

The reservoir sand C (3446.00 – 3468.09) mRKB in the A-W1 well falls within the Highstand system tracts (HST) with a gross and net thickness of 22.09 m and 4.54 m respectively (Table 5.1). The gamma ray signature within the reservoir interval reflects an aggradational sequence having an even blocky shape with a sharp top and base which could be attributed to a fluvial setting (<http://strata.geol.sc.edu/log-char.html>). The resistivity log at depth 3460m shows a high resistivity signature with a corresponding high and low bulk density (RHOB) and neutron porosity (NPHI) log respectively, this could possibly be the hydrocarbon saturated zone within the reservoir, petrophysical evaluation at the later stage in this chapter should reveal the water and hydrocarbon saturation potential.

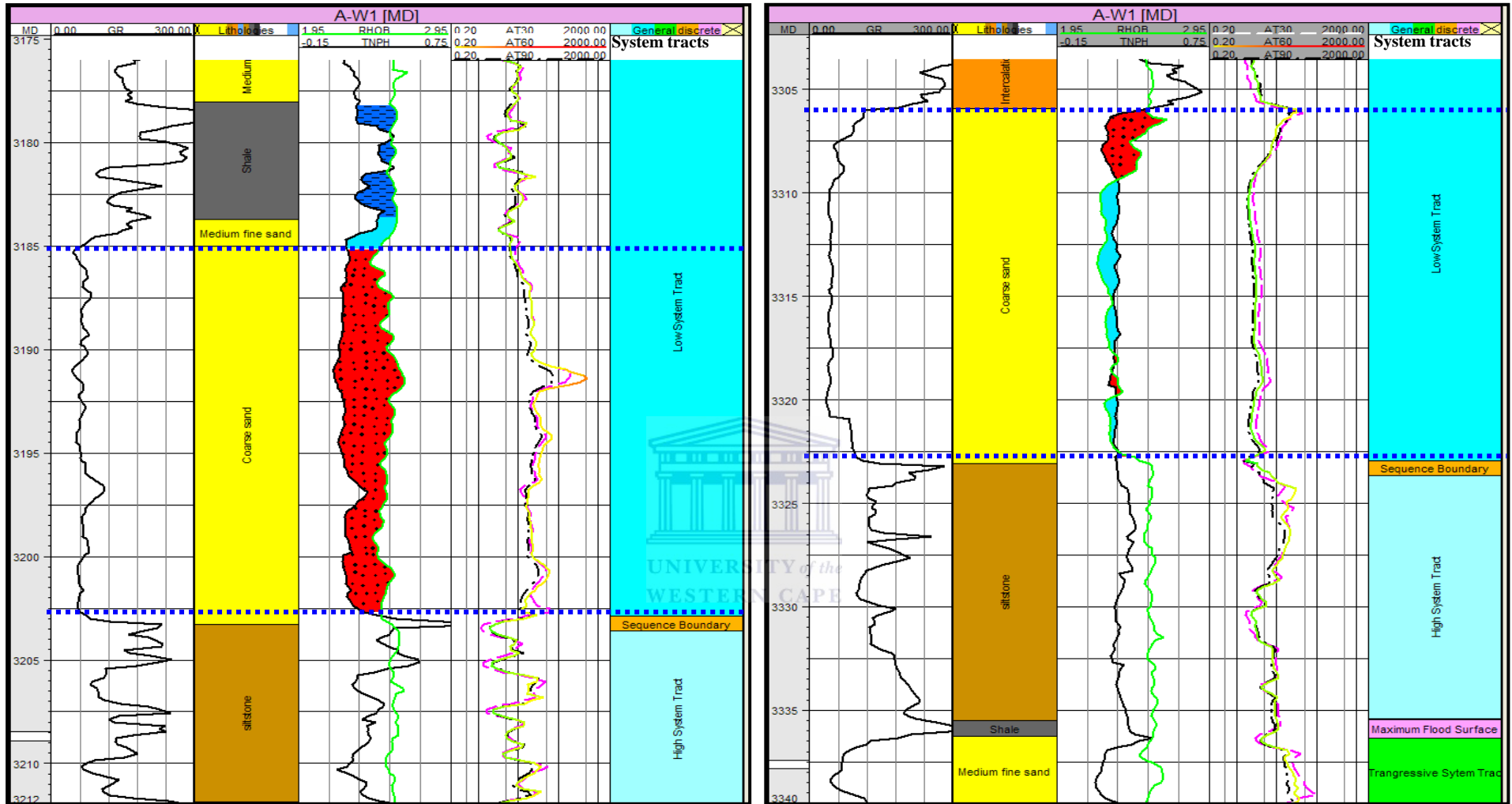
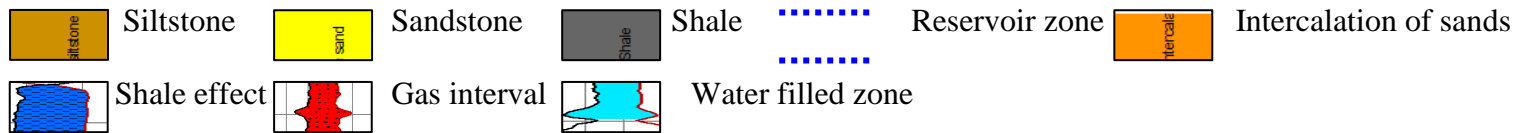


Figure 5.5.6: (A) showing Reservoir sand A (3185.20 – 3202.78) mRKB (B) showing Reservoir sand B (3306.03 – 3322.85) mRKB in A-W1 well.



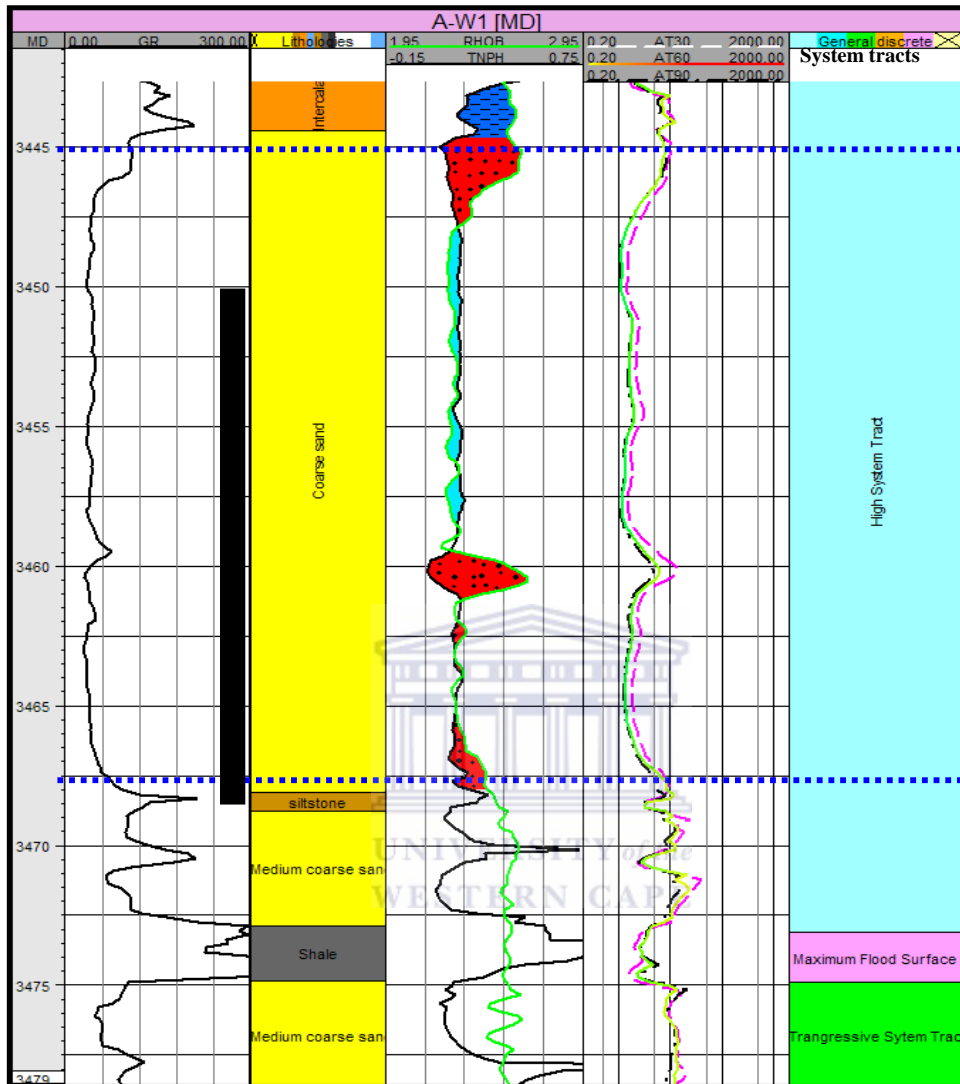
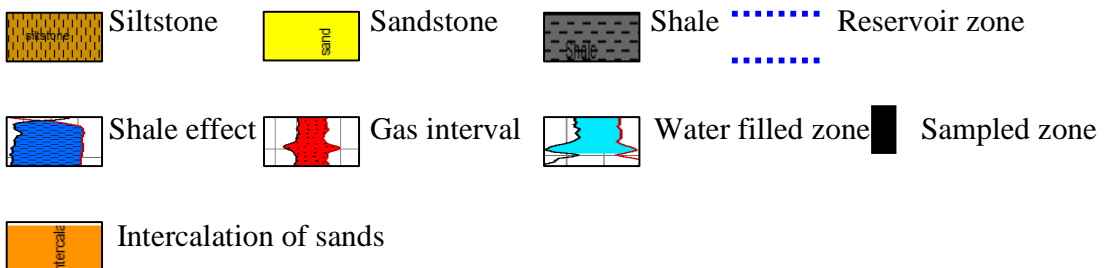


Figure 5.5.7: (A) showing Reservoir sand C (3446.00 – 3468.09) mRKB in A-W1 well



**Table 5.1:** Summary of the Geophysical Well Logs Interpretation of the Reservoir Units of the Wells in this Study.

Well Name (mbKb)	Reservoir Unit	System tracts	Gross (m)	Net pay(m)
A-K1	3230.10 – 3240.00	LST	9.90	3.19
	3274.13 – 3287.10	TST	12.97	3.00
	3354.00 – 3370.70	TST	16.70	2.04
A-G1	3181.50 – 3196.50	LST	15.00	5.41
	3309.98 – 3331.04	LST	21.00	8.38
	3368.11 – 3375.75	HST	7.64	2.11
	3391.40 – 3406.36	TST	14.96	3.9
A-K2	3107.73 – 3122.87	HST	15.14	10.64
	3236.33 – 3257.46	HST	21.13	11.67
A-W1	3185.20 – 3202.78	LST	17.58	2.86
	3306.03 – 3322.85	LST	16.82	4.65
	3446.00 – 3468.09	HST	22.09	4.54
A-Y1	3195.95 – 3228.77	HST	32.82	13.42
	3332.59 – 3389.87	TST	6.51	4.06

### 5.6: Mineralogical Predictions from Well Logs

Rocks are made up of mixture of minerals; consequently their physical properties influence the measured log responses. These log responses are not only functions of the characteristics and their relative amount present in the rock, but also on the nature and amount of the fluids occupying the pore spaces (Serra, 1986). The most common reservoir rocks are generally formed of two or three of these groups (silicates, clays, carbonates, evaporites). The log responses of the principal rocks forming minerals are shown in the report of Serra, (1986)

and Bassiouni (1994). On the other hand, the clay minerals are frequently associated with the sedimentary rocks. Thus, it is important here to throw some light on their log characteristics. This group includes kaolinite, chlorite, montmorillonite and illite. Montmorillonite is distinguished by its low density and its high neutron response.

The identification of the matrix components is well defined through the different crossplot technique. The basic idea of such a technique is that different types of matrix appear by combining different well log parameters. However, this research work is limited to the density (RHOB) – Neutron (NPHI) crossplot (for mineralogical predictions). It is worth mentioning that density and neutron crossplots which is not the only tool for differentiating the clay minerals, because all the clays generally possess high radioactivity (Abu El Ata and Basel, 1989). By this way, the rock types of the Albian age reservoir sands in the five studied wells can be illustrated especially where there are no core samples available for laboratory analysis.

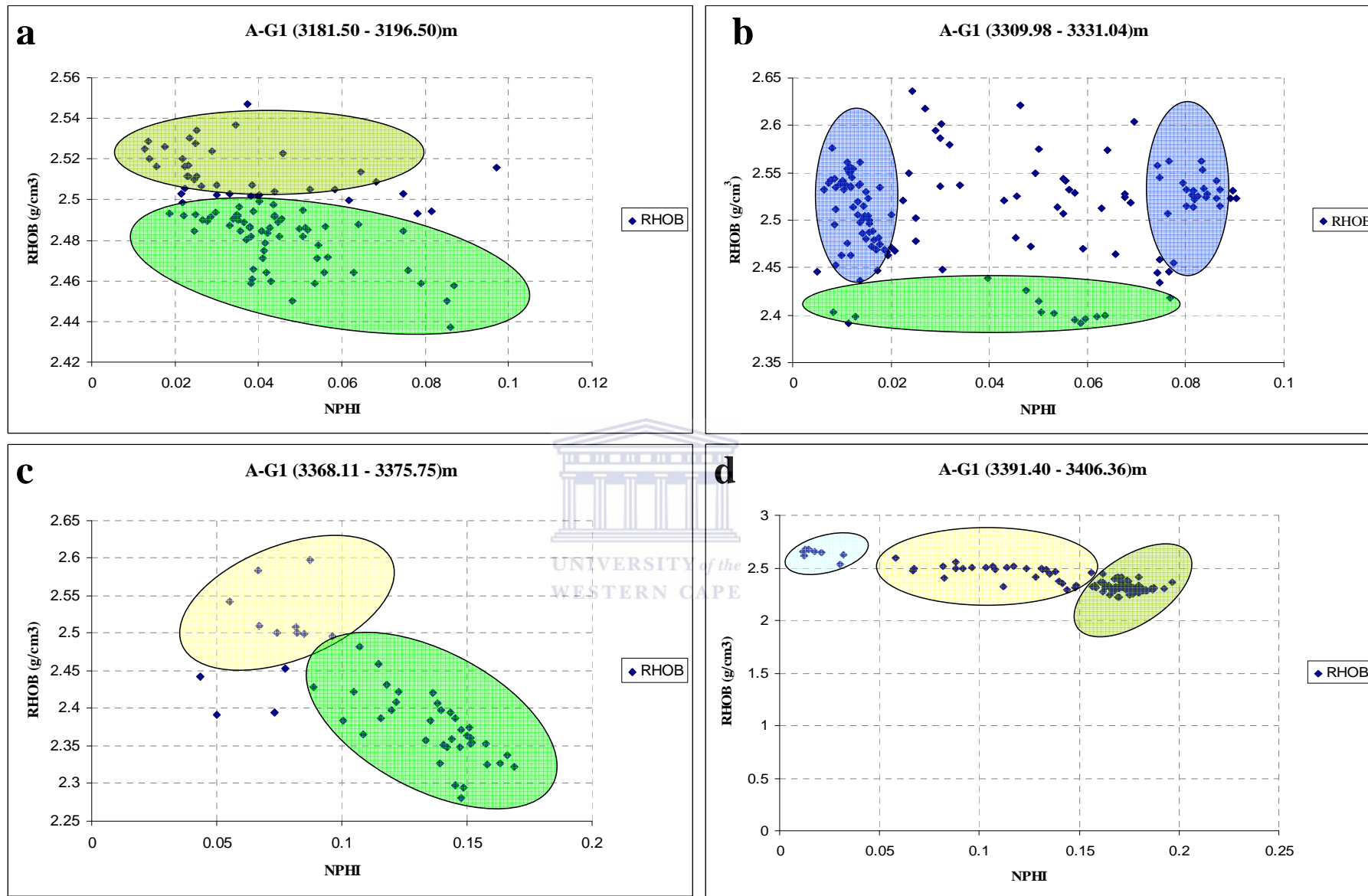
#### 5.6.1 A-G1 Well

Four reservoir intervals were interpreted from the Albian age section of this well (Fig. 5.6.1) and the density-neutron crossplots (Fig. 5.6.1a & b) reflect two distinct clusters. The upper clusters (deep green) indicates the existence of feldspar (both alkali & plagioclase) (Serra, 1986) with regard to table 5.2 and a corresponding very low neutron log values indicates a low porosity within that zone while the lower cluster (light green) reveals the presence of kaolinite with a low neutron log readings as well (Bassiouni, 1994). The second reservoir interval in this well (Fig. 5.6.1b) shows three prominent cluster, one to the right and the other to the left (light blue), both are characterized by the presence/abundance of feldspathic minerals associated with quartz while the later (light green) reveals the presence of kaolinite and some microcline feldspar. The third reservoir interval (Fig. 5.6.1c) shows two clusters in which the first cluster in light yellow colour could be attributed to presence of illite, feldspar (orthoclase & plagioclase) with a low neutron reading while the second cluster (light green) reveals the possibility of the zone containing kaolinite associated with feldspar. Figure 5.6.1d (fourth reservoir) reveals three clusters, the top left light blue coloured one indicates the presence of quartz, the second cluster (light yellow) suggest the existence of feldspar (microcline & orthoclase) & illite with a fair to good neutron porosity reading while the third cluster light green contains montmorillonite and kaolinite indicating a very good porosity potential.

**Table 5.2:** Log Responses of Major Groups (After Serra, 1986 & Bassiouni 1994).

<b>MINERALS &amp; LOGS</b>	<b>Density (g/cm<sup>3</sup>)</b>
<b>SILICATES</b>	
Quartz	2.65
Garnet	4.30
Hornblende	3.13
Tourmaline	3.15
<b>CLAY</b>	
Kaolinite	2.41
Chlorite	2.76
Illite	2.52
Montmorillonite	2.33
<b>CARBONATES</b>	
Calcite	2.71
Dolomite	2.88
Ankerite	2.86
Siderite	3.89
<b>EVAPORITE</b>	
Halite	2.04
Anhydride	2.98
Gypsum	2.35
Trona	2.08
Sylvite	1.86
Carnallite	1.57
Langbeinite	2.82
Polyhalite	2.72
Epsomite	1.71
<b>MICA</b>	
Muscovite	2.79
Biotite	3.10
<b>FELDSPAR-ALKALI</b>	
Orthoclase	2.52
Anortoclase	2.59
Microcline	2.35
<b>FELDSPAR PLAGIOCLASE</b>	
Albite	2.59
Anorthite	2.74

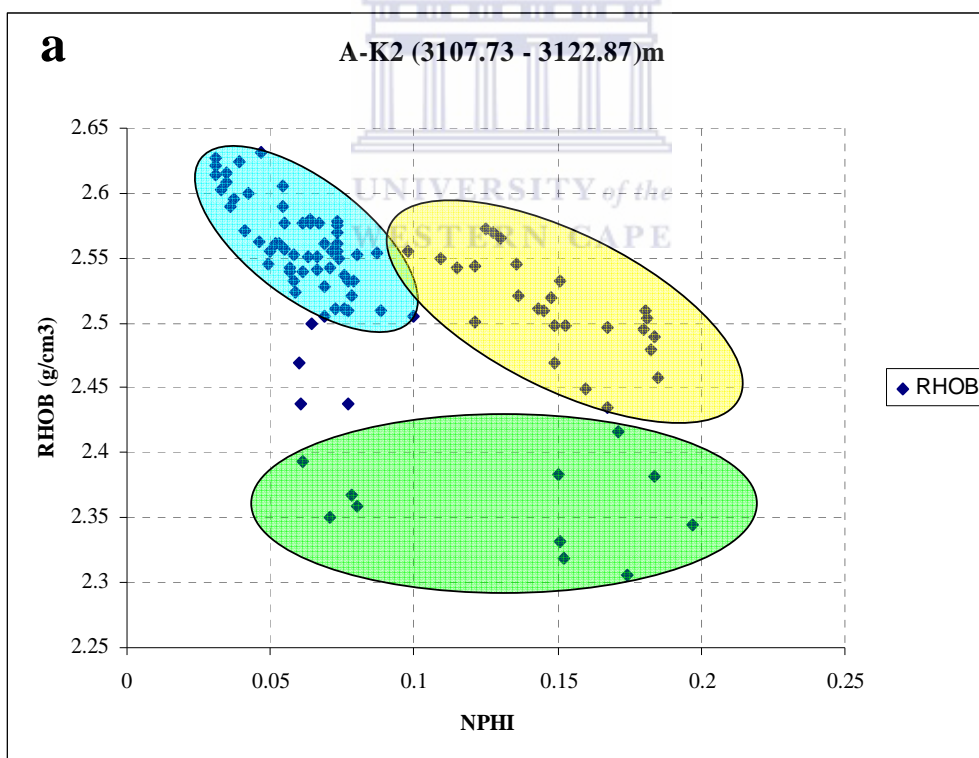




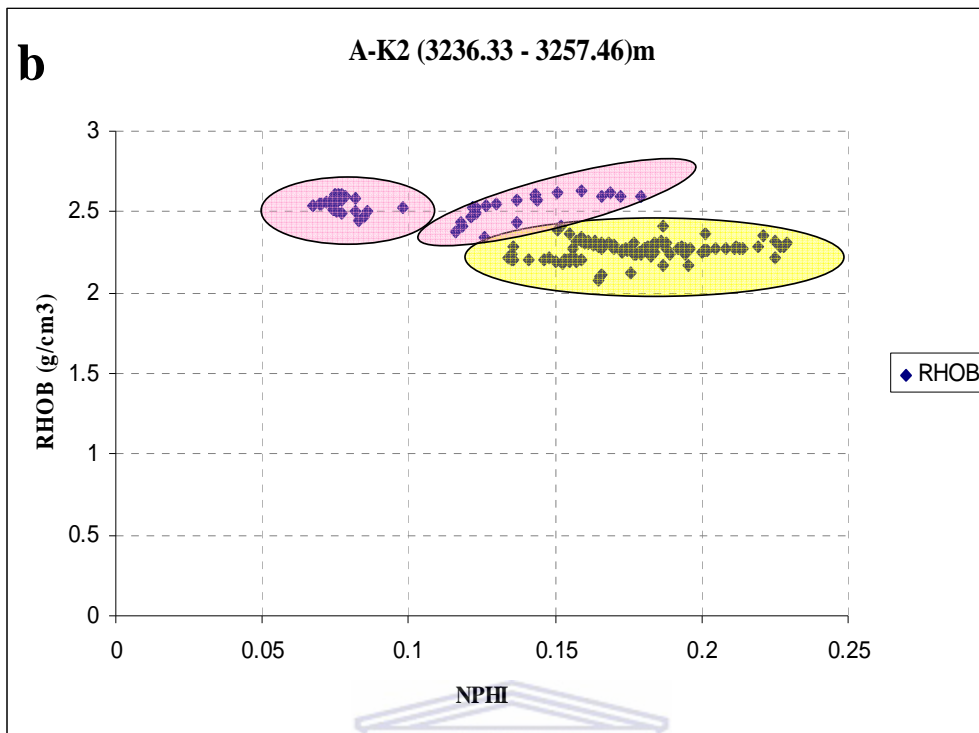
**Figure 5.6.1:** Crossplots of Density (RHOB) against Neutron (NPHI) for mineralogical predictions in A-G1 well.

### 5.6.2 A-K2 Well

A-K2 well does not have any core samples therefore; the mineralogical knowledge depends solely on the predictions from the wireline logs (density- neutron crossplots). Two reservoir intervals were identified from the Albian age (Fig. 5.6.2a) with the first one showing three clusters, the light blue coloured cluster to the top left indicates the abundance of feldspar (albite) and quartz, the second cluster reveals (light yellow) shows the presence of illite and kaolinite within the zones with a relatively good porosity readings (Serra, 1986, Bassiouni, 1994). Light green scattered points (third cluster) reveals the presence of evaporate (gypsum), feldspar (microcline) and kaolinite minerals (Bassiouni, 1994). The second reservoir interval (Fig. 5.6.2b) contains three clusters with the two light pink coloured ones indicating the abundance of feldspar (albite), illite and kaolinite while the second cluster (light yellow) reveals the presence of montmorillonite displaying a low density with a corresponding high neutron response (Serra, 1986).



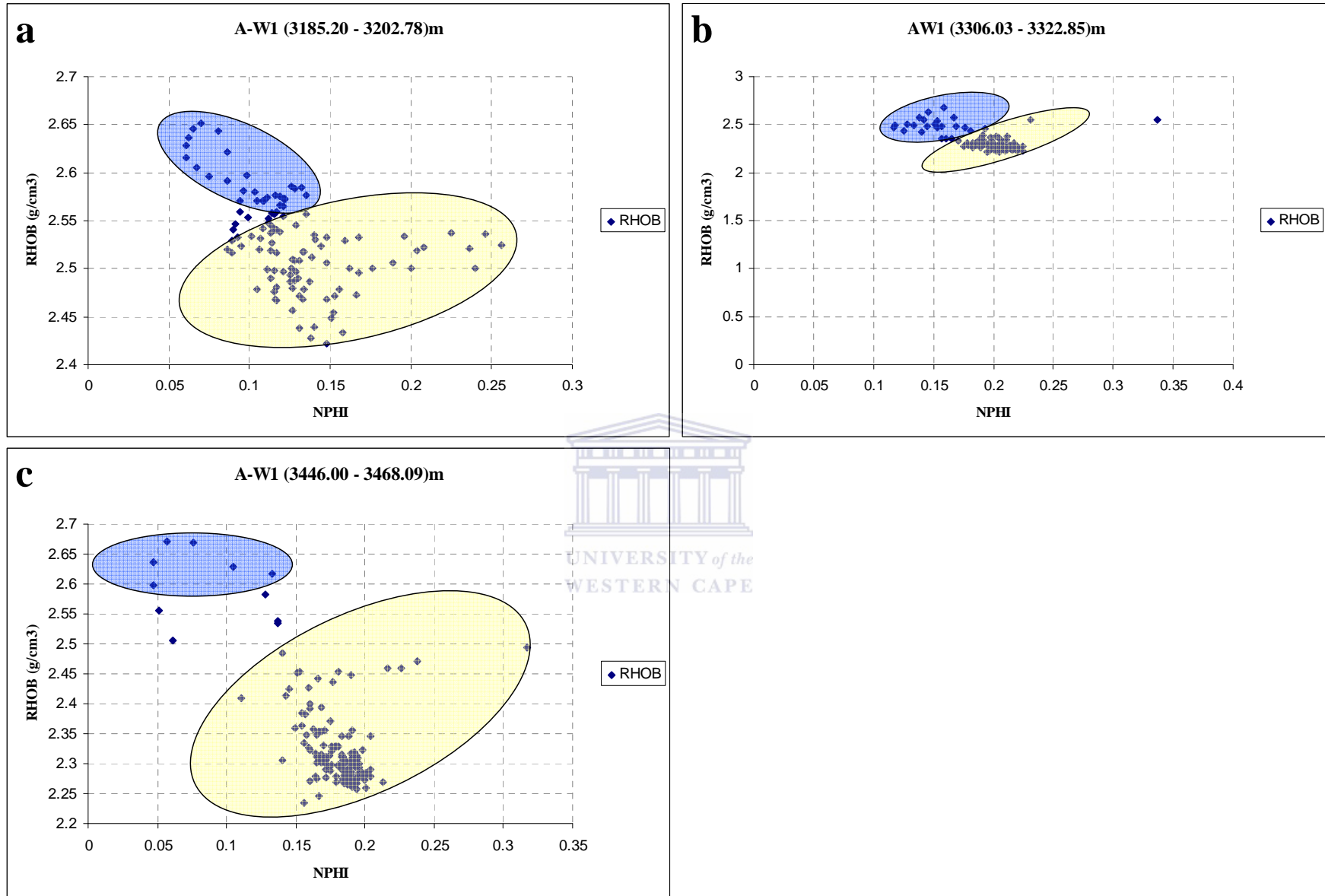
**Figure 5.6.2a:** Crossplots of Density (RHOB) against Neutron (NPHI) for mineralogical predictions in A-K2 well.



**Figure 5.6.2b:** Crossplots of Density (RHOB) against Neutron (NPHI) for mineralogical predictions in A-K2 well.

### 5.6.3 A-W1 Well

The density-neutron crossplots of the first reservoir interval (Fig. 5.6.3a) shows two clusters with the light blue cluster indicating the presence of quartz and feldspar (albite) while the second cluster (in light yellow) delineate the existence of illite, montmorillonite and kaolinitic clays within that reservoir (Bassiouni, 1994). The second reservoir interval 3306.03 – 3322.85m (Fig. 5.6.3b) reflects the restriction of most majority of points to the upper right part giving rise to the presence of some clay minerals and quartz as the dominant mineral within that zone (blue clusters). The second yellow cluster also indicates the presence of montmorillonite and microcline feldspar with a fair to good porosity reading from the neutron log values as seen in figure 5.6.3a. The studied crossplot of the evaluated Albian age section (Fig. 5.6.3c) of the A-W1 well reflects two clusters, one at the upper left hand corner with a light blue colour cluster showing the presence of calcite associated with some quartz, the second cluster (light yellow) reveals the existence of feldspar (microcline), montmorillonite and kaolinite within the reservoir sand.



**Figure 5.6.3:** Crossplots of Density (RHOB) against Neutron (NPHI) for mineralogical predictions in A-W1 well.

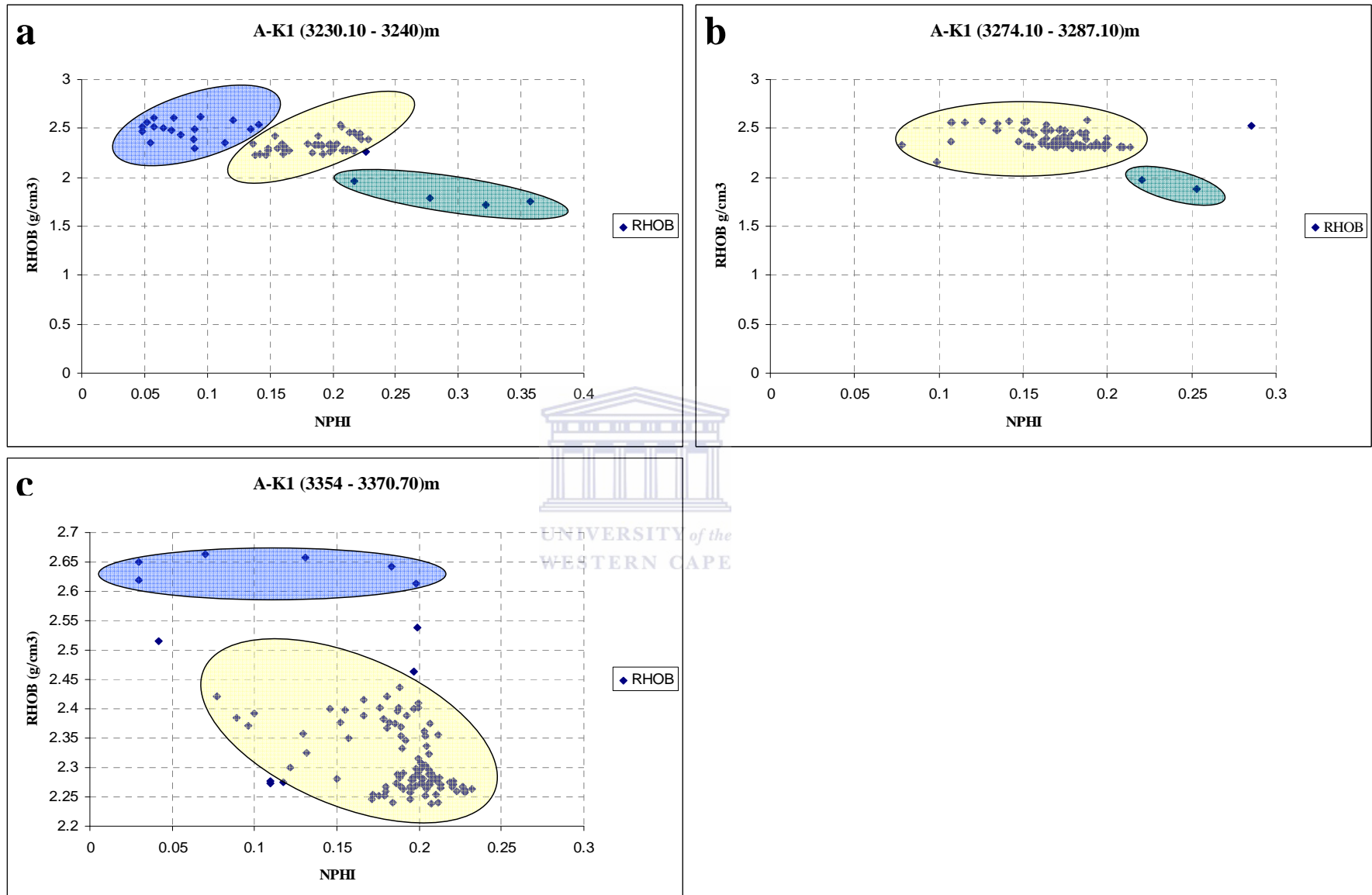
#### 5.6.4 A-K1 Well

Three clusters were delineated from the first cross plot in A-K1 (Fig. 5.6.4a), the light blue enclosed coloured cluster representing the presence of some clay mineral (kaolinite and montmorillonite) associated with quartz, the second light yellow coloured clusters reveals the existence of evaporite (halite and essonite) while the light green cluster (third) shows the existence of some micaceous minerals. Figure 5.6.4b (second reservoir) reveals the presence of two clusters with the light yellow having some illitic mineral associated with montmorillonite and kaolinite within the zone and the light green enclosure shows the presence of some evaporite like halite (rock salt) and sylvite (potassium chloride) which could be an insight for pore water geochemistry study within this zone. The density-neutron crossplots (Fig. 5.6.4c) show one largest cluster (light yellow enclosure) which is characterized by the occurrence of montmorillonite and kaolinite within the zone while the second blue scattered cluster contains predominantly quartz.

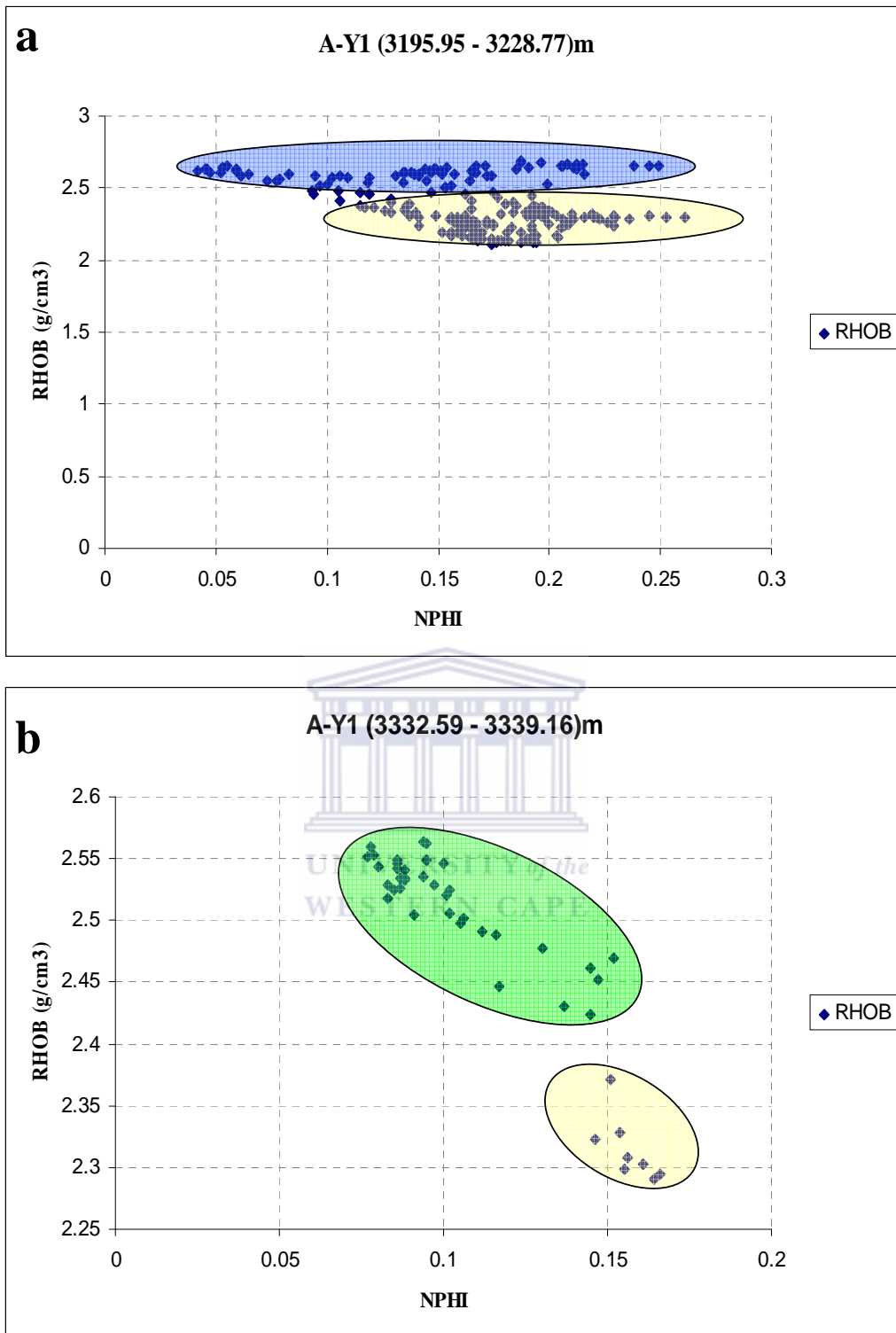
#### 5.6.5 A-Y1 Well

The density-neutron crossplots (Fig. 5.6.5a) in A-Y1 well show two connected clusters. The largest one at the bottom (light yellow) contains more clusters than the light blue cluster right on top of it. The yellow cluster reveals the presence of microcline feldspar and some evaporite (gypsum) with a good neutron porosity reading while the light blue indicates the existence of illite, alkali feldspar associated with quartz and also taken the same direction of the yellow cluster.

Fig. 5.6.5b also reveals two distinct clusters with the upper one (light green) representing the occurrence of albite and kaolinite within that zone while the lower right part of this crossplot shows the presence of montmorillonite associated with alkali feldspar possessing an averagely good neutron porosity reading.



**Figure 5.6.4:** Crossplots of Density (RHOB) against Neutron (NPHI) for mineralogical predictions in A-K1 well.



**Figure 5.6.5:** Crossplots of Density (RHOB) against Neutron (NPHI) for mineralogical predictions in A-Y1 well.

## **5.7 Well Correlation and Stratigraphic Analysis**

### **5.7.1 Log Correlation**

The developments of geologic patterns display by structural and stratigraphic units are equivalent in time, age, or stratigraphic position through the use of electric wireline logs is generally referred to as log correlation (Rider, 1996). The geological factor to be resolved must be the guiding factor for choosing the correlation-attributes in well-to-well log matching. Opting for a smoothed version of the sonic logs leads to the matching of equivalent lithologic units, whereas using an attribute that measures the local relative variability of the logs results in the correlation of iso-chronological events (Carlos, 1997). However, gamma ray log in conjunction with the well tops obtained from petroleum Agency of South Africa (PASA) were used as correlative tool for this research work.

Primarily, electric well log curves were used to delineate the boundaries of subsurface units for the preparation of a variety of subsurface maps and cross sections (Doveton, 1986). To a greater extent, the accuracy of geological interpretation made is determined by the correctness of correlations carried out (Olajide, 2005). Based on the depth range covered by the available data, stratigraphic units within the interval in the study area have been correlated using composite logs (image format) from five wells.

### **5.7.2 Description of Correlated Section**

The correlated section of the study area along North West – South East direction is shown in figure 5.7.6. The sandstone and shale sequences are correlated over a distance of about 30km across five wells: A-G1, A-Y1, A-K1, A-K2 and A-W1. Correlated unit (Fig. 5.7.6) reveals a gradual facies change from East to West with regards to 14At1 ranging from coarse dominated sandstone to medium dominated sandstone (A-K1 well) and the intercalation of sand (A-K2 well) while M2KI reveals also a trend of change from medium sandstone package (A-Y1 well ) to coarse sandstone in A-W1 well. Looking at the trend of changes from the correlated section in relation to the stratigraphic positioning of the studied wells in figure 1.1, it could be interpreted that the movement of sediment from east towards the western section shows a fining trend in the sand texture (coarse to medium texture).



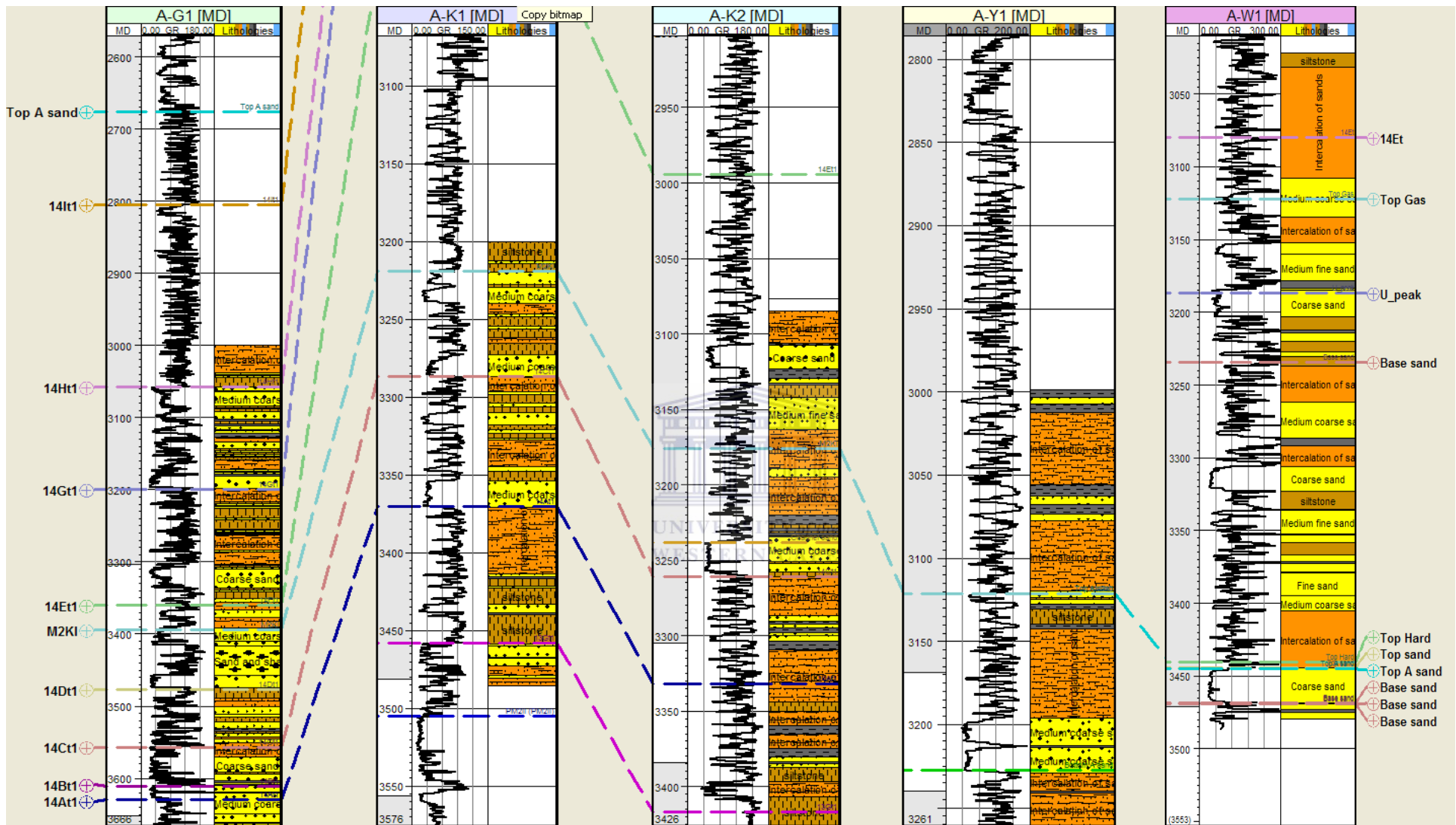


Figure 5.7.1 Stratigraphic cross-section across the studied wells (East-West direction).

## 5.8 PETROPHYSICAL ANALYSES

The study of the Albian age sandstone of the Orange Basin has been the focus of this research work, earlier discussion has been built on the qualitative interpretation of wireline logs using sequence stratigraphic approach and also the cross plot of density and neutron logs to predict the plays within the Albian age sandstone. The integration of the geologic information and petrophysical parameters has helped in understanding the reservoir properties and facies association of the study area. Through the qualitative interpretation of correlated well logs (image format), it is observed that sandstone units of the Lowstand tracts within the analysed sequence are characterized with high resistivity, low neutron and high density log response indicative of presence of hydrocarbon. The low gamma ray values imply sandstone lithology as well as their likelihood of being a hydrocarbon reservoir zone. Table 5.1 shows the summary and variation in the interpreted system tract as seen in Fig. (5.5.1 – 5.5.7) above ranging from Lowstand – Highstand - Transgressive system tract of the different reservoirs observed from the 5 wells under study. The base and top of these system tracts within the respective depositional sequences in which they occur are defined by 14Ht1 and M2K1 well top surfaces for A-G1 and 14Et1 and 14Ct1 for A-K1 wells, the availability of the surfaces for this two wells has made the correlation much easier which was also use as a basis for the correlation of other studied wells with no well tops.

The sorted digitized wireline log data within these reservoir intervals serve as input data into Schlumberger PETREL software in order to carry out the petrophysical analyses on them.

The digitized wireline log data are:

- i. Depth (reference to KB)
- ii. Gamma Ray Log (GR)
- iii. Spontaneous Potential (SP)
- iv. Density Log (RHOB)
- v. Neutron Log (NPHI) or Thermal Neutron Log (TNPHI)
- vi. Sonic Log (DT)
- vii. Deep Laterolog (LLD) or Deep resistivity Log (HLLD) or Deep Induction Log AT90
- viii. Medium resistivity (HLLG) Medium induction AT60

- ix. Shallow Laterolog (LLS), shallow resistivity (HLLS) or shallow Induction AT30
- x. Deep Induction Log (ILD)
- xi. Spherically Focused Log (SFLU)
- xii. Microspherically Focussed Log (MSFL)
- xiii. Caliper Log (CALI)

The above listed digitized data were displayed as curves in the well section window of PETREL and corrected for depth with reference to Kelly bushing. Through the use of Group Pane function, the combined displays of NPHI-RHOB, ILD-SFLU-MSFL and AT90-AT60-AT30 were made possible. Petrophysical properties were derived from output results of the input data for the selected interval across the wells through the use of PETREL calculator function and syntax to run appropriate equation.

These petrophysical properties nomenclatures are listed below:

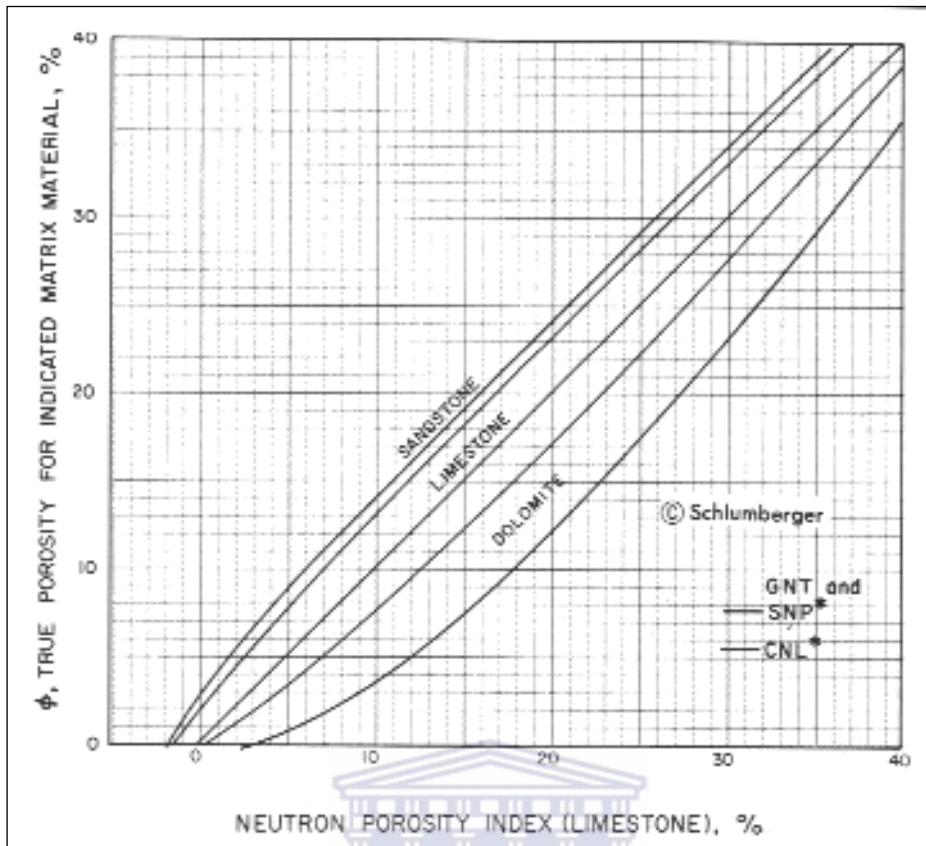
<b>Description &amp; symbol</b>		<b>Units</b>
i.	Shale Index ( $I_{sh}$ )	API
ii.	Volume of shale ( $V_{sh}$ )	fraction
iii.	Total Porosity ( $\Phi_T$ )	% or fraction
iv.	Effective Porosity ( $\Phi_{eff}$ )	% or fraction
v.	Resistivity of formation ( $R_t, R_w$ )	$\Omega m$
vi.	Water saturation ( $S_w$ )	% or fraction
vii.	Hydrocarbon saturation ( $S_{hc}$ )	% or fraction
viii.	Irreducible water saturation ( $S_{wir}$ )	% or fraction
ix.	Bulk volume of water ( $V_b$ )	fraction
x.	Formation factor (F)	Constant
xi.	Permeability (K)	millidarcies (mD)
xii.	Permeability scale factor fractional (G)	Constant
xiii.	Gamma ray in zone of interest ( $\gamma_{log}$ )	API
xiv.	Gamma ray for shale baseline ( $\gamma_{sh}$ )	API
xv.	Gamma ray for cleanest formation ( $\gamma_{cl}$ )	API
xvi.	Matrix/grain density ( $\rho_{ma}$ )	$g/cm^3$
xvii.	Fluid density ( $\rho_f$ )	$g/cm^3$
xviii.	Porosity from density log ( $\Phi_D$ )	$g/cm^3$
xix.	Porosity from reservoir unit ( $\rho_{res}$ )	$g/cm^3$

xx.	Porosity from shale above the reservoir unit ( $\rho_{sh}$ )	% or fraction
xxi.	Porosity from neutron log ( $\Phi_N$ )	% or fraction
xxii.	Corrected Porosity from neutron log ( $\Phi_{CNL}$ )	% or fraction
xxiii.	True formation resistivity ( $R_t$ )	$\Omega m$
xxiv.	Formation water resistivity ( $R_w$ )	$\Omega m$
xxv.	Porosity exponent (m)	Constant
xxvi.	Saturation exponent (a)	Constant
xxvii.	Resistivity of formation when 100% saturated with formation water ( $R_0$ )	$\Omega m$

**Table 5.8.1:** Well information used for petrophysical evaluation in the studied wells.

Well Name	Mud weight	BS	Drilling fluid	Drilling fluid density	RMS	Mud Temp.	RMF	RMC
A-G1	-	8.5	KCL polymer	1.12	0.173	64	0.16	0.23
A-K1	-	12.25	Polymer	1.1	0.193	31	0.181	0.533
A-K2	9.8	8.5	Gel polymer	9.8	0.374	72	0.2763	0.711
A-W1	9.8	8.5	Low pH starch	10.2	0.734	69	0.574	0.877
A-Y1	10.5	8.5	Gel polymer	9.8				

**Note:** The recorded values for drilling fluid density in A-K2, A-W1 and A-Y1 are too high for evaluation; therefore the density of salt water ( $1.1g/cm^3$ ) was used for the evaluation.



**Figure 5.7.2:** Environmental correction chart for neutron porosity (NPHI) log to compensated neutron Log (CNL) modified from Schlumberger 1972.

UNIVERSITY of the  
WESTERN CAPE

**Table 5.8.2** Summary for the sampled data of Log derived petrophysical properties of the Albian age sandstone of the five wells.

Well Name	Zone name	Top (m)	Bottom (m)	Gross (m)	Net pay (m)	N/G	V <sub>sh</sub>	Porosity $\Phi_{eff}$	Porosity $\Phi_T$	Sw	Swir	S <sub>h</sub>	K (md)
A-G1	Sand A	3185.50	3196.50	15.00	5.41	0.36	0.03	0.15	0.16	0.34	0.33	0.63	2.80
	Sand B	3309.98	3331.04	21.00	8.38	0.39	0.07	0.24	0.26	0.08	0.08	0.99	1.30
	Sand C	3368.11	3375.75	7.14	2.11	0.27	0.10	0.09	0.11	-	-	-	-
	Sand D	3391.40	3406.36	14.96	3.90	0.26	0.07	0.08	0.09	0.77	0.75	0.23	0.01
A-K2	Sand A	3107.73	3122.87	15.14	10.64	0.70	0.08	0.06	0.06	0.90	0.90	0.10	0.00
	Sand B	3236.33	3257.46	21.30	11.67	0.55	0.12	0.11	0.12	0.33	0.33	0.67	0.74
A-W1	Sand A	3185.20	3202.78	17.58	2.86	0.13	0.11	0.14	0.16	0.30	0.26	0.70	4.40
	Sand B	3306.03	3322.85	16.82	4.65	0.27	0.07	0.16	0.17	1.00	1.00	0.00	0.00
	Sand C	3446.00	3468.09	22.09	4.54	0.21	0.05	0.12	0.13	1.00	1.00	0.00	0.00
A-K1	Sand A	3230.10	3240.00	9.90	3.19	0.32	0.05	0.14	0.15	0.71	0.64	0.29	0.01
	Sand B	3274.13	3287.10	12.97	3.00	0.23	0.07	0.16	0.17	-	-	-	-
	Sand C	3354.00	3370.70	16.70	2.04	0.12	0.04	0.12	0.12	1.00	0.12	0.00	0.03
A-Y1	Sand A	3195.95	3228.77	32.82	13.42	0.41	0.18	0.09	0.12	0.58	0.56	0.42	0.13
	Sand B	3332.59	3339.10	6.51	4.06	0.62	0.09	0.07	0.08	0.70	0.70	0.30	0.01

**Note:** N/G = net to gross ratio

### 5.8.1 Petrophysical Evaluation of the Wells

Table 5.7.2 above presents the summary for calculated log derived petrophysical parameters for the five studied wells. The number of reservoir intervals delineated from the wireline log varies from a minimum of two to a maximum of four across the wells under study. A-G1 well shows a considerable gross thickness of the four delineated reservoir intervals but with a very low net pay given rise to a low N/G ratio in the well however, the effective porosity ( $\Phi_{\text{eff}}$ ) within the reservoir shows a fair to good trend (0.9 – 0.15) with an averagely good permeability while the reservoir also reveals a good trend of water saturation except for reservoir sand D having a considerably high water and irreducible water saturation (0.77 or 77 % and 0.75 or 75 %) and also the volume of shale parameters are low confirming the sandy nature of the reservoir.

A-K2 well reveals two reservoir intervals with a good N/G trend but a low effective porosity (0.06 or 6 % and 0.11 or 11 %) values (Table 5.7.2), the water saturation and irreducible water saturation are very high and also of the same value based on the calculation which implies that the zone is obviously a hydrocarbon bearing zone (Bassoioni, 1994). The permeability (K) of the reservoir sands is generally low although that of sand B shows a promising value of 0.74 mD however; optimization mechanism is suggested to be put in place for the well.

A-W1 well reveals three reservoir intervals each with promising gross thicknesses, their effective porosity ( $\Phi_{\text{eff}}$ ) values are generally fair but with an extremely low permeability except for reservoir sand A which possesses a permeability (K) value of 4.40 mD which is considerably fair as compared to others with absolute zero (md) values. The water and irreducible water saturation are extremely high with value 1.0 or 100 % which shows that the reservoir zones are highly water saturated except for sand A that has water saturation value of 0.3 or 30 %.

A-K1 well petrophysical results having three interpreted reservoir units reveals a relatively good gross thickness, effective porosity ( $\Phi_{\text{eff}}$ ), high water saturation but a very low permeability. This shows that the well is more porous but less permeable relative to other studied wells. They also underscore the fact that though permeability (K) is related to effective porosity but it does not always depend on it. Permeability (K) is controlled by the size of the connecting passages (pore

throat & morphology or capillaries) between pore while effective porosity is a measure of the amount of interconnected pores in a volume of rock. Therefore, a higher effective porosity value does not always imply higher permeability values.

The two reservoir units from A-Y1 well show a very good and considerable effective porosity ( $\Phi_{\text{eff}}$ ) values with the permeability (K) of sand A revealing a promising interval (Table 5.7.2). The water and irreducible water saturation values in sand B explain the obvious hydrocarbon bearing zone of the units by having the same values (0.70 or 70 %) but with low permeability (0.01 mD).

Generally, the results suggest the presence of greater proportion of wider interconnected pore throat in A-K1 and A-W1 (average effective porosity of 0.15 or 15 %) though with a low permeability followed by A-G1, A-K2 and A-Y1 respectively which are characterized by narrower interconnected pore throats.





## CHAPTER SIX

### **6.0 PETROGRAPHY & GEOCHEMISTRY**

---

#### **6.1 Results and Discussion**

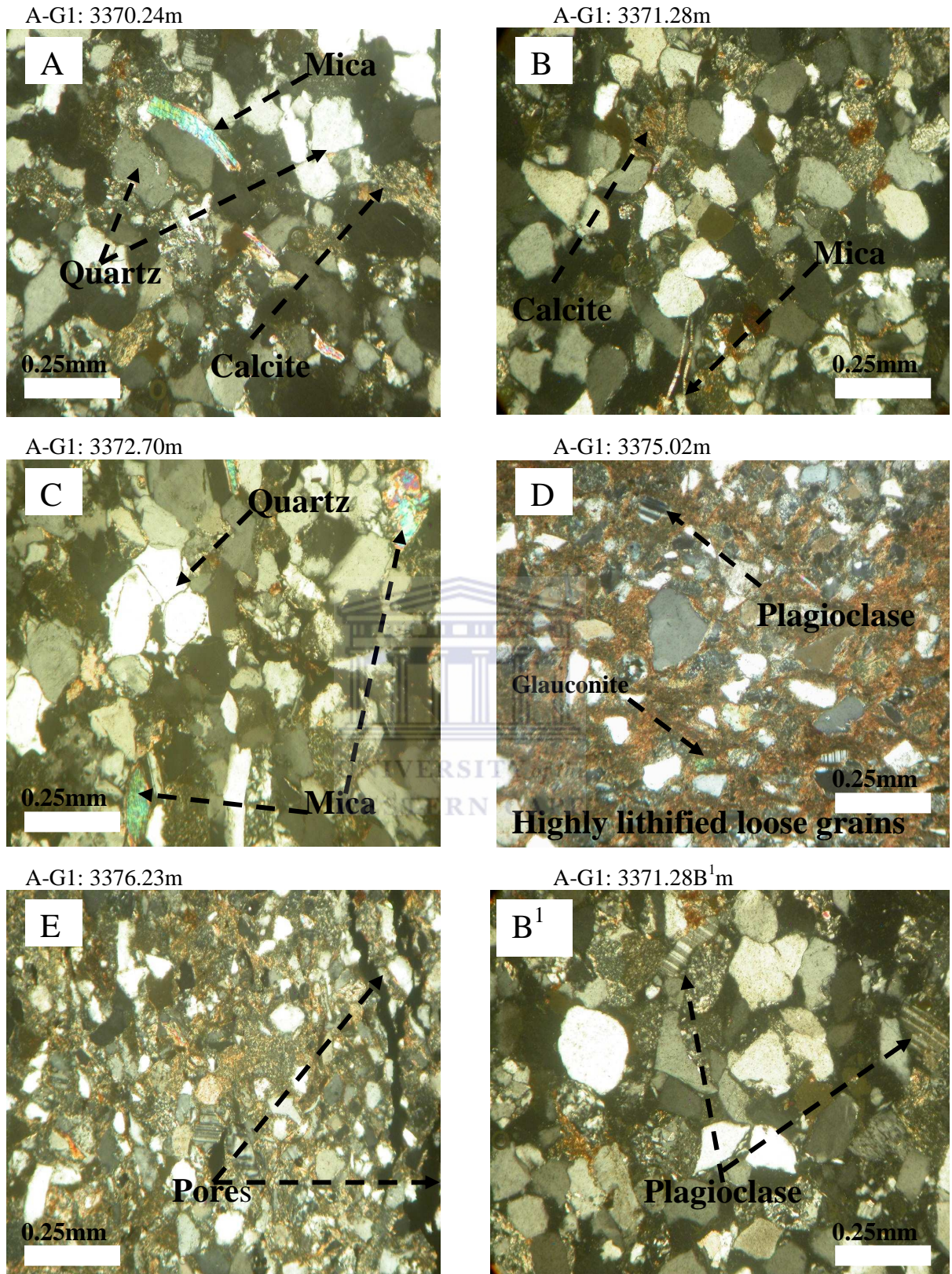
The standard petrographic microscope was used to investigate the mineralogy in order to identify the various factors related to the origin of sediments that filled the Albian age siliciclastic sandstone in the Orange Basin. Mineralogy and textural maturity depend on the content of fine-grained material, sorting and roundness of grains and the basic mineral composition. Petrographic approach to the identification of sandstone constituents includes the investigation of undulosity and polycrystallinity of quartz grains, types of feldspar present and lithic fragments. Relief and climate of source was inferred from grain roundness and average degree of feldspar alteration (Folk, 1980). Thin section made from the core samples selected at the reservoir zones were described with special focus on the major rock forming and diagenetic minerals.

##### **6.1.1 Thin section petrography for well A-G1**

The major rock forming minerals based on thin section observation in the A-G1 well are quartz, feldspar (plagioclase, microcline) and mica while the diagenetic minerals includes chlorite and calcite (Fig 6.1.1). These sandstones show abundant less stable minerals such as feldspar and rock fragments though, quartz and calcite appears to be the most abundant minerals present based on microscopic observations. Looking critically at figure 6.1.1A, the abundance of quartz was noted having partial grain contacts with calcites and some altered feldspar. There has always been a confusion in distinguishing between quartz, calcite and feldspar, however, during the laboratory observation, quartz was distinguished based on some optical features it exhibits that differentiates it amongst others, bearing in mind that the thin section was cut at 20 microns and viewed under crossed polarized light, it appears as shades of gray (Fig. 6.1.1) while at times it displays a 1<sup>st</sup> order colours, the feldspar present is unstable and it has low resistance compared to quartz, as a result it has been altered which makes it easier for identification. Figure 6.1.1B shows that the grain contact is prominent which connotes that the porosity at that depth would be considerably reasonable. Quartz grains are sub-angular to sub-rounded framework (Fig. 6.1.1B & D) having low to medium sphericity with calcite cement. Texturally, the grain size is coarse to fine quartz with normal extinction, the finer grains shows more angularity than the coarser grains. Their degree of sorting ranges from well sorted to moderately sorted and occasionally poorly sorted ones are encountered. The sandstones are to a

variable degree, lithified by compaction and silica cements, also by, quartz which has been observed as the main cement material and main control on reservoir properties (porosity and permeability reduction). Towards the deeper buried parts of the well (Fig. 6.1.1D, & E), the amount of cementation increases. It was noted during core visualization that the depths mentioned above are shaly and silty respectively which explains the change in grain size and cementation. Besides the prevailing quartz cement, the sandstones are weakly lithified with calcite and minor quartz cement. Probably compaction also played a role in the reduction of porosity and lithification. Compaction comprised mechanical re-arrangement of grains (Figs. 6.1.1A & 6.1.1I) as well as chemical compaction throughout this well at shale-sandstone contacts and within the shaly zone which could be responsible for reduction in grain size with respect to leaching (Ahmad, 2005).

Calcite group is one of the most important minerals of sedimentary rock. Calcite cementation is present throughout the examined samples as indicated by floating clasts which can be attributed to dissolution from shelly materials and the precipitation of  $\text{CaCO}_3$  from fluid-sediment interface. The light coloured calcite grains as seen in figure 6.1.1A, B & C have large grain size ranging from sub-angular to sub-rounded and most importantly the grain contacts are visible. Some of the diagnostic features when viewed under microscope are; it shows no pleochroism, it is colourless, with variation in its relief as it's rotated on the stage. Lamellar twinning is observed parallel to one edge, the rate of dissolution varies with the optical orientation of the section when tested with hydrochloric acid (as described in chapter five). The observed variability in mineralogy of the fringe cement (observed across the samples) could be an intrinsic explanation for hydrodynamic flow and the involvement of sea water. This variability may point to different growth rates and degrees of saturation of involved fluids reflecting locally change in environmental conditions in terms of energy and changes in sediment texture (Rushdi et al., 1992). Differential early calcite cementation and late calcite cementation mechanism are noted in the thin section of samples in this well, the later cementation is more prominent due to changes in the rock type and textural differences with notable exception of laterally non-extensive early cemented deposits, the early cementation resulted in low permeability lenses (Fig. 5.2).



**Figure 6.1.1:** Thin section photomicrographs of the reservoir zone in A-G1 well.

The common heterogeneity of early marine cementation (as discussed in chapter five A-G1 core descriptions) reflects the process involved and the constrained factors on that process such as sedimentary textures, framework mineralogy and time. Having inferred in chapter five that the depositional environment could be of marine settings, early cementation when dependent on hydrodynamic flows and external supply is strongly constrained by the permeability of sediment and the presence and force of supply mechanism (Harris et al. 1985). Possible mechanism to move sea water through the sediment are waves and tidal currents operating in shallow marine environment and at platform edges, the occurrences on glauconite (Fig. 6.1.1D) confirms the depositional environment as shallow marine. The source of calcite cement under burial conditions often remains an enigma. Apart from the dissolution of detrital carbonate, additional potential of Ca source is feldspar alterations which are evident across the samples in this well, comprising the dissolution and albitization of plagioclase and also illitization of smectite (Fig. 6.3.1). Diffusional transport may cause limited calcite cementation in feldspathic sandstones under burial conditions (Morad et al., 1990).

Mica being one of the member of group of lamellar, silicate minerals (feldspar, mica, quartz and olivine) are distinguish from each other mainly by their ratio and elasticity, their ductility (mica) as revealed in figure 6.1.1A is attributed to their high resistance to mechanical stress coupled with the lustrous properties they possess. Detrital muscovite and biotite are common in clastic rocks of North Sea and other basins (Morad, 1990), these minerals were also observed in Orange Basin. Many minerals result from alteration of these mica and some particularly clay minerals can significantly lower the permeability of the reservoir rocks (Pallat et al., 1984) as observed in the Albian sandstones of the Orange basin. Muscovite can expand and illitize (Fig. 6.1.1A & B) i.e. alteration of mica in sandstone of A-G1 well possibly retarded silica cementation (Fig. 6.1.1D) whereas growth of carbonates and feldspar along cleavage planes of mica was enhanced probably due to high pH of this micro-chemical environment (Fig. 6.4.1A see pH graph of A-G1).

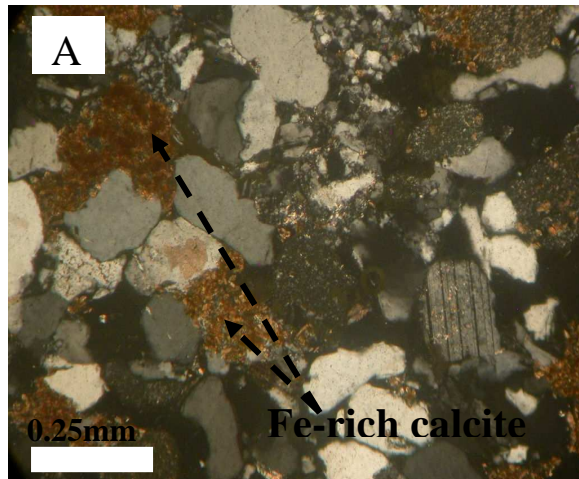
### **6.1.2 Thin section petrography for well A-K1**

The major rock forming minerals with regards to thin section examination of samples from A-K1 well are quartz, plagioclase, mica and calcite (Figs. 6.1.2A & C & 6.1.3A & B). In strongly cemented samples (Figs. 6.1.2A & C & 6.1.3C & F) all quartz grains have overgrowth, but the thickest overgrowth are present in

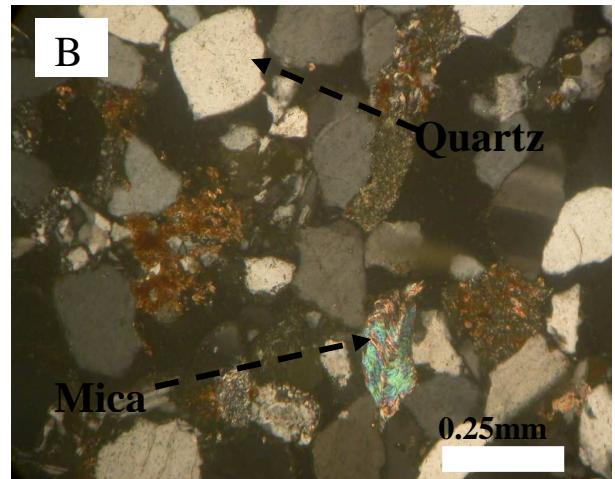
monocrystalline angular to sub-angular quartz grains as observed across the whole slide except (Slides E & F in figures 6.1.2 and 6.1.3). The presence of overgrowths resulted in long compromised boundaries between adjacent quartz grains. The quartz grain is non-luminescent without zonation suggesting few changes in pore fluid chemistry during quartz precipitation or single cement precipitation phase (Nicolaas, 2008). Figure 6.1.2E which falls within facie 3 in chapter five (Fig. 5.3,) shows a homogenous degree of cementation with the grains densely packed while figure 6.1.3D reveals a contact point that delineate texturally finer sands (silt) from coarse sand (sandstone). An unconsolidated sand was also noted (Fig. 6.1.3F) with variations in the grain packing, poorly sorted and highly lithified. In the A-K1 Albian sandstone well, some detrital grains have been dissolved and replaced by calcite cement (Fig 6.1.2A). Both quartz and feldspar grains were corroded along grain boundaries and cleavage planes.

The main cementing material in the A-K1 well reservoir is quartz, which occurs as syntaxial overgrowth on detrital grains in most A-K1 samples and all sandstone facies (Fig 5.3). Heterolithic sandstones may lack quartz cement when they are matrix supported because of bioturbation (Nicolas, 2006). Quartz cement partly fills pore spaces and is one of the main causes of porosity loss within the Albian sandstone reservoirs in A-K1 well. Detrital quartz grains are evident across both core 1 & core 2 in A-K1 well with irregular shapes and few grain contacts coupled with a very high degree of cementation (Figs. 6.1.2B, D & 6.1.3B). The development of calcite rim cement occurs as micritic coating on grains while some occurs as superficial pore filling between grains (Figs. 6.1.2A, B & 6.1.3C). In some thin sections characterized by Fe-calcite cement (Figs. 6.1.2A, B & 6.1.3B), the corroded quartz grains exhibit calcite cement infilling. This evidence suggests the presence of syn-depositional calcite cement, which was later replaced by Fe-calcite cement during deep burial. The early precipitation of carbonate cement takes place a few centimetres below the sediment water interface (Bjorlykke, 1983). This type of cementation occurs by exchange of interstitial marine pore water either by meteoric water or by pore water expelled from the underlying sediments (Bjorlykke, 1983). On the other hand, the dark brown coating of Fe-calcite cement on detrital grains may be extra-basinal weathering generated during deep burial (Walkers, 1994).

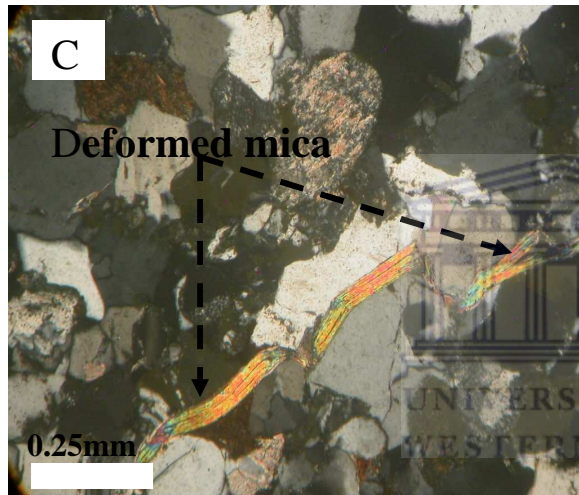
A-K1: 3236.27m



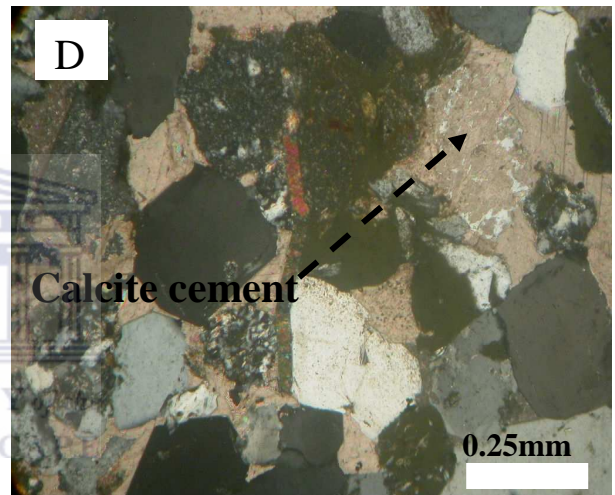
A-K1: 3236.96m



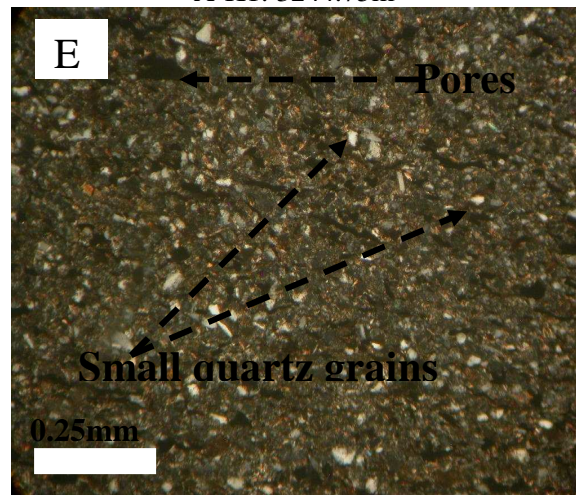
A-K1: 3238.35m



A-K1: 3239.18m

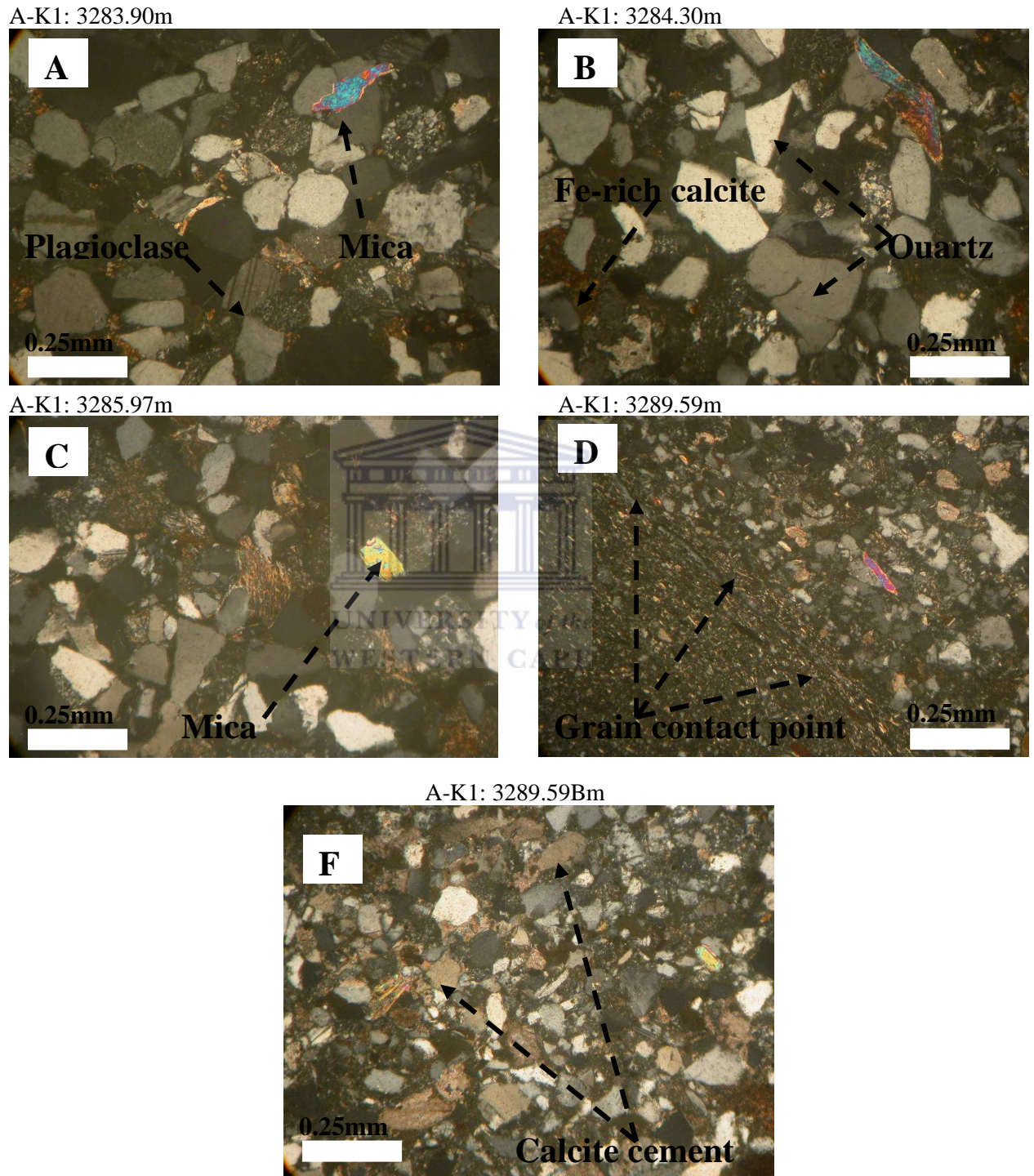


A-K1: 3244.75m



**Figure 6.1.2:** Thin section photomicrographs of the reservoir zone in A-K1 well Core 1 well.

In some of the sandstone samples, (Figure 6.1.2E & 6.1.3D), silty or clayey matrix is present in varying amounts which might have influenced the diagenetic processes by supplying Fe and reducing porosity and permeability by pore occlusion.



**Figure 6.1.3:** Thin section photomicrographs of the reservoir zone in A-K1 well Core # 2.

Besides mechanical compaction, pressure dissolution can occur in sandstone along discretely spaced surface, such as mica formation which is parallel to bedding plane showing evidence of differential stress field (Fig. 6.1.2C) along traces of cleavage planes. The occurrence of authigenic mica derived from complete diagenetic transformation of smectite into illite/smectite with 100 % illitic layers has been reported in the literature (Arostegui, 1989, Zulaga, 1995, Arostegui et al. 2006). Progressive burial of sediments and subsequent increase of diagenetic grade are responsible for this transformation (Perry and Hower 1970, Nieto et al., 1996; Altaner and Ylagan 1997). Yet, the occurrence and distribution of mica in studied sediments might not be due to diagenesis, because the diagenetic grade of the entire sedimentary sequence is far from that necessary for such diagenetic transformation. However, a detrital origin for the identified mica is also deduced from their occurrence as highly stressed, deformed and mainly wrapped around other detrital grains (Figs. 6.1.2B & C). Plagioclase feldspar is also observed from some of the slides with its twinning effect (Figs. 6.1.2C & 6.1.3A); its formation might be due to metasomatism which involves the reconstruction of partially degraded feldspar to form potash feldspar and late albite as revealed in the XRD section (Figs 6.3.2 & 6.3.3).

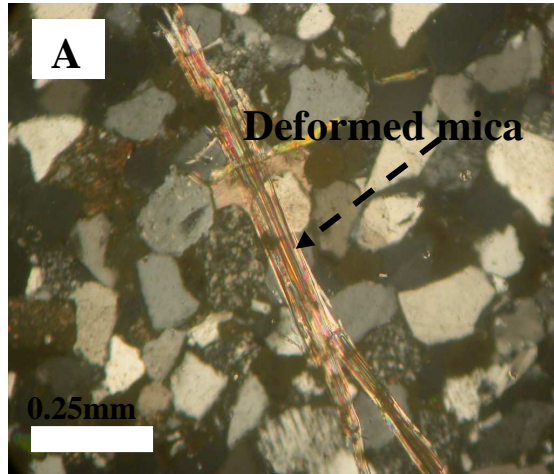
### **6.1.3 Thin section petrography for well A-W1**

The major observed minerals in the thin section of samples from this well are quartz, mica, calcite and feldspar (Figs. 6.1.4 & 6.1.6). The nature of point contacts and contact index are helpful in understanding the package of the rocks. In this particular well, the closely packed sandstones exhibit three types of grain contact, which includes point, long (line contact) and concavo-convex contacts (Taylor, 1950), (Figs. 6.1.4A & B). In other case, framework grains constitute about 35 % (optical observation) of the rock and are embedded in a siliciclastic-carbonate matrix. This primary pore filling matrix appears to have influenced mechanical compaction and cementation as evident by the strained detrital quartz grains floating in Fe-calcite cement (Figs 6.1.6G, I & K). The contact index (average number of grain contacts a grain has with its neighbouring grains (Pettijohn et al. 1987), also gives an indication about the degree of compaction of sediments. Concavo-convex contacts as revealed in (Figs. 6.1.6G & 6.1.5C) could suggest a limited pressure solution activity in this sandstone. It is well known that the original porosity of sandstones generally varies between (30-50) percent which can be reduced through mechanical compaction by

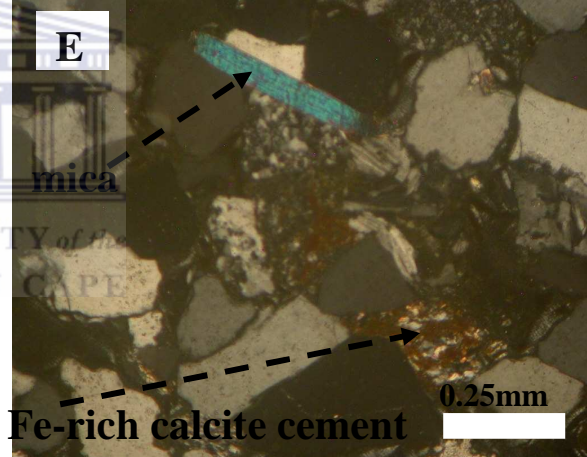
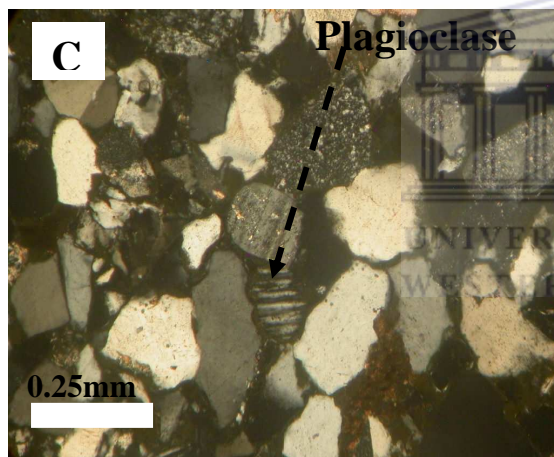
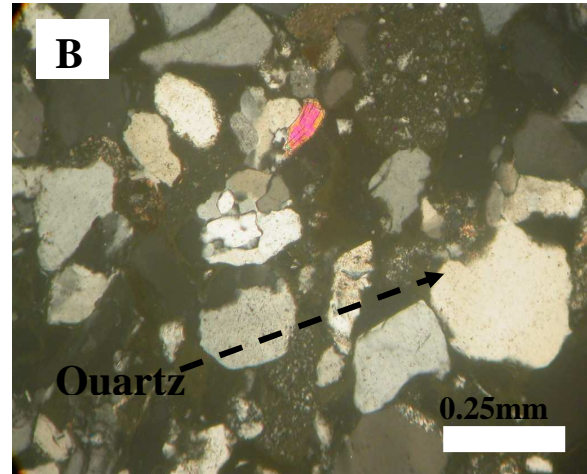


(10-17 % (Pryor, 1973; Beard & Weyl, 1973). The initial high porosity is attributed to loose packing of sediments at onset of deposition. In addition to compression, rotation of grains and their mechanical breakage (Fig. 6.1.6I) during burial also reduces porosity in sandstones.

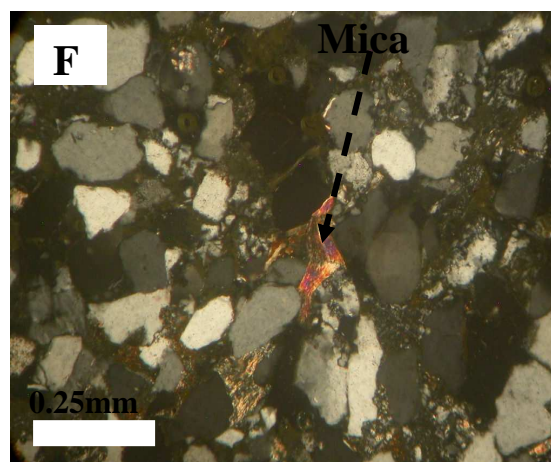
A-W1: 3450.50m



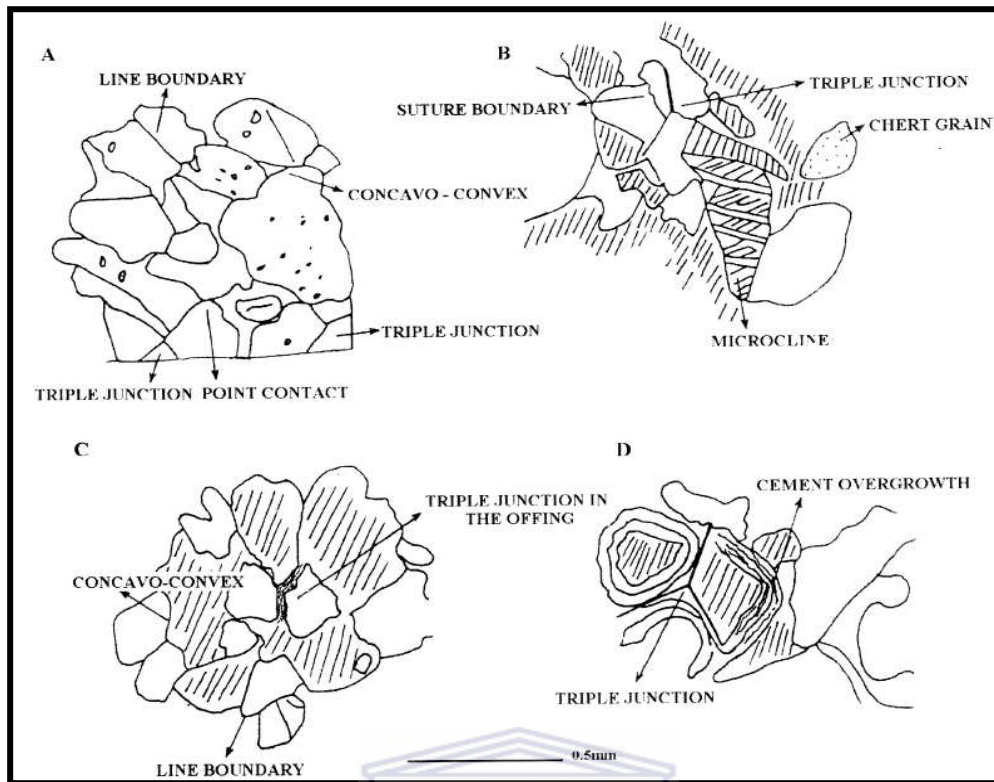
A-W1: 3452.50m



A-W1: 3455.50m



**Figure 6.1.4:** Thin sections photomicrographs of the reservoir zone in A-W1 well.



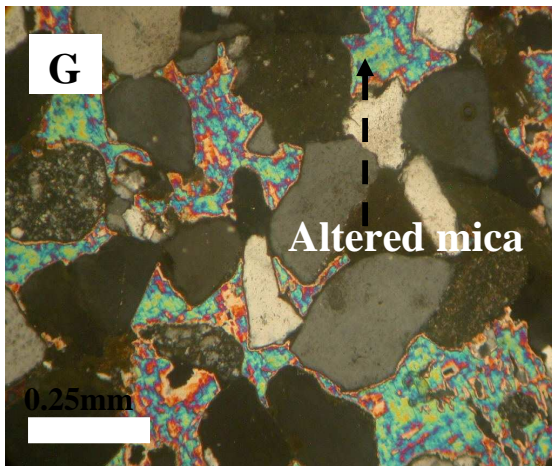
**Figure 6.1.5: Line drawings of different diagenetic features and altered mineral constituents observed in thin sections of Dhosa Sandstone Member closely related to that of A-W1 Albian sandstone; hachuring of the grains indicates extinction position while the spots in white grains indicate mineral inclusions (Ahmad et al., 2005).**

The A-W1 Albian sandstone exhibits distinct cement-grain boundaries (Figs. 6.1.4A & 6.1. 6H) in a few samples. Line boundaries form between adjacent overgrowth quartz crystal, if there is enough pore space available for cement overgrowth (Dapples, 1979). This implies that cement/neomorphic quartz crystals grow in favourable sites where enough pore space is available. The sediments may retain this type of pore space during early stages of burial. The line boundaries are recognized as somewhat unstable and prone to recrystallization under conditions of pronounced folding, deep burial and significant movement of fluids undersaturated in silica (Dapples, 1979). This study reveals the presence of interpenetrating and straight line boundaries (Fig. 6.1.5A) in the quartz grains while the signatures are related to intermediate burial and tectonic uplift. The interpenetrating (sutured/incoherent) boundaries (Fig. 6.1.5B) are formed under the combined influence of mechanical pressure and chemical solution i.e. pressure solution processes (Waldschmidt, 1941; Heald, 1950; Taylor, 1950). At places, three planar crystal boundaries meet at about

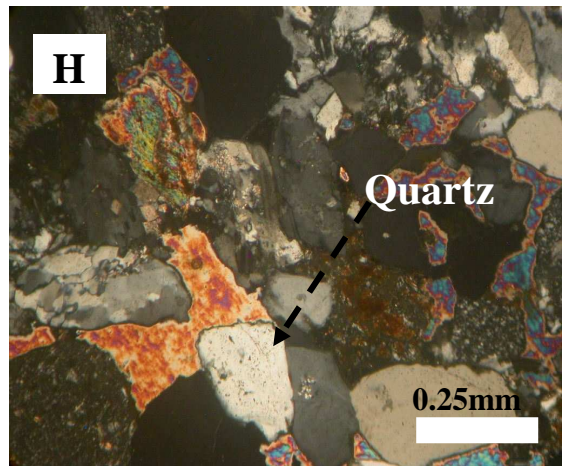
120° triple junction (Figs. 6.1.5A & B), straight/planar boundaries and the triple junctions reflect the stable grain arrangements and best use of accommodation under deep burial diagenesis. The grain to grain boundaries observed in this wells appear to have culminated into triple junctions, this culmination evolved through different stages of diagenesis, the grain-grain interlock in the form of concavo-convex and sutured grain boundaries (Figs. 6.1.4C & 6.1.5A) is the result of intermediate burial diagenesis. During this stage of diagenesis, grain boundaries interlock forms due to dissolution of silica at the points of grain contact (Waldschmidt, 1941) suggesting two processes of operation re-deposition (interstitial transport of dissolved material). Figures 6.1.6 G & H reveal the formation of neomorphic quartz (recrystallization of quartz involving both grain diminution and enlargement) crystals at the expense of monocrystalline quartz grain. These diminutions was initiated on the periphery of the grain, however, this type of selective recrystallization begins at the point of stress concentration within a rock (Blatt, 1992). Similarly, difference in stress at various points within a grain may lead to difference in the rate of crystallization. This could be the reason that these neomorphic crystals show a great variation in crystal size within a detrital quartz grain.

The thin sections of the samples in this well show the presence of calcite (Fig. 6.1.4E) but in varying degrees, the occurrence of calcite cement in A-W1 well has been mostly altered probably due to the Fe mineralization contemporaneously with the calcite cement formation. Calcite principally occurs as fracture filling and poikilotopic cement. Two chemically distinct types of calcite are present, one relatively enriched in Fe, the other in Mg (hereafter referred to as Fe-rich and Mg-rich calcite, respectively). Based on optical examination, it was noted that Fe-rich calcite mostly occurred in the well A-W1 Albian sandstone. This was inferred with reference to the alteration colours of the calcite cement (Figs. 6.1.4A & E, 6.1.6I). Some of the pore-filling Fe-rich calcite occurs in samples that experienced only minor compaction prior to precipitation in the undeformed ductile framework grains whereas others (Fe-rich calcite) fill pores in more compacted samples with a highly deformed ductile framework grains (Fig. 6.1.4A).

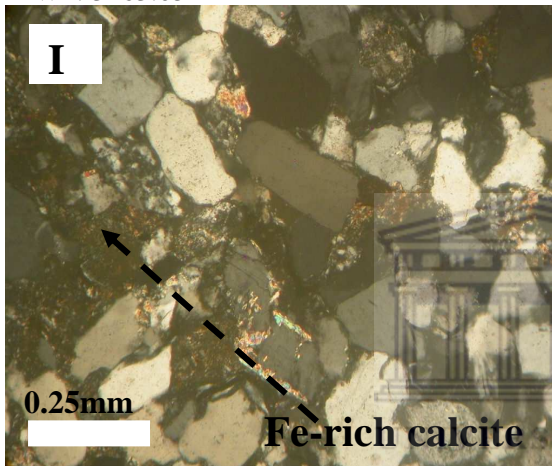
A-W1: 3460.24m



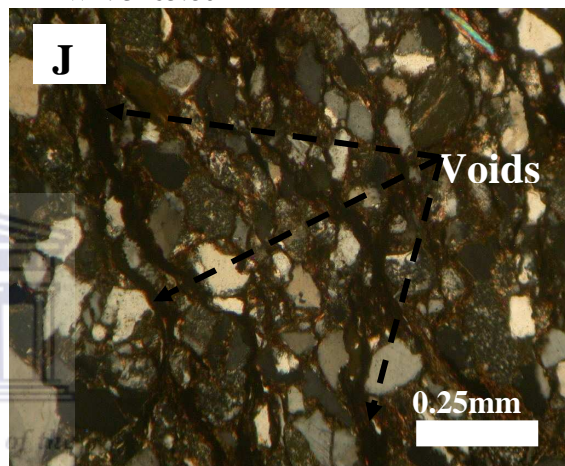
A-W1: 3460.24Bm



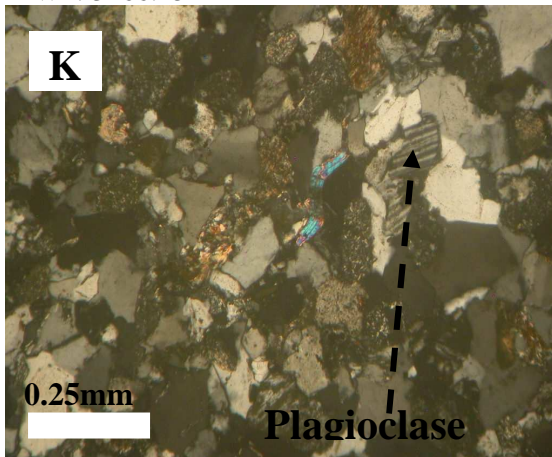
A-W1: 3463.05m



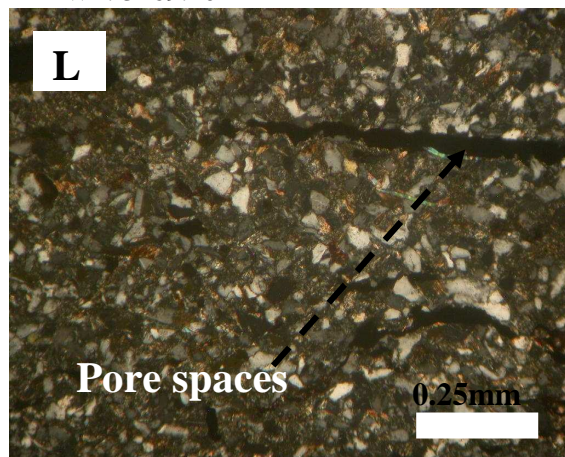
A-W1: 3465.80m



A-W1: 3466.45m



A-W1: 3469.20m



**Figure 6.1.6:** Thin sections photomicrographs of the reservoir zone in A-W1 well.

The fracture/pore filling calcite apparently formed very late in the calcite-cemented samples (Fig. 6.1.6J) indicating that some of the pore/fracture filling calcite must have formed after deep burial of the units in the late Cretaceous period. The paragenetic relationship between Fe-rich calcite and quartz overgrowth confirms the presence of

both early and late stage pore filling calcite cements (Stuart et al., 2003). The indistinct presence of quartz overgrowth from the Fe-rich calcite-cemented portions of some samples (Figs. 6.1.4A & 6.1.6G) suggests that the calcite pre-dates overgrowth formation. In other samples however, Fe-rich calcite clearly post date the overgrowth.

Mica was another silicate mineral that was revealed through optical examination of the samples (Fig. 6.1.4A). The evolution of mica was evident in a laminated pattern with indication of stress while other few samples show minor amount of mica, prominent in figure 6.1.6G was mica alteration between the rigid quartz and feldspar grains. The degree of alteration and its effect on the chemistry of pore fluids and the mineralogy will be more revealing in the pore water chemistry section. However, it is imperative to bear in mind that authigenic mineral by-products of mica alteration includes siderite, K-feldspar, quartz and titanium oxides (Morad, 1990) which would be discussed more in detailed at the SEM, XRD, and XRF interpretation section.

Plagioclase is a very important series of tectono-silicate minerals with the feldspar family; its crystal shows a distinct banding effect called polysynthetic twinning (Fig. 6.1.6K). It doesn't show pleochroism when rotated on stage, it is hard to discern between detrital and authigenic feldspar due to its unstable nature. Feldspar may be lost in transit or by solution, it may however form in the buried sediment so its provenance is difficult to constrain by geologist. Nevertheless, the character of this feldspar may also be transformed by diagenesis, conversion of more calcic plagioclase to nearly pure albite has been reported in the Eocene sands of the Gulf of Mexico (Boyles, 1982), and these can also be linked to its occurrence in the study area.

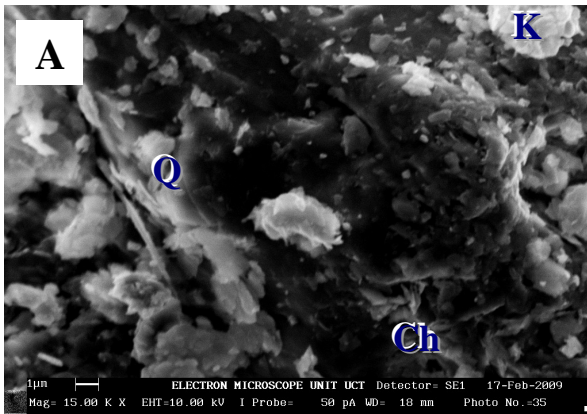
Figure 6.1.6J & L shows a variation in grain size and the reservoir properties especially porosity from physical and microscopic observations seem to be fair, the permeability might not be good i.e. poor due to inability of the grains to make contacts with each other, the sudden change at both depths (Fig. 6.1.6J & L) is justified by the silty nature of the sand which differentiate them from the other analysed samples within this reservoir sands.

### 6.2.1 SEM results and discussion for A-G1 well

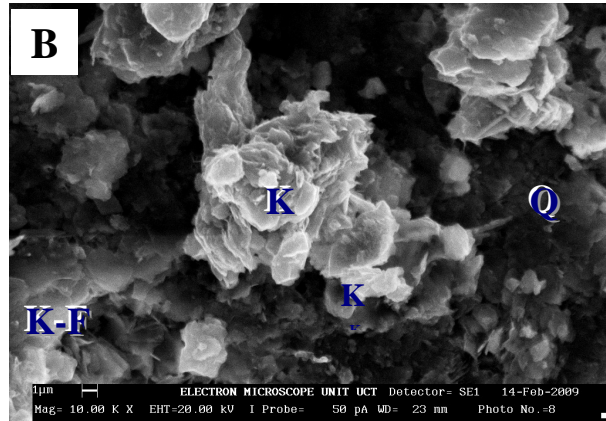
Kaolinite was observed across the whole A-G1 reservoir sand analysed with blocky kaolinite platelets locally resting on traces of grain rimming chlorite in the Albian sandstones (Figs. 6.2.0A & B). Extensive formation of kaolin occurred during burial diagenesis and is commonly associated with degraded feldspar and mica. Its occurrence across the reservoir unit in this well might be due to meteoric flushing of channel sandstones. The dissolution of potassium feldspar which partially to entirely covers detrital feldspar grain with a distinct euhedral to subhedral outline is revealed in the mineral architecture (Fig. 6.2.0B). K-feldspar overgrowths engulfed by coarse pore filling calcite that precipitate during progressive sediment burial and quartz overgrowth observed in the thin section (Fig. 6.1.1B) of same depth (3371.28 m). Feldspar overgrowths are more abundant in the fluvio-deltaic HST sandstone (El-ghali et al. 2008) than in anastomosing fluvial TST and shallow marine, foreshore to shore face, this was observed in the geophysical logs of this well that have been discussed in chapter 5 (Figs. 5.6 & 5.6.1). The occurrence of illite flakes around detrital grain booklets and vermicular like crystal with fibrous terminations supports its diagenetic origin (Morad et al 2000, Lemon and Cubitt 2003). Illite which typically forms during progressive burial (mesogenesis) under elevated temperature 90-130°C requires high  $a_{K^+}/a_{H^+}$  (potassium to hydrogen) ratio in pore waters (Ehrenberg et al., 1999, Morad and De Ros, 1994; Morad et al., 2000). The high  $a_{K^+}/a_{H^+}$  ratio required to achieve illitization in the sandstone is attributed partially to simultaneous albitization of K-feldspar observed in figure 6.2.0B before the noticeable illite fibres (Fig. 6.2.0C) which contributed the required K ions to the pore waters (Morad 1998). The flaky habit of the illite that is arranged sparsely around detrital grains (Fig. 6.2.0D) suggests possible transformation from infiltrated clays that was formed by the percolation of mud-rich surface water into the fluvio-deltaic HST sandstones during the late stage of HST (El-ghali et al. 2008).

The occurrence of mica at 3376.23m is mainly related to detrital origin. On the other hand, occurrence of authigenic mica derived from complete diagenetic transformation of smectite into illite-smectite with 100% illitic layers has been reported in the literature (Arostegui et al., 1989, Zulaga, 1995). Progressive burial of sediments and subsequent increase of their diagenetic grade are responsible for this transformation (Perry and Hower 1970, Nieto et al., 1996).

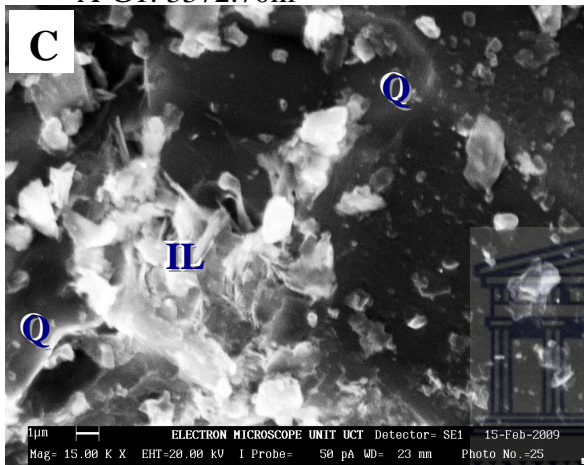
A-G1: 3370.24m



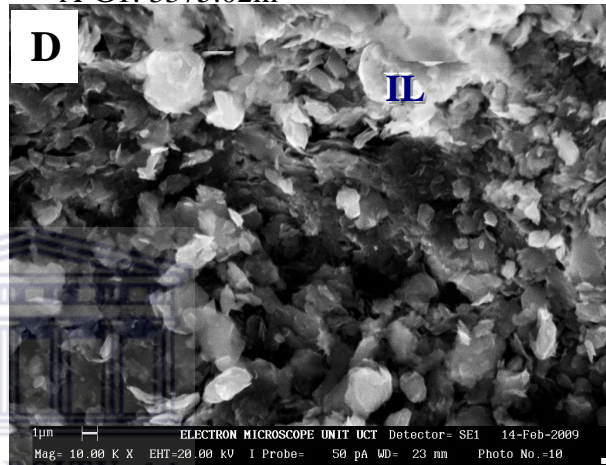
A-G1: 3371.28m



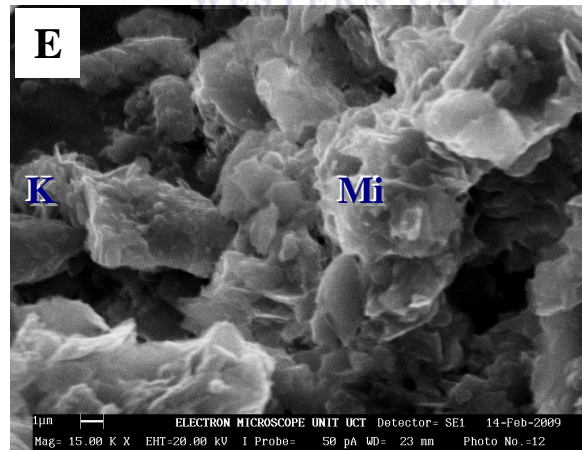
A-G1: 3372.70m



A-G1: 3375.02m



A-G1: 3376.23m



**Figure 6.2.0:** (A) SEM images of vermiform kaolinite on quartz grains and traces of chlorite flakes (B) SEM image of pore filling K-feldspar and kaolinite. (C) Fibrous illite and detrital quartz. (D) Flakes of lamellar mixed illite-smectite on quartz grains. (E) Detrital pseudo-hexagonal plates of kaolinite and larger plates of mica.

**Note:** M = mica, Ch = chlorite, IL = illite, Q = quartz, K = kaolinite, K-F = K-feldspar.

Nevertheless, the occurrence and distribution of mica in the samples in this well cannot be due to diagenesis alone, because the diagenetic grade of the entire reservoir interval is far from that necessary for such diagenetic transformation (Arostegui et al., 2006). However, a detrital origin of the identified micas is also deduced from their occurrence as deformed, broken plates (Fig. 6.2.0E) mainly laid on detrital grains.

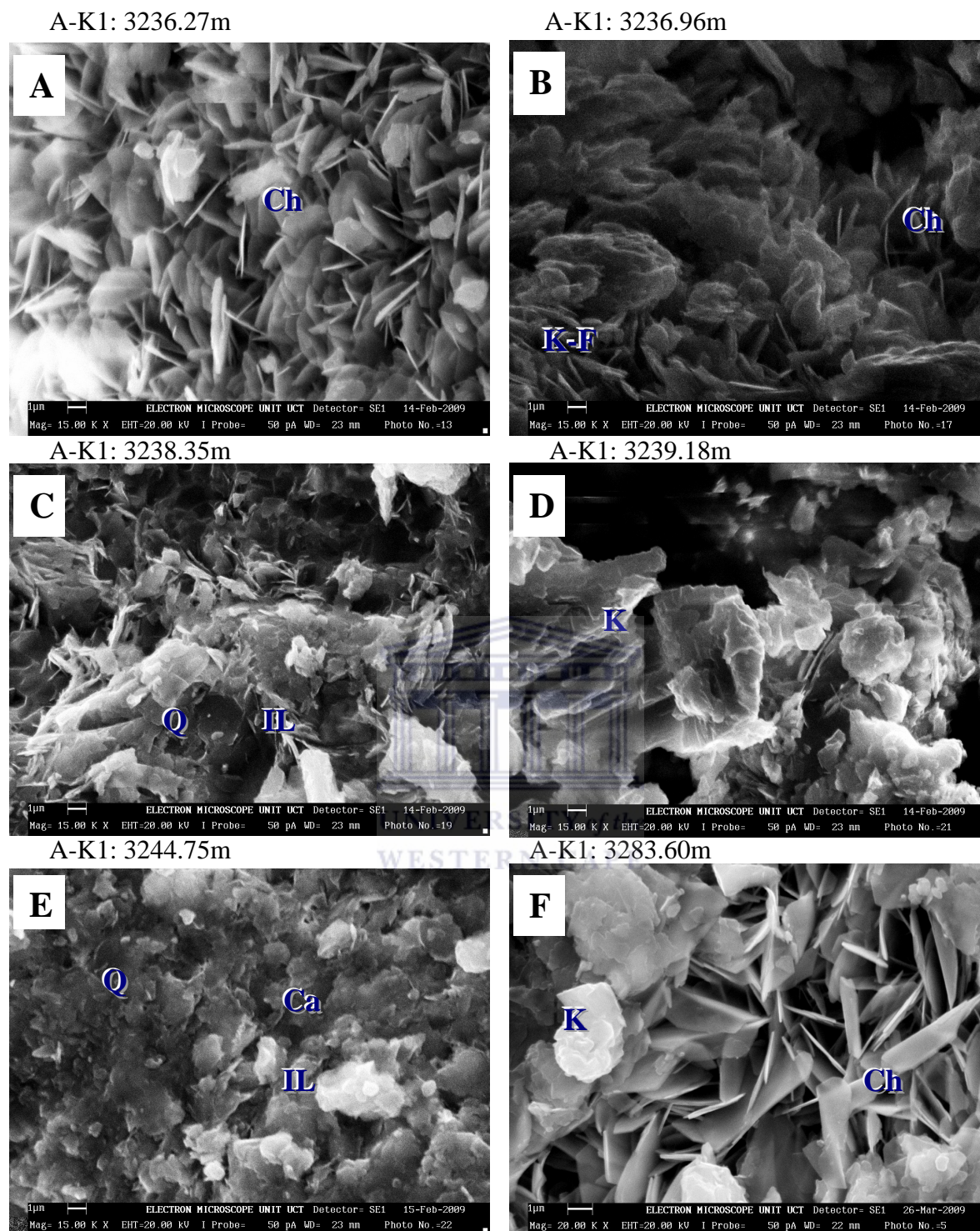
**Table 6.2:** Energy dispersive spectrometry (EDS) results of A-G1 well.

	3370.24m		3371.28m		3372.70m		3375.02m		3376.20m	
Element	Weight%	Atomic%	Weight%	Atomic%	Weight%	Atomic%	Weight%	Atomic%	Weight%	Atomic%
C	0.00	0.00	22.75	44.94	0.00	0.00	70.66	84.95	33.03	56.88
O	5.83	12.69	6.84	10.14	6.38	12.48	5.38	4.85	6.95	8.98
Mg	0.30	0.42	0.32	0.31	0.53	0.69	0.00	0.00	0.35	0.30
Al	6.49	8.38	4.56	4.01	5.65	6.56	2.60	1.39	6.16	4.72
Si	35.29	43.73	27.15	22.93	51.32	57.19	10.62	5.46	22.53	16.59
S	0.71	0.77	0.64	0.48	1.40	1.37	0.56	0.25	0.41	0.27
K	4.91	4.37	3.04	1.84	4.47	3.58	3.32	1.22	4.66	2.46
Ca	0.91	0.79	1.84	1.09	3.84	3.00	0.56	0.20	0.79	0.41
Ti	4.56	3.32	4.24	2.10	3.68	2.40	0.73	0.22	1.27	0.55
Fe	40.99	25.54	28.62	12.16	22.72	12.74	5.57	1.44	23.87	8.84

### 6.2.2 SEM results and discussion for A-K1 well

Calcite also fills fractures, either alone or as a successor to earlier quartz cement in reactivated fractures (Fig. 6.2.1E). The primary cementing material of the A-K1 Albian sandstone is calcite precipitated in the sub-aerial vadoze zone (Fig. 6.2.1E) due to capillary action under wet and dry climatic conditions (Tandon and Varshney 1991). Not all of the stages of cementation summarized herein occur in single sandstone, but the order of the cements is consistent throughout the examined sample suite. For example, the combination of isopachous chlorite and calcite is present only in some thin sections and SEM, but where present, the chlorite cement always precedes the calcite. For example, chlorite cement may have formed isopachous coats that completely occlude some pore throats, and in those pores no subsequent cementation or dissolution occurred. Corrosion of quartz and feldspar grains by calcite cement is common especially in siltstone sample from optical observations (Fig. 6.1.2E).





**Figure 6.2.1:** SEM images of core# 1 from A-K1 well (A) Chlorite arranged tangentially to each other (B) Chlorite with vermicular habit that resembles kaolinite suggesting chloritization of kaolinite (C) grains coating illite flakes around detrital grains. (D) SEM image showing booklet-like kaolinite crystals. (E) Detrital grains showing high degree of calcite cementation. (F) Kaolinite locally resting on blades of chlorite grains.

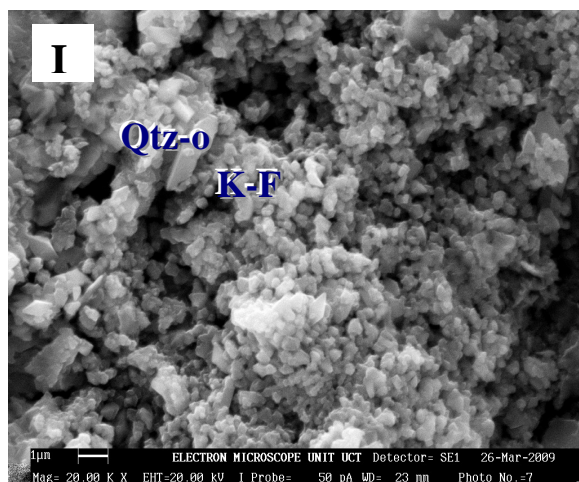
**Note:** M = mica, Ch = chlorite, IL = illite, Q = quartz, K = kaolinite, K-F = k-feldspar, Ca = Calcite.

SEM results of A-K1 reservoir sandstone shows absence of K-feldspar in the younger samples (Fig. 6.2.1) in most cases, whereas in the older samples, K-feldspar is present but has corrosive features (Fig. 6.2.2I). The increase in K-feldspar abundance in the older samples compared to the younger ones could be attributed to the difference (about 39 m) in distance between the two cores and also some changes in temperature and pore fluid indicating that they are not likely to be of same sand body. Several workers suggested that alkali feldspar can undergo extensive dissolution during burial diagenesis of sandstone (Milliken, 1989; Harris, 1992; Wilkinson and Haszeldine, 1996). Dissolution of K-feldspar is probably as a result of interaction with weakly acidic pore fluid formed by decomposition of organic matter. Dissolution of K-feldspar increases K, Al, Fe and SiO<sub>2</sub> concentrations (Table 6.2.1) in the diagenetic fluid, which can cause precipitation of quartz and illite (Zhang et al., 2007).

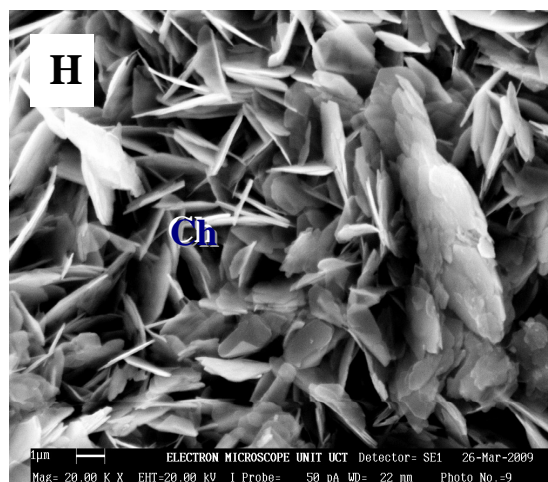
There is an occurrence of kaolinite with blocky platelets locally resting on grain-rimming chlorites in the Albian sandstones in A-K1 well (Figs 6.2.1D & 6.2.2I). This kaolinite formation might have occurred soon after deposition and was due to meteoric flushing of channel sandstones before burial (Knarud and Bergan, 1990). However, this meteoric water can readily access and react with continental fluvial deposits during and soon after deposition. The lack of kaolin in the siltstones and mudstones of well A-K1 (Fig. 6.2.1E) suggests that its incorporation as detrital material during deposition is unlikely.

In this well at depths 3236.27 m and 3284.30 m, chlorite cement forms continuous blade shapes as much as 25 mm thick of rosette structure crystals oriented perpendicular to grain surfaces (Figs 6.2.1A, F & 6.2.2H). The cements form regardless of substrate composition, as demonstrated by equal thickness of cements around grains irrespective of mineralogy. In some pores, chlorite has clearly grown out into the pore space and crystals display regular crystal shape tangential to each others (Figs. 6.2.1A & 6.2.2H). In other pores, although crystal orientation remains perpendicular to detrital grain margins (Figs 6.2.1A & 6.2.2G), the interior surface of the chlorite cement is irregular, suggesting subsequent dissolution by pore waters. Chlorite cements subjected to later dissolution are commonly very thin in parts of a thin section (Cookenboo et al. 1998), and may be absent altogether in other parts where dissolution was apparently complete.

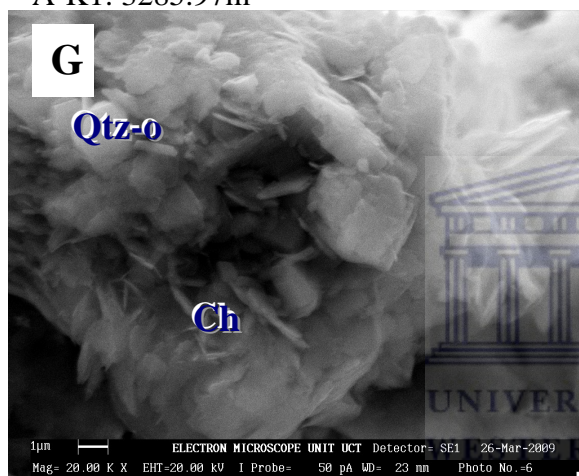
A-K1: 3283.90m



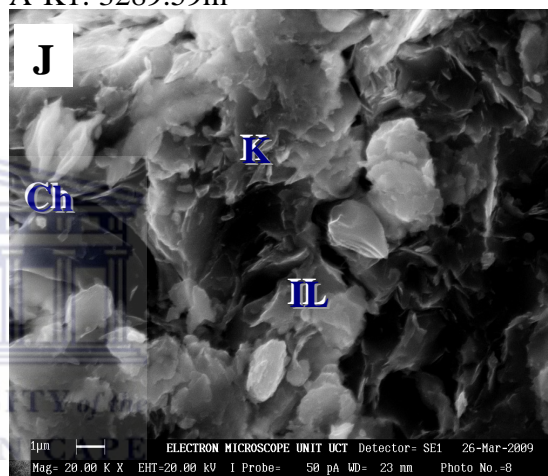
A-K1: 3284.30m



A-K1: 3285.97m



A-K1: 3289.59m



**Figure 6.2.2:** SEM images of core# 2 from A-K1 well (I) Very prominent pyrite framboids grown on detrital K-feldspar. (H) Scanning electron micrograph shows authigenic “rosette” type chlorite. (G) Quartz overgrowth occurring along with rosette shaped chlorite (J) scanning electron micrograph showing rare illite filling pore spaces and kaolinite overgrowing quartz cements.

**Note:** M = mica, Ch = chlorite, IL = illite, Q = quartz, K = kaolinite, K-F = K-feldspar, Otz-o = quartz overgrowth.

The chlorite cement was formed early, as demonstrated by its formation directly on grain surfaces (Fig. 6.2.2G) and its isopachous habit, which implies growth into empty pore space. However, some compaction preceded chlorite cementation, as evidenced by the common occurrence of long grain contacts between sand grains (Fig. 6.2.1F). The formation of this chlorite was also related to: (1) smectite illitization with increasing burial-depth, and (2) dioctahedral clay mineral (kaolinite and mica) reactions with carbonates. The expelled cations ( $\text{Fe}^{2+}$  and  $\text{Mg}^{2+}$ ) from such mineralogical transformations along with dissolved  $\text{SiO}_2$  from these and other sources would have encouraged chlorite precipitation (Hutcheon et al., 1980; Hillier, 1993).

This evidence suggests a diagenetic origin for the identified chlorite and its formation is also related to processes such as smectite illitization and reactions of dioctahedral clays with carbonates (see XRD section).

There is presence of illite in A-K1 well with a flaky habit that is arranged tangentially around detrital grains (Fig. 6.2.1C) suggests possible transformation from infiltrated clays that are formed by the percolation of mud-rich surface water into LST sandstones (Figs. 5.6.2 & 5.6.3) during the late stage of LST (Moraes and De Ros, 1992; Ketzer et al., 2003). Presence of illite with booklet- and vermicular-like habits which suggest formation by illitization of kaolinite during mesodiagenesis, which was enhanced by high  $a_{K^+}/a_{H^+}$  ratio in pore waters (De Ros, 1998).

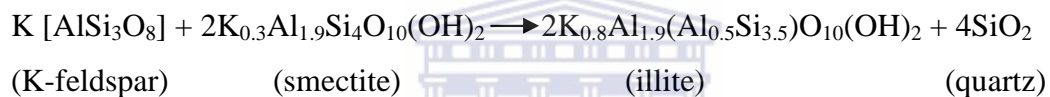
The occurrence of illite as flakes around detrital grains, booklet- and vermicular-like crystals with fibrous and spiny termination support its diagenetic origin (Morad et al, 2000; Lemon and Cubitt, 2003). Illite, which typically forms during progressive burial (mesodiagenesis) under elevated temperature 90–130°C; (Morad et al., 2000), required high  $a_{K^+}/a_{H^+}$  ratio in pore waters (Ehrenberg et al., 1993; Morad and De Ros, 1994). The high  $a_{K^+}/a_{H^+}$  ratio required to achieve illitization in the sandstones is attributed partially to the simultaneous albitization of K-feldspar as revealed in both thin section and XRD (Section 6.3), which contributed the required K ions to the pore waters (Morad, 1988).

**Table 6.2.1:** Energy dispersive spectrometry (EDS) results for A-K1 well.

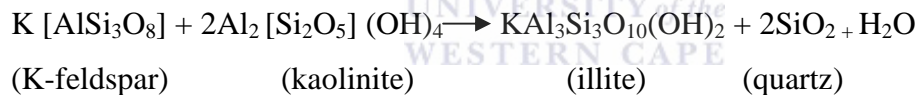
	3236.27m		3236.96m		3238.35m		3239.18m		3244.75m	
Element	Weight%	Atomic%	Weight%	Atomic%	Weight%	Atomic%	Weight%	Atomic%	Weight%	Atomic%
C	44.02	67.08	31.72	57.72	0.00	0.00	0.00	0.00	0.00	0.00
O	6.51	7.45	5.63	7.69	6.43	12.62	12.41	23.64	0.00	0.00
Mg	0.26	0.20	0.56	0.51	0.24	0.31	0.00	0.00	0.50	0.76
Al	4.60	3.12	5.84	4.73	4.63	5.39	3.01	3.40	9.40	12.85
Si	21.76	14.18	17.39	13.54	54.92	61.38	35.32	38.31	33.20	43.62
S	0.27	0.16	0.55	0.38	0.61	0.60	2.18	2.07	1.21	1.39
K	1.61	0.75	0.89	0.50	1.75	1.40	1.35	1.05	9.35	8.82
Ca	0.85	0.39	1.71	0.94	1.60	1.25	29.79	22.64	5.86	5.39
Ti	1.46	0.56	0.49	0.22	3.07	2.01	2.11	1.34	3.93	3.03
Fe	18.65	6.11	35.21	13.78	26.74	15.03	13.83	7.54	36.55	24.14
	3283.60m		3283.90m		3285.97		3289.59m		3284.30m	
Element	Weight%	Atomic%	Weight%	Atomic%	Weight%	Atomic%	Weight%	Atomic%	Weight%	Atomic%
C	7.15	15.18	8.47	17.13	6.05	13.65	9.95	18.61	7.36	16.06
O	0.84	1.17	N/A	N/A	0.85	1.27	0.36	0.44	1.45	2.09
Mg	8.93	11.24	10.67	12.79	7.71	10.31	6.88	7.63	10.89	14.08
Al	34.30	41.49	38.11	43.90	27.44	35.24	47.08	50.16	26.69	33.16
Si	0.64	0.68	N/A	N/A	0.74	0.83	5.63	5.25	0.37	0.41
S	0.40	0.39	N/A	N/A	1.20	1.22	N/A	N/A	1.63	1.60
K	1.94	1.69	2.61	2.16	2.24	2.06	7.02	5.37	0.84	0.75
Ca	0.54	0.46	2.55	2.06	0.74	0.67	0.40	0.30	0.30	0.26
Ti	1.70	1.20	1.93	1.30	8.76	6.59	0.93	0.58	0.63	0.46
Fe	43.56	26.50	35.67	20.66	44.27	29.37	21.76	11.66	49.83	31.13

### 6.2.3: SEM results and discussion for A-W1 well

Quartz cement commonly occurs in this well as overgrowths on detrital grains where calcite and quartz cements co-exists, the edges of quartz cement are irregular or angular and overlain by calcite cement (Fig 6.2.3A & E), indicating that calcite cements post dated quartz overgrowths. However, in many cases the edge of quartz overgrowth is euhedral and appears to be in a growth compromised relationship with calcite cement (Figs. 6.1.4A & 6.2.3A). This may suggest that either the calcite or quartz was precipitated contemporaneously or calcite post dated precipitation. In few cases, two phases of quartz overgrowth can be recognized with a dust line between them (Fig. 6.2.3E). A potential source of silicon dioxides for quartz cement within the sandstone is from intergranular pressure dissolution, dissolved and replaced feldspar and transformation of clay minerals (Zhang et al. 2007). Transformation between clay mineral also releases abundant silicon dioxide. The following reaction indicates that transformation of smectite into illite releases silicon dioxide (Rodrigo and Luiz 2002).

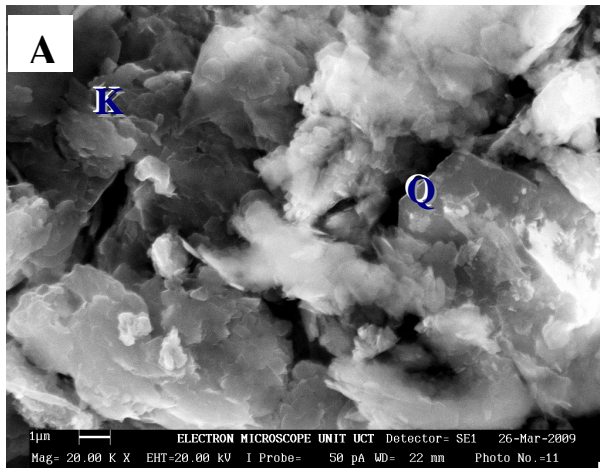


Furthermore, illitization of kaolinite may supply silicon dioxide for mesogenetic quartz precipitation (Rodrigo and Luiz 2002).

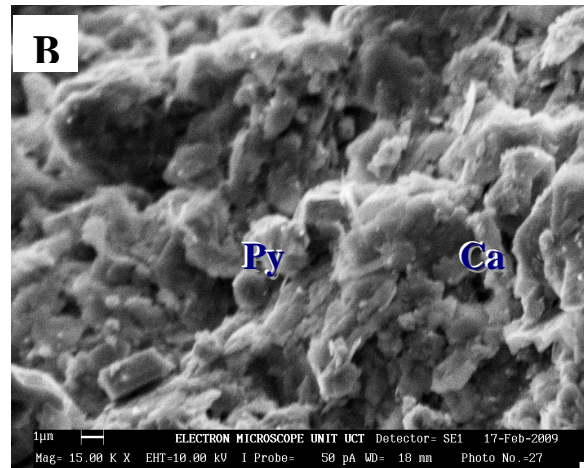


Pyrite is a minor but ubiquitous diagenetic component. Its mineralization in two types of patch was observed in the Albian age sandstone in well A-W1. Its occurrence as disseminated sub-cubic to cenospheric crystal, framboid and closely packed clusters that precipitated within the pore were observed from the SEM images, pyrite in this well displays spherulitic textures of pyrites (Fig. 6.2.3B & F), which requires reducing conditions in relatively dysaerobic environment (Greensmith, 1989). Since pyrite mineralization often takes place along fractures, it may have been precipitated from diagenetic fluids that were passing the fracture system in reducing environment. Table 6.2.2 shows high % of Fe across the samples analyzed which confirm the presence of pyrite within the reservoir unit. Carbonate cement (calcite, ferroan calcite) are wide spread in A-W1 reservoir sands (Figs. 6.2.3B & D). Authigenic calcite (both pore-filling and grain replacing) has the most extensive distribution in some of the samples in A-W1 well.

A-W1: 3450.50m



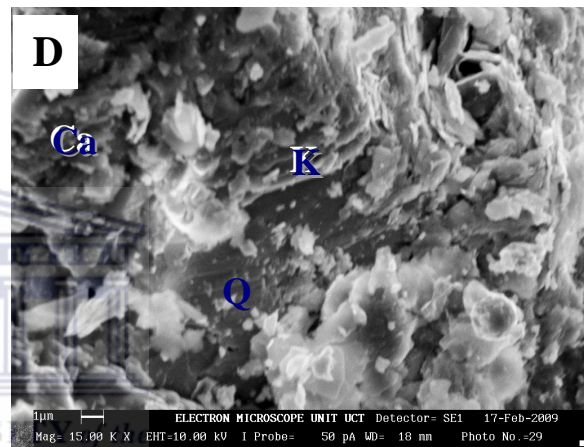
A-W1: 3452.50m



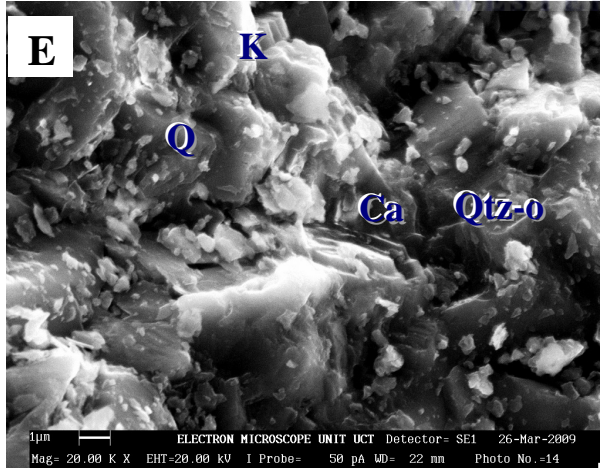
A-W1: 3454.05m



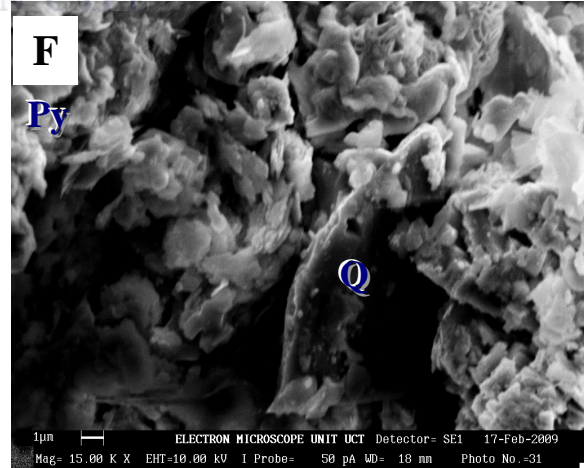
A-W1: 3455.50m



A-W1: 3457.05m



A-W1: 3460.24m

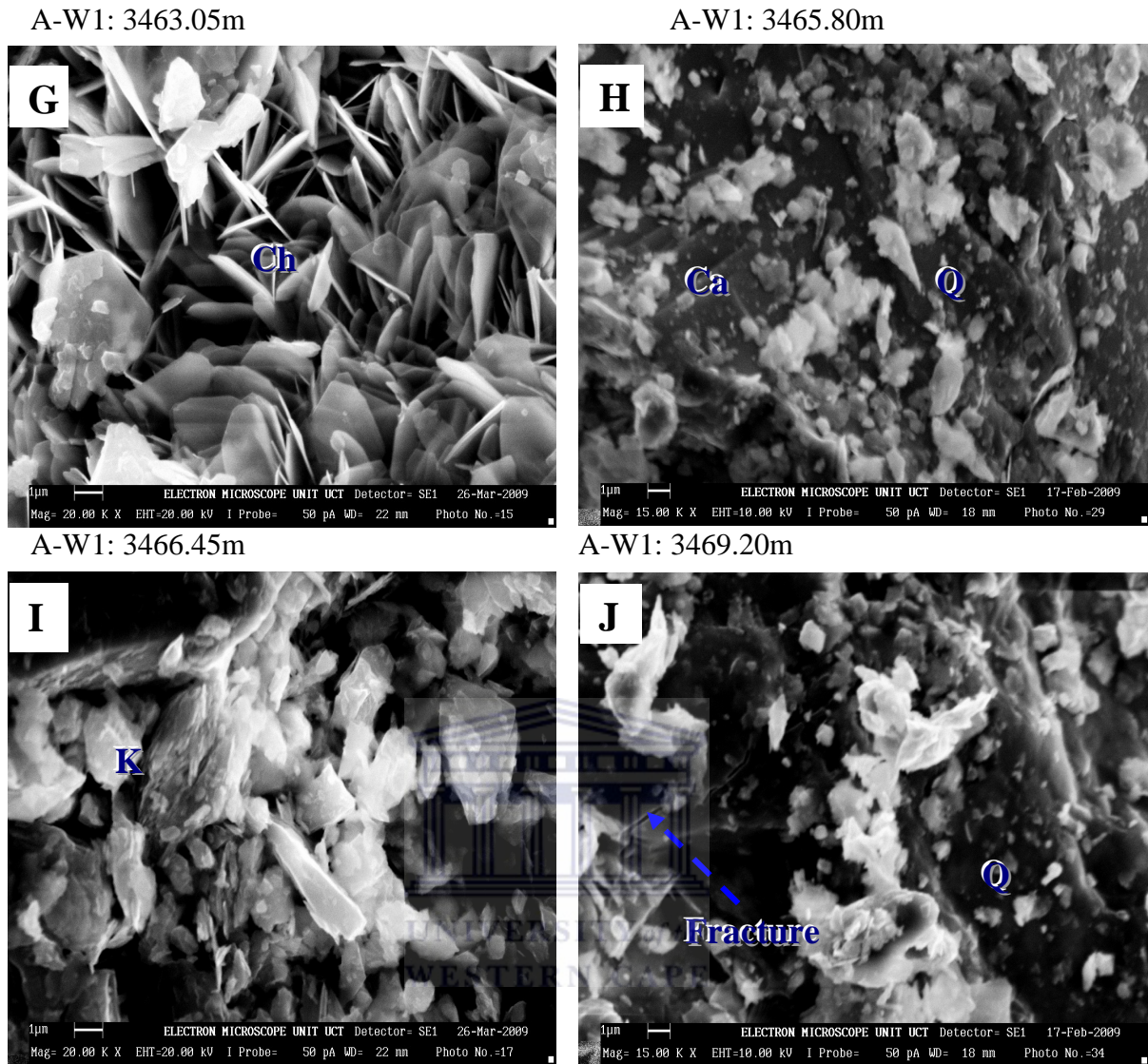


**Figure 6.2.3:** (A) Kaolinite occurring in sheets suggesting mica origin (B) Pore filling calcite, framboid pyrite growing on detrital K-feldspar. (C) Chlorite flakes tangential to each other surrounded by quartz overgrowth. (D) Quartz embedded in poikilotopic calcite cement with traces of kaolinite. (E) Quartz overgrowths engulf, and thus post date K-feldspar overgrowth and traces of kaolinite. (F) Spherulitic texture pyrite blocking voids.

**Note:** M = mica, Ch = chlorite, IL = illite, Q = quartz, K = kaolinite, K-F = K-feldspar, Qtz-o = quartz overgrowth, Py = pyrite, Ca = calcite.

In some samples, porosity is nearly occluded by calcite cement while in most samples calcite cement only partly filled the pore spaces (Fig. 6.2.3F). The observed spread of calcite in some samples was also noted to be accompanied by a very dull imprint (Fig. 6.2.3B) and locally zoned in some samples too (Fig. 6.2.3D). Generally high concentration of Fe as revealed by SEM in this well agrees with the results of the thin section that some of the samples are rich in iron. This enrichment was formed in late diagenetic stage and deeply burial depths (Fig. 6.2.3B & F; depth 3452.50 m & 3457.05 m respectively)

Chlorite was observed in approximately one quarter of the samples examined, where present, it occupies more than 60 % of the total rock volume and typically grows tangentially to the surface of detrital grains (Fig. 6.2.3C) forming a honeycomb type structure. It must have grown shortly after the ferroan poikilotopic calcite precipitation. Feldspar and lithic fragments have been altered during diagenesis, several dissolution textures can be identified due to the grain–contact discussed earlier under thin section, (i) grain-contact dissolution (pressure dissolution) of plagioclase (Fig. 6.1.6K) (ii) replacement of feldspar by carbonates and (iii) the partial to complete dissolution of framework grains. Sutured intergranular quartz and chlorite blade contacts (Fig. 6.2.3C) provide evidence of grain-contact quartz and feldspar dissolution. The timing of these processes is difficult to establish based solely on petrographic evidence. Kaolinite is one of the authigenic clay mineral present in the samples in this well. It occurs as blocky pseudo-hexagonal platelets that vary in size (Fig. 6.2.3A) and verms, likely replacing carbonate cement (Fig. 6.2.3D). Although kaolinite appears similar in morphology to dickites as reported by McAulay et al., 1993 and Ehrenberg et al., 1993, their difference will be distinguished using XRD. Based on SEM observations, it is termed kaolinite as recommended by Ehrenberg et al 1993. Kaolinite also occurs in association with expanded detrital mica (Fig. 6.2.3A). The high amount of  $\text{TiO}_2$  at 3450.50 m, 3452.50 m and 3460.24 m (Table 6.2.2) are 3.16 %, 3.69 % and 3.57 % respectively, this suggest an intergrowth of chlorite in pore space (Ryan and Reynold 1997).



**Figure 6.2.4:** (G) Tangential chlorite blades (H) Calcite cementation (I) shows of Kaolinite (J) fracture within the quartz grains.

**Table 6.2.2:** Energy dispersive spectrometry (EDS) results for A-W1 well.

	3450.50m		3452.50m		3454.05m		3455.50m		3457.05m	
Element	Weight%	Atomic%	Weight%	Atomic%	Weight%	Atomic%	Weight%	Atomic%	Weight%	Atomic%
C	6.82	14.52	45.35	70.43	8.56	17.63	49.69	71.42	9.59	20.37
O	0.65	0.91	5.04	5.87	0.99	1.35	7.63	8.23	0.54	0.76
Mg	9.43	11.90	0.23	0.17	8.10	9.89	0.26	0.19	2.26	2.85
Al	33.14	40.19	3.49	2.41	35.87	42.06	3.95	2.53	28.67	34.68
Si	0.91	0.97	15.78	10.48	0.91	0.94	16.45	10.11	0.13	0.14
S	0.38	0.37	0.59	0.35	2.01	1.87	0.88	0.47	0.37	0.35
K	4.07	3.55	1.03	0.49	1.48	1.25	2.86	1.26	0.31	0.27
Ca	0.36	0.30	0.53	0.25	0.47	0.39	0.53	0.23	21.7	18.39
Ti	3.16	2.25	3.69	1.44	1.22	0.84	1.40	0.50	0.41	0.29
Fe	41.07	25.04	24.28	8.11	40.38	23.81	16.35	5.06	N/A	N/A
	3460.24m		3463.05m		3465.80m		3466.45m		3469.20m	
Element	Weight%	Atomic%	Weight%	Atomic%	Weight%	Atomic%	Weight%	Atomic%	Weight%	Atomic%
C	50.96	74.57	8.51	18.55	28.22	53.99	10.88	20.53	26.91	48.90
O	5.24	5.76	1.27	1.83	5.59	8.03	0.75	0.93	9.13	12.46
Mg	0.18	0.13	10.84	14.03	0.28	0.27	7.47	8.37	0.40	0.36
Al	3.06	1.99	24.09	29.93	3.19	2.72	48.01	51.63	5.86	4.74
Si	14.06	8.80	0.14	0.15	11.93	9.76	0.33	0.31	25.84	20.08
S	0.35	0.19	1.57	1.54	7.88	5.65	0.27	0.23	0.37	0.25
K	0.88	0.39	0.86	0.76	0.88	0.52	1.39	1.07	4.11	2.29
Ca	0.29	0.12	0.70	0.61	10.73	6.15	0.41	0.31	0.71	0.39
Ti	3.57	1.31	0.86	0.63	0.58	0.28	1.53	0.97	1.66	0.76
Fe	21.42	6.74	51.17	31.97	30.71	12.64	28.96	15.66	25.01	9.77

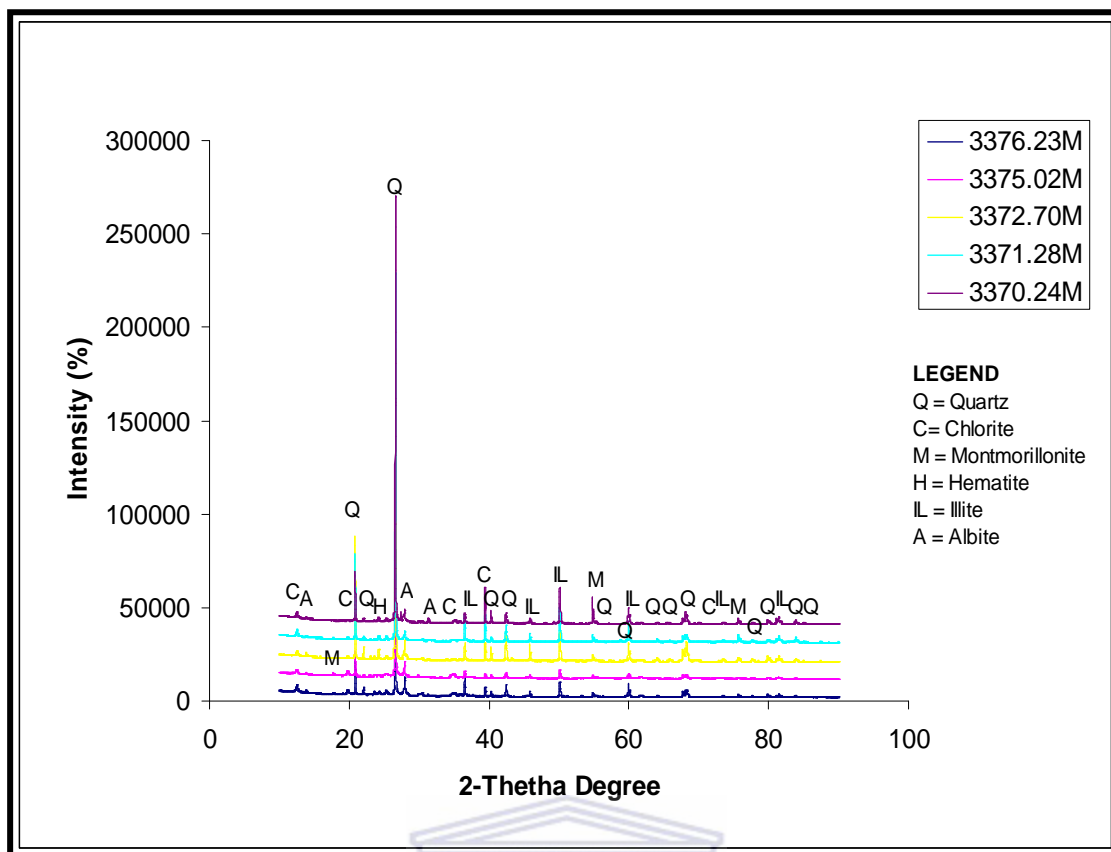


### 6.3 XRD RESULTS

The most effective basis for mineralogical analysis is XRD, which distinguishes minerals from each other based on their atomic or crystal structure rather than their optical properties or chemical composition. This is particularly important for components such as clay minerals which are difficult to identify by any other means (Ward et al. 2005). X-ray diffraction analysis provides relatively precise compositional information, along with phase identification of minerals. Clay analysis is particularly important in determining the proportion of swelling and non-swelling clays which is crucial for potential formation damage.

#### 6.3.0 XRD results of A-G1 well

The results of XRD analysis of the Albian age sandstone samples from well A-G1 show that quartz is the dominant mineral (Fig. 6.3.1) which was found to be present throughout the intervals sampled. The major clay minerals present in the depth intervals in this well are chlorite, illite and montmorillonite. In addition to these minerals, the sands have shown the presence of hematite and albite but not as widespread as other earlier mentioned minerals (Fig. 6.3.1). Generally, authigenic feldspar cement forms in mesogenesis, occurring as overgrowth on feldspar grains (Fig. 6.1.1F) and intergranular pore fill (Zhang et al., 2007). Conditions with sufficient silica, potassium and reasonable pressure and temperature in pore fluid are conducive for generation of albite. Diagenetic albite with typical pure end member composition is common ( $K_{0.2}Na_{0.8}AlSi_3O_8$ ), occurring as a replacement of feldspar and as overgrowth on feldspar grains. Both detrital K-feldspar and plagioclase as observed in the thin section and SEM images of intervals in this well were albitized, with replacement occurring after partial grain dissolution as evident by the variable amount of voids within these grains (Figs. 6.1.1E & 6.2.0A). Figure 6.3.1 shows that both illite and chlorite are dominant clay minerals. A wide range of conditions (e.g. temperature, redox, water composition) in the detrital mineral assemblages can influence the type of clay minerals being supplied to the sediment. From the general paleo-environmental understanding (Worden and Morad 2003), it is presumed that dioctahedral smectite (montmorillonite) as observed within the intervals in this well must have been formed due to diagenetic alteration from its parent mineral (smectite).



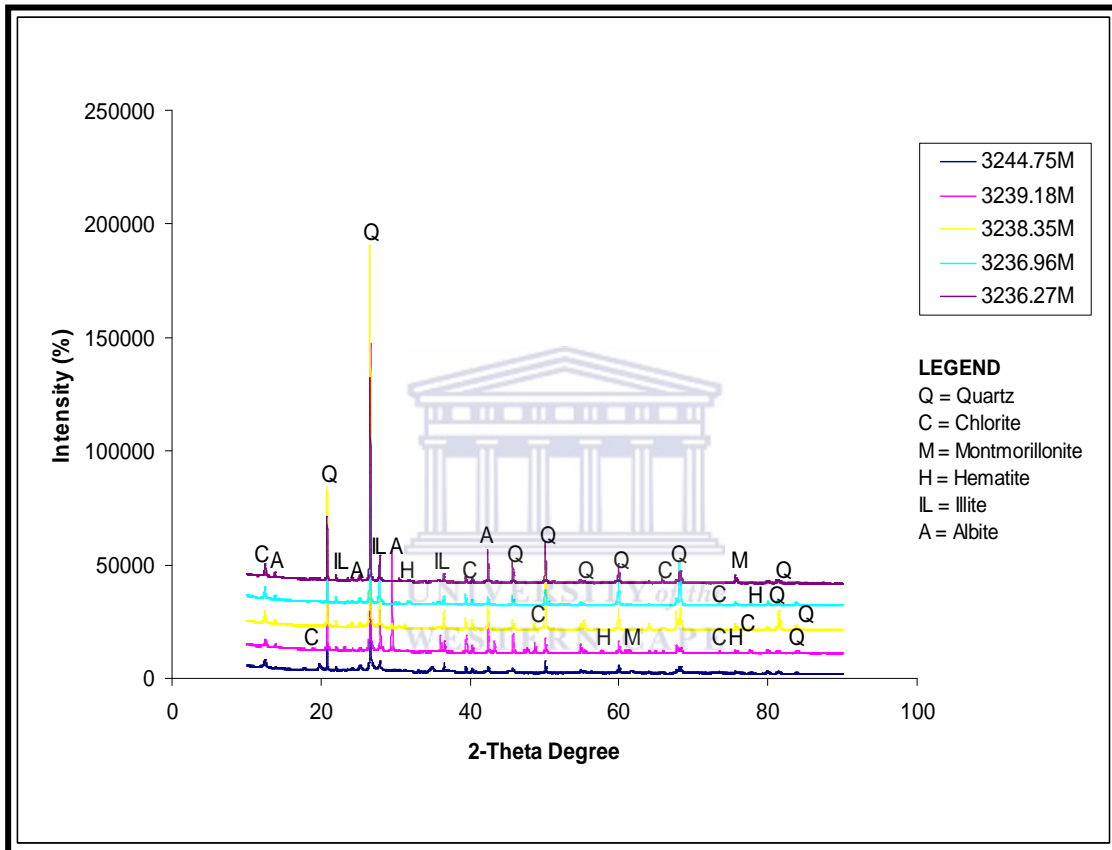
**Figure 6.3.1:** XRD spectra of A-G1 well.

The importance of opaque mineral is often neglected when investigating diagenetic evolution of sediments, opaque detrital minerals such as hematite as revealed in this well though not wide spread across the reservoir zones can often be one of the most insightful minerals to environmental changes. The presence of hematite ( $\text{Fe}_2\text{O}_3$ ) is an indicator of redox conditions during alteration. Hematite usually occurs as hexagonal or pseudo-hexagonal platy crystals (Schwertmann and Taylor, 1989).

### 6.3.1 XRD results of A-K1 well

The minerals in both core 1 and core 2 of A-K1 well are dominated by quartz (Figs. 6.3.2 & 6.3.3), which was found to be present throughout the intervals sampled for the study. Montmorillonite was identified only in few sampled depths (Fig. 6.3.2, depth 3239.18m & 3236.27m). In many geologic systems, mobilization and precipitation of iron oxides and sulphides (Figs. 6.2.2I & 6.3.2) requires specific variation in fluid chemistry (Taylor, 1999). Iron is likely sourced internally from hematite coating. Near surface meteoric water and processes of weathering commonly distribute disseminated iron films that acted as the element causing alteration within the calcite cement as revealed by thin section and core 2 peaks identification. The disseminated iron oxide are commonly mobilized and removed by reducing fluid,

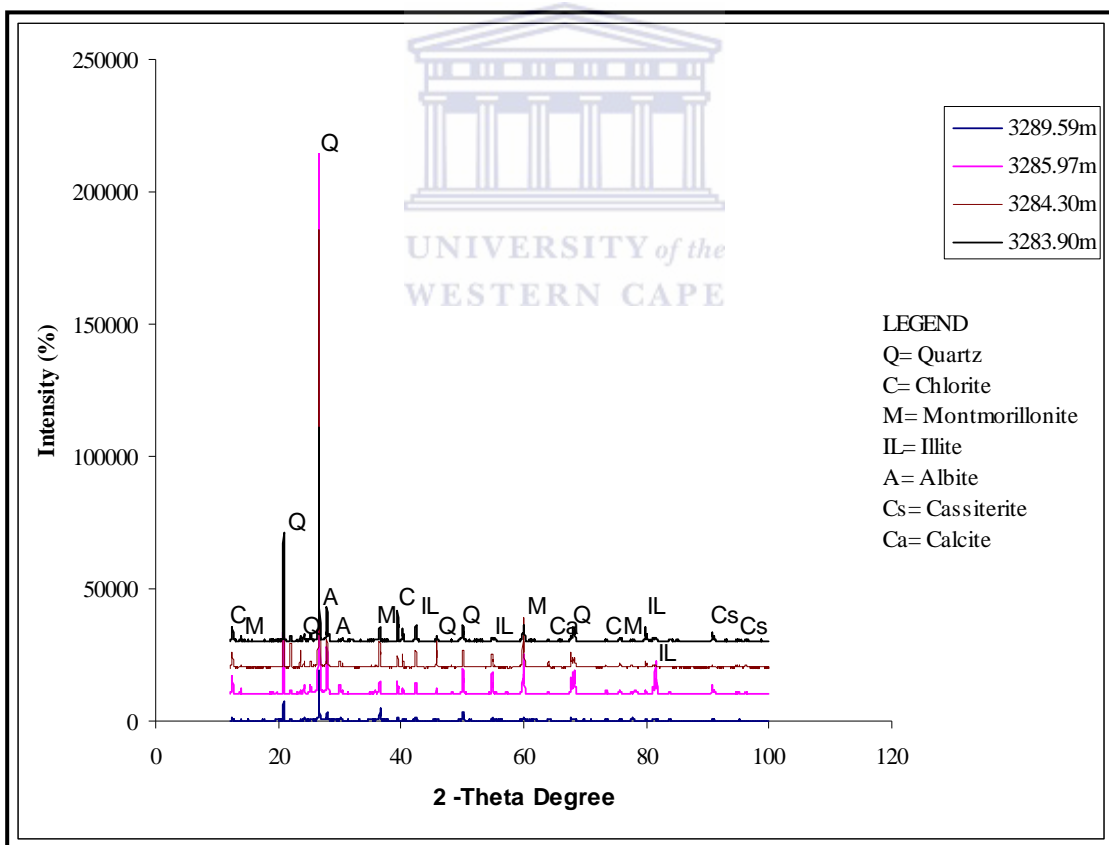
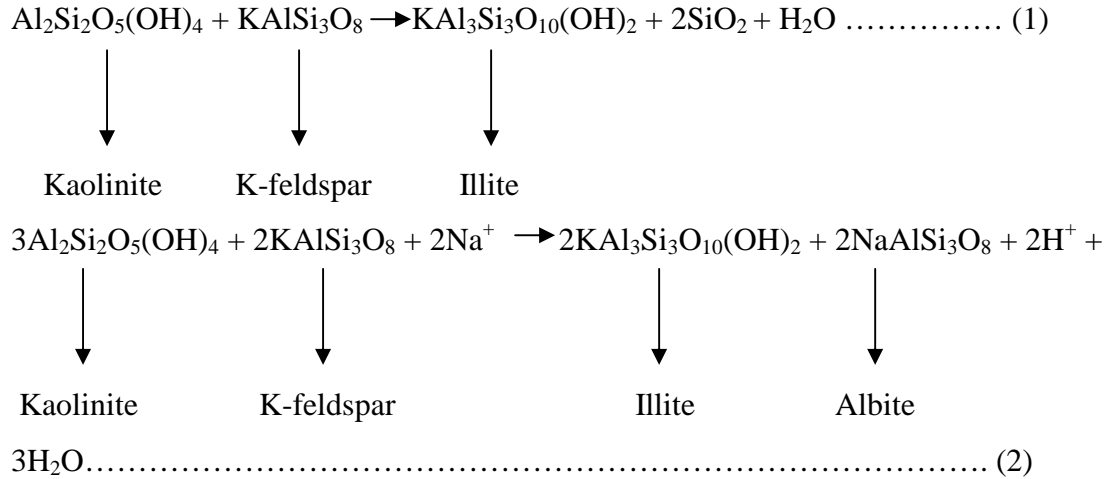
when these fluids mix with oxidizing species in groundwater in the well (concentrated hematite precipitates, the presence of hematite ± other iron oxide minerals) records evidence of past fluid flow and reactions in subsurface sedimentary rock. These are probably products of low temperature, near surface, hydrologic chemical diagenetic reactions (Weibel, 2004). The instability of hematite as revealed from both cores spectra indicates reducing acid-neutral conditions (Garrels and Christ 1965, Adams et al., 1974).



**Figure 6.3.2:** XRD spectras of A-K1 Core 1.

Montmorillonite is a very soft phyllosilicate group which belongs to smectite family. It typically forms microscopic or at least small platy micaceous crystal as revealed by thin section results (Figs. 6.1.2B & 6.1.3C). The reactions that formed this mineral are undoubtedly complex, but hydration and alteration of partially and completely devitrified lithic fragments in the original materials (feldspar) must have played an important role in its formation. However, experimental work by Hemley (1962) indicates that low temperature feldspar alters to phyllosilicates; the reaction is controlled by temperature, pressure and the alkali ion/H<sup>+</sup> ratio of the solutions and is favoured by high pH. Having observed the presence kaolinite and K-feldspar in the SEM images (Figs. 6.2.1B & D), it is therefore predicted that the illite and albite

could be formed based on the understanding of the reactions below. Utilizing the principle of aluminium conservation, the illitization of kaolinite may take place through two different overall reactions (Bjørlykke, 1995):



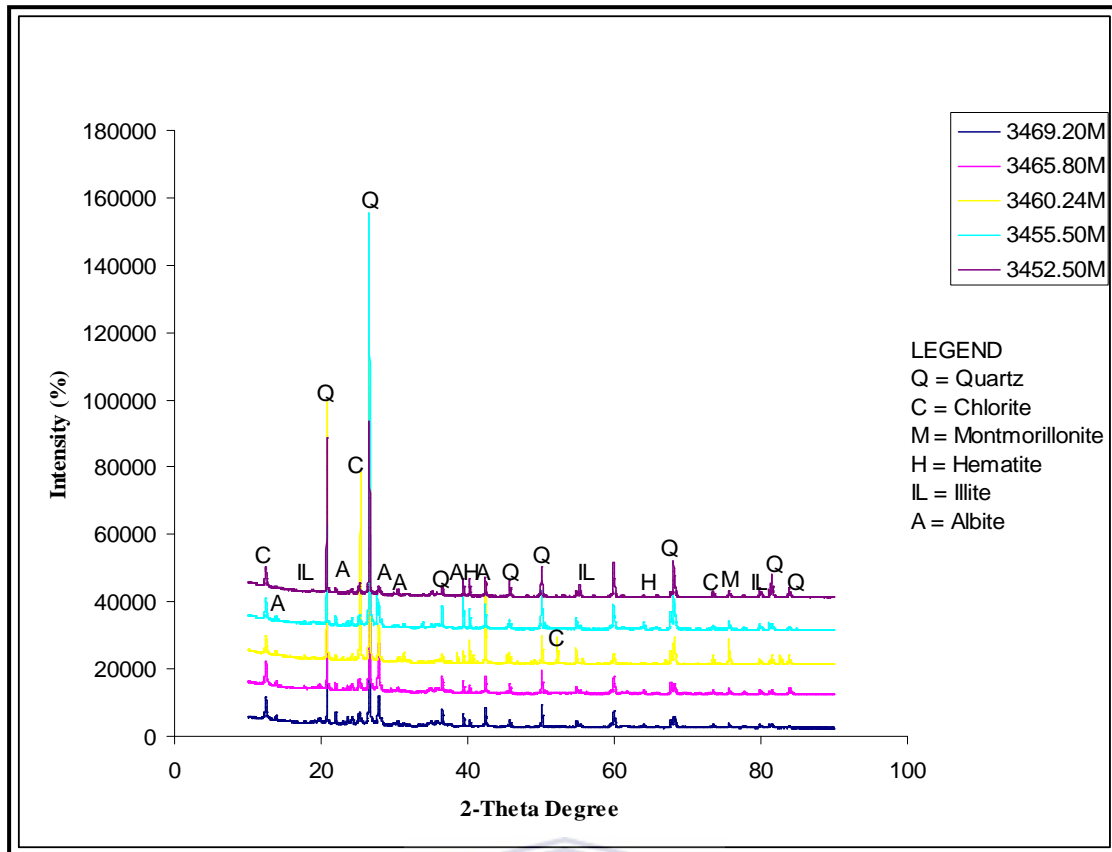
**Figure 6.3.3:** XRD spectras of A-K1 Core 2

The presence of illite (Fig. 6.3.3) could be attributed to the dissolution of feldspar and kaolinite releasing aluminum and hereby precipitating in illite, often replacing kaolinite and leaving secondary pore after K-feldspar. However, if the pore water is supersaturated with respect to albite, reaction (2) may take place. Albite as observed

in Figure 6.3.2 & 6.3.3 is likely from pseudomorphic replacement of K-feldspar with albite and little secondary porosity could be developed (Saigal et al., 1992). In this case, excess release of silica is unlikely reaction (1) which implies that aluminium is transported (by diffusion) from the dissolving K-feldspar to the site of illite growth. If illite grows primarily on dissolving kaolinite, the distance from the K-feldspar (Fig. 6.2.1B) grains to the kaolinite minerals (Figs. 6.2.1D & F) may be important in determining whether K-feldspar is dissolved or albitized. K-feldspar and albite is also extremely pure end member of alkali and plagioclase feldspar. They are frequent as an early diagenetic mineral and predate tectonic deformation, their occurrence is not likely related to hydrothermal activity, and they form almost exclusively as overgrowths on detrital feldspar grains. The geologic conditions that seem to be necessary are moderately elevated temperatures, a source of silica, either from skeletal parts of organisms or hydrolyzing silicates and abundant Na<sup>+</sup> and/or K<sup>+</sup> ions that come from pore waters (Francis et al. 1972).

### 6.3.2 XRD for A-W1 well

Quartz is the dominant mineral in all the samples analysed in this well. The occurrence of plagioclase feldspar as discussed in thin section likely represent feldspar association with volcanic and metamorphic lithic fragments having albite (Fig. 6.3.4) as pure end member. High temperature grain coating albite cement is seldom reported in the literature although the occurrence of high temperature albitization of detrital K-feldspar and plagioclase has been well documented (Ramseyer et al., 1993). Albite is relatively common in reservoir sands, it has been suggested that in reservoirs, most chemical compaction occurs at micaceous clay-quartz intergranular contacts (BjØrkum, 1996). As quartz cementation is the main sink of dissolved silica, chemical compaction cannot usually occur until ~90°C. The samples examined in this well showed evidence of both grain-contact quartz and plagioclase dissolution (Figs. 6.1.4C & 6.1.6K). The dissolution of Ca-rich plagioclase and the precipitation of albite can consume dissolved silica and may provide a mechanism to allow grain contact quartz dissolution to occur at temperature lower than 90°C (Schmid, 2003).



**Figure 6.3.4:** XRD spectras of A-W1 well.

The origin of albite cannot be uniquely defined although the abundance of detrital plagioclase and the occurrence of irregular, microstylolite contacts (pressure dissolution feature in layered reservoir, often a vertical permeability barrier) between plagioclase grains strongly suggest that albite is locally sourced.

Hematite occurrence as revealed in figure 6.3.4 is more pronounced in A-W1 well unlike the earlier discussed wells. Early diagenesis includes all the processes that occur at or near the surface of the sediments where the chemistry of the interstitial waters is controlled mainly by the depositional environment (Choquette & Pray 1970). This is the regime where the influence of original depositional pore water dominates and so includes soil development in continental depositional settings; hematite might have been formed from the oxidation of ferrous ion released by dissolution of unstable ferromagnesian minerals during early burial (Weibel, 2004).

The little occurrence of montmorillonite in the depth intervals of A-W1 well (Fig. 6.3.4) could be as a result of post-depositional transformation of this clay mineral to illite which is suggested to be a possible of source of silica cement (Kenneth, 1962) as revealed by thin section study (Figs. 6.1.4 & 6.1.6). Depth of burial appears to be important factor in effecting this change, the changes in mineralogy indicates that silicon should be released to the general geologic environment (Kenneth, 1962).

## 6.4 FTIR Results

FTIR spectroscopy relies on detection of vibrational modes, i.e. lattice vibrations and/or molecular group vibrational modes. Mineral identification is possible because minerals have characteristic absorption bands in the range of the infrared (4000 to 400  $\text{cm}^{-1}$ ). The vibrational spectrum of a molecule is considered to be a unique physical property and is a characteristic of the molecule (Coates, 2000). As such, the infrared spectrum can be used as a fingerprint for identification by the comparison of the spectrum from an unknown with previously recorded reference spectra (Fig. 6.4).

The results are presented in Tables 6.4.1 & 6.4.2 A & B respectively while Figure 6.4, 6.4.1 & 6.4.2 represents the spectra of depth intervals in each studied wells. The band parameters were closely observed and interpreted below as the functional group identification (alkanes, alkenes and alkynes) and also for silicate/carbonate minerals as explained by Farmer (1974) in comparison with published spectra in other literature (Table 6.4). Below are the key extract from the above mentioned literature for the mineral identification:

**Table 6.4:** Key peaks used in identifying clay minerals in FTIR.

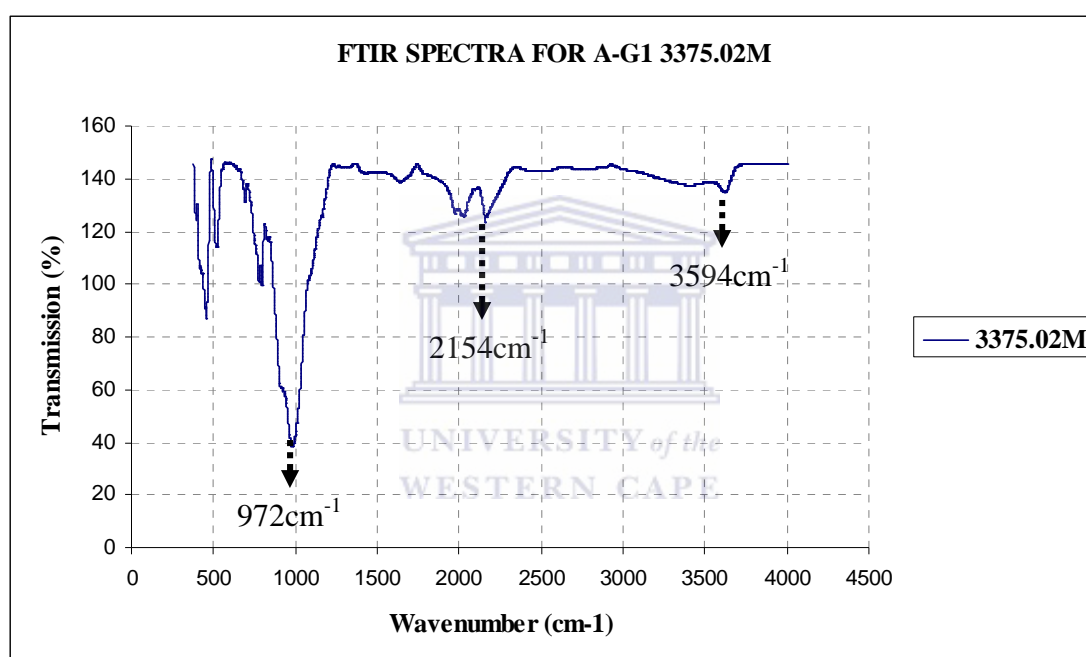
Clay Mineral	Peak Position ( $\text{cm}^{-1}$ )
Kaolinite	3697, 3669, 3652, 3620, 1036, 1016, 912, 540.
Illite	3620, 916, 831, 659, 527.
Smectite	3620, 1088, 1008, 916, 796, 525, 467.
Chlorite	3563, 3432, 1082, 668, 520, 431.
Illite-Smectite	1031, 840, 755, 524, 469.
Chlorite-Smectite	3676, 3567, 1088, 669, 463.
Allophane	3530, 3420, 971, 962, 874, 793, 668, 581, 509, 428.
Gibbsite	3620, 3463, 581, 505, 448.
Quartz	798, 779.

(Russell et al., 1981; Wilson, 1994; Madejová and Komadel, 2001; Ohashi et al., 2002; Post and Borer, 2002; Pironon et al., 2003; Certini et al., 2006).

### 6.4.1 FT-IR results of A-G1 well

Infrared spectroscopic data can be used to predict the presence of hydrocarbon and well minerals in reservoir sandstone wells. The reservoir sandstone of A-G1 well does not show any evidence of alkanes group with reference to published chart

(Appendix I). However, terminal Alkyne ( $\equiv\text{C-H}$ ) can be found at band  $3339\text{cm}^{-1}$  –  $3338\text{cm}^{-1}$  (Table 6.1) Notable depths are 3375.02m and 3376.20m containing bands wavenumber of  $3592\text{cm}^{-1}$  and  $3601\text{cm}^{-1}$  respectively which can be attributed to the O-H (free) bond. Mineral identification of the obtained bands with reference to the table 6.4 reveals the presence of kaolinite ( $3601\text{cm}^{-1}$ ,  $510\text{cm}^{-1}$ ), Allophane ( $509\text{cm}^{-1}$ ), illite ( $647\text{cm}^{-1}$ ,  $969\text{cm}^{-1}$ ), smectite ( $771\text{cm}^{-1}$ ), chlorite ( $681\text{cm}^{-1}$ ,  $689\text{cm}^{-1}$ ), illite smectite ( $519\text{cm}^{-1}$ ), gibbsite ( $444\text{cm}^{-1}$ ,  $448\text{cm}^{-1}$ ) and quartz ( $775\text{cm}^{-1}$ ,  $771\text{cm}^{-1}$ ). The presence of these bands suggests the presence of clay minerals discussed earlier from the petrographic results of A-G1 well. A representative of the FTIR spectra is presented in figure 6.4.



**Figure 6.4:** Representative FTIR spectra of A-G1 well

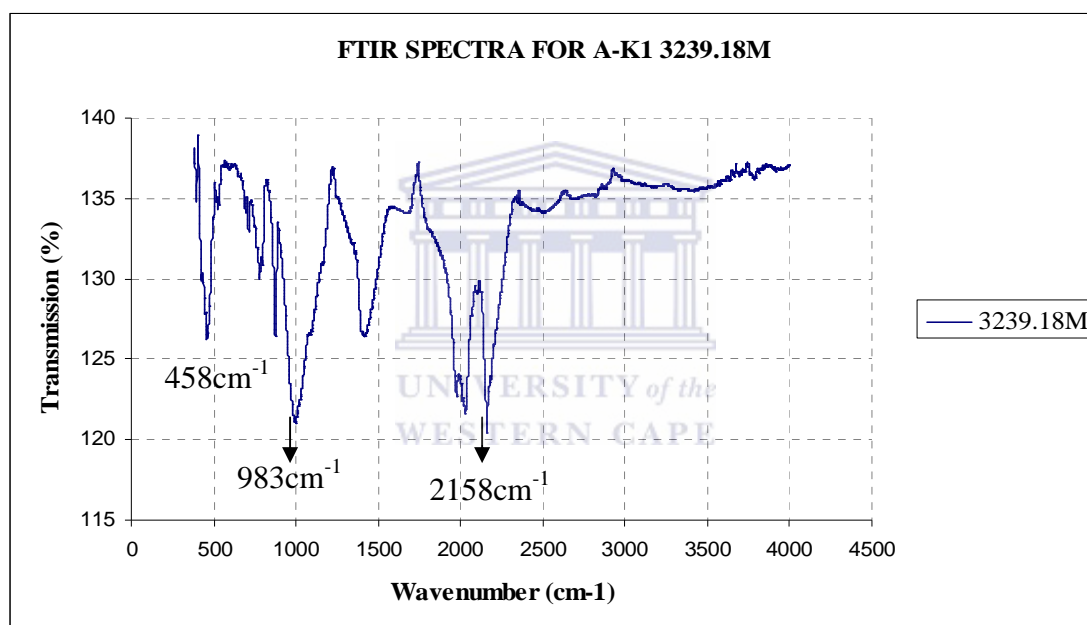
The bands at  $967\text{--}975\text{cm}^{-1}$  is probably from glassy aluminosilicate phase, which contains basic cations as modifiers (Mollah, 1999). The bands around wavenumber  $491\text{cm}^{-1}$  are attributed to the O-Si-O bending vibration (Farmer, 1988) and in case of tecto-silicates such as quartz e.t.c. The bands from  $2002\text{cm}^{-1}$  -  $2154\text{cm}^{-1}$  (Table 6.4.2) are attributed to carbonate phase which contains basic cations (calcitic minerals).

#### 6.4.2 FT-IR results of A-K1 well

The FT-IR data obtained from the core samples along the depths are presented in Table 6.4.1. The FTIR analysis that was performed on the various samples was stirred by the previous XRD results which indicate the presence of clay minerals. The samples from both core 1 ( $3236.0\text{m}$  –  $3245.75\text{m}$ ) and core 2 ( $32883.60$  –  $3283.90\text{m}$ )



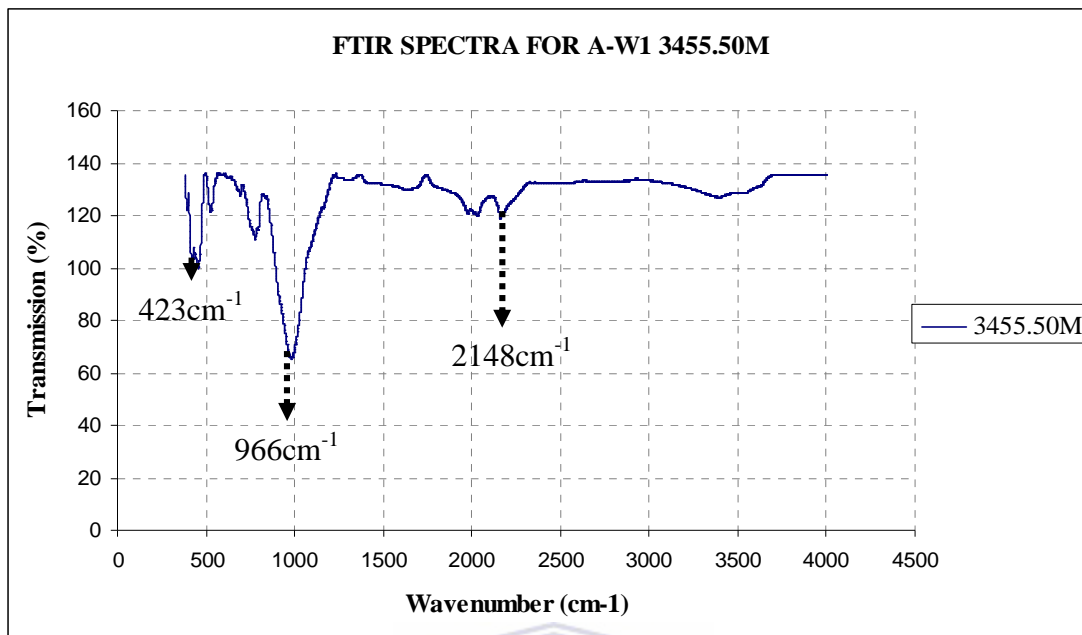
showed absorption frequencies that are diagnostic of some functional groups e.g.  $2843\text{cm}^{-1}$  (Appendix I) belongs to the saturated alkane group with C-H bond, also noted was the O-H bond with a diagnostic wavenumber of  $3320\text{cm}^{-1}$ ,  $3339\text{cm}^{-1}$  and  $3407\text{cm}^{-1}$ . Diagnostic peaks for chlorite were observed at  $433\text{cm}^{-1}$ ,  $521\text{cm}^{-1}$ ,  $668\text{cm}^{-1}$ ,  $3524\text{cm}^{-1}$ . Quartz is present with at  $770\text{-}776\text{cm}^{-1}$  and illite is identified with the peak at  $521\text{cm}^{-1}$  and  $523\text{cm}^{-1}$ . The interstratified illite smectite component of the sandstone was more easily identified in FTIR than XRD with a strong peak present at  $759\text{cm}^{-1}$ . The bands at  $\sim 3695\text{cm}^{-1}$  and  $917\text{cm}^{-1}$  suggests the presence of kaolinite (Breen et al., 2007) nevertheless; Farmer, (1974) confirms the identification of kaolinite at  $\sim 3755\text{cm}^{-1}$  as uniquely distinctive which can be seen at depth 3239.18m. A representative of the FTIR spectra is presented in figure 6.4.1.



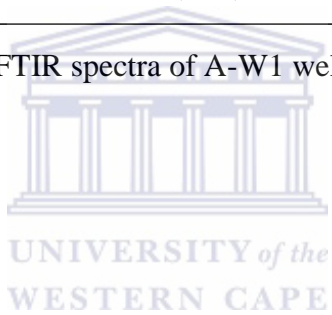
**Figure 6.4.1:** Representative FTIR spectra of A-K1 well.

### 6.4.3 FT-IR results of A-W1 well

Infrared spectroscopic data for A-W1 well could be used to identify the presence of the minerals. A-W1 well samples did show evidence of alkanes group with reference to published chart (Appendix I). Diagnostic peaks for chlorite and illite were observed at  $3436\text{cm}^{-1}$  and  $657\text{cm}^{-1}$  respectively, this is justified by the presence of chlorite and illite in earlier discussed petrography. The presence of a strong band at around  $3592\text{cm}^{-1}$  (Table 6.4.1) together with the O-H band (Appendix I) is consistent as being Muscovite (Farmer, 1974).



**Figure 6.4.2:** Representative FTIR spectra of A-W1 well.



**Table 6.4.1:** showing the wave numbers ( $\text{cm}^{-1}$ ) of different minerals in the studied well.

Depth (m) FTIR band position of well A-G1 ( $\text{cm}^{-1}$ )														A	
3370.24	384	647	734	964	1959	2008	2153	3844	Na	Na	Na	Na			
3371.28	448	491	681	768	970	1968	1988	2154	3388	Na	Na	Na			
3372.7	444	491	689	762	975	1648	1962	2008	2153	3388	Na	Na			
3375.02	448	510	689	775	967	1390	1609	1961	2002	2152	3592	Na			
3376.2	392	416	445	516	687	771	969	1962	2002	2154	3339	3601			
Depth (m) FTIR band position of well A-K1 ( $\text{cm}^{-1}$ )														B	
3236.27	420	443	521	668	757	959	1966	2002	2149	3339	3368	3524	Na	Na	Na
3236.96	422	462	523	690	772	973	1392	1619	1973	2008	2159	2464	3320	3825	Na
3238.35	442	491	684	759	965	1968	2000	2156	3475	Na	Na	Na	Na	Na	Na
3239.18	457	501	711	776	871	983	1396	1972	2023	2158	2455	2785	2843	3407	3755
3244.75	443	472	690	771	963	1390	1619	1962	2003	2154	3320	3592	Na	Na	Na
3283.60	419	491	749	956	1619	1968	2149	3339	3883	Na	Na	Na	Na	Na	Na
3283.90	414	433	511	736	957	1619	1964	2008	2148	3310	Na	Na	Na	Na	Na
3284.30	417	508	738	953	1382	1601	1966	1988	2148	3329	Na	Na	Na	Na	Na
3285.97	420	501	674	757	958	1956	2008	2145	3349	Na	Na	Na	Na	Na	Na
3289.59	450	512	686	770	966	1597	1963	1988	5154	3339	3592	Na	Na	Na	Na
Depth (m) FTIR band position of well A-W1 ( $\text{cm}^{-1}$ )														C	
3450.50	420	746	960	1648	1960	1988	2152	3339	Na	Na	Na	Na	Na	Na	Na
3450.50	418	491	764	952	1599	1968	1978	2149	3339	Na	Na	Na	Na	Na	Na
3454.05	423	523	679	759	957	1621	1974	2010	2157	2474	2843	3349	3710	3835	Na
3455.50	445	516	673	762	966	1602	1962	1994	2150	3329	3519	Na	Na	Na	Na
3457.05	447	488	709	764	869	969	1388	1765	2066	2309	2727	3436	Na	Na	Na
3460.24	420	489	638	738	959	1962	1998	2153	3339	Na	Na	Na	Na	Na	Na
3463.05	417	491	657	752	952	1395	1959	2008	2152	3339	3767	Na	Na	Na	Na
3465.80	454	593	671	773	976	1396	1599	1974	2012	2156	2464	2785	3358	3504	3874
3466.45	442	515	690	765	968	1954	1998	2146	3388	Na	Na	Na	Na	Na	Na
3469.20	422	516	689	771	966	1988	2154	3349	3592	Na	Na	Na	Na	Na	Na

## **6.5 HIGH RESOLUTION TRANSMISSION ELECTRON MICROSCOPY**

High resolution transmission electron microscopy (HRTEM) has been widely and effectively used to determine crystal structure and lattice imperfections in various kinds of advance materials on an atomic scale. However, few published articles are available (Baronnet, 2003, Beaufort, 1997, Billault, 2003) using this powerful tool to unravel the complexities of authigenic clays. Few samples were selected from each well for analysis based on the petrographic results obtained from methods earlier used. Due to its high resolution, it is an invaluable tool to study nanoscale properties of crystalline materials.

### **6.5.1 HR-TEM Results of A-G1 Well Reservoir Zone**

Authigenic kaolins are with illitic minerals, one of the most common clay minerals encountered within the sandstone reservoirs. In this study, the term kaolin refers broadly to the different minerals of kaolin group (i.e. kaolinite, dickite and nacrite). However, at present, the origin and petrogenetic significance of these kaolin minerals are not clearly understood and are still debated in petroleum exploration. High resolution transmission electron microscopy study (HR-TEM) shows the occurrence of clay minerals like kaolinite, chlorite and illite in well A-G1 (Fig. 6.5.1). In sandstone, diagenetic kaolins usually crystallize in two distinct sites (Beaufort, 1997). These kaolins are characterized by a range of size and morphologies which are described below. In diagenetic sandstones, the dissolution of feldspar increases with increasing burial depth leading to progressive replacement of feldspar by secondary pores (Beaufort, 1997). The morphological characters of kaolin investigated in this work shows that the pseudo hexagonal morphology of kaolinite as observed in Figure 6.5.1a at a nanometric scale predominate over coarser crystals with vermiform habit as observed in SEM (Fig. 6.2.0).

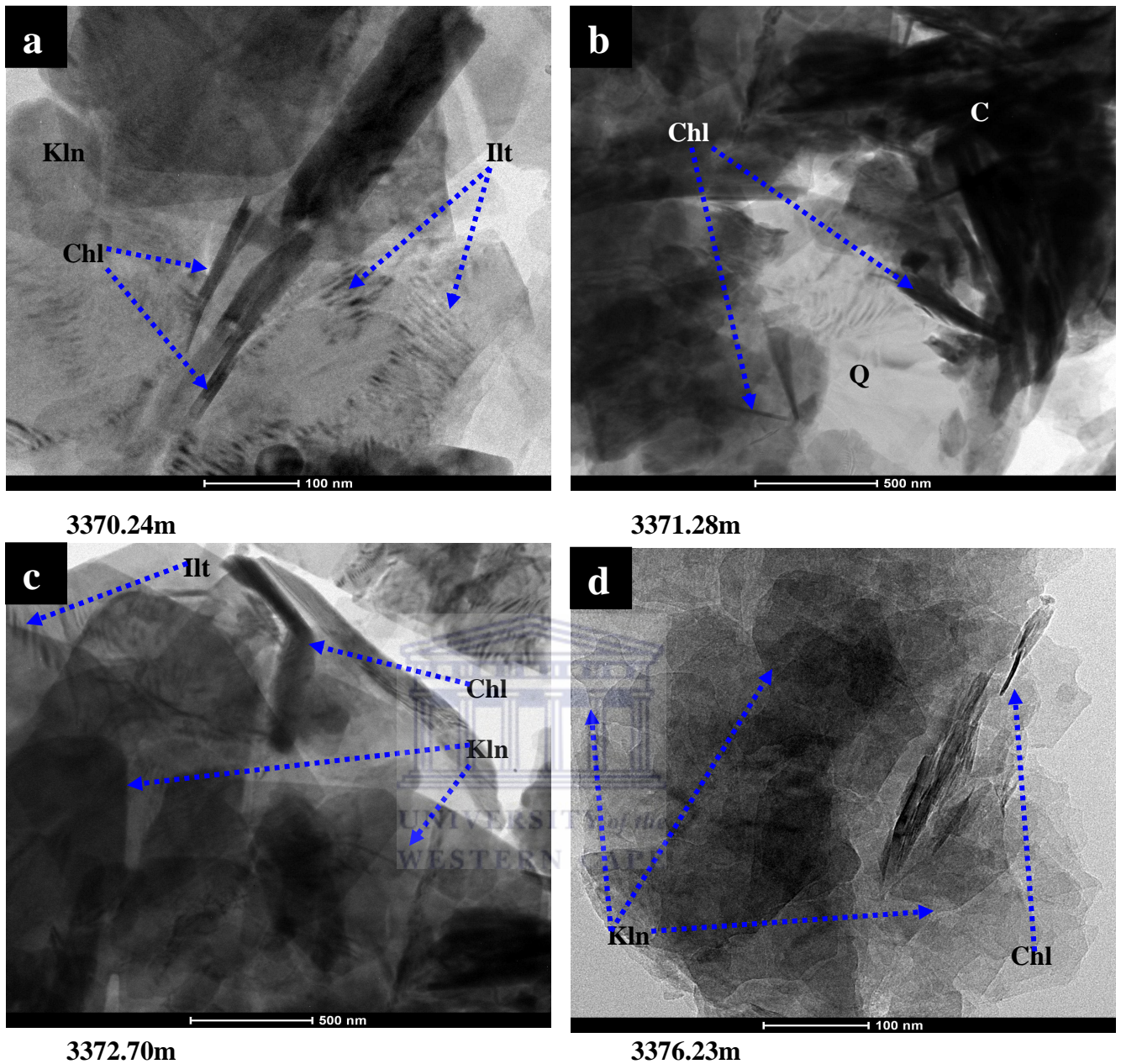
The non-linear variation in the concentration of Fe and Al (Table 6.5.1) shows that the occurrence of kaolinite might be from different origins. The low percentage of Al at depth 3370.24m (Table 6.5.1) suggests that Al silicate released by the alteration of feldspar contributed to the growth process of authigenic kaolinite while the varying euhedral shapes of kaolinite might not result from detrital sedimentation stage (Beaufort, 1997) but from authigenic crystallization during burial. This does not mean that kaolinite was not present in the previous detrital assemblages but only implies that this is sedimentary kaolinite, if any recrystallized during the diagenetic processes. Less frequently, diagenetic kaolinite also crystallizes as an alteration product of

detrital micas (biotite and muscovite). In these cases, it is noteworthy that the size and morphology of this kaolinite are strongly influenced by initial shapes of the mica as observed in the thin section photomicrograph (Fig. 6.1.1A & C) which have been partially or completely replaced during diagenesis (pseudo-morphs of micas). Some samples of Albian sandstone investigated in this well contain illite spatially associated with kaolinite (Fig. 6.5.1c) in primary pores. In detailed petrographic and crystallographic study, Lanson et al. (1996) established that crystallization of illite postdates that of kaolinite. The HR-TEM analysis of A-G1 sandstone was focused on kaolinite formed in pores because they constitute the bulk of kaolin materials as observed in figure 6.5.1, and also because of their authigenic occurrence in pore space, they are very suitable for coupled textural and crystal-chemical investigations.

Contrary to the commonly held view of titanium immobility (Hayes et al., 1996), there are abundant evidences in siliciclastic sedimentary rocks for dissolution of titanium-bearing phases, and the mobility and precipitation of titanium (Parnell, 2004). The alteration of detrital micas to titanium oxides, the precipitation of titanium oxides in altered feldspars, the precipitation of authigenic sphenes and rutile cements in sandstones has been recorded in rocks from Archean to Cenozoic age by Ixer et al., (1979), Saager and Stupp (1983), Smith (1984), Morton (1984) Morad (1988) and van Panhuys-Sigler and Trewin, 1990 which account for the anomalous presence and decreasing concentration of Ti as observed in table 6.5.1 (depth 3370.24 m). The non-linear trend of titanium could also be attributed to its association with carbonate ions or organic ligands (Hayes et al. 1996).

**Table 6.5.1:** HR-TEM/EDS data of A-G1 well sandstone samples.

A-G1 Well			
A	3370.24m	3371.28m	3376.23m
Elements	Weight (%)	Weight (%)	Weight (%)
C	5.43	5.08	18.20
O	27.59	41.93	44.38
Na	0.00	0.00	0.00
Mg	0.52	2.54	1.35
Al	3.11	12.70	12.35
Si	2.88	14.92	20.51
K	0.00	0.69	0.55
Ti	55.96	0.15	0.00
Fe	4.48	21.96	2.61



**Figure 6.5.1:** HRTEM observation at a nanometric scale from selected reservoir sandstones of A-G1 well. (a) Lattice fringe images showing packets of illite (Ilt) layers interstratified with chlorite sticks. (b) Detrital quartz substratum (Q) carpeting by chlorite grain (C) coating. (c) Stratified layers of illite (Ilt) with enlarged sticks of chlorite (Chl). (d) Photomicrograph of kaolins buried at 3376.23m showing the typical pseudo hexagonal morphology of kaolinite.

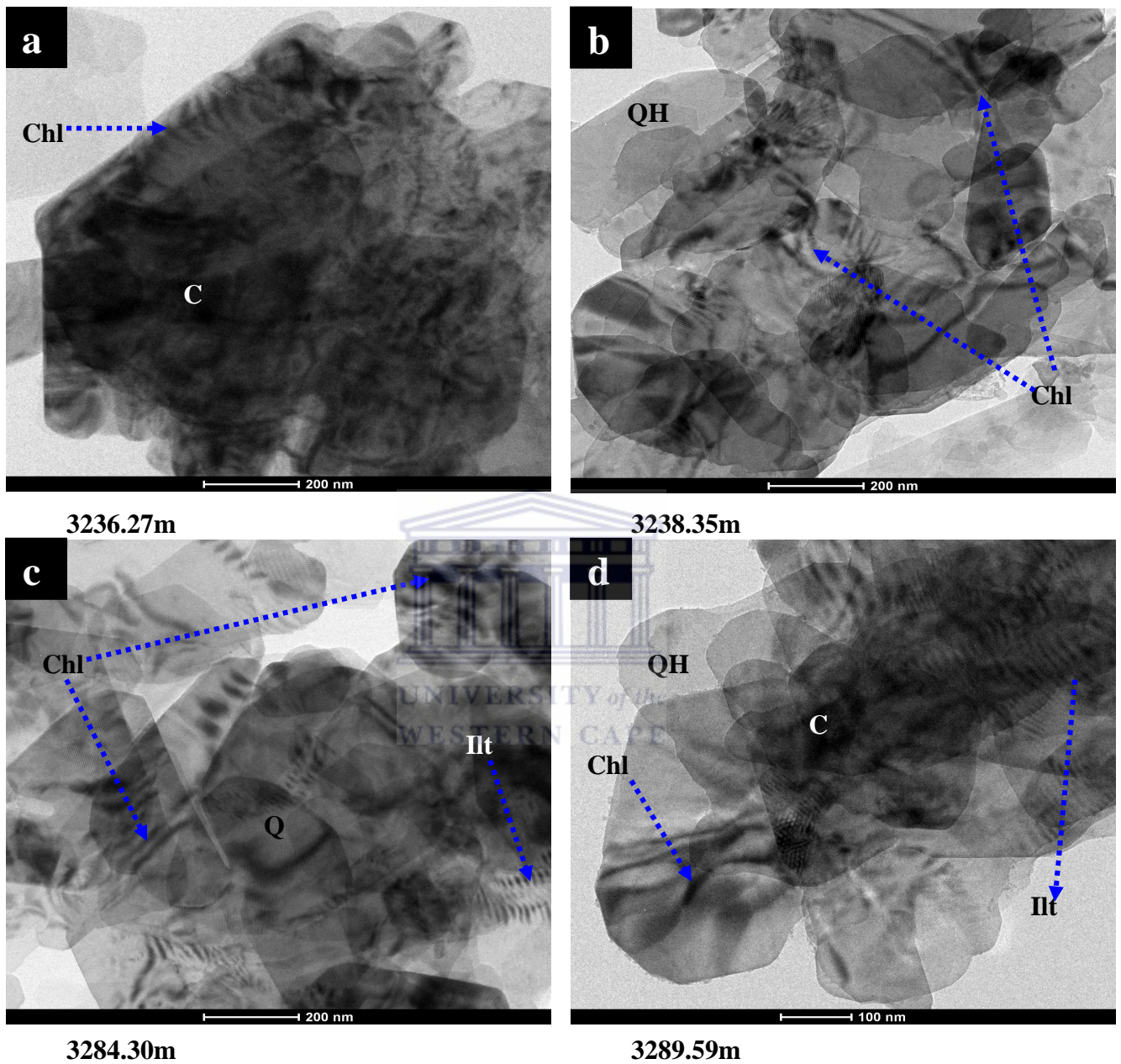
## 6.5.2 HR-TEM Results of A-K1 Well Reservoir Zone

Authigenic chlorites are well known for their major influence on the reservoir quality of deeply buried sandstones. Numerous published works have shown that diagenetic chlorites, most often the Fe-rich varieties, tend to inhibit the formation of quartz overgrowths in the primary pores of sandstones. (Pittman & Lumsden, 1968; Dutton, 1977; Thomson, 1979; Tillman & Almon, 1979; Larese et al., 1984; Dixon et al., 1989) and consequently have a determinant role in the preservation of unusually high primary intergranular porosity in deeply buried reservoirs (Ehrenberg, 1993). The mechanism by which chlorite contributes to the preservation of porosity are still being debated despite the establishment of the relationship between the occurrence of chlorite and the preservation of porosity in a deeply buried sandstone reservoir.

Observation from SEM photomicrograph showed that, in most of the samples from A-K1 well, chlorite coating carpet the clastic minerals. The fact that, in certain places, chlorite rims form hollow structure (Fig. 6.2.2) which outline the original grain boundary of dissolved grain feldspar, this indicates early origin of the chloritization process. The TEM observation indicates that in A-K1 well, the chlorite which constitute some packets with orientation tangential to oblique with reference to edge of detrital quartz (Q) in figure 6.5.2C. The size and width of chlorite packets range from 100 and 500 nm and between 10 and 20 nm respectively. A TEM observation of the cross-section through the detrital quartz substratum (Q) and its overlying chlorite grain coating in A-K1 sandstone is presented in figure 6.5.2C. This image does not permit examination of the full section of chlorite grain coating. However, it does illustrate the progressive change in both arrangement and texture of the chlorite particles between the contact with the substratum and further towards the centre of the pore. It can be seen that most of the chlorite particles observed near the surface of the detrital grains are parallel or slightly oblique to the detrital grain surface and that their size does not exceed a few hundred nanometers.

Quartz overgrowths (QH) are rare in sandstones cemented by chlorite and they occurred in zones where the coating of chlorite appears discontinuous at the scale of optical microscope (Billault, 2003). Features of crystallization of chlorite on secondary quartz substratum have never been observed (Billault, 2003). Inversely, SEM observation indicates that when secondary quartz is associated with chlorite, the chlorite grain coating preceded the precipitation of the quartz overgrowth which

presents many features of growth stopping at the contact of authigenic crystals of chlorite that constitute the outer area of the clay coatings (Fig. 6.2.2G).



**Figure 6.5.2:** HRTEM observation at a nanometric scale from selected reservoir sandstones of A-K1 well. (a) Illustrating a progressive change in both arrangement and texture of chlorite particles with illitic layers within it. (b) Chlorite displaying a pore lining trend with some detrital grain surface corresponding to quartz overgrowth (QH). (c) Stratified illitic layers underplayed by quartz overgrowth (QH) with some sticks of chlorite adjacent to the illitic layers. (d) Prominent illitic layers carpeting some chlorite grain coating (C).

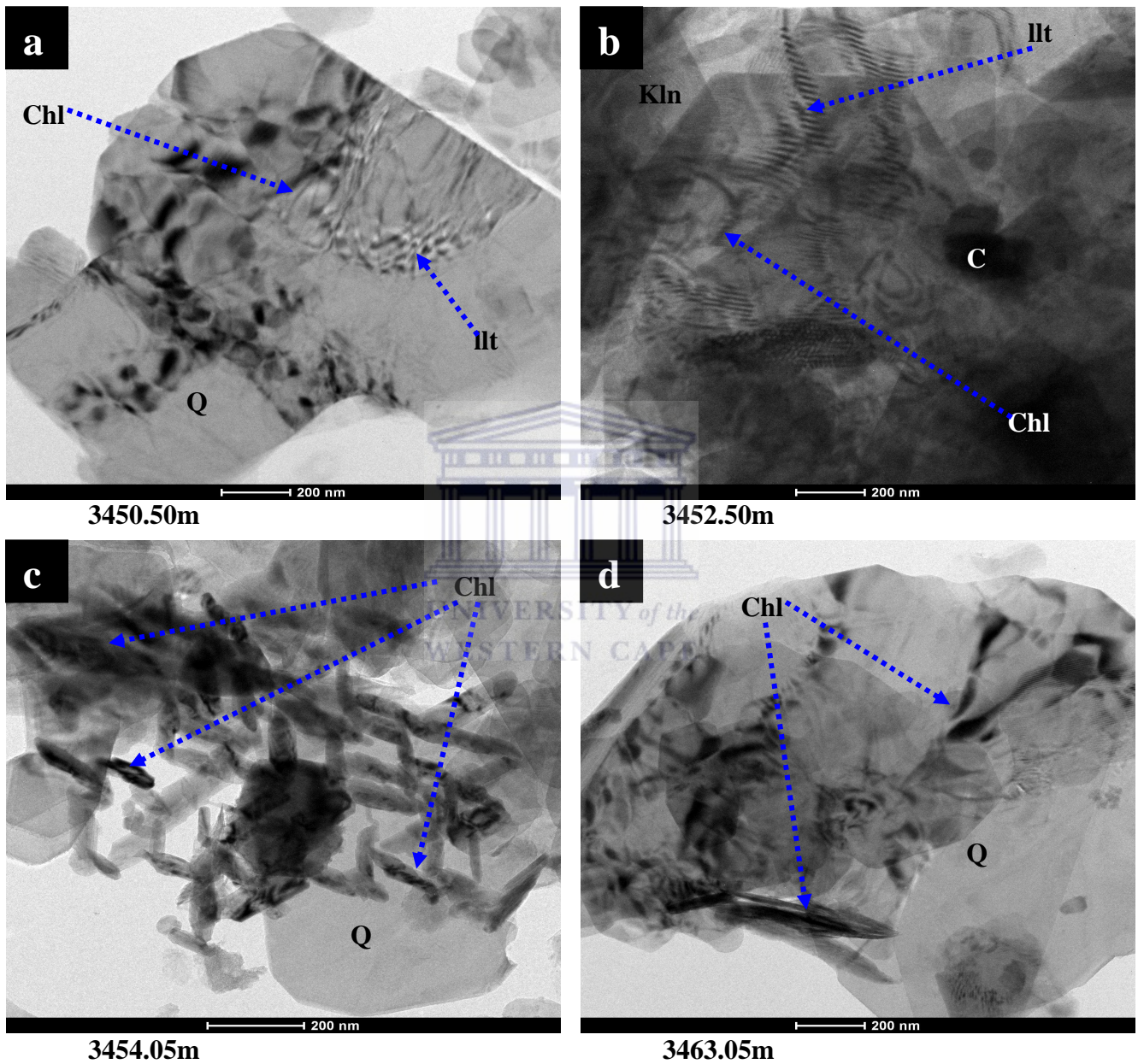


### 6.5.3 HR-TEM Results of A-W1 Well Reservoir Zones

Many investigators have suggested that kaolinite is a major source of Al and Si for chlorite during burial diagenesis because chlorite generally increases in abundance over the same depth interval in which kaolinite decreases in abundance (Muffler and White, 1969, Perry and Hower, 1970, Heling, 1978, Boles and Franks, 1979). Boles and Frank, 1979 suggested that the high aluminium content of chlorite from Wilcox sandstone was inherited from kaolinite and proposed a reaction of kaolinite to chlorite with  $\text{Fe}^{2+}$  and  $\text{Mg}^{2+}$  being supplied by smectite during its transformation to illite. Energy dispersive spectroscopic data (Table 6.5.3) show a relatively high percentage of Al with a trend of increasing in concentration with increasing depth of burial as compared to other studied wells which could be attributed to the dissolution of potassium feldspar within the sandstone thus providing aluminium that is being absorbed by the chloritization of mica observed from the thin section photomicrograph (Figs. 6.1.4 & 6.1.6) and the chemical formula obtained from XRD analysis ( $\text{Al}_{4.5}(\text{Al}_{1.8}\text{Si}_{3.2})\text{O}_{10}(\text{OH})_8$ ; see appendix H). All incipient stage chlorites from Albian sandstone (Fig. 6.5.3C) occur exclusively as parts and within the grains with a chain-like architecture. This distribution strongly implies that the formation of chlorite was closely related to kaolinite formed from alteration of mica (chloritization of mica) as seen in thin section photomicrograph (Fig. 6.1.6).

The compositional structure of the whole chlorite grain coatings crystallized at the walls of the primary pore space could be interpreted as the super-imposition of two distinct history of these sandstones: (1) an early stage during which chlorite crystallized in replacement of Fe-rich clay precursor as proposed by Ehrenberg, (1993) and (2) a later stage during which radially oriented authigenic chlorite crystallized upon the previous chlorite coating. The first stage would occur at shallow burial depth in a rock that was still not completely consolidated (i.e. before the sand grains had come in contact and acquired their present relative position by mechanical compaction. The second stage would occur at greater burial depth and results in growth of authigenic coarse-grained euhedral chlorites by redistribution of the chloritic materials of the first chlorite coating through Ostwald process only at the wall of the remaining pore space after total consolidation of sandstone (Jahren, 1991; Grigsby, 2001). The nanopetrographic relationships established by TEM in both types of chlorite grain coatings call into question the hypothesis of two distinctive events of chlorite crystallization. The inner chlorite coating observed (Fig. 6.5.3a) at contact

between adjacent sand grains suggests that it did not suffer the dissolution expected in the case of recrystallization of euhedral chlorite by Ostwald process and consequently invalidate the growth of a second generation of chlorite by cation redistribution (Jahren, 1990; Baronnet, 2003).



**Figure 6.5.3:** HRTEM observation at a nanometric scale from selected reservoir sandstones of A-W1 well. (a) Photomicrograph of an illitic layers showing a fibre-like trend. (b) Stratified parallel arrangement of illite (Ill) underlain by some pseudo-hexagonal shape of kaolinite (Kln). (c) Chain-like crystals of chlorite (Chl) forming a diamond shape acting as occlusion to pore spaces within the reservoir sand. (d) Occurrence of sticks of chlorite with detrital quartz (Q).

**Table 6.5.2: HR-TEM/EDS results of A-K1 well sandstone samples.**

A-K1 Well			
B	3236.27m	3238.35m	3284.30m
Elements	Weigth (%)	Weigth (%)	Weigth (%)
C	6.29	4.80	11.44
O	46.27	42.39	42.81
Na	0.30	0.56	0.81
Mg	2.96	0.07	3.85
Al	11.25	0.81	9.63
Si	15.57	50.92	8.92
K	0.00	0.11	0.26
Ca	0.00	0.00	0.00
Fe	17.31	0.30	22.23

**Table 6.5.3: HR-TEM/EDS results of A-W1 well reservoir samples**

A-W1 Well			
C	3450.50m	3454.05m	3463.05m
Elements	Weigth (%)	Weigth (%)	Weigth (%)
C	5.58	5.17	4.31
O	39.25	42.77	37.23
Na	0.53	0.30	0.00
Mg	4.52	3.09	3.66
Al	11.54	11.92	12.71
Si	12.32	13.55	12.21
K	0.13	0.00	0.00
Ca	0.00	0.02	0.00
Fe	26.09	23.15	29.84

#### 6.5.4 Semi-quantitative x-ray diffraction (XRD) results

Table 6.5.4 presents the results of the semi-quantitative XRD (in wt %) of some selected samples within wells A-G1, A-K1 & A-W1 sandstones. Few samples were selected from each well based on the trend of the results obtained from the earlier discussed petrographic analysis (thin section, SEM, XRD phase identification and FTIR) so as to have an idea of the distribution of carbonates, feldspars, silica and clay minerals in the study area.

X-ray diffraction (XRD) data of the samples from the reservoir sands across the examined wells show very high percentages of quartz (average 81 %, by weight) indicating that the reservoir intervals are silica rich, calcite shows almost a negligible abundance within the intervals of interest, chlorite (average 6.5 %, by weight), Mica (1.6 %, by weight) and illite/smectite interstratified shows significant presence in A-G1 well (Table 6.5.4) but with no trace in other wells except for A-K1 (3236.27 m). The significance of illite/smectite could be attributed to the transformation of mica into kaolinite before the kaolinitic clay becomes illitized as discussed in the A-G1 petrographic results. Illitic clays especially mixed layer illite/smectite are highly expandable and can disaggregate when exposed to fresh water thereby causing a reduction in the permeability as observed from the petrophysical results (Table 5.3) of A-G1 reservoir sand C & D. Quartz is the dominant framework grain type in all samples analyzed with lesser amounts of feldspar and lithic fragments. The relatively significant amount of plagioclase feldspar present likely represents feldspars association with volcanic and metamorphic lithic fragments (Figs. 6.1.1, 6.1.2, 6.1.3, 6.1.4 & 6.1.6)

**Table 6.5.4:** XRD semi-quantitative estimate of the phase abundance (% weight) for selected samples across the wells in the study area.

Samples	Depth (m)	Calcite	Siderite	Halite	Kfeldspar	Plagioclase	Quartz	Chlorite	Mica	Amphibole	Illite/Smectite
A-G1-9	3376.23	X	X	X	X	15	56	13	5	X	11
A-G1-7	3370.24	X	X	X	trace	5	88	4	1	X	2
A-K1-1	3236.27	X	X	1	X	7	77	10	2	X	2
A-K1-2	3238.35	1	trace	X	X	6	89	3	1	X	X
A-K1-3	3284.3	X	X	X	X	8	86	5	1	X	X
A-W1-4	3450.5	X	X	X	X	6	90	3	1	X	X
A-W1-5	3454.05	X	X	X	3	4	85	6	1	1	X
A-W1-6	3463.05	X	X	X	1	5	84	8	1	1	X
<b>Average</b>						<b>7</b>	<b>81.88</b>	<b>6.5</b>	<b>1.63</b>		

Note: X signifies not detected

## **6.6 Pore water geochemistry**

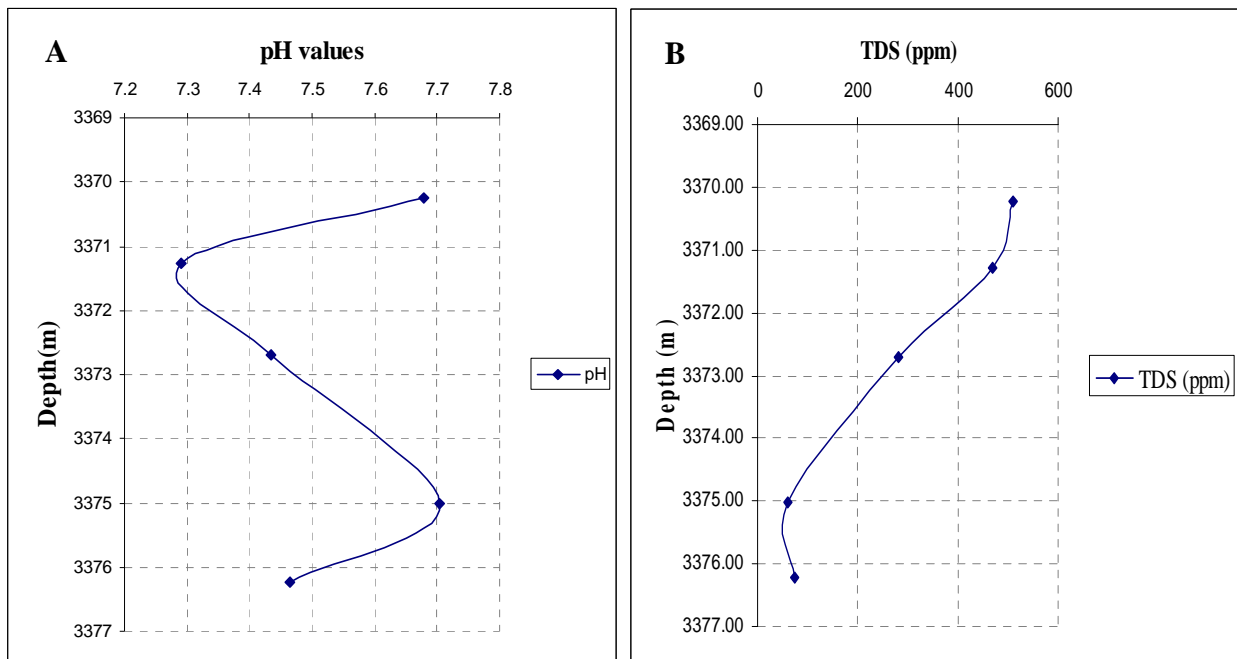
This section presents the results and interpretation of the pore water chemical analysis derived from the pulverized core samples. The understanding of the behaviour of the subsurface, types of subsurface water, pore water chemistry of different minerals at their cementation stage, the total dissolved salts (TDS) and the electrical conductivity (EC) of the minerals is very important for accurate interpretation. On the pH scale pure water has pH 7, although you will probably never see water pure enough for such pH. Air always contains small amounts of carbon dioxide which dissolves in water making it slightly acidic with pH of about 5.7. All values on the pH scale lower than 7 denote solutions that are acidic on the contrary solutions with pH above 7 are basic.

### **6.6.1 Pore water geochemistry of A-G1 well**

Petrographic analysis shows variation in the composition of major rock forming and authigenic minerals within the reservoir zones (quartz, kaolinite, calcite, illite, chlorite, mica, plagioclase e.t.c.). Different mineralogies of cement precipitate in response to changing in pore fluid temperature, pressure and composition. The integration of the different textural observation (core description) and petrographic interpretation with the pore fluid results will serve as basis for building a paragenetic sequence for cements in the study area. Original depositional textures and cement paragenesis are obscure in some samples (see petrography), because of severe compaction which has eliminated intergranular porosity. However, some samples in which abundant early cementation occurred preserved the depositional texture (Fig. 6.1.1D). Such rare samples, with well preserved intergranular cements coupled with the pH measurement permit the cements paragenesis to be deciphered. pH results (Fig. 6.6.1A) shows values of pH ranging from 7.29 – 7.47 with an average of 7.38 denoting that the reservoir zone diagenetic history was in neutral to slightly basic medium however, the mineralogy that was inferred from chapter five (section 5.3.4) clearly explains the presence of glauconite within the reservoir interval of study, glauconite is typically known to form close to the marine sediment interface, at oxic-sub-oxic boundary, which is slightly alkaline water (pH 7-8) with variability in Al, Si, Fe and K<sup>+</sup> as observed from EDS quantification (Table 6.2) Odin, (1982 & 1985). The occurrence of kaolinite was significant during the scanning electron micrographic

examination; this clay mineral is originally known to form in acidic medium. Pore fluid alterations, and cations exchange might also be responsible for its formation in a basic medium. Kaolinite precipitation follows illite, suggesting that the  $K^+$  may have been depleted during illite precipitation. Acidity in the pore waters may have increased simultaneously, assuming organic acids were produced by the maturation of organic matter in associated mudstones however, pH analysis results doesn't support the influence of organic matters in the reservoir zone. The trends of decreasing  $Mg^{2+}$  and  $K^+$  combined with increasing  $H^+$  activity might have led to pore water conditions favouring kaolinite precipitation (Cookenboo et al. 1998). The salinities of interstitial water of shale and porous rocks have provided useful clues in distinguishing a normally pressured zone from an overpressured one (Sahay, 1999).

Interstitial waters from shale and sandstone show a contrast in conception and composition (Fig. 6.6.1C). According to Sahay (1999), water in sandstone from normally compacted sediment increases in total dissolved solids with increasing depth at a rate of 20,000-50,000 mg/L per 1000ft. However, A-G1 well was logged in meters (m) and the TDS value reveals a decreasing trend with increasing depth. If an average of 0.305 m should give 20 mg/L with regards to Sahay's 1999 calculation (1ft = 0.305 m), then decreasing trend of the total dissolved solid within the A-G1 well sandstone could be attributed to an overpressured zone.

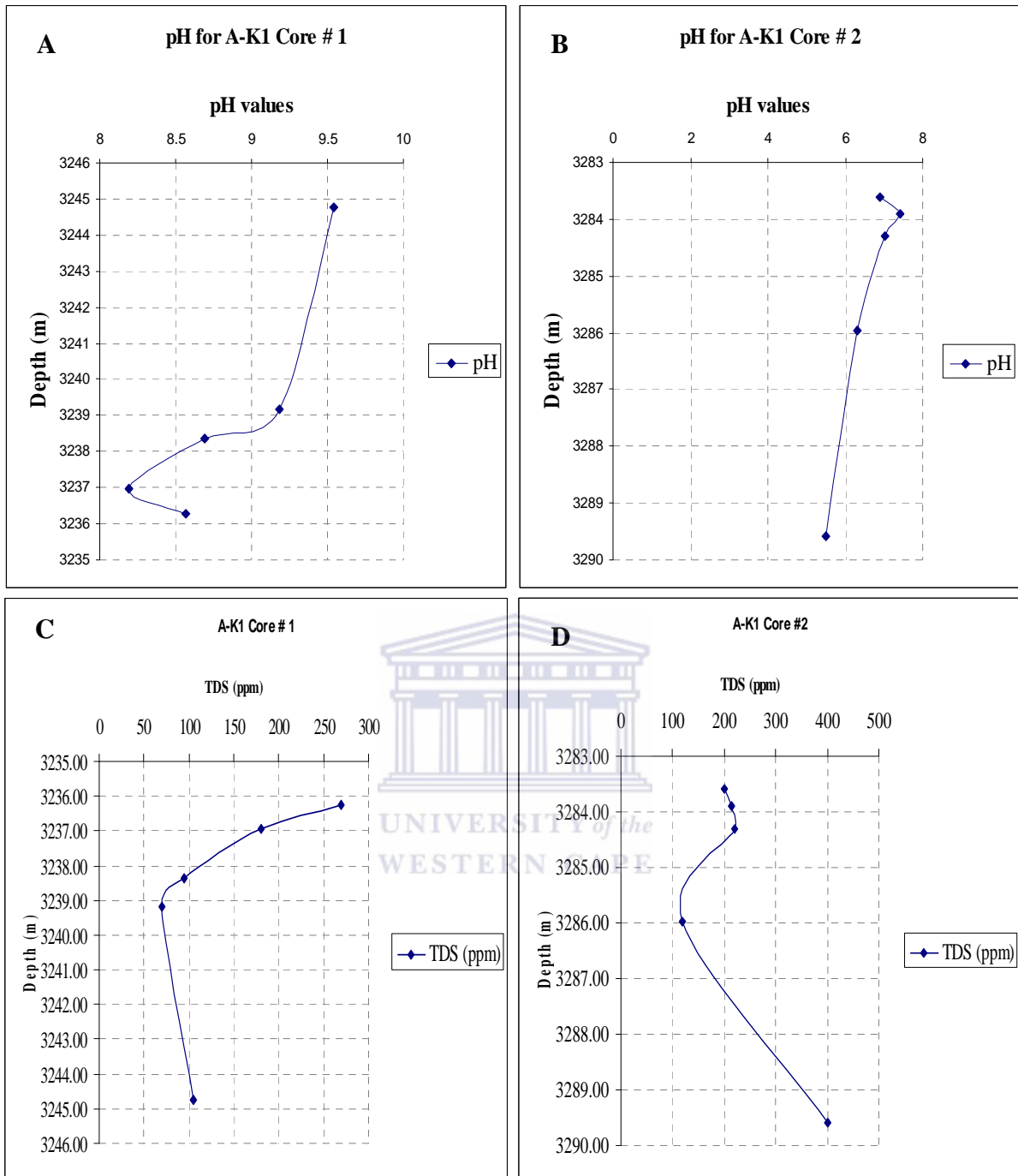


**Figure 6.6.1:** (A) pH plot of A-G1 reservoir zone (B) total dissolved solid within the reservoir zone.

## 6.6.2 Pore water geochemistry of A-K1 well

Chlorite as one of the dominant clay minerals in A-K1 well is one of the sensitive minerals because of its cementation behaviour in the reservoir zones. The clearest evidence for chlorite dissolution was observed in SEM, in which some pores are completely occluded with thick isopachous chlorite cements (Fig. 6.2.2H). If acidic waters subsequently move through the remaining connected pores, it can lead to dissolution of chlorite cement (Cookenboo et al., 1998). Dissolution could not occur in pores that were completely occluded during early chlorite cementation, presumably because acid waters could not permeate through the blocked pore spaces. The result is that some pores are filled with chlorite and other pores in the same sandstone lack chlorite altogether (Fig. 6.2.1E).

Kaolinite formation as explained in its occurrence during the SEM discussion was said to have formed due to meteoric flushing of channel sandstones before burial (Knarud and Bergen 1990). Meteoric waters are often acidic because of dissolved humic acid, carbonic and nitric acid (from the atmosphere) although they may quickly become neutralized in the subsurface provided they flow through carbonate rocks (Selley, 1997). Looking critically into the trend of changes in the pore water chemistry parameters (Figure 6.6.2A), it was observed that Core # 1 pore water pH range from 8.19 – 9.55 with an average of 8.87 showing decrease in alkalinity with depth while Core # 2 which ranged from 5.49 – 7.40 with an average of 6.45 which indicate near neutral to acidic medium (acidity increases with depth) and also support the fact that the two cores are likely of different sand bodies. The justification for the acidic-alkalinity medium could be attributed to the mobilization of minerals by pore fluids as they were flushed from interbedded mudstone (Cookenboo et al., 1998). Illite occurs as pore-lining or pore-filling cement in some of the chlorite cemented sandstones (Fig. 6.2.2J). Illite is distinguished from chlorite in SEM images by characteristic filamentous and ribbon-like crystal shapes. Energy-dispersive spectrometry of the samples confirms the occurrence of  $K^+$  and lack of  $Mg^{2+}$  (Table 6.2.1) and thus supports the mineral identification as illite. Experimental work carried out by Chiba (1995) reveals that quartz shows a distinctive difference among alteration minerals by increasing as the rock becomes more acidic, this could be attributed to the decreasing pH value (Fig. 6.6.2) in A-K1 core 2 with regards to the table 6.5.4 which explains the high percentages of quartz across the well.



**Figure 6.6.2:** (A) pH plot of A-K1 reservoir zone (B) the electrical conductivity plot of A-K1 (C) total dissolved solid of A-K1 core # 1 (D) total dissolved solid of A-K1 core # 2.

The inference of basic waters for the chlorite cementation stage described earlier suggests a simple and plausible explanation for the chlorite dissolution stage: the pore waters change from basic to acidic. Such a change to acidic conditions continues the trend of decreasing alkalinity inferred for the illite, kaolinite, and hydrocarbon migration stages (Cookenboo et al., 1998). The apparent dissolution of chlorite

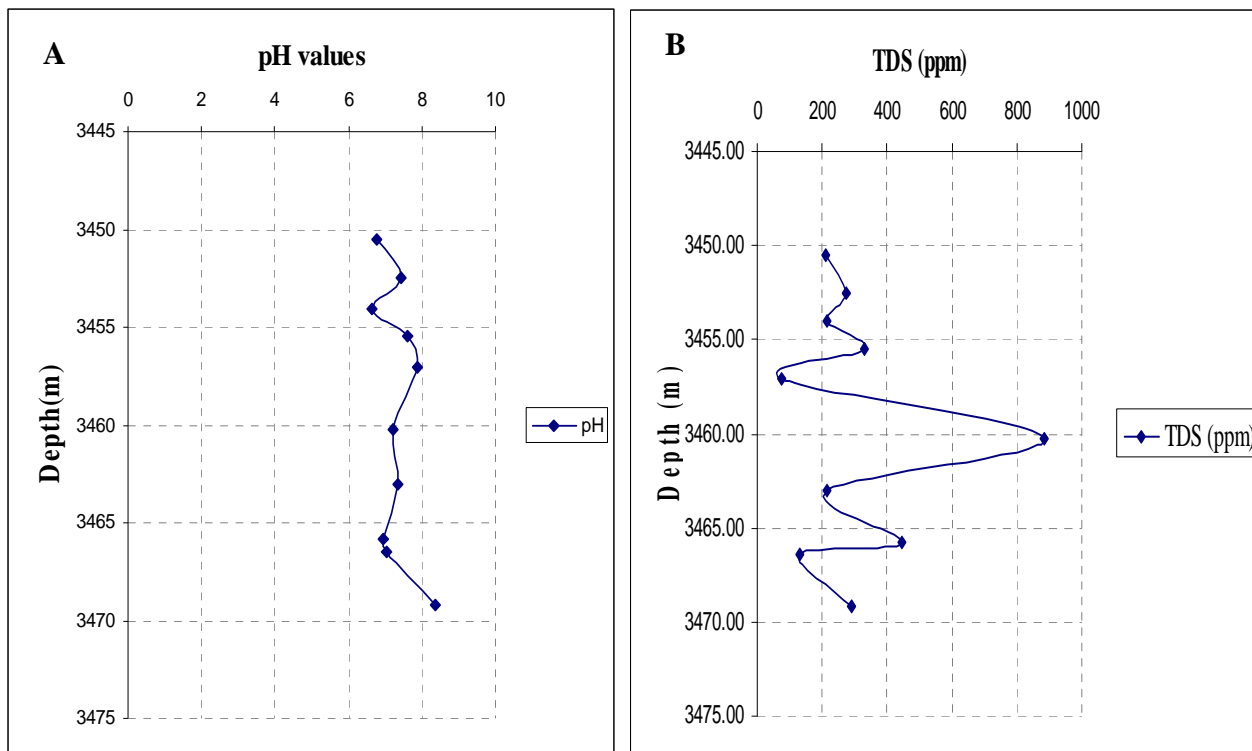


implies that acidic pore fluids overcame any existing pH buffers. Carbonate buffers in siliciclastic successions such as the A-K1 well might be expected to be minor, but clay mineral buffers could have been significant. Interstitial shale water exhibit salinity trends similar to sandstone waters (Fig. 6.6.2C & D) except that the shale sample extract water has much lower total dissolved solid in core 1 (depth 3244.75 m) concentrations than the adjacent sandstone waters. However, comparing A-K1 well with A-G1 well, the total dissolved solid could be attributed to a normally pressured zone.

### **6.6.3 Pore water geochemistry of A-W1 well**

The understanding of the cement succession and grain contact in A-W1 well provides an opportunity to understand pore water evolution at the reservoir zone. Chlorite cement forms continuous isopachous coats as much as 25  $\mu\text{m}$  thick, of tangentially arranged blade-like structures (Figure 6.2.3A & B) in which the crystals are oriented perpendicular to grain surfaces. The cements form regardless of substrate composition as demonstrated by equal thickness of cements around grains irrespective of mineralogy. In other pores, although crystal orientation remains perpendicular to detrital grain margins, the interior surface of the chlorite cement is irregular, suggesting subsequent dissolution by pore waters. The slightly acidic-neutral-slightly alkaline medium (Fig. 6.6.3A) of the samples from A-W1 makes it composite for interpretation however, the presence of chlorite formation causes decrease in pH values due to supplies of Al and  $\text{SiO}_2$  within A-W1 reservoir interval (Chiba, 1995).

Pyrite framboids (Fig. 6.2.3F) are well known to form soon after burial (Gautier and Claypool 1984) in response to the low oxygen-high sulphate pore conditions characteristic of the sulphate reducing zone (Berner, 1981). Such conditions are usually restricted to the upper few metres of organic-rich sediments (Gautier and Claypool 1984). According to Chiba (1995), sulfides minerals such as pyrite increases acidity in most rock types, this could be attributed to one of the reasons for the slight acid-neutral condition within the reservoir interval in figure 6.6.3 (depth 3450.50 m).



**Figure 6.6.3:** (A) pH plot of A-W1 reservoir zone (B) total dissolved solid within the reservoir zone.

The relative timing of the quartz cement stage is interpreted petrographically from the observation that quartz cement occurs in some pores inside thick isopachous chlorite cements. In fractures containing quartz and calcite cements, textural relations consistently indicate that quartz cementation preceded calcite cementation. Quartz cementation, could therefore have followed oil migration, and preceded calcite cementation. The cementation stages described above resulted from changes in the pore water conditions. We interpret those changes presuming: (1) the different cements formed in succession during burial and (2) pore water conditions in the sandstones were significantly affected by organic maturation in the interbedded and underlying mudstones. Both presumptions are consistent with the known geology in the area. For example, petrographic relationships demonstrate the cement stages occur one after another under conditions of increasing compaction, and interbedded (and underlying) strata are organic-rich mudstones, that organic maturation in the mudstones influenced pore fluids in the sandstones is amply demonstrated by the occurrence of pore water results of some depths (3450.50 & 3465.80) m to be slightly above the neutral point in some samples. The pore water result which ranges from 6.79 – 8.36 with an average of 7.575 pH value shows that the reservoir zone under study falls within the neutral-alkaline medium. The presumed influence of pore

conditions on the cements requires significant transport through the sandstones. An increase in pH value in some depths suggests a buffering medium by the presence of albite and quartz (Chiba, 1995). The disappearance of pH buffer probably causes the solution to wander into highly alkaline medium as observed in figure 6.6.3A (depth 3469 m).

## **6.7 Bulk Rock Geochemistry**

With the aim of investigating the history, from source to deposition, of the selected wells in Orange Basin, a total of 25 samples were analyzed for major and trace elements. The geochemical investigation took into account samples from the Albian age of the three wells with core samples available. Major element geochemical data of the Albian age sandstones reported here and used in some diagrams in this section are interpreted based on previous studies from (Van Lente, 2004; Crook, 1974; Herron, 1988; Pettijohn et al., 1972 and Taylor and McLennan, 1985). The sandstone chosen were all fine-to very fine grained.

The bulk composition of terrigenous sedimentary rocks are influenced by several factors such as sedimentary provenance, nature of sedimentary processes within the depositional basin, and the kind of dispersal paths that link provenance to the depositional basin e.g. weathering, transportation, physical sorting and diagenesis (Roser and Korsch, 1986; McLennan et al., 1990; Eriksson et al., 1992; Weltje and von Eynatten, 2004). However, the bulk chemical composition of terrigenous sedimentary rocks can be used to identify tectonic environments and provenance characteristics (e.g. Bhatia, 1983; Mongelli et al., 1996; Ugidos et al., 1997; Gotze, 1998; Holail and Moghazi, 1998; Yang et al., 2004).

Sandstone geochemistry varies systematically with the nature of the source rocks, weathering, diagenesis and metamorphism. In addition, the tectonic setting has been identified as overall primary control on the composition of sedimentary rocks (Bhatia, 1983, Bhatia and Crook, 1986; Pettijohn et al. 1987). Various studies have shown that the chemical signature of some elements such as Mg, Cr, Ni, Co, Zr, Y, Nb, Sr, and Ba is generally preserved in sedimentary rocks through weathering and diagenesis (McLennan et al., 1983; Van de Kamp and Leake, 1985; Culler et al., 1988). Therefore, the geochemical investigation of abundance of these relative immobile elements usually provides information about the source material.

### 6.7.1 Geochemical classification of sandstones

The major elements composition of the Albian age sandstone determined in this study are compared to the mean composition of principal sandstone classes (Pettijohn et al. 1987) and presented in Table 6.7.1. Based on Pettijohn (1987) classification, the results of the wells in this study are therefore compared with the previous work of Pettijohn (1987) as presented in Table 6.7.2. It was observed that A-G1 well generally spans between the lithic arenite and greywacke sandstone classification except for K<sub>2</sub>O and the ratio of Na<sub>2</sub>O/K<sub>2</sub>O that falls within arkosic and quartz arenitic sandstone respectively. A-W1 well also shows similar trend with most of the classification falling within the range of lithic arenite and greywacke except for Na<sub>2</sub>O and MnO both belonging to the arkose sandstone classification. A-K1 well also generally belongs to the lithic arenitic sand which some few exceptions in Na<sub>2</sub>O and MnO belonging to the arkosic sand which is similar with the A-W1 well.

**Table 6.7.1:** Mean composition of principal sandstone classes and average Albian age sandstone for the studied wells

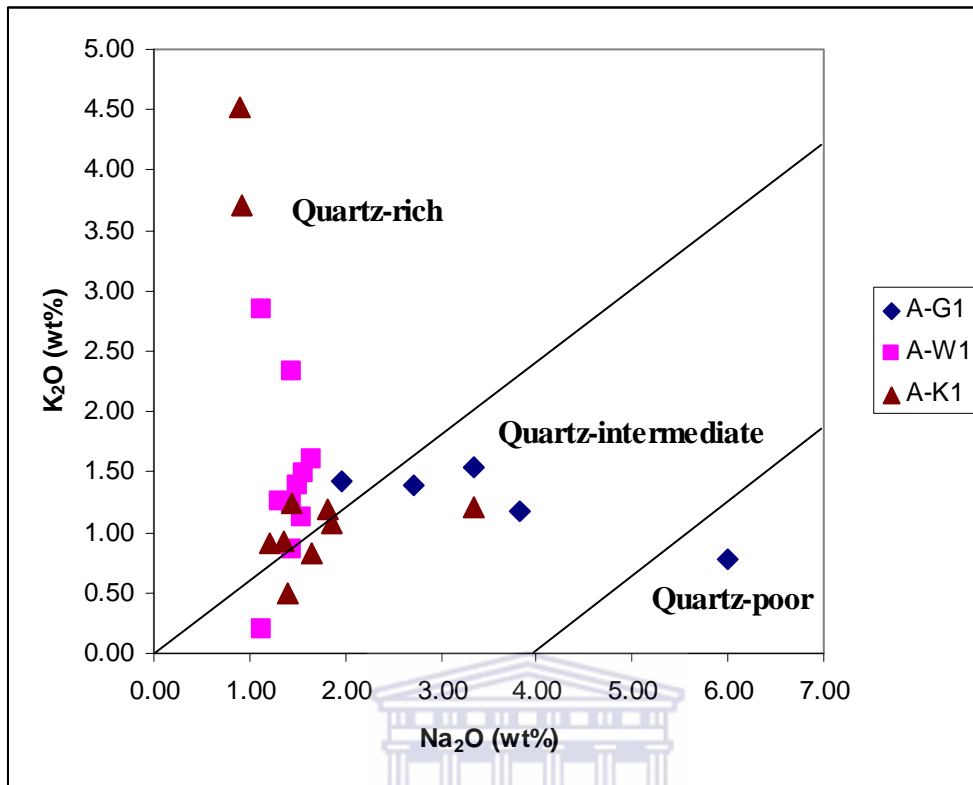
Average sandstones (Pettijohn., 1987)					Average Albian age sandstone			
Major Oxides (%)	Quartz arenite	Lithic arenite	Grey wacke	Arkose	Major Oxides (%)	A-G1	A-W1	A-K1
SiO <sub>2</sub>	95.4	66.1	86.7	77.1	SiO <sub>2</sub>	63.14	53.81	57.96
Al <sub>2</sub> O <sub>3</sub>	1.10	8.10	13.50	8.70	Al <sub>2</sub> O <sub>3</sub>	10.08	8.55	9.19
Fe <sub>2</sub> O <sub>3</sub>	0.40	3.80	1.60	1.50	Fe <sub>2</sub> O <sub>3</sub>	13.20	18.03	16.76
MgO	0.10	2.40	2.10	0.50	MgO	1.59	1.97	1.98
CaO	1.60	6.20	2.50	2.70	CaO	1.10	6.67	4.06
Na <sub>2</sub> O	0.10	0.90	2.90	1.50	Na <sub>2</sub> O	1.26	1.42	1.60
K <sub>2</sub> O	0.20	1.30	2.00	2.80	K <sub>2</sub> O	3.57	1.43	1.61
TiO <sub>2</sub>	0.20	0.30	0.60	0.30	TiO <sub>2</sub>	2.12	3.07	2.22
P <sub>2</sub> O <sub>5</sub>	-	0.10	0.20	0.10	P <sub>2</sub> O <sub>5</sub>	0.15	0.19	0.18
MnO	-	0.10	0.10	0.20	MnO	0.08	0.19	0.16
Na <sub>2</sub> O/ K <sub>2</sub> O	0.50	0.69	1.45	0.53	Na <sub>2</sub> O/ K <sub>2</sub> O	0.43	1.50	1.53
SO <sub>3</sub>	-	-	0.30	-	SO <sub>3</sub>	0.16	0.68	0.16

The first well (A-G1) reveals the highest average value of SiO<sub>2</sub> and Al<sub>2</sub>O<sub>3</sub> having 63.14 and 10.08 %, respectively while the other two wells (A-W1 & A-K1) reveals richness in the percentage of Fe<sub>2</sub>O<sub>3</sub>, MgO and TiO<sub>2</sub> (Table 6.7.1). However, the results of the three wells under study reveal that A-G1 has Na<sub>2</sub>O/K<sub>2</sub>O of 0.43 and MgO/CaO of 2.40; A-W1 also has Na<sub>2</sub>O/K<sub>2</sub>O of 1.50 and MgO/CaO of 1.96; and A-K1 contains Na<sub>2</sub>O/K<sub>2</sub>O of 1.53 with MgO/CaO of 1.76. The values of Al<sub>2</sub>O<sub>3</sub> and Fe<sub>2</sub>O<sub>3</sub> indicate that the wells could be attributed to the greywacke class of sandstones as expected for most marine prone environment (Pettijohn, 1975).

It is possible to recognize a number of varieties of greywacke. Those rich in rock fragments have been called lithic greywacke and those rich in feldspar are the feldspathic greywackes. The studied wells which are characterized by high alkali ( $\text{Na}_2\text{O} + \text{K}_2\text{O}$ ) content, low  $\text{SiO}_2/\text{Al}_2\text{O}_3$  and  $\text{Na}_2\text{O} < \text{K}_2\text{O}$ , are closer to lithic greywackes (Pettijohn et al., 1987).

Crook (1974) subdivided greywackes on the basis of  $\text{SiO}_2$  content and the relative  $\text{K}_2\text{O}/\text{Na}_2\text{O}$  ratio into three classes and assigned each to plate tectonic setting and provenance. The quartz-poor variety, characterized by low  $\text{SiO}_2$  content is typical of volcanic provenance. The quartz-rich (average 89 %  $\text{SiO}_2$ ,  $\text{K}_2\text{O}/\text{Na}_2\text{O} > 1$ ) content indicates a sedimentary provenance and the quartz-intermediate (average 68-74 %  $\text{SiO}_2$ ,  $\text{K}_2\text{O}/\text{Na}_2\text{O} < 1$ ) being of mixed provenance. Crook (1974) attributed the quartz-poor types to the island arc environment, the quartz-rich class to tectonically inactive continental margins, and the intermediate type to tectonically active margins of continental or micro-continents.

The majority of the Albian reservoir sands have  $\text{SiO}_2$  range of 71.66 – 53.38 and  $\text{K}_2\text{O}/\text{Na}_2\text{O}$  greater than 1 which could be classified as quartz-rich and therefore explains the sedimentary provenance with a tectonically inactive continental margins region for most of the samples in A-W1 well (Fig. 6.7.1) while A-K1 samples also have the  $\text{K}_2\text{O}/\text{Na}_2\text{O}$  ratio to be greater than one but spans between the quartz-rich and quartz-intermediate zone mostly at the transition zone between the quartz-rich and that of quartz-intermediate indicating both the tectonically inactive continental margin zone and a mixed provenance (Fig. 6.7.1). Samples in A-G1 well mostly fall within the quartz-intermediate classification with the  $\text{K}_2\text{O}/\text{Na}_2\text{O}$  ratio greater than 1 which is therefore attributed to the mixed provenance.



**Figure 6.7.1:** Analysis of alkali content of the Albian age sandstones based on major element geochemistry (Modified from Crook, 1974).

UNIVERSITY of the  
WESTERN CAPE

**Table 6.7.2:** Major oxides (wt %) of the selected sandstone samples of the Albian age gas bearing formation along with their calculated chemical index of alteration (CIA).

<b>Major Oxides for A-G1 well</b>															
Well Name	Depth (m)	SiO <sub>2</sub>	Al <sub>2</sub> O <sub>3</sub>	CaO	Fe <sub>2</sub> O <sub>3</sub>	K <sub>2</sub> O	MgO	MnO	Na <sub>2</sub> O	SO <sub>3</sub>	TiO <sub>2</sub>	P <sub>2</sub> O <sub>5</sub>	LOI	CIA	Total
A-G1	3370.24	63.08	9.14	0.85	15.35	3.34	1.56	0.08	1.54	0.11	3.15	0.20	1.60	61.45	100.00
A-G1	3371.28	62.91	8.37	1.22	16.57	2.72	1.58	0.15	1.39	0.09	2.74	0.16	2.10	61.11	100.00
A-G1	3372.70	71.66	6.88	2.50	9.21	1.97	0.98	0.07	1.43	0.23	1.80	0.16	3.11	53.85	100.00
A-G1	3375.02	57.24	13.52	0.42	12.59	6.00	1.93	0.06	0.78	0.20	1.43	0.11	5.71	65.25	99.99
A-G1	3376.23	60.79	12.50	0.49	12.26	3.83	1.89	0.05	1.17	0.18	1.47	0.13	5.23	69.50	99.99
<b>Average</b>		<b>63.14</b>	<b>10.08</b>	<b>1.10</b>	<b>13.20</b>	<b>3.57</b>	<b>1.59</b>	<b>0.08</b>	<b>1.26</b>	<b>0.16</b>	<b>2.12</b>	<b>0.15</b>	<b>3.55</b>	<b>62.23</b>	
<b>Major Oxides for A-W1 well</b>															
A-W1	Depth (m)	SiO <sub>2</sub>	Al <sub>2</sub> O <sub>3</sub>	CaO	Fe <sub>2</sub> O <sub>3</sub>	K <sub>2</sub> O	MgO	MnO	Na <sub>2</sub> O	SO <sub>3</sub>	TiO <sub>2</sub>	P <sub>2</sub> O <sub>5</sub>	LOI	CIA	Total
A-W1	3450.50	61.61	9.25	1.07	17.04	1.49	2.17	0.07	1.57	0.12	4.19	0.23	1.19	69.12	100.00
A-W1	3452.50	50.10	7.78	2.61	23.77	1.40	2.14	0.17	1.50	0.13	7.88	0.27	2.25	58.57	100.00
A-W1	3454.05	55.26	6.99	2.50	25.54	1.60	1.94	0.25	1.64	0.13	3.22	0.23	0.71	54.94	100.00
A-W1	3455.50	58.03	9.25	0.62	19.40	1.24	2.17	0.13	1.44	0.05	5.62	0.22	1.83	73.75	100.00
A-W1	3457.05	22.53	2.55	37.82	12.86	0.20	0.63	0.54	1.13	0.01	1.48	0.09	20.00	6.10	99.85
A-W1	3460.24	44.30	6.46	17.91	17.64	0.86	1.89	0.32	1.44	5.56	1.45	0.17	2.00	24.23	100.00
A-W1	3463.05	61.30	8.24	1.70	19.39	1.12	2.40	0.21	1.55	0.05	2.21	0.21	1.61	65.33	100.00
A-W1	3465.80	54.47	13.02	0.49	18.49	2.84	2.34	0.06	1.13	0.37	2.10	0.13	4.55	74.48	99.99
A-W1	3466.05	69.04	8.49	1.50	13.32	1.25	1.74	0.06	1.32	0.26	1.27	0.20	1.54	67.57	100.00
A-W1	3469.20	61.43	13.44	0.46	12.89	2.34	2.33	0.05	1.44	0.08	1.24	0.19	4.11	76.00	100.00
<b>Average</b>		<b>53.81</b>	<b>8.55</b>	<b>6.67</b>	<b>18.03</b>	<b>1.43</b>	<b>1.97</b>	<b>0.19</b>	<b>1.42</b>	<b>0.68</b>	<b>3.07</b>	<b>0.19</b>	<b>3.98</b>	<b>57.01</b>	
<b>Major Oxides for A-K1 well</b>															
Well Name	Depth (m)	SiO <sub>2</sub>	Al <sub>2</sub> O <sub>3</sub>	CaO	Fe <sub>2</sub> O <sub>3</sub>	K <sub>2</sub> O	MgO	MnO	Na <sub>2</sub> O	SO <sub>3</sub>	TiO <sub>2</sub>	P <sub>2</sub> O <sub>5</sub>	LOI	CIA	Total
A-K1	3236.27	60.58	8.43	1.61	19.18	0.83	2.61	0.18	1.66	0.06	1.78	0.22	2.86	67.25	100.00
A-K1	3236.96	53.38	8.36	2.17	26.09	0.93	2.55	0.30	1.37	0.08	1.18	0.22	2.86	65.20	100.00
A-K1	3238.35	70.64	6.05	2.27	13.03	0.92	1.21	0.09	1.22	0.05	2.21	0.21	2.86	57.85	99.99
A-K1	3239.18	43.83	3.62	28.88	10.49	0.49	0.61	0.47	1.41	0.02	0.83	0.11	2.86	10.53	99.95
A-K1	3244.75	56.44	13.84	0.80	12.46	4.52	1.87	0.07	0.90	0.25	1.46	0.13	2.86	68.97	99.98
A-K1	3283.60	60.34	10.78	0.93	18.27	1.20	2.36	0.11	1.83	0.03	1.60	0.19	2.86	73.15	100.00
A-K1	3283.90	64.60	8.37	1.22	15.58	1.08	2.19	0.13	1.87	0.04	2.10	0.20	2.86	66.74	100.00
A-K1	3284.30	58.45	9.08	1.31	17.75	1.20	2.05	0.15	3.33	0.10	3.97	0.22	2.86	60.81	100.00
A-K1	3285.97	54.91	10.04	0.83	21.06	1.25	2.38	0.10	1.45	0.06	5.65	0.19	2.86	74.03	100.00
A-K1	3289.59	56.43	13.37	0.57	13.71	3.72	1.94	0.04	0.93	0.94	1.38	0.11	2.86	71.95	99.98
<b>Average</b>		<b>57.96</b>	<b>9.19</b>	<b>4.06</b>	<b>16.76</b>	<b>1.61</b>	<b>1.98</b>	<b>0.16</b>	<b>1.60</b>	<b>0.16</b>	<b>2.22</b>	<b>0.18</b>	<b>2.86</b>	<b>61.65</b>	

Note: CIA= [Al<sub>2</sub>O<sub>3</sub>/ (Al<sub>2</sub>O<sub>3</sub>+CaO+Na<sub>2</sub>O+K<sub>2</sub>O)] \* 100

## 6.7.2 Weathering and paleo-environmental conditions during deposition.

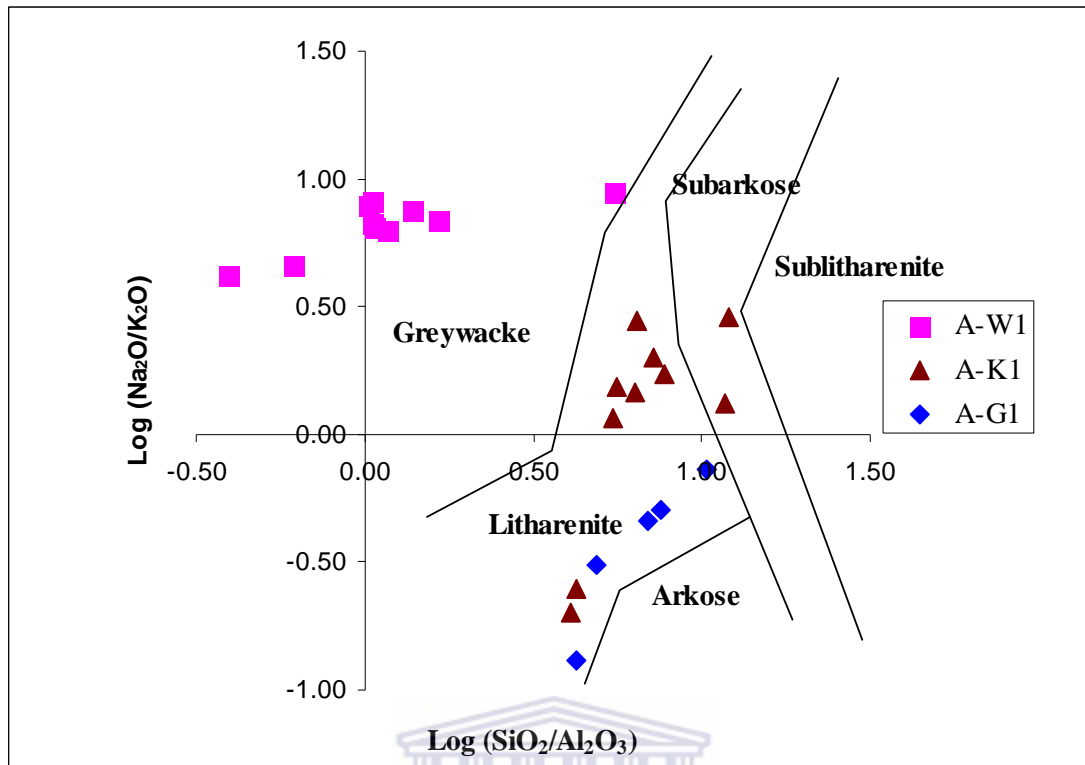
### 6.7.2.1 Sediments maturity

Sediment maturity may be measured in terms of the  $\text{SiO}_2$  content and the  $\text{SiO}_2/\text{Al}_2\text{O}_3$  ratio (Potter, 1978), which reflect the relative abundance of quartz, feldspar and clay. Feldspar content can also be determined from whole rock chemistry using alkali elements content ( $\text{Na}_2\text{O} + \text{K}_2\text{O}$ ). Using the index of chemical maturity  $\text{SiO}_2/\text{Al}_2\text{O}_3$  and  $\text{Na}_2\text{O}/\text{K}_2\text{O}$  ratio, Pettijohn et al., (1972) proposed a classification of terrigenous sands based upon a plot of  $\text{Log} (\text{Na}_2\text{O}/\text{K}_2\text{O})$  versus  $\text{Log} (\text{SiO}_2/\text{Al}_2\text{O}_3)$ . This classification diagram which has been redrawn by Herron (1988), shows the relationship between elemental composition, mineralogy and rock type. This was applied to the Albian age reservoir sands since there has been no major loss of K and Na during diagenesis.

Generally, the studied wells shows markedly higher  $\text{SiO}_2/\text{Al}_2\text{O}_3$  ratios and consequently lower  $\text{Na}_2\text{O} + \text{K}_2\text{O}$  contents reflecting their quartz-rich, poor clay nature. On the average, the  $\text{SiO}_2/\text{Al}_2\text{O}_3$  ratio for A-G1, A-W1 and A-K1 are 6.78, 6.73 and 7.09, respectively and the  $\text{Na}_2\text{O} + \text{K}_2\text{O}$  of 4.83, 2.85 and 3.21, respectively (Appendix M), indicating that the sediments are within the transition zone of mature and immature nature of the greywackes because greywackes have an  $\text{SiO}_2/\text{Al}_2\text{O}_3$  equal to 5 wt% with the  $\text{Na}_2\text{O} + \text{K}_2\text{O}$  ratio equal to 4.9 wt% (Pettijohn, et al., 1987) and the results obtained reveals that  $\text{SiO}_2/\text{Al}_2\text{O}_3$  ratio is greater than 5 wt% but the  $\text{Na}_2\text{O} + \text{K}_2\text{O}$  ratio is less than 4.9.

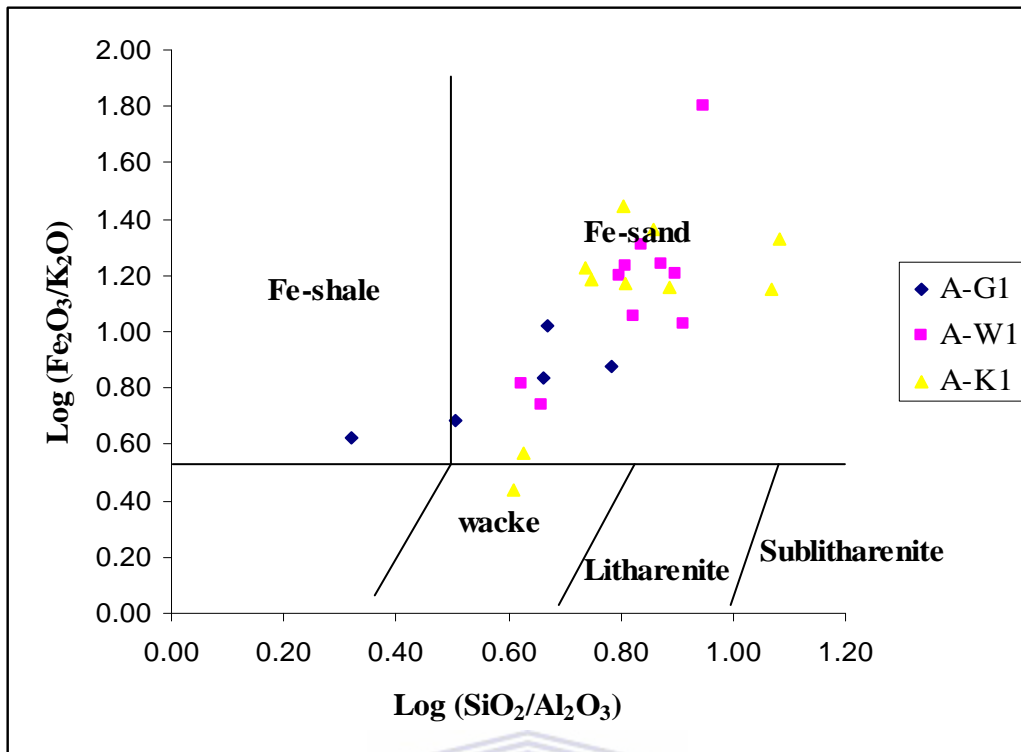
On the Pettijohn et al., (1972) and Herron, (1988) sandstone classification diagram, the Albian age sandstone plot on the boundary spans between Arkose, litharenite and greywacke but with the majority of the samples falling within litharenite and greywacke region. Both greywacke and litharenite are chemically immature sandstones. This may suggest minimum amount of weathering during erosion and deposition and limited transport.





**Figure 6.7.2:** Classification of terrigenous sandstone using Log (Na<sub>2</sub>O/K<sub>2</sub>O) versus Log (SiO<sub>2</sub>/Al<sub>2</sub>O<sub>3</sub>) from Pettijohn et al., (1972), modified by Herron (1988).

Herron (1988) modified the diagram of Pettijohn et al. (1972) using Log (Fe<sub>2</sub>O<sub>3</sub>/K<sub>2</sub>O) along the Y-axis instead of Log (SiO<sub>2</sub>/Al<sub>2</sub>O<sub>3</sub>). The ratio Fe<sub>2</sub>O<sub>3</sub>/K<sub>2</sub>O buttresses the Fe-rich sand that has been predicted from the earlier discussed TEM results (Section 6.5) and it is a measure of mineral stability. Thus, in the plot of Log (Fe<sub>2</sub>O<sub>3</sub>/K<sub>2</sub>O) versus Log (SiO<sub>2</sub>/Al<sub>2</sub>O<sub>3</sub>), all the three wells consisting of 25 samples mostly fall in the Fe-sand field (Fig. 6.7.3) with one sample in A-K1 and A-G1 falling in the wacke and Fe-shale field respectively. This plot is in good agreement with the petrography results which reveals the Fe-rich reservoir sand during the clay analysis.



**Figure 6.7.3:** Geochemical classification of samples from Albian age sandstone based on Log (SiO<sub>2</sub>/Al<sub>2</sub>O<sub>3</sub>) vs. Log (Fe<sub>2</sub>O<sub>3</sub>/K<sub>2</sub>O) diagram (after Herron, 1988).

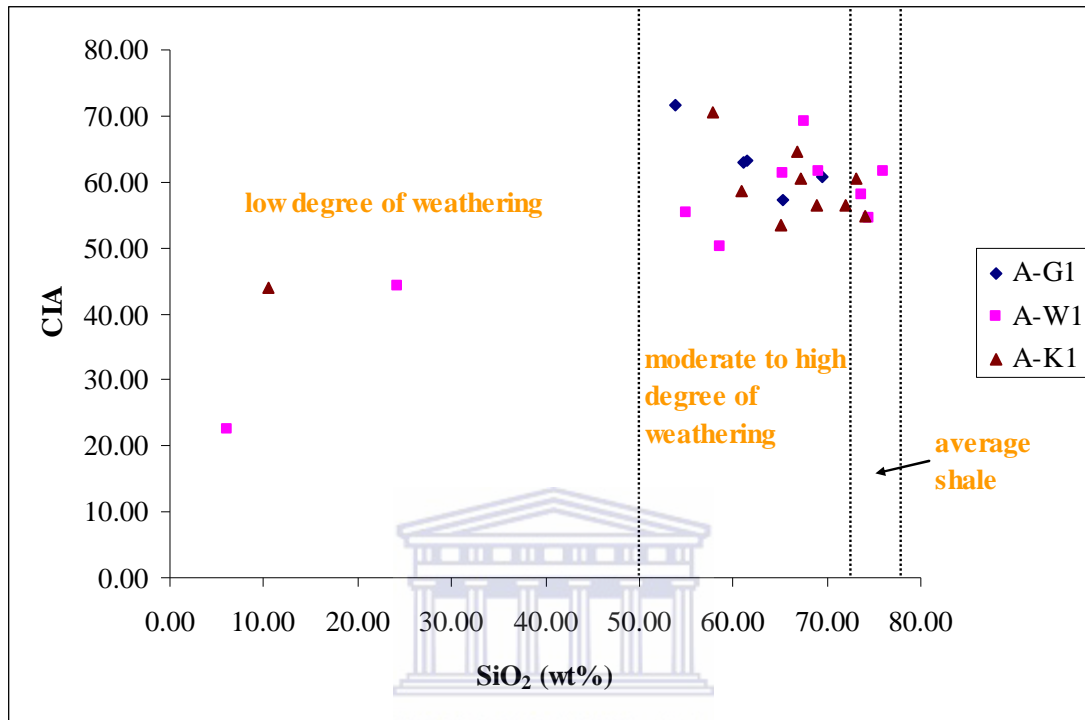
### 6.7.2.2 Paleo-weathering

Alteration of rocks during weathering results in depletion of alkali and alkaline earth elements and preferential enrichment of Al<sub>2</sub>O<sub>3</sub> in sediments. Alteration of mineral due to chemical weathering mainly depends on the intensity and duration of weathering. During weathering, calcium, sodium, and potassium are largely removed from feldspar (Nesbit et al., 1980). The amount of these chemical elements surviving in the sediment is a sensitive index of the intensity of weathering (Nesbit et al., 1997). A good measure of the degree of weathering can be obtained by calculating the chemical index of alteration (CIA) (Nesbit and Young, 1982) using the formula (molecular proportion):

$$\text{CIA} = [\text{Al}_2\text{O}_3 / (\text{Al}_2\text{O}_3 + \text{CaO} + \text{Na}_2\text{O} + \text{K}_2\text{O})] \times 100$$

Chemical index of alteration (CIA) can also be used to determine the climatic conditions that existed during the formation of clastic sedimentary rocks. The CIA is a good measure of paleo-weathering conditions, and is essentially monitors the progressive weathering of feldspar to clay minerals (Fedo et al., 1995); Armstrong-Altrin et al., 2004). High values (i.e. 76 – 100) indicate intensive chemical weathering in the source areas whereas low values (i.e. 50 or less) indicates unweathered source areas. Chemical data from the Albian age sandstone were plotted according to the

strategy of Nesbit and Young (1982). The average alteration of A-G1, A-W1 and A-K1 are 62.23 %, 57.01 % and 61.65 % respectively. The results are therefore presented in figure 6.7.4 which shows that rock samples in the studied well fall in the fields of moderate to high degree of weathering.



**Figure 6.7.4:** SiO<sub>2</sub> vs. CIA (Chemical alteration index) of the studied Albian age sandstones.

### 6.7.2.3 Climate

Previous work according to Nesbitt and Young (1982) reveals Pleistocene till having CIA values of around 52, Pleistocene glacial clays having an average value of around 65 % or Pleistocene varved clays with an average CIA value of around 62 % were formed in extremely cold conditions, whereas residual clays with CIA values greater than 90 % and Amazon cone muds that have average CIA values between 82 % and 86 % are likely to have been formed in hot, humid climates (Nesbitt and Young, 1982).

The Albian age sandstones from A-G1 well with CIA values varying between 57.24 % and 71.66 % with an average value of 62.23 % are likely to have been formed in a relatively cold environment while A-W1 samples having a CIA value that ranged from 6.10 % – 76.00 % with an average of 57.01 % could formation under cold environment and A-K1 well samples with CIA values varying from 10.53 – 74.03 % with an average of 61.65 % also reflects a relatively cold environment but

tending towards the transition zone from cold to hot or humid zone. A large abundance of angular to sub-rounded quartz grains (Chapter five) could be typical of tectonic arkose (Folk, 1980), a characteristic sediment near uplifted basement. The source area uplifted and eroded so rapidly that sufficient time was not available for weathering to be completed. Another possibility is the probable existence of plagioclase rich arkose, due to its feldspathic constituent and again a case of rapid deposition short-circuiting weathering. The term climatic and tectonic arkose have been introduced to sedimentology to characterize sediments due to their high feldspar contents to climate (too cold or too dry) and rapid basement uplift respectively (Nguem, 2005).

### **6.7.3 Tectonic setting and source rock lithology of the source area**

On the basis of sandstone subdivision diagram modified from Crook (1974), the Albian sandstone samples were classified as quartz-rich and quartz-intermediate (Fig. 6.7.1). Quartz-intermediate sediments are indicative of Andean type active continental margin (Crook, 1974. The convergence type takes place when the surface of one plate is continental and other oceanic. It is maintained by subduction of oceanic plate beneath the continental plate; the oceanic lithosphere is consumed deep in the mantle below the continental margin (Pettijohn et al. 1987). The Albian age reservoir sands are immature to mature litharenite and greywackes (Fig. 6.7.2). Thus, suggesting supracrustal provenance (volcanic, low grade metamorphic and sedimentary rocks) (Pettijohn et al. 1987)

Various authors have utilized bivariate plots based on major element geochemistry, developed by Bhatia (1983), to investigate the tectonic setting of greywackes (McCann, 1991; Holail and Moghazi, 1998). The four tectonic settings defined by Bhatia (1983) are the oceanic island arc (OIA), passive margin (PM), active continental margin (ACM) and continental island arc (CIA). The significant enrichment of  $\text{SiO}_2$  and depletion in  $\text{Al}_2\text{O}_3$ ,  $\text{TiO}_2$ ,  $\text{Na}_2\text{O}$  and  $\text{CaO}$  and also the ratio of  $\text{K}_2\text{O}/\text{Na}_2\text{O}$  that is greater than one in the Albian sandstone samples in the wells under investigation in this study indicates passive margin history of these samples (Nguem, 2005). This is in agreement with the previous work done on the tectonic settings of Orange Basin which was indicated as passive margin nature by Hirsch et al. (2007).

## **6.8 General Diagenetic Sequence for the Studied Wells**

The diagenetic sequence was developed by the examination of the relative occurrence of the various diagenetic products. The diagenetic features that occurred at the earlier stages before burial may no longer exist in these samples due to dissolution and replacement. Based on thin section analysis, scanning electron microscopic (SEM), x-ray diffraction (XRD) and high resolution transmission electron microscopic (HR-TEM) results, a schematic generalized paragenetic sequence is provided in figures 6.8.1, 6.8.2 & 6.8.3.

### **Compaction**

Variation in intergranular volume among these samples results from the differences in mineral composition, detrital matrix content and authigenic cement. Mechanical compaction was largely inhibited after quartz overgrowth and carbonate cements developed.

### **Chlorite Authigenesis**

Authigenic grain coating components are present in all samples in each of the wells though A-G1 exhibits more of kaolinite than chloritic clay. Well developed grain coating chlorite clay occurs as blades and rosette shape which are attached to the framework grains. Textural relationships indicate that chlorite formed before quartz overgrowth in all the diagenetic models constructed (Figs. 6.8.2 & 6.8.3) except for A-G1 well whereby it forms almost contemporaneously with quartz overgrowth.

### **Feldspar Overgrowth**

Minor amount of plagioclase overgrowth are developed on detrital plagioclase grains, partially occluding adjacent intergranular pores. Microscopic examination of thin sections for each well reveals that several plagioclase overgrowths have been incorporated by quartz cement.

### **Quartz Overgrowth**

Due to the rigidity of quartz overgrowth cement and its resistance to later dissolution processes, it is considered a major inhibitor of mechanical compaction until the burial pressure exceeds the compressive strength of quartz.

### **Fe-calcite**

Ferroan-calcite is the most significant cementing material especially in A-K1 and A-W1 wells occurring as pore filling cement. It exhibits a variable patchy distribution, and occurs in minor amounts. Trace amount of ferroan-calcite are associated with the

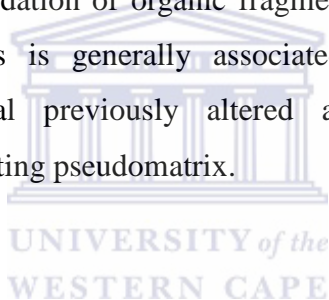
replacement of detrital grains, matrix clays and/or fossil fragments indicating that is also forms as relatively mid-late cement.






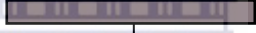






#### **Authigenic pore filling clay**

Kaolinite which is more significant in A-G1 well was detected in every sample by examination of the thin sections and SEM analysis, kaolinite occurs as pore filling or as replacement of feldspar. Both intergranular and dissolution pore types are filled by kaolinite, at the later stage probably due to increase in temperature with depth of burial, the illitization of kaolinite took place thereby transforming the kaolinite into illite which could be responsible for the low permeability in the sampled reservoir (Table 5.3).

#### **Iron/Titanium Oxides**



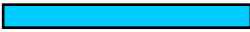








Titanium oxides and/or Fe/Ti oxides are present in all samples but in variable quantity across the wells (Table 6.2, 6.2.1, 6.2.2), it usually occurs as a structural replacement of less stable grains. The oxidation of organic fragments and/or organic material in argillaceous lithic fragments is generally associated with late-stage diagenetic processes. However, several previously altered argillaceous fragments were compacted during burial, creating pseudomatrix.



Diagenetic events	Early	Middle	Late
Mechanical infiltration of detrital clay			
Physical compaction			
Chlorite authigenesis			
Opaque minerals Precipitation			
K-feldspar overgrowth			
Carbonate cementation			
Mica formation			
Grain dissolution			
Quartz overgrowth			
Kaolinite formation			
Illitization of kaolinite			
Iron & Titanium Oxides			

**Figure 6.8.1:** Paragenetic sequence of reservoir sandstone of the Albian formation, well A-G1.













**Note:** No time scale implied

Diagenetic events	Early	Middle	Late
Mechanical infiltration of detrital clay			
Physical compaction			
Chlorite authigenesis			
Opaque minerals Precipitation			
K-feldspar overgrowth			
Fe-rich calcite			
Mica formation			
Grain dissolution			
Quartz overgrowth			
Authigenic pore-filling clays			
Chloritization of kaolinite			

**Figure 6.8.2:** Paragenetic sequence of reservoir sandstone of the Albian formation, well A-K1.

**Note:** No time scale implied



Diagenetic events	Early	Middle	Late
Mechanical infiltration of detrital clay			
Physical compaction			
Chlorite authigenesis			
Opaque minerals Precipitation (Hematite & pyrite)			
K-feldspar overgrowth			
Fe-rich calcite			
Mica formation			
Grain dissolution			
Quartz overgrowth			
Authigenic pore-filling clays			
Chloritization of illite			
Iron Titanium Oxides			

**Figure 6.8.3:** Paragenetic sequence of reservoir sandstone of the Albian formation, well A-W1.

**Note:** No time scale implied

## CHAPTER SEVEN

### 7.0 **Conclusions and Suggestions for future work**

---

---

The sandstone reservoir units intersected in the five wells were comprehensively investigated using various methods. The geophysical log signatures in all the five wells studied generally show a good quality due to borehole conditions. However, SP log and caliper log show very poor signatures and it has been reported in the well completion report to be poor due to borehole rugosity.

#### 7.1 **Core and Well Log**

✚ The three wells studied (A-G1, A-K1 and A-W1) with core samples were examined in details and therefore classified into three lithofacies associations on the basis of lithological description. Three lithofacies were delineated in this study, these include

- (i) Fine grained sandstone (F1)
- (ii) Very fine grained siltstone (F2)
- (iii) Mudstone (F3)

Lithofacies association F1 contains medium-coarse massive sandstone, and minor climbing ripples with some parallel lamination in A-G1 well while A-K1 well reveals some current ripple laminations, mud drapes and soft sediment deformation and A-W1 shows a massive sandstone with burrowing structures, soft sediment deformation and mud drapes within it. This facies reflects mostly a fluvial environment with a marine offshore transition zone. The decreasing in grain size (upward coarsening sequence) in A-K1 lithofacies F2 might have been caused by progressive sediment accumulation and hinterland denudation.

✚ Generally, the three studied wells reflect transgressive-regressive sea-level changes with regards to the sequence stratigraphic interpretation carried out within the reservoir interval. Wireline log results reveal that most of the reservoirs span between Lowstands and Highstand with few within the Transgressive system tracts while petrophysical evaluation reveals high water saturation within most of the reservoir intervals. The log derived porosity has average of about 15, 14 and 15 % and permeability of 2.05, 1.00 and 0.01 mD in A-G1, A-W1 and A-K1 respectively. Thus suggesting poor to fair reservoir quality.

- ✚ Both Core description and wireline results indicate that the reservoirs are sealed by marine shale.

## 7.2 Petrography and geochemical characteristics

- ✚ The primary detrital mineralogy in the sandstone samples within the reservoir intervals of the wells studied (A-G1, A-K1 & A-W1) was originally quartz, K-feldspar and mica and were identified as greywacke and litharenite from major oxides results. The authigenic assemblages present are chlorite, illite, calcite, quartz (cement and microquartz), pyrite, hematite and minor amount of mica.
- ✚ The mineralogical composition and texture of the sandstone samples in the studied wells suggest that the rocks have undergone high-grade diagenesis to low-grade regional metamorphism. Authigenic clays like chlorite and illite have been reported to have being formed during mesogenetic period with an approximate burial temperature and depth of 70 °C and >2 km respectively (Morad et al., 2000). The observed authigenic clays (Chlorite, illite and kaolinite) within the Albian age of the wells studied fall at depths greater than 2 km which agrees with the previous work done by Morad et al. (2000) in other basin.
- ✚ The relative timing of diagenetic processes in all the wells studied (A-G1, A-K1 & A-W1) are suggested to be mica and K-feldspar weathering and alteration to kaolinite, pore filling and alteration of kaolinite to illite especially in A-G1. This was followed by the ductile deformation of detrital chlorite and the formation of quartz overgrowths while the movement of formation waters was still relatively unrestricted and porosity and permeability much higher, authigenic chlorite was finally formed.
- ✚ The studied wells (A-G1, A-K1 & A-W1) are generally more siliciclastic with less lithic fragments. Overall, the sandstone samples are more of medium grained with better sorting and less angular. A possible reason for this might be a relatively longer transport distance of the sediments to the younger environment where deposition took place.
- ✚ Cementation of these sandstones samples appears to have been initiated with calcite crystallization followed by Fe calcite and silica cements. The plot of  $K_2O$  vs.  $Na_2O$  revealed that the source area of these sandstone samples as quartz-rich and intermediate rock with their tectonic settings attributed to a

passive margin history due to enrichment of  $\text{SiO}_2$  with corresponding depletion of other major oxides.  $\text{Al}_2\text{O}_3$ ,  $\text{Na}_2\text{O}$ ,  $\text{CaO}$ .

- ✚ The oxides in the sandstones are concentrated in the following minerals:  $\text{Al}_2\text{O}_3$  in illite, K-feldspar and albite;  $\text{TiO}_2$  in mica and illite,  $\text{Fe}_2\text{O}_3$  in chlorite and illite;  $\text{Na}_2\text{O}$  in albite and  $\text{K}_2\text{O}$  in illite and K-feldspar. Based on these, there is a very little variation between sandstones from each of the studied wells.
- ✚ The results of XRD semi-quantitative analysis carried out on some selected samples across the studied well agreed with the geochemical classification (litharenite and greywacke) with respect to percentages of quartz present in different reservoir intervals of each well.
- ✚ The mineralogical and pore water geochemical data from the sandstone samples from the Albian age samples show that there was loss of K-feldspar and kaolinite and a sharp increase in illite content presently at the depths greater than 2km with the exception of A-G1 well where kaolinite was present throughout the sampled core. The low wt %  $\text{K}_2\text{O}$  categories from the studied well show a decline in K-feldspar with decreasing kaolinite and increasing illite content in sandstone. Illitization and redistribution and conservation of potassium are therefore interpreted to have taken place in a relatively closed system and to have been controlled by local availability of potassium.

### 7.3 Pore water geochemistry

- ✚ Pore water geochemistry revealed a combination of processes including subsurface calcite dissolution, late burial precipitation of Fe-chlorite, meteoric water infiltration in the studied wells. This is characterized by the alternate decrease and increase in pH values along the depths.

### 7.4 Suggestions for future work

- ✚ Stable isotope analysis of  $\delta^{13}\text{C}$  &  $\delta^{12}\text{C}$  and  $\delta^{18}\text{O}$  &  $\delta^{16}\text{O}$  of the samples in order to ascertain the isotopic composition of the precipitating pore fluids and/or temperature of mineral formation which in-turn could reveal the depositional environments.
- ✚ Analysis of pore water of these samples from these wells for cations and anions are also recommended to adequately understand the distribution of the different minerals observed.
- ✚ Seismic interpretation is also suggested to look into the trapping system of the studied well.

## REFERENCES

---

- Abu El Ata, A.S.A., and Basal, A.M.K (1989).** Lithology make-up identification and determination, using well logging analysis: clays model: In Aly, S.A, El-Sayed, M., & El-Shawadfy, A., (2003) Application of well logs to assess the effect of clay minerals on the Petrophysical parameters of Lower Cretaceous reservoirs, North Sinai, Egypt
- Adams, S.S., Curtis, H.S., Hafen, P.L., (1974).** Alteration of detrital magnetite–ilmenite in continental sandstones of the Morrison Formation, New Mexico. Formation of Uranium Ore Deposits. International Atomic Energy Agency, Vienna, pp. 219– 253.
- Ahmad, A.H.M., Bhat, G.M., (2005).** Petrofacies, provenance and diagenesis of the dhosa sandstone member (Chari Formation) at Ler, Kachchh sub-basin, Western India
- Allen J.R.L. (1984).** Current Ripples; their Relationship to Patterns of Water and Sediment Motion. North-Holland publishing Company, Amsterdam, pp. 433
- Al-Ramadan, K., Morad, S., Proust, J.N., and Al-Asam, I., (2005).** Distribution of diagenetic alterations in siliciclastic shoreface deposits within a sequence stratigraphic framework: evidence from the Upper Jurassic, Boulonnais, NW France. Journal of Sedimentary Research, **75**, pp. 943-959.
- Altaner, S.P., Ylagan, R.F., (1997).** Comparison of structural models of mixed layer illite/smectite and reaction mechanisms of smectite illitization. Clays and Clay Minerals **4**, pp. 517-533.
- Arostegui, J., (1989).** La diagénesis en los materiales pelíticos de la zona central de la Cuenca Vasco-Cantábrica y Anticlinorio de Bilbao. Ph.D thesis, Universidad del País Vasco, Spain, pp. 222
- Arostegui, J., Sanguesa, J., Nieto, F., Uriarte, J.A., (2006).** Thermal models and clay diagenesis in the Tertiary-Cretaceous sediments of the Alava block (Basque-Cantabrian Basin, Spain). Clay Minerals **41**, pp. 791-809.
- Baas, J.H. (2003)** Ripple, ripple marks and ripple structure. In Encyclopaedia of Sediment and Sedimentary Rocks (Middleton, G.V., ed.), pp. 565-568. Springer.
- Baker, J. C., Havord, P.J., Martin K.R., and Ghori, A.R., (2002) Diagenesis and Petrophysics of Early Permian Moogooloo Sandstone, Southern Carnarvon Basin, Western Australia: AAPG Bulletin, Vol. 84, pp. 250-265.

- Basan, P.B., (ed.) 1(1978).** Trace Fossils Concepts, SEPM Short Course No. 5. pp. 142 – 143.
- Bassoioni, Z., (1994).** Theory, measurement, and interpretation of well logs. SPE Text book series Vol. 4. pp. 92 - 339
- Bateman, R. (1985).** Open hole log analysis and formation evaluation: Boston International Human Resources Development Corporation pp. 647.
- Beard, D.C., Weyl, P.K., 1973.** Influence of texture on porosity and permeability of unconsolidated sand. Bulletin of the American Association of Petroleum Geologists 57, pp. 349–369.
- Ben Avraham, Z., Smith, G., Recife and Jungslager, E., (2002).** Gas hydrate and mud volcanoes on the South African continental margin off South Africa. Geology, 30 (10), pp. 927-930.
- Berner, R.A., (1970).** Sedimentary pyrite formation American Journal of Science 268, pp. 1-23.
- Berner, R.A., (1981)** A new geochemical classification of sedimentary environments. J. Sediment. Petrol. 51, pp. 359–365.
- Bjørkum, P. A. (1996).** How important is pressure in causing dissolution of quartz in sandstones? Journal of Sedimentary Research, 66, pp. 147–154.
- Bjørkum, P. A., Mj-s, R., Walderhaug, O. and Hurst, A. (1990).** The role of the late Cimmerian unconformity for the distribution of kaolinite in the Gullfaks Field, northern North Sea Sedimentology 37, pp. 395-406.
- Bjørlykke, K. Aagard, P., & Egerberg K., (1995).** Geochemical constraints from formation water analyses from the North Sea and Gulf Coast Basins on quartz, feldspar and illite precipitation in reservoir rocks. The Geochemistry of Reservoir Geological Society Special publication No. 86. pp. 33 – 50.
- Bjørlykke, K., (1983).** Diagenetic reactions in sandstones. In: Parker, A., Sellwood, B.W. (Eds.), Sediment Diagenesis. Reidel Publishing, Holland, pp. 169–213.
- Boyles J.M., Scott A.J. (1982)** A model for migrating shelf bar sandstones in upper Mancos shale (Campanian) north-western Colorado. A.A.P.G. Bulletin 66, pp. 491-508.
- Broad, D., (2004).** South Africa Activities and Opportunities, an unpublished Power Point Presentation to PetroChina.
- Brown, L.F. Jr., Benson, J.M., Brink, G.J., Doherty, S., Jollands, A., Jungslager, E.H.A., Keenan, J.H.G., Muntingh, A. and Van Wyk, N.J.S (1996).** Sequence

stratigraphy in offshore South Africa divergent basins. An atlas on exploration for Cretaceous Lowstand traps by SOEKOR (Pty) Ltd A.A.P.G. Stud. Geol., 41, pp 184.

**Bucher, W.H. (1919).** On ripples and related sedimentary surface forms and their paleogeographic interpretation. American Journal of Sciences, 47, pp. 149 – 210, 241 – 241 – 269.

**Cannon, D.E., and Coates, G.R., (1990).** Applying Mineral Knowledge to Standard Log Interpretation SPWLA 31<sup>st</sup> Annual Logging Symposium. Pp. 6-24.

**Carlos A. C (1997).** Well-to-well log correlation: choosing the matching attribute, Stanfor Exploration project

**Catuneanu, O., (2002).** Sequence stratigraphy of clastic systems: concepts, merits, and pitfalls, Journal of African Earth Sciences, Volume 35, Issue 1, pp. 1-43

**Catuneanu, O., (2006).** Principles of sequence stratigraphy, Elsevier pp. 375.

**Chiba, H., (1995).** Chemical modeling of sea water-rock interaction: effect of rock-type on the fluid chemistry and mineral assemblage. Eds. H. Sakai and Y. Nozaki, pp. 469-486. Terra scientific publishing company, Tokyo

**Choquette, P. W., & Pray, L., (1970).** Geologic nomenclature and classification of porosity in sedimentary carbonates. American Association Petroleum Geologists Bulletin, 54, pp. 207–250.

**Cody, J., Youn, S., Riddy, A. and Gittins, S. (2001).** Implication of Reservoir “Compartments” on the design and execution of Christina Lake Thermal Recovery Project. PanCanadian Resources, 150-9<sup>th</sup> Avenue, Calgary AB.

**Cookenboo H.O., Bustin R.M (1998).** Pore water evolution in sandstones of the Groundhog Coalfield, northern Bowser Basin, British Columbia. Sedimentary Geology 123, (1999) pp. 129–146.

**Crain, E.R. (2004).** Crain’s Petrophysical Handbook: Canada, Spectrum 2000 Mindware, 3rd Millennium Edition. URL: <http://www.spec2000.net/lcmain.htm>

**De Ros, L.F., (1998).** Heterogeneous generation and evolution of diagenetic quartzarenites in the Silurian–Devonian Furnas Formation of the Parana Basin, southern Brazil. Sedimentary Geology 119, pp. 99–128.

**Dingle, R.V, Siesser, W.G & Newton, A.R (1983).** Mesozoic and Tertiary Geology of Southern African. A.A. Balkema/Rotterdam. pp. 99-106.

**Douglas J.C. (1987).** Subsurface Facies Analysis, Geological Survey of Canada, 3303-33<sup>rd</sup> St. N.W Calgary, Alberta.

**Doveton, J.H. (1986).** Log analysis in subsurface geology: New York, NY, John

Eastern England. Sed. Geol Vol. 131 pp. 77-86.

**Ehrenberg, S. N., Aaraard, P., Wilson, M. J., Fraser, A. R. and Duthie, D.M.L., (1993).** Depth-dependent transition of kaolinite to dickite in sandstones of the Norwegian Continental Shelf Clay Miner. 28, pp. 325-352.

**El-ghali, M.A.K, Morad, S., Mansurbeg, H., Miguel, A.C., Sirat, M., Ogle, N., (2008).** Diagenetic alterations related to marine transgression and regression in fluvial and shallow marine sandstone of Triassic Buntsandstein and Keuper sequence, the Paris Basin, France.

**Embry, A.F., Johannessen, E.P., (1992).** T–R sequence stratigraphy, facies analysis and reservoir distribution in the uppermost Triassic- Lower Jurassic succession, western Sverdrup Basin, Arctic Canada. In: Vorren, T.O., Bergsager, E., Dahl-Stamnes, O.A., Holter, E., Johansen, B., Lie, E., Lund, T.B. (Eds.), Arctic Geology and Petroleum Potential, vol. 2 (Special Publication). Norwegian Petroleum Society (NPF), pp.121–146.

**Emerson, D.W., (2000).** The Petrophysics of Hawkesbury Sandstone- A preliminary study in G.H McNally and B.J. Franklin, eds., Sandstone City: Sydney's Dimension Stone and Other Sandstone Geomaterials: Sydney, Geological Society of Australia, Environmental and Hydrogeology Specialist Group, Monograph 5. pp. 197-213.

**Emery, D., and Myers, K.J., (1996).** Sequence stratigraphy: Oxford, Blackwell Science, pp. 297.

**Fedo, C. M., Nesbitt, H. W., Young, G. M., (1995).** Unraveling the Effects of Potassium Metasomatism in Sedimentary Rocks and Paleosols, with Implications for Paleoweathering Conditions and Provenance. *Geology*, 23: 921–924

**Fanning, D.S., Keramidas, V.Z., El-Desoky, M.A., (1989).** Micas, In: Dixon, J.B., Weed, S.B. (Eds.), Minerals in Soil Environments, 2nd edition. Published by Soil Science Society of America, Madison, WI, pp. 1–634.

**Folk, R.L., (1980).** Petrology of Sedimentary Rocks. Hamphill, Austin, Texas, p. 182. France.

**Frost, E.J., Fertl, W.H., (1981).** Integrated Core and Log Analysis Concepts in Shaly Clastic Reservoir: The Log Analyst, Vol. 22, pp. 3-16.

**Garrels, R.M., Christ, C.L., (1965).** Solutions, Minerals and Equilibria. Harper and Row, New York, pp. 172– 266.



- Gautier, D.L., Claypool, G.E., (1984).** Interpretation of methanic diagenesis in ancient sediments by analogy with processes in modern diagenetic environments. In: McDonald, D.A., Surdam, R.C. (Eds.), *Clastic Diagenesis*. Am. Assoc. Pet. Geol. Geology, Tulsa, OK, US, pp. 197–208.
- Gerhard, E., (2000).** *Sedimentary Basins—Evolution, Facies and Sediment budget*. Springer-Verlag, New York.
- Gize, A.P., (1985b).** The development of thermal mesophase in bitumens from high temperature ore deposits. In: Dean, W.E (ed), *Organics in ore deposits*. Proceedings of the Denver Region Exploration Geologists Society Symposium pp. 137 – 150.
- Grecula, M. Flint S., Wickens, deV, H., Johnson, S., (2003).** Upwards-thickening patterns and lateral continuity of Permian sand rich turbidite channel fills, Laingsburg Karoo, South Africa. *Sedimentology* 50, pp. 831-853.
- Guest, K., (1990).** The Use of Core-derived Quantitative Mineralogical Data to improve Formation Evaluation: European Core Analysis Symposium. Pp. 187-29
- Haq, B.U., Hardenbol, J. and Vail, P.R., (1988).** Mesozoic and Cenozoic chronostratigraphy and eustatic cycles of sea-level change. In: *The geology of South Africa* edited by M.R Johnson, C.R Anhaesser and R.J Thomas. 2006.
- Harris, N.B., (1992).** Burial diagenesis of Brent sandstone: a study of statford, hutton and Lyell fields. In: Morton, A.C., Haszeldine, R.S., Giles, M.R., Brown, S. (Eds.), *Geology of the Brent Group*, Geological Society, London. Special Publications, vol. 61, pp. 351– 376.
- Harris, P.M., Kendall, C.G.S.C. & Lerche, I. (1985).** Carbonate cementation – a brief review In: *carbonate cements* (Eds Schneidermann, N. & Harris, P.M.) Spec. Publ. Soc. Econ. Paleont. Miner, Tulsa, 36, 79-95.
- Harris, P.M., Kendall, C.G.S.C. and Lerche, I., (1985).** Carbonate cementation: a brief review. In: Molenaar, N. Zijlstra, J.J.P. *Differential early diagenetic low-Mg calcite cementation and rhythmic hardground development in Campanian-Maastichtian chalk*. *Sedimentary Geology* Vol. 109, pp. 261 – 281.
- Harwood, G., (1988).** *Microscopic Techniques II: Principles of Sedimentary Petrography*, in Tucker, ed., *Techniques in Sedimentary*: Oxford, Blackwell, pp. 108-173.
- Hean C.L., Ebanks W. J., Tye R.S. & Ranganathan V. (1984).** Geological factors influencing reservoir performance of the Hartzog Draw Field, Wyoming. *J. Petrol. Tech.* August, pp. 1335-1344.

- Helland-Hansen, W., Martinsen, O.J., (1996).** Shoreline trajectories and sequences: description of variable depositional-dip scenarios. *Journal of Sedimentary Research* 66 (4), 670–688.
- Hemley, J. J., (1962).** Alteration studies in the systems  $\text{Na}_2\text{O}-\text{Al}_2\text{O}_3-\text{SiO}_2-\text{H}_2\text{O}$  and  $\text{K}_2\text{O}-\text{Al}_2\text{O}_3-\text{SiO}_2-\text{H}_2\text{O}$  (abst.). Abstracts for 1961. *Geol. Soc. Amer. Spec. Paper*, 68, pp.196.
- Hillier, S., (1995).** Erosion, sedimentation and sedimentary origin of clays. In: Velde, B. (Ed.), *Origin and Mineralogy of Clays. Clays Environment*, Springer, Berlin, pp. 162-219.
- Hirsch K.K., Scheck-Wenderoth M., Paton D.A, di Primo R., Horsfield B., Cloetingh S.A.P.L F. Beekman F. (2007).** 3D Gravity Modeling and Subsidence Analysis in the Orange Basin, Southwest African Continental Margin *Geophysical Research Abstract*, Vol. 9, 06275.
- Houseknecht, D.W., Pittman, E.D. (Eds.), (1987).** Origin, diagenesis, and petrophysics of clay minerals in sandstone. *Soc. Econ. Paleont. Mineral. Spec. Publ.*, 47-65.
- Howard, J.J., (1992).** Influence of authigenic clay minerals on permeability. In: Hunt, D., and Tucker, M.E., (1992). Stranded parasequence and the forced regressive wedge systems tract: deposition during base-level fall, *Sedimentary Geology*, 81, pp. 1-9.
- Hunt, D., and Tucker, M.E. (1995).** Stranded parasequence and the forced regressive wedge systems tract: deposition during base-level fall-reply, *Sedimentary Geology*, 95, pp. 147-160.
- Hurst A., (1984).** The role of sedimentary facies in the control of clay mineral diagenesis in sandstones: examples from the North Sea. *Clay Minerals Soc. Ann. Meeting, Baton Rouge*, abstracts, 64.
- Hurst, A., and Nadeau, P.H., (1995).** Clay microporosity in reservoir sandstones: an application of quantitative electron microscopy in petrophysical evaluation. *American Association of Petroleum Geologists*, 79, pp. 563-573.
- Hutcheon, I., Oldershaw, A., Ghent, D., (1980).** Diagenesis of Cretaceous sandstones of the Kootenay Formation at Elk Valley (south-eastern British Columbia) and Mt. Allan (south-western Alberta). *Geochimica et Cosmochimica Acta* 44, pp. 1425-1435.

- Islam M. A., (2009).** Diagenesis and reservoir quality of Bhudan sandstones (Neogen) Titas Gas Field, Bengal Basin, Bangladesh. *Journal of Asian Earth Sciences* 35 pp. 89 – 100.
- Jahasz, I., (1990).** Core Analysis – Opportunity and Challenges in the 1990's: Europe Core Analysis Symposium, pp. 1-15.
- Jahren, J. S., (1990).** Evidence of Ostwald ripening related recrystallization of diagenetic chlorites from reservoir rocks offshore Norway. *Clay minerals* vol. 26 pp. 169-178.
- Jikelo, A.N. (2000).** Petroleum Prospectivity of deepwater orange Basin, South Africa Petroleum Agency S.A Parow South Africa.
- Jinliang Zhang., Linjuan Qin., Zhongjie Zhang., (2007).** Depositional facies, diagenesis and their impact on the reservoir quality of Silurian sandstones from Tazhong area in central Tarim Basin, western China. College of Marine Geology, Ocean University of China, Qindao 266003, China.
- Kaufman, R.L Ahmed A.S, Elsinger, R.J (1990).** Gas Chromatography as development and production tool for fingerprinting oils from individual reservoir: application in the Gulf of Mexico. GCSSEPM Foundation 9<sup>th</sup> Annual research conference proceeding, October 1 pp. 263 – 282.
- Keller, W. D., (1978).** Classification of kaolinite exemplified by their textures in scan electron micrographs *Clays Clay Miner.* 26, 1-20.
- Kenneth M. T., (1962).** Clay Mineral Diagenesis as a Possible Source of Silica Cement in Sedimentary Rocks. Abstract from *Journal of Sedimentary Research*, Vol. 32.
- King, G. E., (1992).** Formation clays: Are they really a problem in production. In: Houseknecht, D. W. and Pittman, E. D., eds., *Origin, diagenesis and petrophysics of clay minerals in sandstones*, Oklahoma, SEPM special publication no. 47, pp. 264 – 272.
- Knarud, R. and Bergan, M., (1990).** Diagenetic history of Upper Triassic-Lower Jurassic alluvial sandstones and mudstones of the Lunde and Statfjord Formations, Snorre Field, Norwegian North Sea [abstract]. In: 13th International Sedimentological Congress, Nottingham, UK, pp. 276-277.
- Kuhlmann G. Paton D. di Primio, Van der spuy D, Horsfield B. (2007).** Petroleum system modeling at a passive continental margin settling, Orange Basin (South Africa). *Jahrestagung der Afrikagrupe deutscher Geowissenschaftler (Postdam)*.

- Kunle, D., Mojisola A. (2004).** Relationship between reservoir properties of the Galesville sandstone and diagenesis of Eau Claire shale, Cambrian of Illinois Basin. AAPG Annual meeting Dallas, Texas. Bulletin Vol. 88 (2004) pp. 13.
- Lambert-Aikhiobare, D.O., Shaw, H.F., (1982).** Significance of clays in the petroleum geology of the Niger Delta. Clay Minerals vol. 17, pp. 91-103.
- Lee, K., Tomasso, M., and Ambrose, W.A., (2007).** Integration of GPR with stratigraphic and lidar data to investigate behind-the-outcrop 3D geometry of a tidal channel reservoir analog, upper Ferron Sandstone, Utah. Bureau of Economic Geology, Austin, USA. The leading edge Abstract vol. 26 pp. 994 – 998. Society of Exploration Geophysicists.
- Lemon, N.M., Cubitt, C.J., (2003).** Illite fluorescence microscopy: a new technique in the study of illite in the Merrimelia Formation, Cooper Basin, Australia. In: Worden, R.H., Morad, S. (Eds.), Clay Mineral Cements in Sandstones, vol. 34. International Association of Sedimentologists (Special Publication), pp. 411–424.
- Lewis, D.W., and McConchie, D., (1994).** Analytical sedimentology: New York, Chapman Hall, pp. 197.
- Lofts, J., Harvey, P. and Lovell, M., (1995).** Reservoir characterization from down hole, mineralogy, marine and petroleum Geology Vol. 12. No 3 pp. 233- 246.
- Lovely, D.R. (1991).** Dissimilatory Fe (III) and Mn (IV) reduction: Microbiology Review, V. 55, pp. 259-287.
- Martinius, A. W. & Molenaar, N., (1991).** A coral-mollusc (*Goniaraea-Crassatella*) dominated hardground community in a siliciclastic-carbonate sandstone (the lower Eocene Roda Formation, southern Pyrenees, Spain). SEPM Society for Sedimentary Geology. Vol. 6; pp. 142 – 155.
- McAulay, G.E., Burley, S.D. and Johnes, L.H. (1993).** Silicate mineral authigenesis in the Hutton and NW Hutton fields: implications for sub-surface porosity development. In: Petroleum Geology of Northwest Europe: Proceedings of the 4th Conference (Ed. J. R. Parker), Geological Society, London, pp. 1377-1394.
- McHardy W.J., Wilson M.J. and Tart J.M., (1982).** Electron microscope and X-ray diffraction studies of filamentous illite clay from sandstones of the Magnus Field. Clay Miner. 17, pp. 23-29.
- McHardy, W.J., Wilson, M.J., Wilson, J.M.J., and Tait, J.M., (1982).** Electron Microscope and X-ray Diffraction Studies of Filamentous Illitic Clay from Sandstones of the Magnus Field: Clay Minerals, V. 17 pp. 23-39 Mem. 37, 111–123.

- Milliken, K.L., (1989).** Petrography and composition of authigenic feldspars, Oligocene Frio formation, South Texas. *Journal of Sedimentary Petrology* 59, pp. 361–374.
- Mitchum Jr., R. M., (1977).** Seismic Stratigraphy and Global Changes of Sea Level: Part 11. Glossary of Terms used in Seismic Stratigraphy: Section 2. Application of Seismic Reflection Configuration to Stratigraphic Interpretation, *Memoir* 26 pp. 205 - 212.
- Moody, G.B (1961).** *Petroleum Exploration Handbook, A practical Manual Summarizing the application of Earth Sciences to Petroleum Exploration.*
- Morad, S., (1998).** Carbonate cementation in sandstones; distribution patterns and geochemical evolution. In: Morad, S. (Ed.), *Carbonate Cementation in Sandstones.* International Association of Sedimentologists (Special Publication), vol. 26, pp. 1–26.
- Morad, S., Bergan, M., Knarud, R., Nystuen, J.P., (1990).** Albitization of detrital plagioclase in Triassic reservoir sandstones from the Snorre Field, Norwegian North Sea. *Journal of Sedimentary Petrology* 60, pp. 411–425.
- Morad, S., De Ros, L.F., (1994).** Geochemistry and diagenesis of stratabound calcite cement layers within the Rannoch Formation of the Brent Group, Murchison Field, North Viking Graben (northern North Sea); discussion and reply. *Sedimentary Geology* 93, pp. 135–147.
- Morad, S., Ketzer, J.M., De Ros, F., (2000).** Spatial and temporal distribution of diagenetic alterations in siliciclastic rocks: implications for mass transfer in sedimentary basins. *Sedimentology* 47 (Suppl. 1), pp. 95–120.
- Moraes, M.A.S., De Ros, L.F., (1992).** In: David, W.H., Edward, D.P. (Eds.), *Depositional Infiltrated and Authigenic Clays in Fluvial Sandstones of the Jurassic Sergi Formation, Reconcavo Basin, northeastern Brazil. Origin, diagenesis, and Petrophysics of clay minerals in sandstones*, vol. 47. SEPM, Society for Sedimentary
- Morris, K.A. and Shepperd, (1982).** The role of clay minerals in influencing porosity and permeability characteristics in the Bridport sands of Wytch farm, Dorset: *Clay minerals* Vol. 17, pp. 41 – 54.
- Muntingh, A. (1993).** Geology, prospect in Orange Basin offshore western South Africa: *Oil and Journal*, January 25 P. pp. 106 – 108.
- Nesbitt, H. W., Markovics, G., (1997).** Weathering of Granodioritic Crust, Long-Term Storage of Elements in Weathering Profiles, and Petrogenesis of Siliciclastic Sediments. *Geochimica et Cosmochimica Acta*, 61: 1653–1670

- Nesbit, H.W., Young, G.M., (1982).** Early Proterozoic climates and plate motions inferred from major element geochemistry of lutites. *Nature* 299, 715–717.
- Nguem, O.P., (2005).** Petrology, geochronology and provenance of the Laingsburg and Tanqua Karoo submarine fan systems, Ecca group, South Africa. M.Sc thesis, University of Stellenbosch, South Africa.
- Nieto, F., Ortega-Huertas, M., Peacor, D.R., Arostegui, J., (1996).** Evolution of illite/smectite from early diagenesis through incipient metamorphism in sediments of the Basque-Cantabrian Basin. *Clays and Clay Minerals* 44, pp. 304-323.
- Nyberg, Ø., Lien, K. Lindberg, P.A. and Smistad, J.K., (1978).** Mineral Composition, An Aid in classical Log Analysis Used in Jurassic Sandstones of Northern North Sea: SPWLA 19<sup>th</sup> Annual Logging Symposium
- Odin, G.S., (1982).** How to measure glaucony ages? In: Odin, G.S. (Ed.), *Numerical Dating in Stratigraphy*. Wiley, Chichester, pp. 387–403.
- Odin, G.S., (1985).** Significance of green particles (glaucony, berthierine, chlorite) in arenites. In: Zuffa, G.G. (Ed.), *Provenance of Arenites*. D. Riedel Publications, Dordrecht, pp. 279–307.
- Odin, G.S., Matter, A., (1981).** De glauconiarum origine. *Sedimentology* 28, pp. 611–641.
- Odom, I.E., (1984).** Glauconite and celadonite minerals. In *Evolution patterns of glaucony maturity: A mineralogical and geochemical approach*. Deep-sea Research II Vol. 54, pp. 1364-1374.
- Olajide, O., (2005).** The Petrophysical Analysis and Evaluation of Hydrocarbon Potential of Sandstone Units in the Bredasdorp Central Basin. Unpublished M.Sc thesis, University of the Western Cape, Cape Town. South Africa.
- Pallat, N., Wilson, M.J., and McHardy, W.J., (1984).** The relationship between permeability and the morphology of diagenetic illite in reservoir rocks: *J. Petrol. Tech.* 14, 2225- 2227. Paris, France.
- Paton, D.A., Di Primio, R., Kuhlmann, G., Van der Spuy, D. and Horsfield, B. (2007).** Insights into the Petroleum System Evolution of the southern Orange Basin, South Africa. *South African Journal of Geology*, Geological Society of South Africa, Volume 110, pp 261-274.
- Perry, E., Hower, J., (1970).** Burial diagenesis in Gulf Coast pelitic sediments. *Clays and Clay Minerals* 18, pp. 165-177.

**Petroleum Agency SA (2004/005/006/007).** Petroleum Exploration Information and Opportunities: Petroleum Agency Brochure.

**PetroSA Report, (2003).** Ibhubesi field Geological Evaluation Orange Basin, Block 2 South Africa.

**Pettijohn, F.J, Edwin, P., Siever, R., (1972).** Sand and Sandstone diagenesis: recent and ancient- Google Book pp. 462. Available Online at <http://books.google.co.za/books>

**Pittman, E.D., Larese, R.E., & Heald, M.T., (1992).** Clay coats: Occurrence and relevance to preservation of porosity in sandstones. In D. W. Houseknecht, & E. D. Pittman (Eds.), Origin, diagenesis, and petrophysics of clay minerals in sandstones (pp. 241–264). SEPM Special Publication 47, Society of Economic Paleontologists and Mineralogists.

**Plint, A.G., Nummedal, D., (2000).** The falling stage systems tract: recognition and importance in sequence stratigraphic analysis. In: Hunt, D., Gawthorpe, R.L. (Eds.), Sedimentary Response to Forced Regression, vol. 172. Geol. Soc. London Special Publ., pp. 1–17.

**Posamentier, H.W., Allen, G.P., (1999).** Siliciclastic sequence stratigraphy: concepts and applications. SEPM Concepts in Sedimentology and Paleontology no. 7, pp. 210.

**Posamentier, H.W., Jervey, M.T., Vail, P.R., (1988).** Eustatic controls on clastic deposition. I. Conceptual framework. In: Wilgus, C.K., Hastings, B.S., Kendall, C.G.St.C., Posamentier, H.W., Ross, C.A., Van Wagoner, J.C. (Eds.), Sea Level Changes—An Integrated Approach, vol. 42. SEPM Special Publication, pp. 110– 124.

**Posamentier, H.W., Vail, P.R., (1988).** Eustatic controls on clastic deposition. II. Sequence and systems tract models. In: Wilgus, C.K., Hastings, B.S., Kendall, C.G.St.C., Posamentier, H.W., Ross, C.A., Van Wagoner, J.C. (Eds.), Sea Level Changes—An Integrated Approach, vol. 42. SEPM Special Publication, pp. 125– 154.

**Pryor, W.A., (1973).** Permeability-porosity patterns and variations in some Holocene sand bodies. Bulletin of the American Association Petroleum Geologists 57, pp. 162– 189.

**Ramm, M., (2000).** Reservoir quality and its relationship to facies and provenance in Middle to upper Jurassic sequence, Northeastern North Sea: Clay Minerals, Vol. 35, pp. 77-95.

- Ramm, M., and BjØlykke, (1994).** Porosity/ Depth Trends in Reservoir Sandstones: Assessing the Quantitative effect of Varying Pore-Pressure, Temperature History and Mineralogy, Norwegian Shelf Data Clay Minerals, Vol. 29, pp. 475-490.
- Ramseyer, K., Diamond, L.W., & Boles, J.R., (1993).** Mechanism of plagioclase albitization. *Journal of Sedimentary Petrology*, 63, pp. 1092–1099.
- Reading, H.G., (1996).** Sedimentary environments: processes, facies and stratigraphy. Edition 3 pp. 688-1996.
- Reineck, H.E., and Singh, I. B. (1973).** Depositional Sedimentary Environments. With Reference to Terrigenous Clastics. Springer, Berlin, pp. 439.
- Rider, M., (1996).** The Geological Interpretation of Well Logs: Caithness, Whittles Publishing, pp. 280.
- Rider, M.H., (1996).** The geological interpretation of well logs .Petroleum Exploration consultant Rider-French consultant Ltd Cambridge and Sutherland. Halsted press, a division of John Wiley and Sons, New York.
- Rider, M.H., (1996).** The Geological interpretation of well logs. Petroleum Exploration Consultant, Rider-French Consulting Ltd. Halsted press, a division of John Wiley and Sons, New York.
- Rossi, C., Kalin, O., Arribas, A., and Tortosa, A., (2002).** Diagenesis, Provenance and Reservoir Quality of Triassic TAGI Sandstones from Ourhoud Field, Berkine (Ghadames) Basin, Algeria: *Marine and Petroleum Geology*, Vol. 19, pp. 117-142.
- Ryan, P.C. and Reynolds, R.C. JR. (1997).** The chemical composition of serpentine/chlorite in the Tuscaloosa formation, United States gulf coast: EDX vs. XRD determinations, implications for mineralogic reactions and the origin of anatase. *Clay and clay minerals*, Vol. 45. No. 3, pp.339-352.
- Sahay, B., (1999).** Pressure regime in oil and gas exploration. Allied publisher, Ltd., New Delhi 70. pp. 1999-475.
- Saigal, G.C., BjØrlykke, K. & Larter, S.R. (1992).** The effects of oil emplacements on diagenetic processes - Examples from the Fulmar Reservoir sandstones, Central North Sea. *American Association of Petroleum Geologist, Bulletin*, 76, pp. 1024 – 1033.
- Scheffler, K., Buehmann, D., Schwark, L., (2006).** Analysis of late Paleozoic glacial to postglacial sedimentary succession in South Africa by geochemical proxies response to climate evolution and sedimentary environment. *Paleogeography, paleoclimatology, paleoecology* 240: pp. 180-203.



- Schlumberger, (1972).** Log interpretation principles, volume I, Schlumberger Ltd.
- Schlumberger, (1972).** The essentials of log interpretation, practice, Schlumberger Ltd, Paris, France.
- Schlumberger, (1982).** Essentials of NGS, Introduction, Schlumberger Ltd., Paris,
- Schmid, S., Worden, R.H., & Fisher, Q.J., (2003).** Diagenesis and reservoir quality of the Sherwood Sandstone (Triassic), Corrib Field, Slyne Basin, west of Ireland. *Journal of Marine and Petroleum Geology* 21 (2004) pp. 310-312.
- Schwertmann, U., Taylor, R.M., (1989).** Iron oxides. In: Dixon, J.B., Weed, S.B. (Eds.), *Minerals in Soil Environments*, 2nd ed. Soil Science Society of America, Madison, WI, USA, pp. 379– 438.
- Selley R.C. (1997).** *Elemental Petroleum Geology Book*. Academic press, pp. 133 – 139.
- Selley, R.C. (1978).** Concepts and methods of subsurface facies analysis: American Association of Petroleum Geologists, Continuing Education Course Notes Series 9, p. 82.
- Serra, O. (1986).** *Development in Petroleum Science: Fundamentals of Well Log Interpretation 2. The Interpretation of Logging Data*, V. 15B: New York, Elsevier Science Publishing Company Inc., pp. 684.
- Serra, O. (1986).** *Fundamentals of well log interpretation, volume II: Developments in Petroleum Science*, El-Sevier. Publ. Co., Amsterdam.
- Serra, O., (1984).** *Fundamentals of Well Log Interpretation (Vol. 1): The Acquisition of Logging Data: Dev. Pet. Sci., 15A: Amsterdam (Elsevier).*
- Silverstein, R.M., Bassler, G.C and Morrill, T.C., (1974).** *Spectrometric identification of organic compounds (3<sup>rd</sup> edition)*. Wiley, London.
- SPWLA Glossary, (1984 – 1997).** URL: [www.spwla.org/library\\_info/glossary.htm](http://www.spwla.org/library_info/glossary.htm)
- Stevenson, I. R., and McMillan, I.K., (2004).** Incised valley fill stratigraphy of the Upper Cretaceous succession, proximal Orange Basin, Atlantic margin of southern Africa. *Journal of the Geological Society*, De Beers Marine, Geological Society Publishing House, pp. 1-18.
- Stuart, D.B, Richard, H.W., (2003).** *Sandstone diagenesis: recent and ancient-* Google Book. Available Online at <http://books.google.co.za/books>
- Swanson, J., (2001).** *Weathering Characteristics of Sandstones for Building Purpose from Eastern Australia*. In: *Influence of Mineralogy on Petrophysical Properties of*

Petroleum Reservoir Beds, M.Sc Thesis, University of New South Wales, Sydney, pp. 19-25.

**Tandon, S.K., Varshney, S.K., (1991).** Origin of selective carbonate cemented (concretionary) layers within multistoried sandstone bodies of the Neogene Middle Siwalik Subgroup, NW Hima- P. Sanyal et al. / *Sedimentary Geology* 180 (2005) 57–74 73 laya, India. Abstract, Birbal Sahni Birth Centenary Symposium on the Siwalik Basin, WIHG, Dehra Dun, India, pp. 45.

**Taylor, J.M., (1950).** Pore-space reduction in sandstones. *Bulletin of the American Association Petroleum Geologists* 34, pp. 701–716.

**Taylor, K.G., Macquaker, J.H.S., (1999).** Early diagenetic pyrite morphology in a mudstone-dominated succession: the Lower Jurassic Cleveland Ironstone Formation, **Theodoor W.F., (2000).** Petrophysical properties from small rock samples using image analysis techniques, ISBN 90-9014-338-6.

**Tokar, F.J., and Evans, J.E., (1993).** Depositional environments of the pictured cliffs sandstone, Late Cretaceous near Durango, Colorado. *Ohio Journal of science*, Vol. 4, pp. 83-89.

**Vail, P.R., (1987).** Seismic stratigraphy interpretation procedure. In: Bally, A.W. (Ed.), *Atlas of Seismic Stratigraphy*, vol. 27. American Association of Petroleum Geologists Studies in Geology, pp.1–10.

**Van der Plas, L., and Tobi, A.C., (1965).** A Chart for Judging the Reliability of Point Counting Results: *American Journal of Science*, vol. 263, pp. 87-901.

**Van Wagoner, J.C., Mitchum Jr., R.M., Campion, K.M., Rahmanian, V.D., (1990).** Siliciclastic sequence stratigraphy in well logs, core, and outcrops: concepts for high-resolution correlation of time and facies. *American Association of Petroleum Geologists Methods in Exploration Series* 7, pp. 55.

**Van Wagoner, J.C., Mitchum, R.M., Campion, K., and Rahmanian, V.D., (1990).** *Siliciclastic Sequence Stratigraphy in well Logs, Cores and Outcrops*: American Association of Petroleum Geologists, Tulsa, pp. 55.

**Van Wagoner, J.C., Posamentier, H.W., Mitchum, R.M., Vail, P.R., Sarg, J.F., Loutit, T.S., Hardenbol, J., (1988).** An overview of sequence stratigraphy and key definitions. In: Wilgus, C.K., Hastings, B.S., Kendall, C.G. St. C., Posamentier, H.W., Ross, C.A., Van Wagoner, J.C. (Eds.), *Sea Level Changes—An Integrated Approach*, vol. 42. SEPM Special Publication, pp. 39–45.

**Visser, D.J.L., (1994).** The Geotectonic Evolution of South Africa and Offshore Areas, Geological Survey of South Africa.

**Walker, T.R., (1994).** Formation of red beds in moist tropical climate. A hypothesis. Bulletin of the American Association Petroleum Geologists 84, pp. 633–638.

**Ward, C.R., Nunt-jaruwong, S., Swanson, J., (2005).** Use of mineralogical analysis in geotechnical assessment of rock strata for coal mining. International Journal of Coal Geology 64, pp. 156–171.

**Weibel, R. & Friis, H., (2004).** Opaque minerals as keys for distinguishing oxidizing and reducing diagenetic conditions in the Lower Triassic Bunter Sandstone, North German Basin. Sedimentary Geology 169 (2004) 129 – 149. Wiley and Sons, 2<sup>nd</sup> Edition, pp. 273.

**Wilkinson, M., Haszeldine, R.S., (1996).** Aluminum loss from arkoses produces diagenetic quartzites and secondary porosity: Fulmar Formation, North Sea. Journal of the Geological Society (London) 154, pp. 747–751.

**Wilson, M.D., (1992).** Inherited grain-rimming clays in sandstones from eolian and shelf environments: their origin and control on reservoir properties. In: Houseknecht, D.W., Pittman, E.D., Keller, W.D.F. (Eds.), Origin, Diagenesis, and Petrophysics of Clay Minerals in Sandstones. SEPM, Special Publication, vol. 47, pp. 209–225.

**Worden, R. H., & Morad, S., (2003).** Clay minerals in sandstones: A review of the detrital and diagenetic sources and evolution during burial. In R. H. Worden, & S. Morad (Eds.), Clay cement in sandstones (pp. 3–41). International Association of Sedimentologists, Special Publication 34.

**Zuluaga, M.C., (1995).** Estudio diagenético y sedimentario de la Formación Gordexola (Flanco Sur del Anticlinorio de Bilbao, Vizcaya). Unpublished PhD thesis, Universidad del País Vasco, Spain pp. 259.

#### **Related Websites:**

<http://www.le.ac.uk/chemistry/pdf/teachersworkshops.pdf>

<http://www.chembuddy.com/?left=pH-claculation&right=ionic-strength-activity-coefficients>

<http://www.chembuddy.com/?left=pH-claculation&right=pH-scale>

<http://strata.geol.sc.edu/log-char.html>).

APPENDIX A

AG - 1										
Depth (m)	Rock type	Colour	Grain Size	Texture (Roundness)	Sorting	Cement/Matrix	Fossil/Accessories	Sed. Structures	Porosity/Oil show	HCL effect
3370.00	s.stn	lt grey	Fine	Sub angular to sub rounded	Well sorted	Glauconite	weathered chert mica	carbonaceous material forming laminations, climbing ripple laminations, micaceous spots, parallel lamination with carbonized materials	Porous	no reaction
3371.18	s.stn	lt grey	Fine	Sub rounded	Well sorted	Chlorite, glauconite	small show of mica	carbonaceous material forming laminations, climbing ripple laminations, micaceous spots, parallel lamination with carbonized materials	Porous	no reaction
3372.25	s.stn	lt grey	Fine	Sub rounded	Well sorted	Chlorite, glauconite	Mica weathered chert	Claystone drops over ripple lam	Porous	no reaction
3372.92	s.stn	lt grey	Fine	Rounded	Well sorted	Vague chlorite & glauconite	Siderite	Claystone drops over ripple lam	Porous/oil show	Bubbles little or no reaction
3373.22	Silt/claystone	Dark to lt grey	V. fine	Rounded	Well sorted	Vague chlorite & glauconite	Carbonized material mica	Siltstone with claystone drope. m	Slightly	little or no reaction
3374.15-3375.52	Siltysand	Med. to lt grey	V. fine	Rounded	V. well sorted	Vague chlorite & glauconite	Small spots of mica, coaly material	Migrating ripples, micaceous materials, bioturbation, mud drapes, waxy laminations, ripples	Tight	little or no reaction
3375.52	Siltysand	Med. to lt grey	Fine	Rounded	Well sorted	Chlorite	Clast of carbonized material	Load cast, soft sed deformation, ball structures, burrowing oxidation evidence, flaser & streaky lamination	Slightly	no reaction
3376.57	s.stn	lt grey	Fine	Angular	Well sorted	Glauconite	Clast of carbonized material	s.stn with carbonaceous materials, reactivation/erosional surfaces	Porous/oil show	Large bubbles
3376.83	s.stn	lt grey	Fine	sub angular	Well sorted	Chlorite, glauconite	Siderite	s.stn with carbonaceous materials, reactivation/erosional surfaces	Porous/oil show	small bubbles
3377.81	Shale/silt	Dark grey	V. fine	sub angular	Well sorted	Chlorite, glauconite	Coaly clast	Flaser laminations, load cast, burrowing, pillow structures	Slightly	no reaction
3377.96	Shale/silt	Dark grey	V. fine	sub angular	m. sorted	Chlorite, glauconite	Carbonaceous materials, mica	flaser laminations, mud drapes with some burrowing, impregnated carbonaceous materials	Tight	no reaction
3378.70	Shale	Dark grey	V. fine	sub angular	Well sorted	Chlorite, glauconite	Carbonaceous materials, patchy mica	Mud drops with overturned laminations, pillow structures, flaser, streaky laminations, claystone/siltstone	Tight	no reaction
3379.35	Shale	Dark grey	V. fine	sub angular	Well sorted	Chlorite, glauconite	Carbonaceous materials, patchy mica	Lenticular, streaky laminations, burrowing, migrating ripples	Tight	no reaction
3379.52	Shale	Dark grey	V. fine	sub angular	Well sorted	Chlorite, glauconite	Coaly materials, carbonaceous traces	bioturbation with soft sed deformation, carbonaceous with fingerprint marks	Tight	no reaction
3379.77	Silty/shale	lt to dark grey	Fine	Sub rounded	m. sorted	Chlorite, glauconite	Siderite	Bioturbation, current ripple marks, carbonaceous fingerprint marks, flaser, streaky laminations	Porous/oil show	Bubbles & slow effervescence
3380.05	Shale/claystone	Dark grey	V. fine	Sub rounded	Well sorted	Chlorite, glauconite	Mica spots	Bioturbation, burrowing crystallization of salt due to reaction with wate, coaly materials	Tight	no reaction
3380.65	Shale	Dark grey	V. fine	Sub rounded	Well sorted	Chlorite, glauconite	Coaly materials	burrowing, waxy, streaky laminations, bioturbation pinching out shapes, climbing ripples, evidence of coaly material, parallel lamination	Tight	no reaction

## APPENDIX B

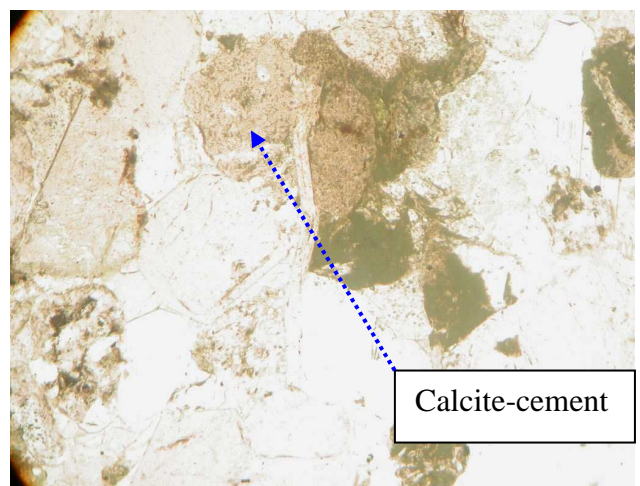
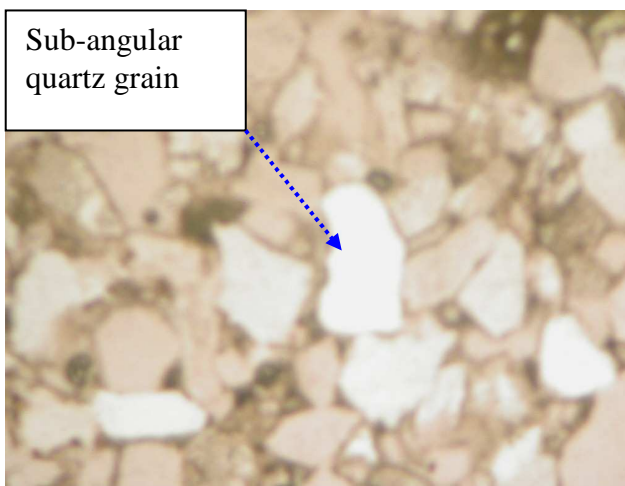
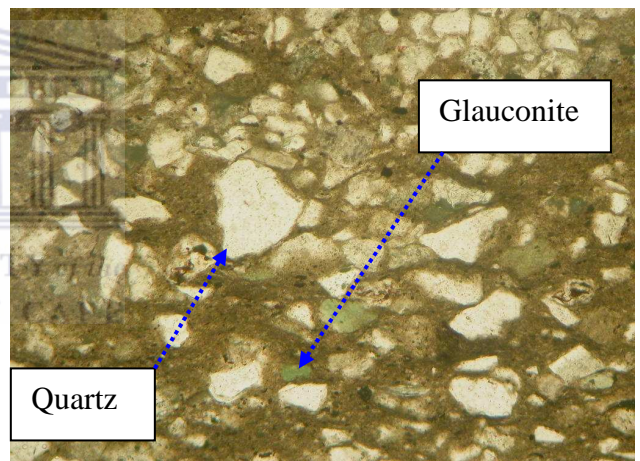
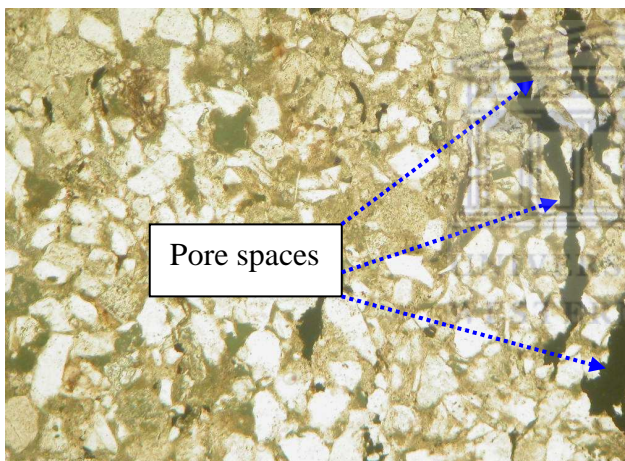
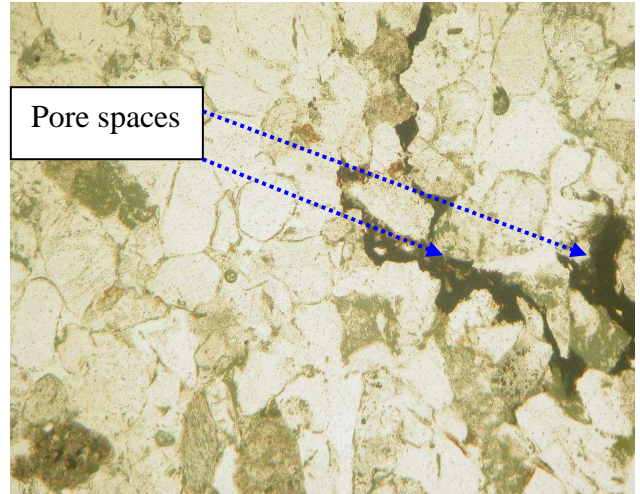
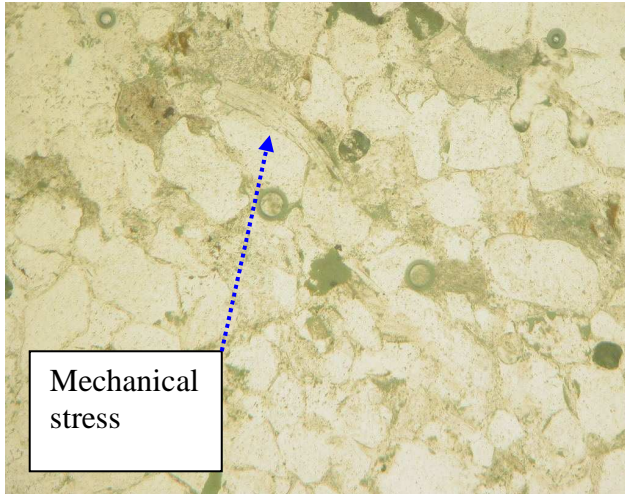
Depth (m)	Rock type	Colour	Grain Size	Texture (Roundness)	Sorting	CORE DESCRIPTION AK-1			Porosity/Oil show	HCL effect	
						Cement/Matrix	Fossil/Accessories	Sed. Structures			
3236.25	s.stn	lt grey to lt brown	Fine (0.25-0.125mm)	Sub rounded	V. well sorted	Glaucounite		massive s.stn with no visible structures	Porous & oil show	no escape	
3237.68	s.stn	lt grey to lt brown	Fine	Sub rounded	V. well sorted	Glaucounite, Patchys of siderite		two directional bedding (heringbone), black colour could be carbonaceous materials	Porous & oil show	no escape	
3238.35	s.stn	lt grey to lt brown	Coarse	Sub angular	Well sorted	Glaucounite, clear transparent grains of s.stn	oxidation observed	wavy carbonaceous laminae, ripple lamination with the planar lamination, brownish lamination, migrating ripple marks	Porous & oil show	no visible escape	
3238.72	s.stn	lt grey to lt brown	Coarse	Sub rounded	Well sorted	Glaucounite, chlorite, siderite, clear transparent grains of s.stn, chert	oxidation observed	Claystone clast, mud drope migrating, brown-reddish spot was observed	Porous	Slow escape	
3239.36	Shale & silt	Grey to med grey	V. fine	Sub rounded	V. well sorted	Pyrite laminated occasionally, siderite is still acting as a matrix here	Plant remain. very vague (carbonized)	Flaser lamination, inter lamination of claystone & silt, streaky lamination, cross ripple lamination, two directional lamination suggesting wave influence overturned & convoluted lamination	Tight	no escape	
3239.72	Shale	Dark grey	V. fine	Sub rounded	V. well sorted	Pyrite laminated occasionally, siderite is still acting as a matrix here	spots of mica (muscovite), carbonized plant remains	Flaser lamination, inter lamination of claystone & silt, streaky lamination, cross ripple lamination, two directional lamination suggesting wave influence overturned & convoluted lamination, migrating ripples	Tight	no escape	
3240.54	Siltyshale	Grey to med grey, occasionally variegated colour becoming rare	V. fine	Sub rounded	m. sorted	calcareous chips	Mica, siderite, plant fragments	overturned lamination, burrowing bioturbation evidence, fossils, coaly materials, vague ripple marks, wavy laminations, lenticular lamination	Tight/oil show	no escape	
3244.71	Shale/silt	grey to med grey	V. fine	Sub rounded	V. well sorted		Mica, coaly materials	plant remain carbonized	Lenticular laminations, climbing ripples laminations, ripple marks, wavy laminations, burrowing, overturned laminations, silty fm matrix with shale	Tight/ no show	no escape
3241.18	Silty/shale s.stn	lt to dark grey	V. fine	Sub rounded	Well sorted	Sandstone parting	carbonized material siderite	parallel laminations, planar bedding plane, climbing ripples, burrowing with in some ripples, brownish thick laminations (could be oxidation)	slightly/no show	no escape	
3250.12	Silty/clay	lt grey	V. fine	Sub rounded	m. sorted	Mica on carbonized materials, carbonized clast vague evidence of siderite iron with silt zone	carbonized material siderite	intercalation of silt with carbonized materials	slightly/no show	slow effect from silky zone	
3283.40	s.stn	lt grey	Fine	Sub rounded to rounded	Well sorted	Glaucounite	weathered chert (lack of reaction with HCL)	Carbonaceous material forming a bedding plane claystone at the top of the core	Porous	No effect	
3285.78	s.stn	lt grey	Fine	Sub rounded	V. well sorted	Glaucounite, weathered chert	Mudstone as clast within the s.stn, siderite but not sure	light occurrence of carbonaceous materials, if traced under x-ray or ultra violet, may form internal bedding	Porous	No effect	
3285.96	s.stn	lt grey	Fine	Sub rounded	V. well sorted	Glaucounite, weathered chert	Glaucounite, siderite, tiny mica visible, chlorite	no prominent bedding, massive s.stn, mud drapes as migrating, carbonaceous materials	Porous	No effect	
3287.85	Shale/silt	Dark grey	V. fine	Sub rounded	sorted	carbonaceous materials as clast	Mica, siderite, plant fragments	landcast, burrowing ball structures, flaser lamination, parallel bedding, interlamination of clay & siltstone	Tight	No effect	
3288.40	Shale	Dark grey	V. fine	Sub rounded	Well sorted	carbonaceous materials as small clast	Mica (tiny)	Claystone interlaminated with silt, some areas have parallel lamination & evidence of flaser lamination	Tight	No effect	
3288.70	Shaly/silt	Dark grey	V. fine	Sub rounded	Well sorted	carbonaceous materials as small clast	Mica materials	Dark with burrowing, plant existence	Tight	No effect	

## APPENDIX C

Depth (m)	Rock type	Colour	Grain Size	Texture (Roundness)	Sorting	A W -1 Cement/Matrix	Fossil/Accessories	Sed. Structures	Porosity/Oil show	HCL effect
3446.00	s.stn	lt grey	Fine	sub rounded to rounded	V. well sorted	Glauconite		vague cross laminations, carbonaceous materials forming bedding plane	Porous/oil shows	Vague bubbles
3447.10	s.stn	lt grey	Fine	Sub angular to sub rounded	Well sorted	Glauconite	Siderite	Two directional bedding (heringbone), cross bedding, carbonaceous laminae	Porous	No effect
3447.80	Claystone	Dark colour	Fine	Sub angular to sub rounded	m. sorted	s.stn clast	striations on the claystone	Mud drapes forming ripple laminations, interlamination of silt/s.stn, mud drape scattered all over the interval wavy & lensoid lamination, coaly materials	Tight	No effect
3448.20	s.stn	lt grey	Fine	Sub angular to sub rounded	Well sorted	Chlorite, glauconite	striations on the claystone	clear quartz, translucent grains, grain contact, occasionally white to light grey	Porous	No effect
3449.34	s.stn	lt grey	Fine	Angular to sub angular	Well sorted	Glauconite	Weathered chert	Thin spots of carbonaceous materials with climbing ripple laminations	Porous	No effect
3451.47	s.stn	lt grey	Fine	Sub angular	Well sorted	Glauconite	Weathered chert	Mud drapes with climbing ripples, vague burrowing evidence	Porous	No effect
3452.60	s.stn	lt grey	Fine	Sub angular to sub rounded	Well sorted	Glauconite	Weathered chert	wavy carbonaceous materials laminae define low angle, cross bedding, planar nature laminations, herringbone	Porous	No effect
3453.73	s.stn	lt grey	Fine	Sub rounded	Well sorted	Mud drapes filling some pores	Mica tiny spots	Carbonaceous materials forming bedding planes, ripple marks, mud drapes that pinch in & out, two directional bedding, different loading, flaring structures, migrating ripples	Porous	No effect
3456.20	silty/clay	lt to dark grey	V. fine	Sub rounded	V. well sorted	Mud drapes filling some pores	Mica tiny spots	current ripple laminations, burrows, brown colour bedding	Tight	No effect
3456.45	s.stn	lt grey	Fine	Sub rounded	m. sorted	Glauconite	Possibly siderite	current ripple laminations, burrows, brown colour bedding	Porous	No effect
3456.70	s.stn/silt	lt grey to lt brown	Fine	Sub angular	m. sorted	Glauconite	Calcareous materials, calcite	Brown bedding colour	Slightly/oil shows	High bubbling
3457.54	s.stn	lt grey	Fine	Sub rounded	Well sorted	Glauconite	Calcareous materials, calcite	parallel laminations, no samples for physical observation	Porous	No effect
3460.00	s.stn	lt grey	Fine	Sub rounded	Well sorted	Glauconite	Mica, weathered chert	Carbonaceous materials as bedding planes, brown colour spots within the core interval	Porous	No effect
3460.61	s.stn	lt grey	Fine	Sub rounded	Well sorted	silt as matrix, small glauconite silt as matrix, chlorite, glauconite	Patchies of mica	Carbonaceous materials as bedding planes, brown colour spots within the core interval, soft sed deformation	Porous	small bubbles
3461.77	s.stn	lt grey	Fine	Sub rounded	Well sorted	Well sorted	Mica	Carbonaceous materials as bedding planes, brown colour spots within the core interval, soft sed deformation	Porous	No effect
3462.46	s.stn	lt grey	Fine	Sub rounded	Well sorted	silt as matrix, glauconite	Weathered chert	soft sed. deformation	Porous	No effect
3463.61	s.stn	lt grey	Fine	Sub rounded	Well sorted	Chlorite or glauconite	Weathered chert	no visible laminations	Porous	No effect
3464.51	s.stn	Occasionally white to lt grey	Fine	Sub angular to sub rounded	Well sorted	Glauconite, silica cement	Weathered chert	climbing ripples, ripple marks, mud drape, ball structures with evidence of oxidation, bioturbation, clean, clear to quartz rare translucent grains, grain contact	Slightly	No effect
3464.67	s.stn	lt grey to occasionally white	Fine	Sub angular to sub rounded	Well sorted	Glauconite, silica cement	Chert or siderite	climbing ripples, ripple marks, mud drape, ball structures with evidence of oxidation, bioturbation, clean, clear to quartz rare translucent grains, grain contact	Slightly	small bubbles
3465.57	s.stn	Occasionally white to lt grey	Fine	Sub angular to sub rounded	Well sorted	Glauconite evidence of chlorite	Chert or siderite	climbing ripples, ripple marks, mud drape, ball structures with evidence of oxidation, bioturbation, clean, clear to quartz rare translucent grains, grain contact	Slightly	little or no reaction
3466.00	Siltysand	Dark to lt grey	V. fine	Sub angular to sub rounded	m. sorted	Glauconite evidence of chlorite	Mica sheet, coaly materials	siltstone with cross bedding, ball shaped structures, burrowing, flame structures, some mud drape, ripple current marks	Slightly	no reaction
3466.06	Siltysand	lt grey	Fine	Sub angular to sub rounded	Well sorted	Glauconite	weathered chert	siltstone with cross bedding, ball shaped structures, burrowing, flame structures, some mud drape, ripple current marks	Porous	little or no reaction
3466.36	Siltysand	lt grey	Fine	Sub angular to sub rounded	Well sorted	Chlorite, glauconite	siderite, mica	occasionally white to very light grey, light brown to medium brown, grain contact, rare access	Porous	little or no reaction

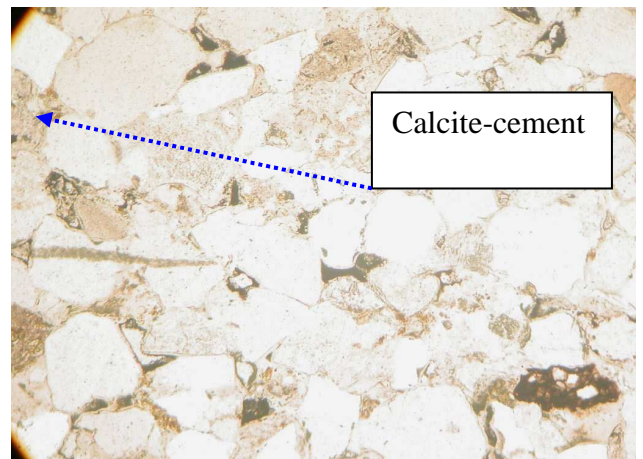
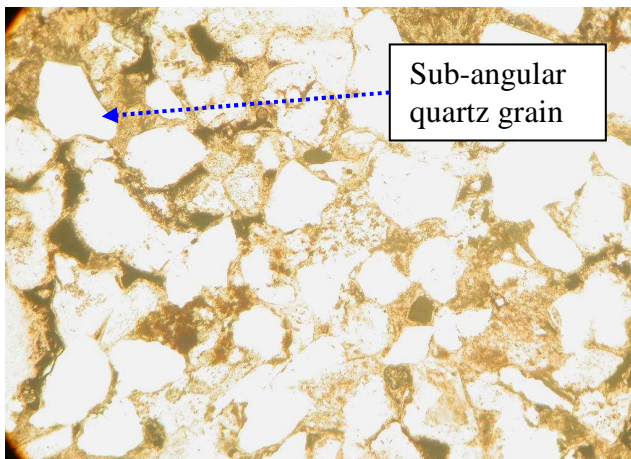
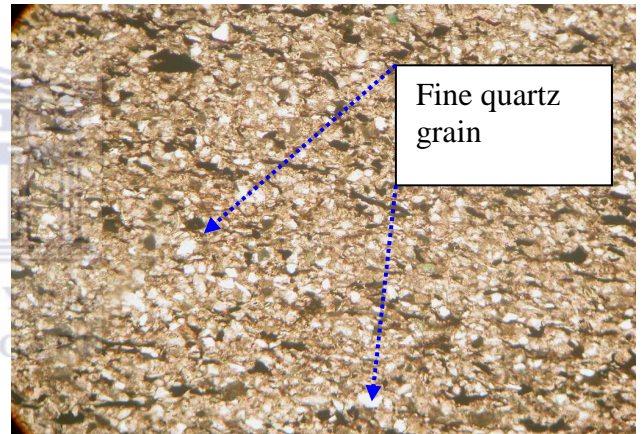
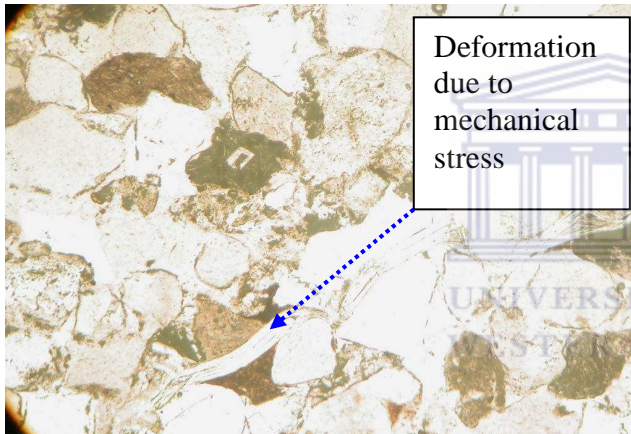
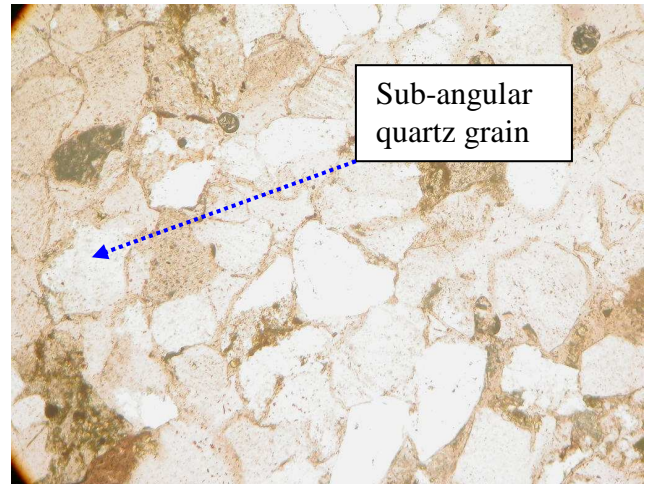
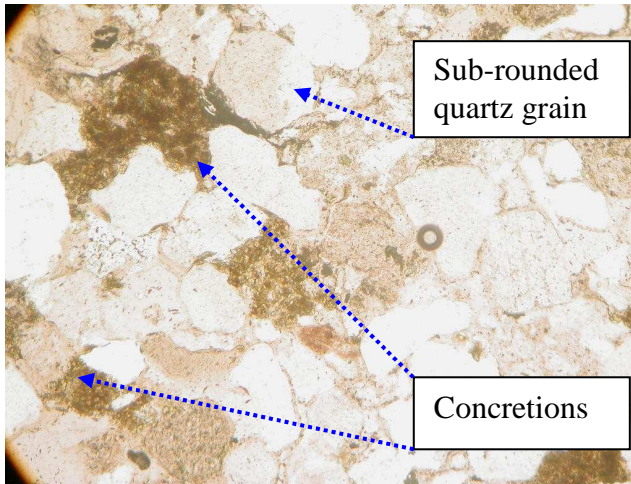
APPENDIX D

A-G1 Plane polarized light photomicrograph



APPENDIX E

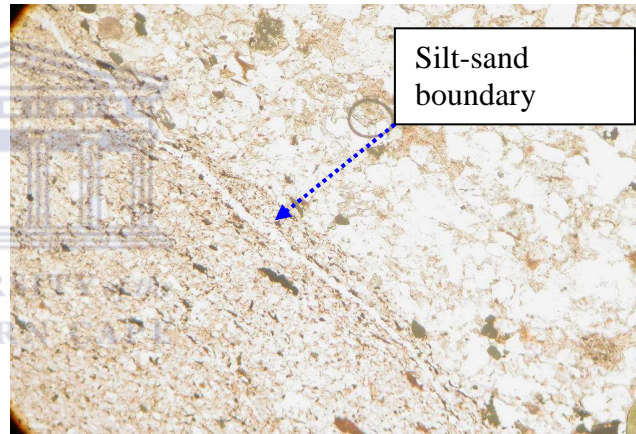
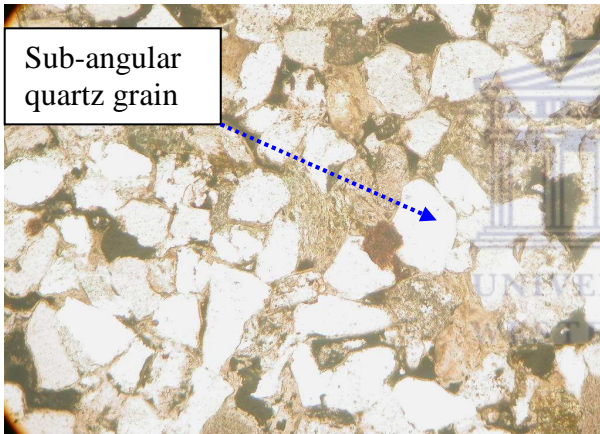
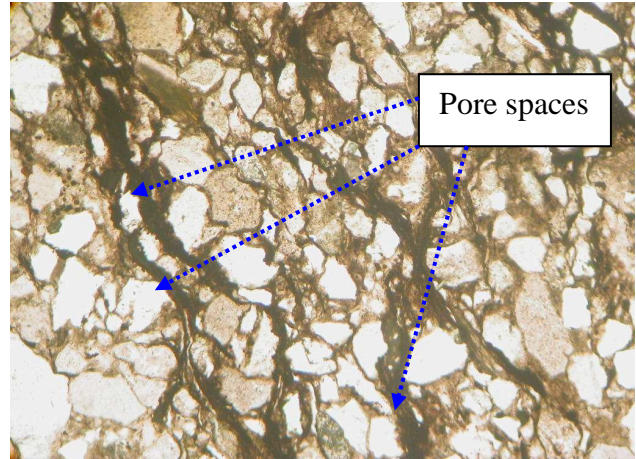
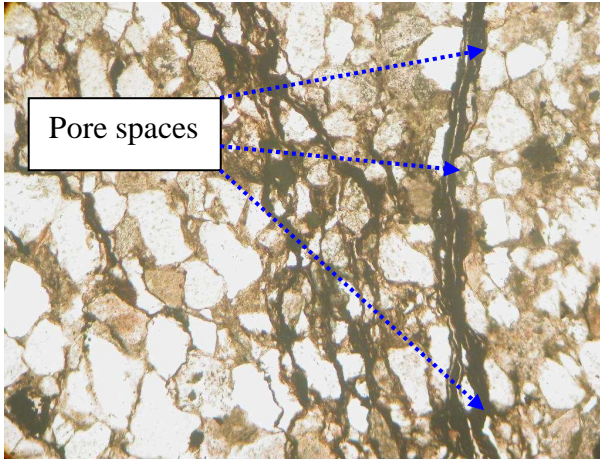
A-K1 Plane polarized light photomicrograph



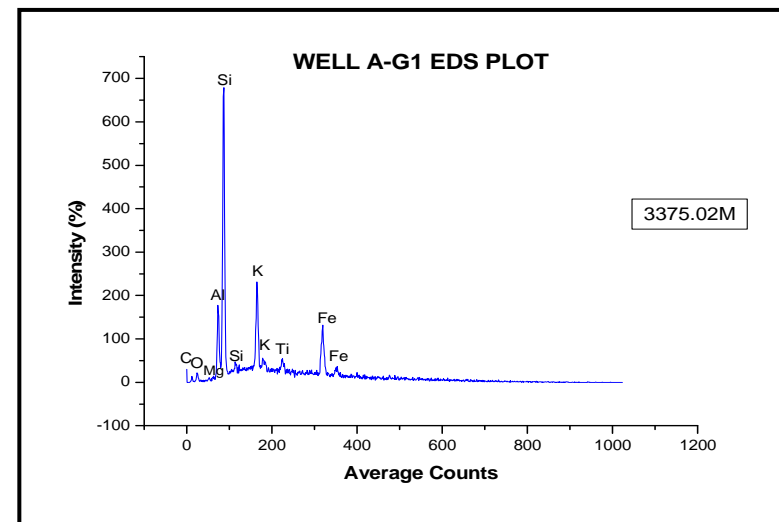
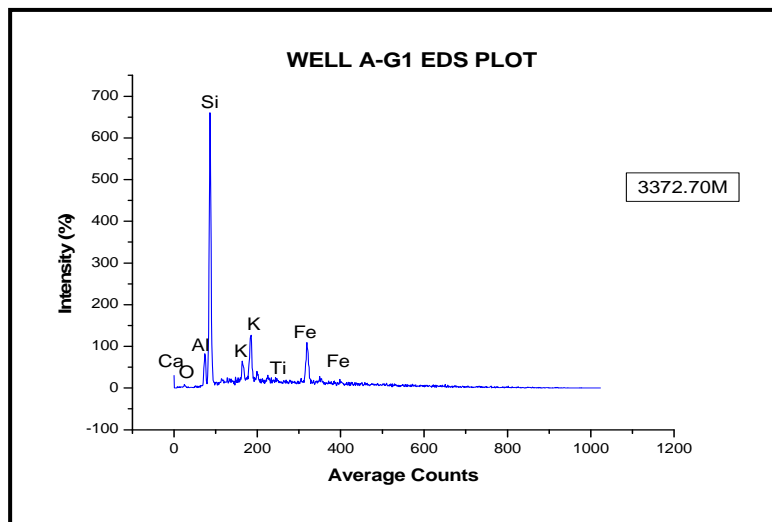
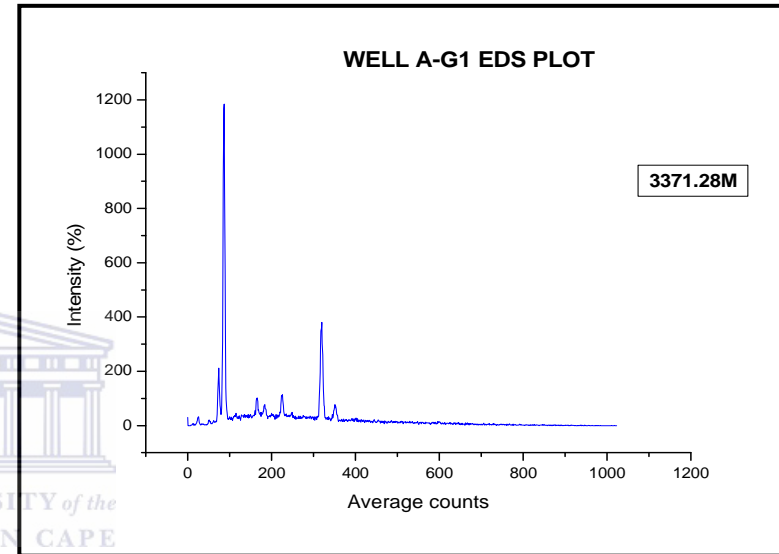
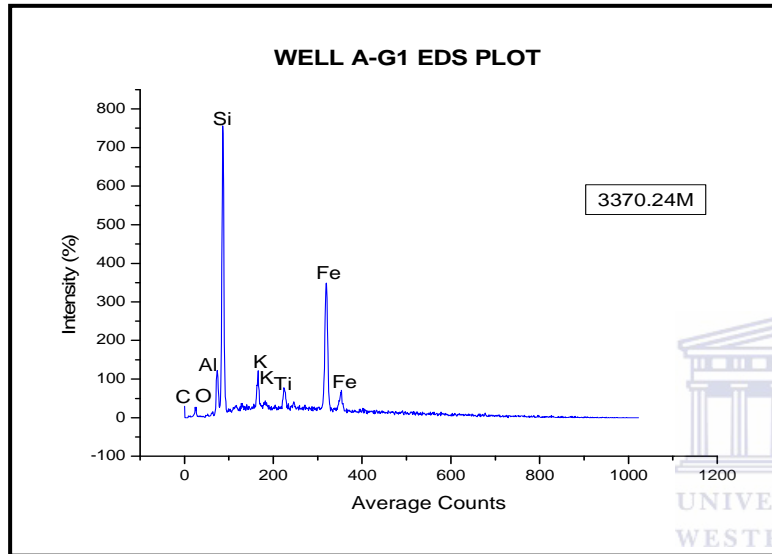


APPENDIX F

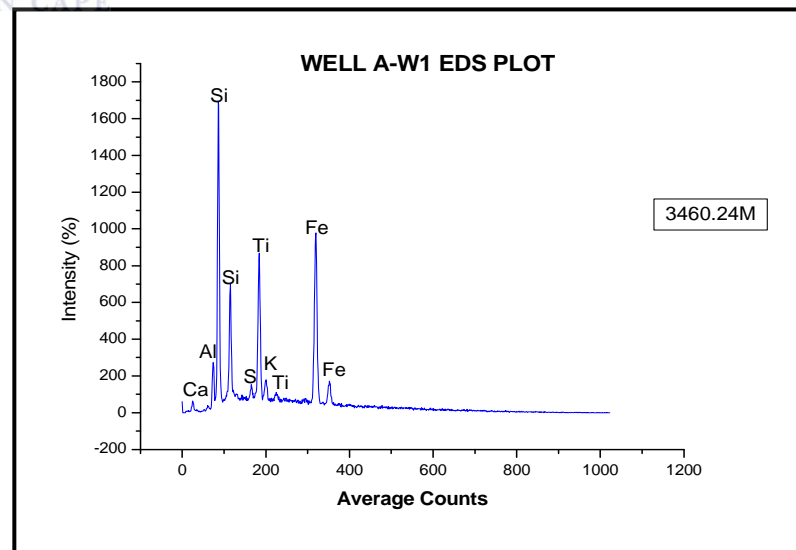
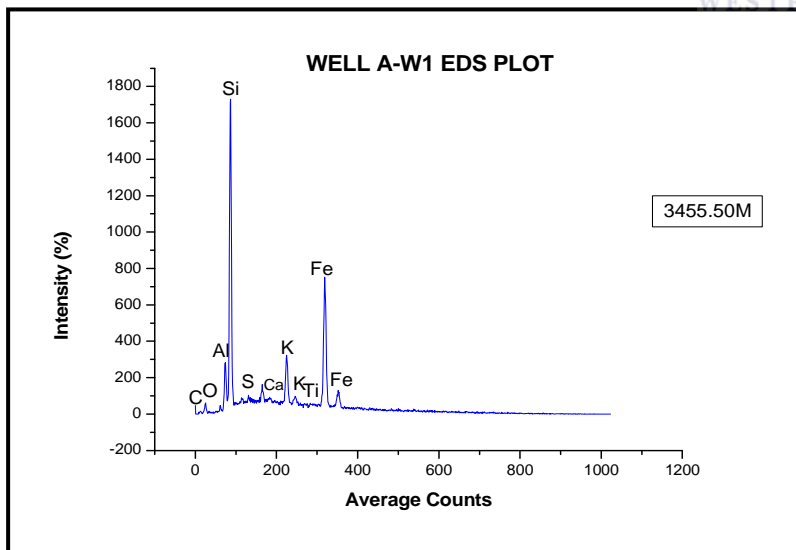
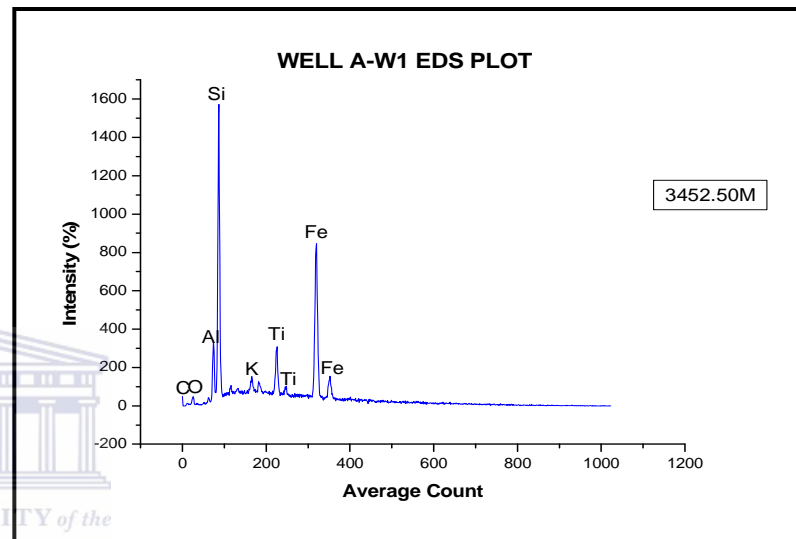
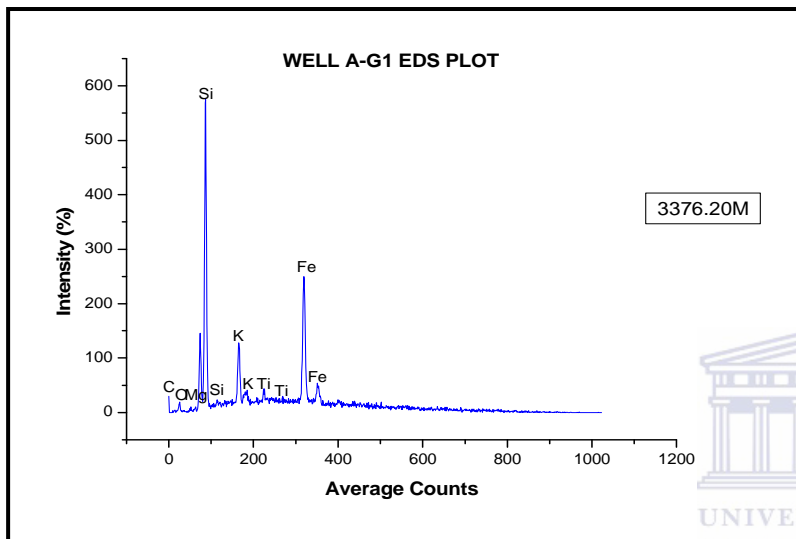
**A-W1 Plane polarized light photomicrograph**



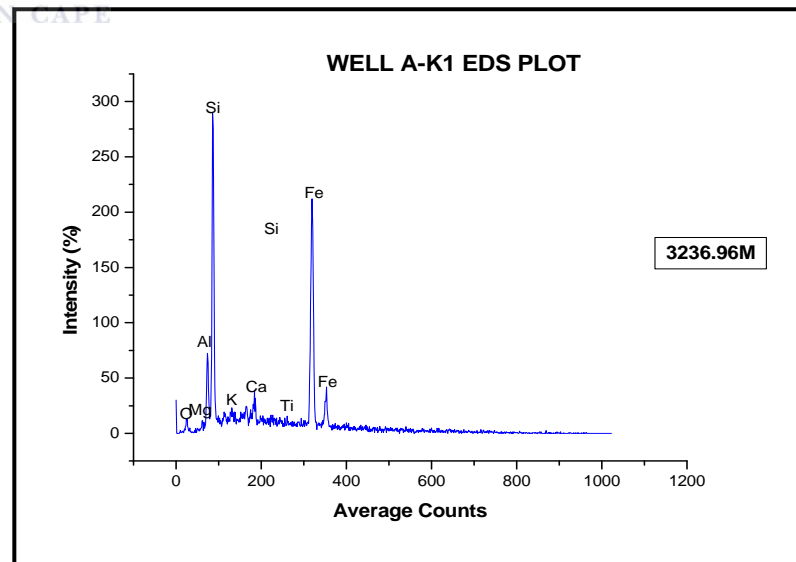
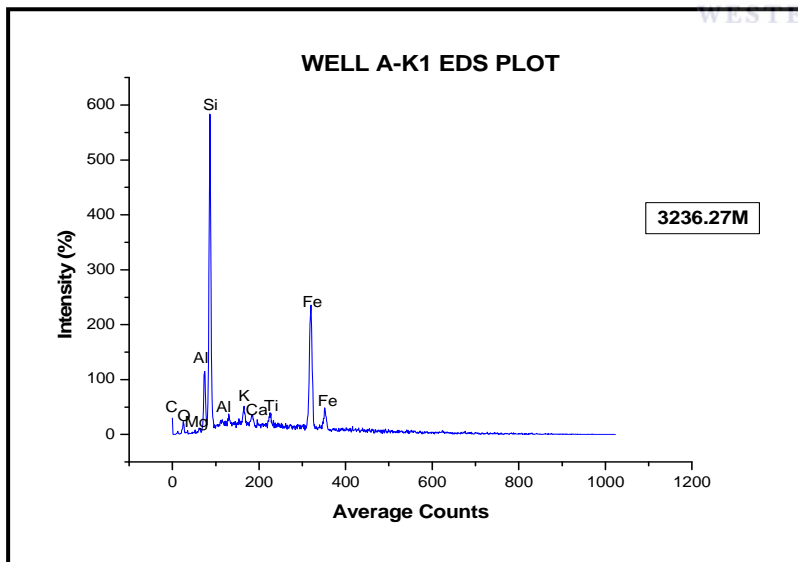
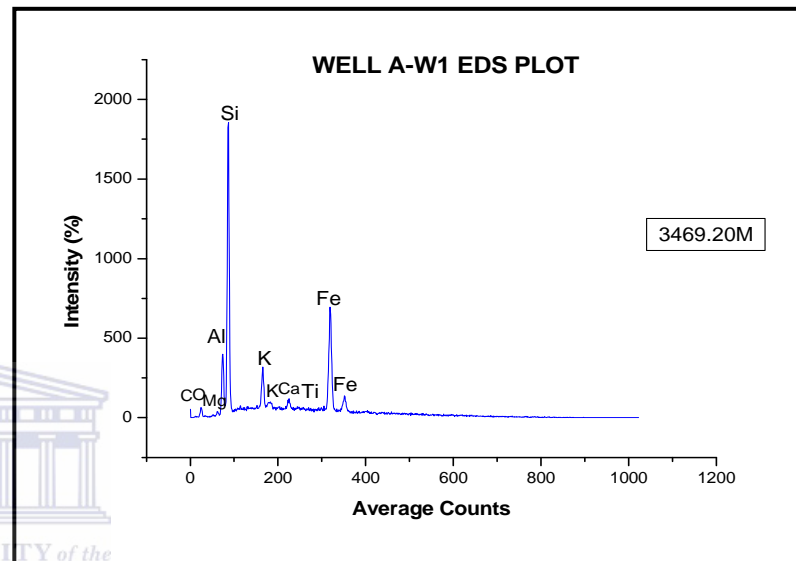
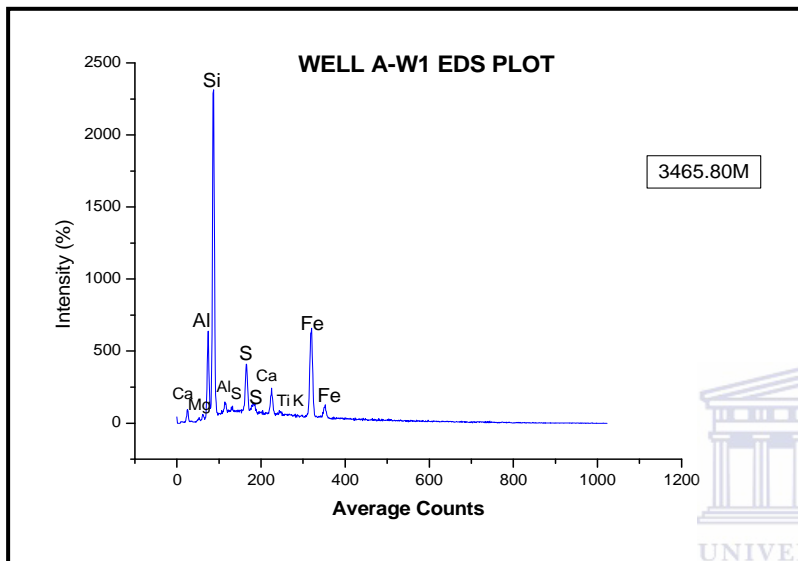
APPENDIX G  
Energy Dispersive Spectrometry (EDS) plots



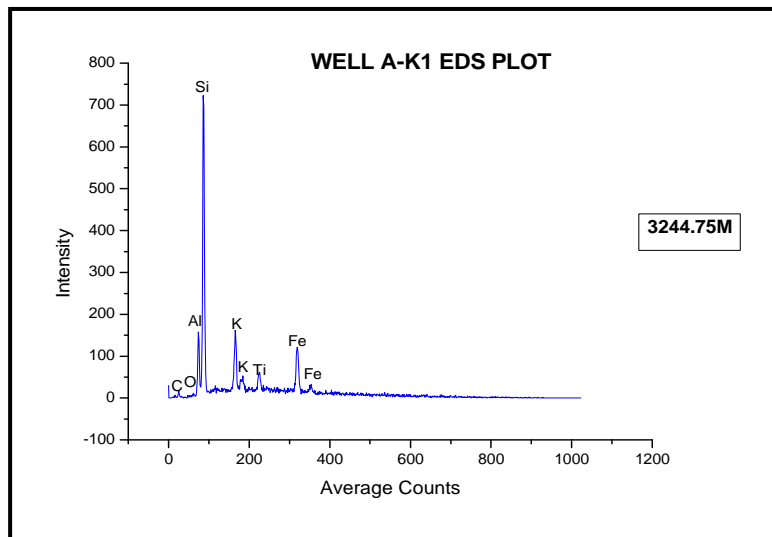
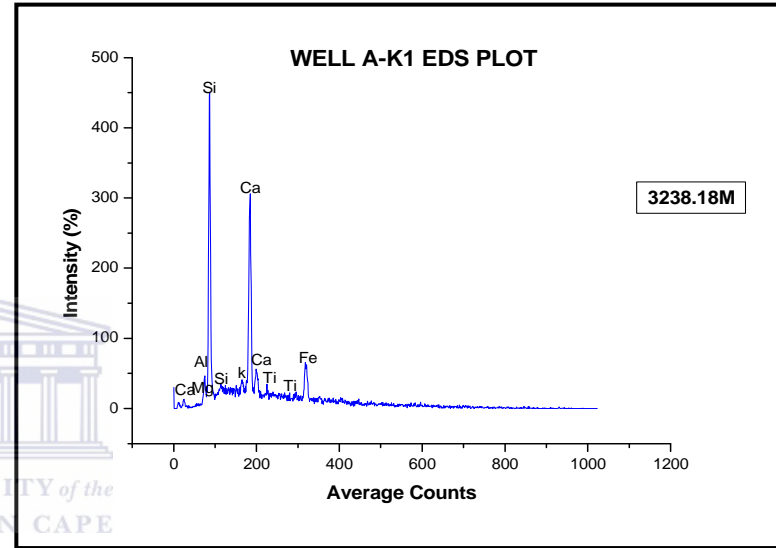
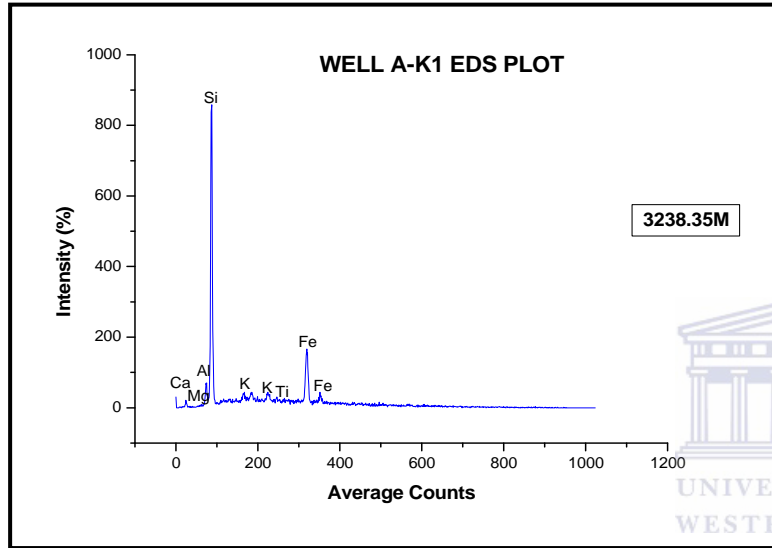
APPENDIX G (continued)



APPENDIX G (continued)

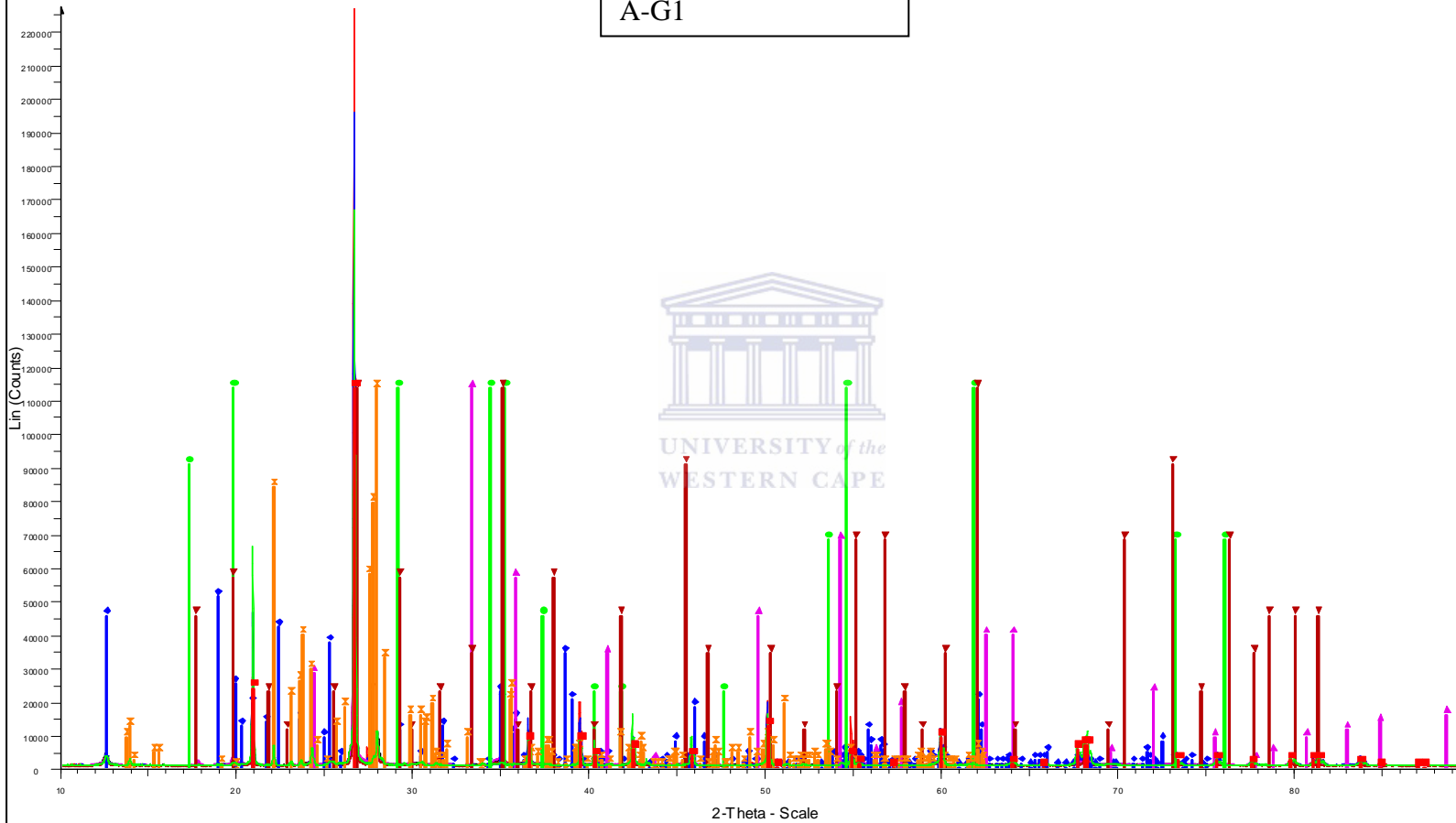


APPENDIX G (continued)



## APPENDIX H

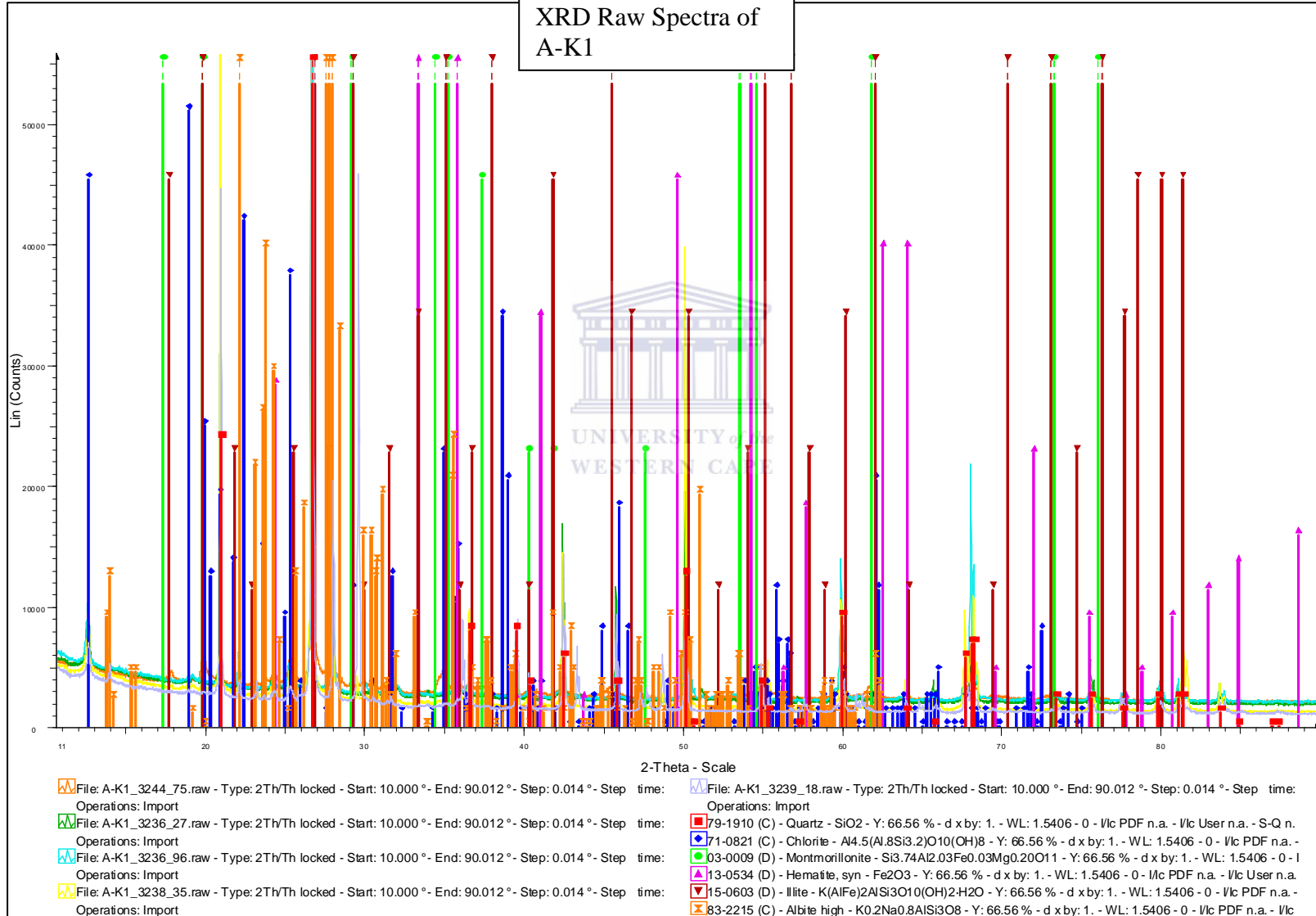
### XRD Raw Spectra of A-G1



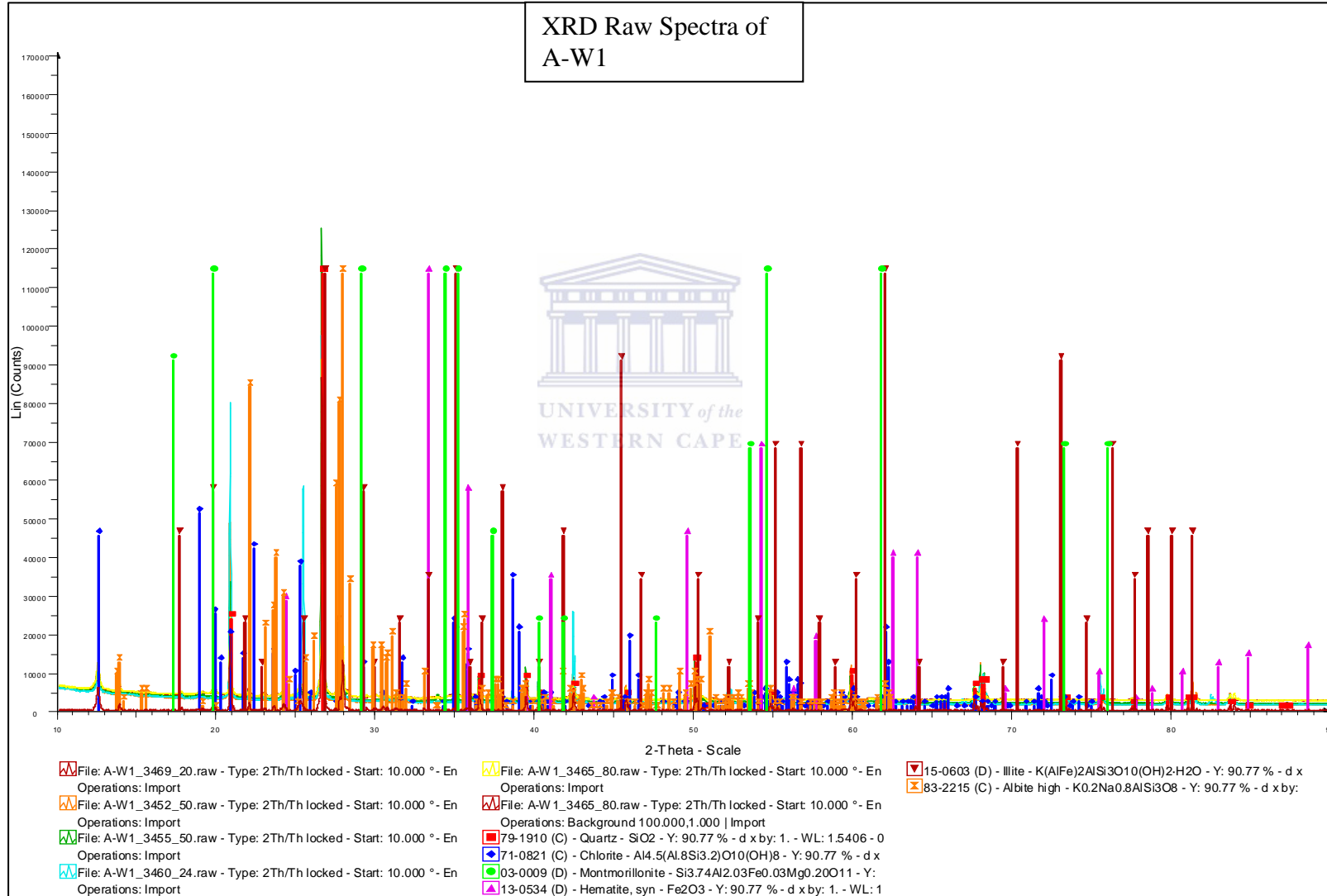
- |   |   |   |
|---|---|---|
| <p>File: A-G1_3376_23.raw - T-type: 2Th/Th locked - Start: 10.000 ° - En<br/>Operations: Y Scale Add 500   Background 0.000,1.000   Import</p> <p>File: A-G1_3370_24.raw - T-type: 2Th/Th locked - Start: 10.000 ° - En<br/>Operations: Y Scale Add 500   Background 0.000,1.000   Import</p> <p>File: A-G1_3371_28.raw - T-type: 2Th/Th locked - Start: 10.000 ° - En<br/>Operations: Y Scale Add 500   Background 0.000,1.000   Import</p> <p>File: A-G1_3375_02.raw - T-type: 2Th/Th locked - Start: 10.000 ° - En<br/>Operations: Y Scale Add 500   Background 0.000,1.000   Import</p> | <p>File: A-G1_3372_70.raw - T-type: 2Th/Th locked - Start: 10.000 ° - En<br/>Operations: Y Scale Add 500   Background 0.000,1.000   Import</p> <p>File: A-G1_3376_23.raw - T-type: 2Th/Th locked - Start: 10.000 ° - En<br/>Operations: Strip kAlpha2 0.500   Y Scale Add 500   Background 0.0</p> <p>79-1910 (C) - Quartz - SiO<sub>2</sub> - Y: 50.00 % - d x by: 1. - WL: 1.5406 - 0</p> <p>71-0821 (C) - Chlorite - Al<sub>4.5</sub>(Al<sub>8</sub>Si<sub>3.2</sub>)O<sub>10</sub>(OH)<sub>8</sub> - Y: 50.00 % - d x</p> <p>03-0009 (D) - Montmorillonite - Si<sub>3.74</sub>Al<sub>2.03</sub>Fe<sub>0.03</sub>Mg<sub>0.20</sub>O<sub>11</sub> - Y:</p> <p>13-0534 (D) - Hematite, syn - Fe<sub>2</sub>O<sub>3</sub> - Y: 50.00 % - d x by: 1. - WL: 1</p> | <p>15-0603 (D) - Illite - K(AlFe)<sub>2</sub>AlSi<sub>3</sub>O<sub>10</sub>(OH)<sub>2</sub>H<sub>2</sub>O - Y: 50.00 % - d x</p> <p>83-2215 (C) - Albite high - K<sub>0.2</sub>Na<sub>0.8</sub>AlSi<sub>3</sub>O<sub>8</sub> - Y: 50.00 % - d x by:</p> |
|---|---|---|

APPENDIX I (continued)

XRD Raw Spectra of  
A-K1

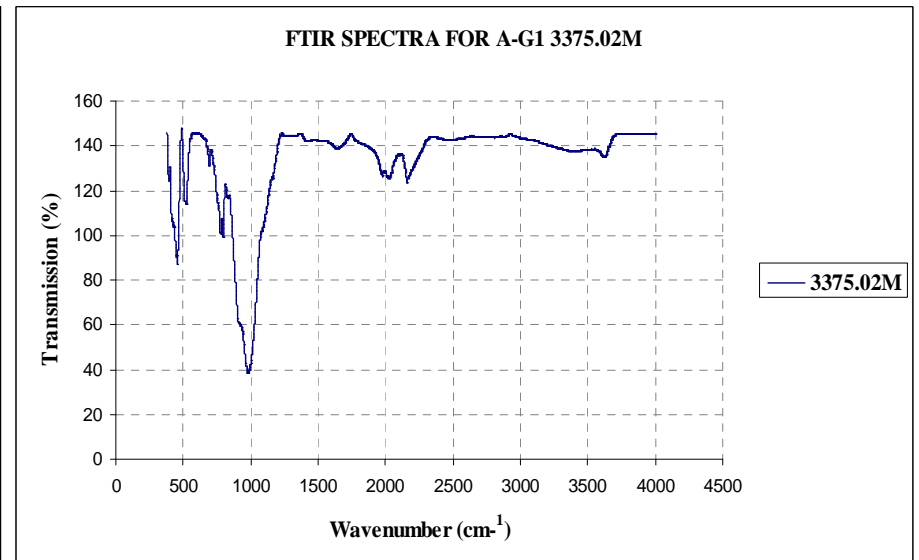
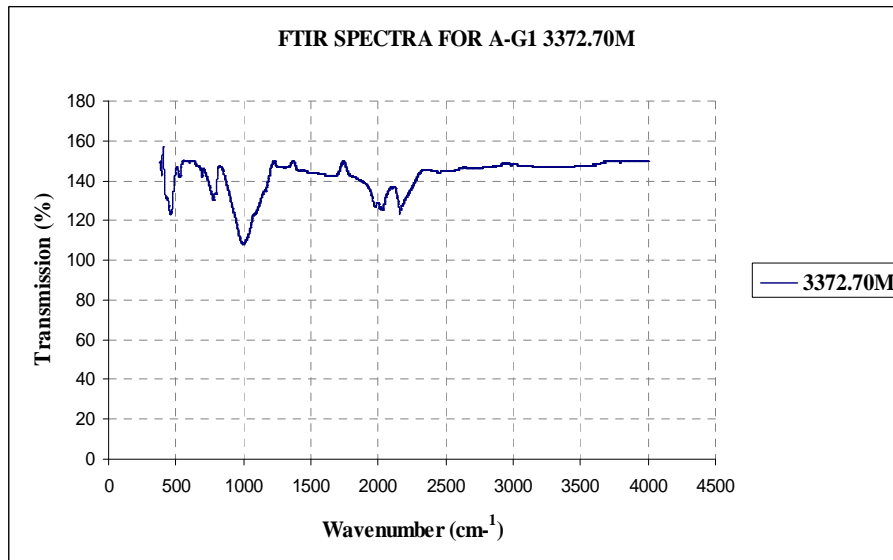
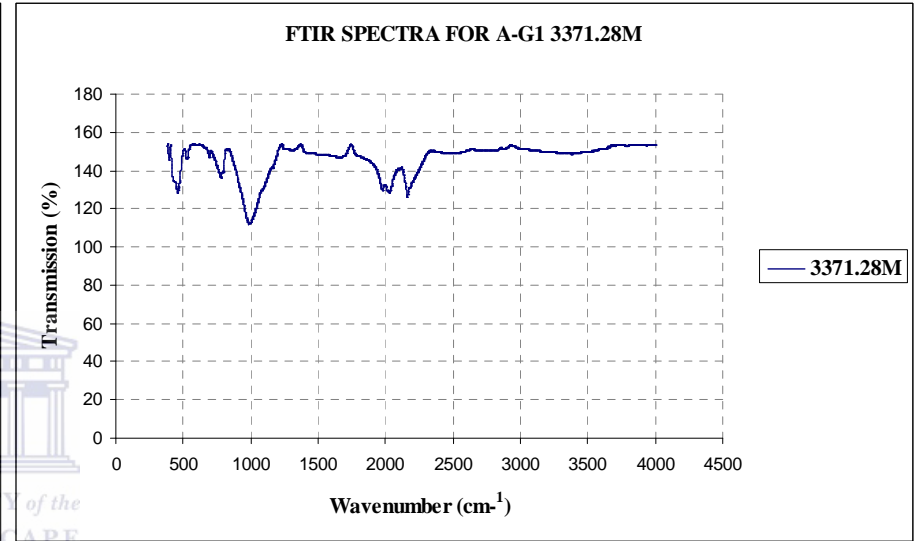
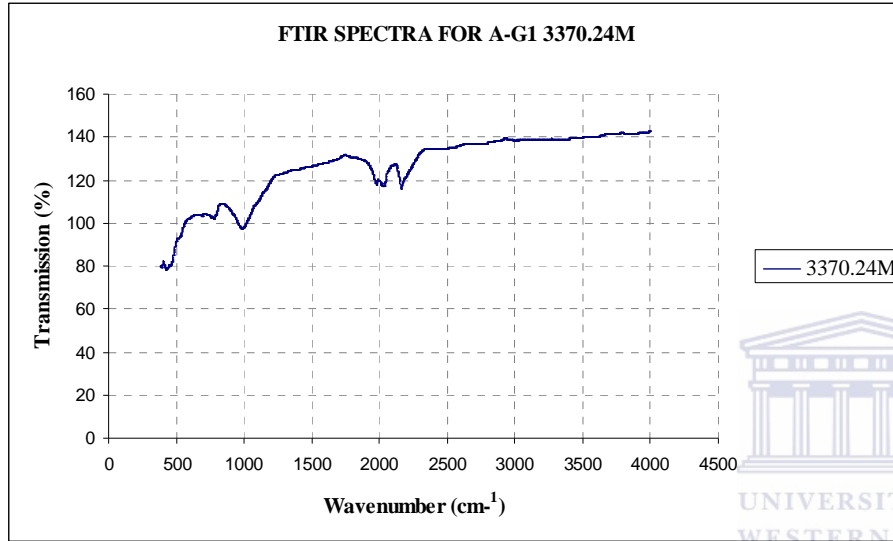


APPENDIX J (continued)

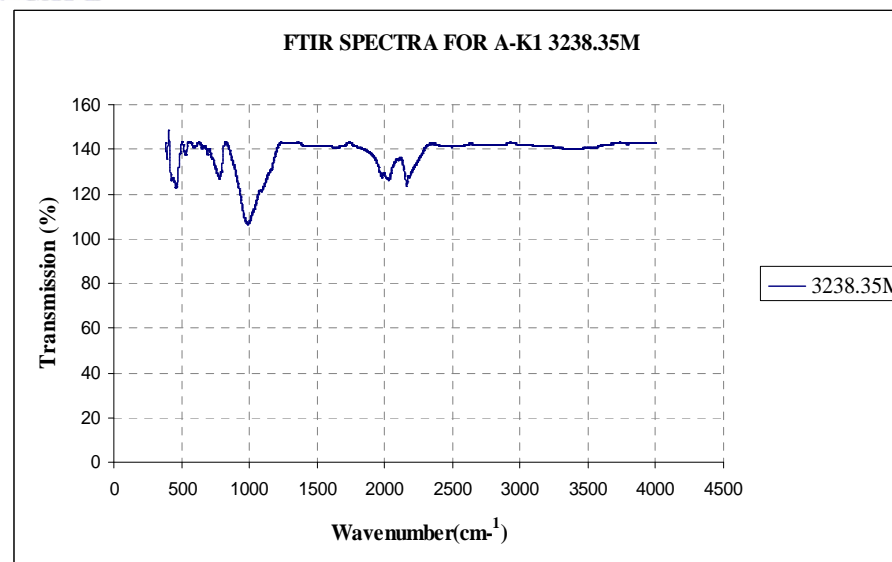
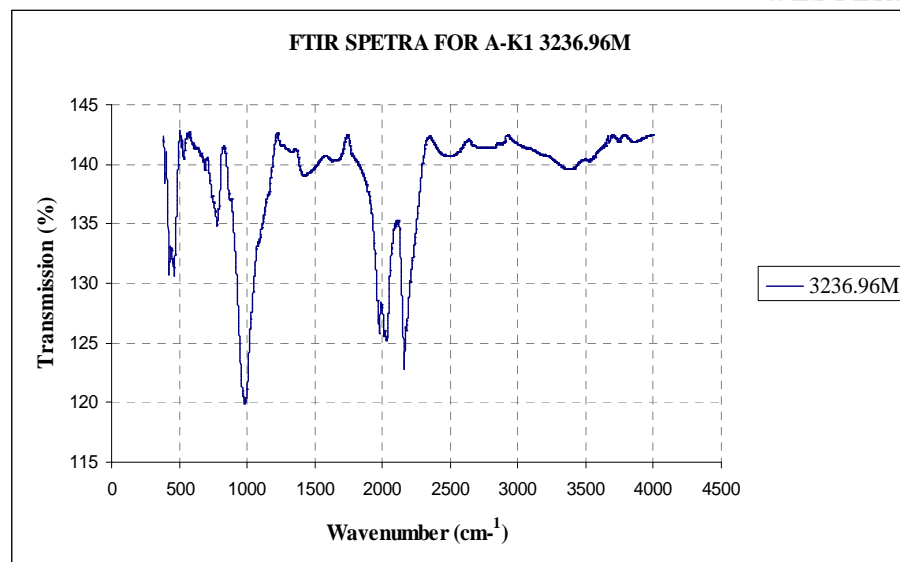
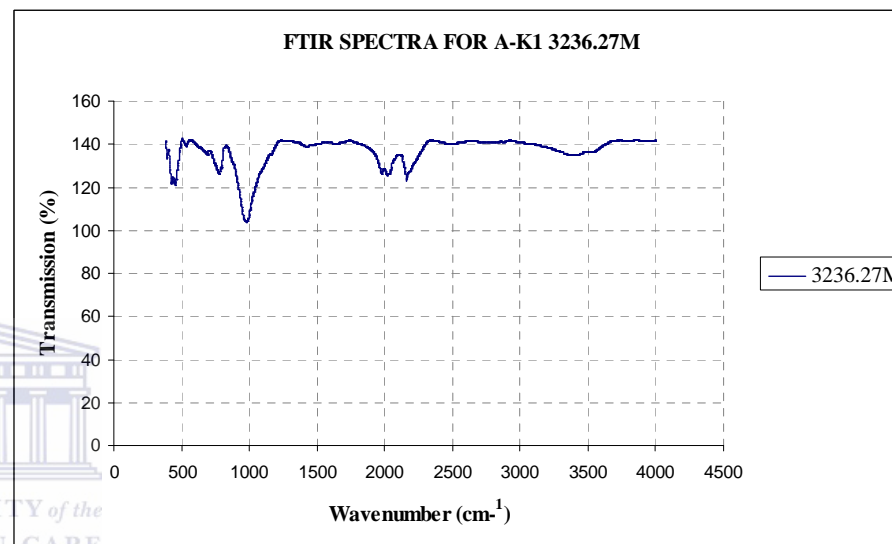
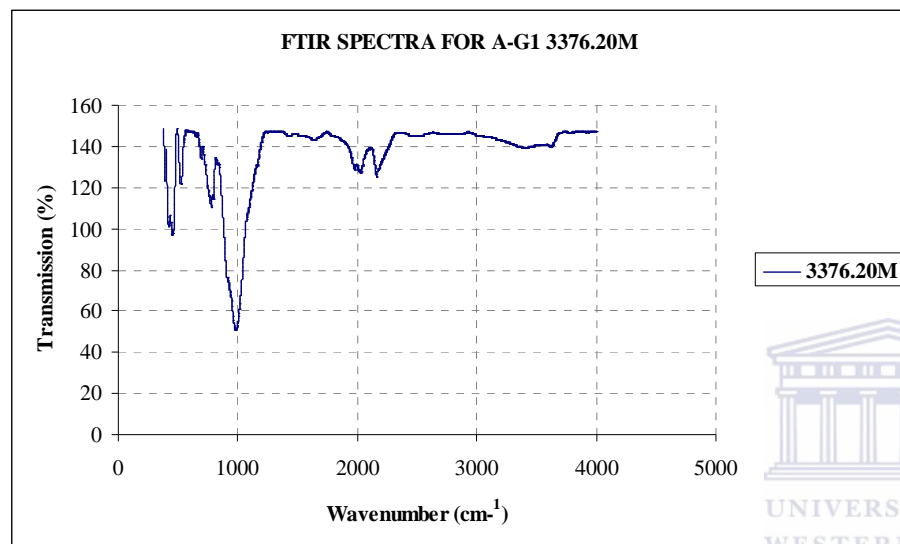




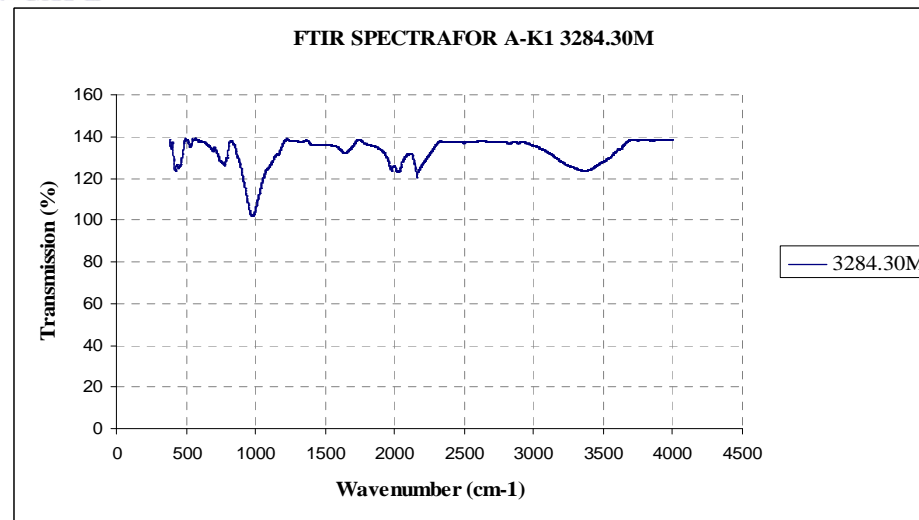
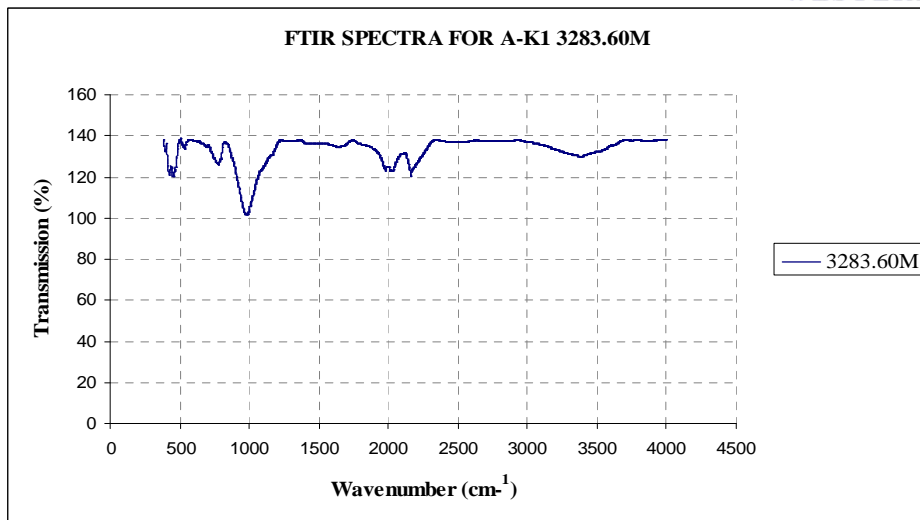
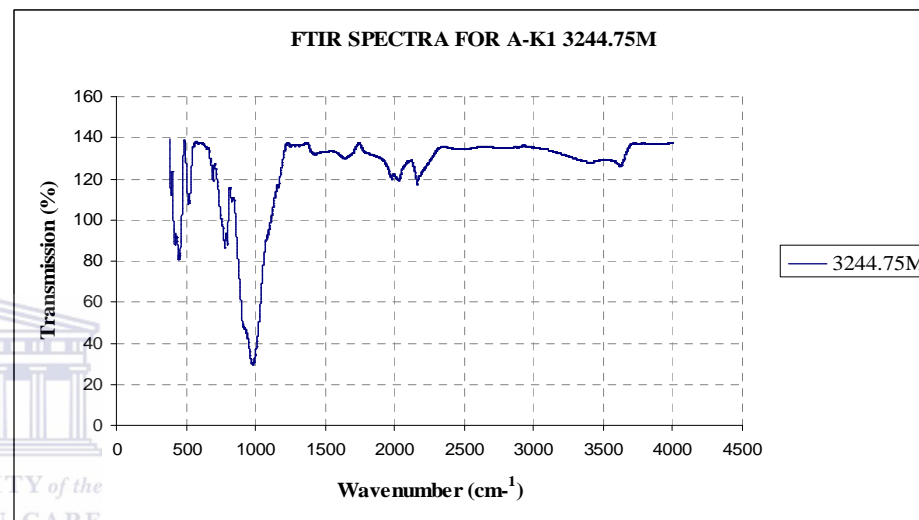
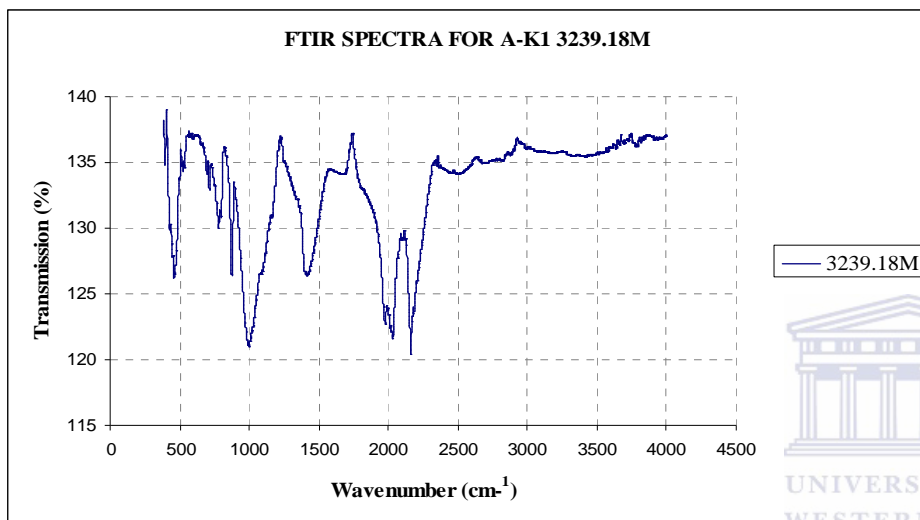
APPENDIX K



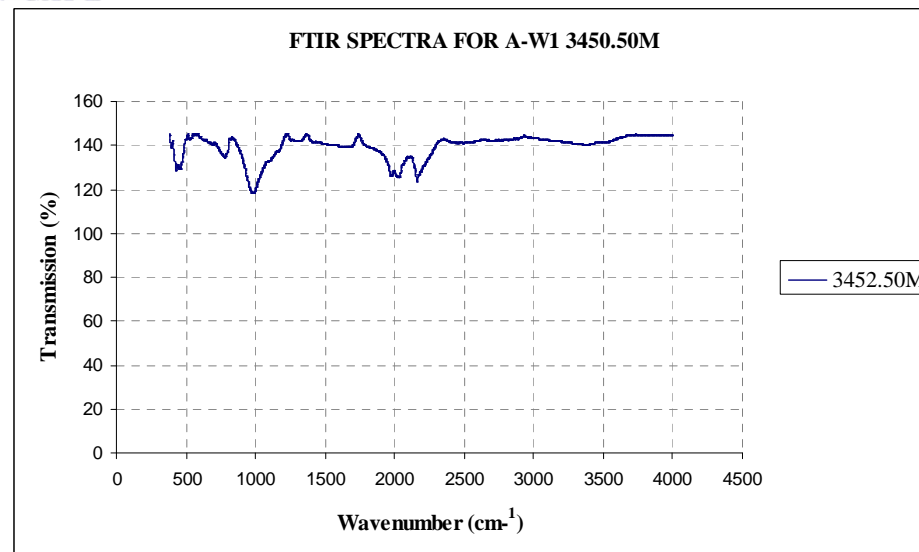
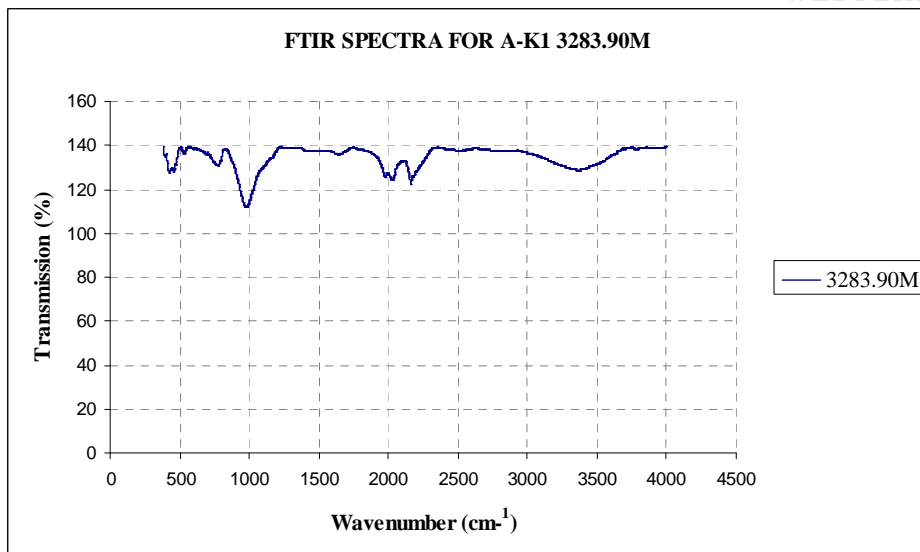
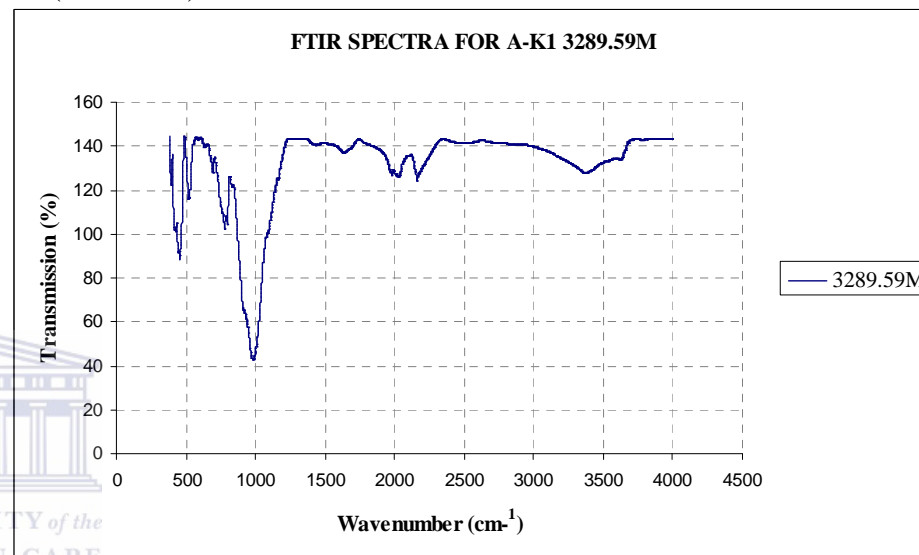
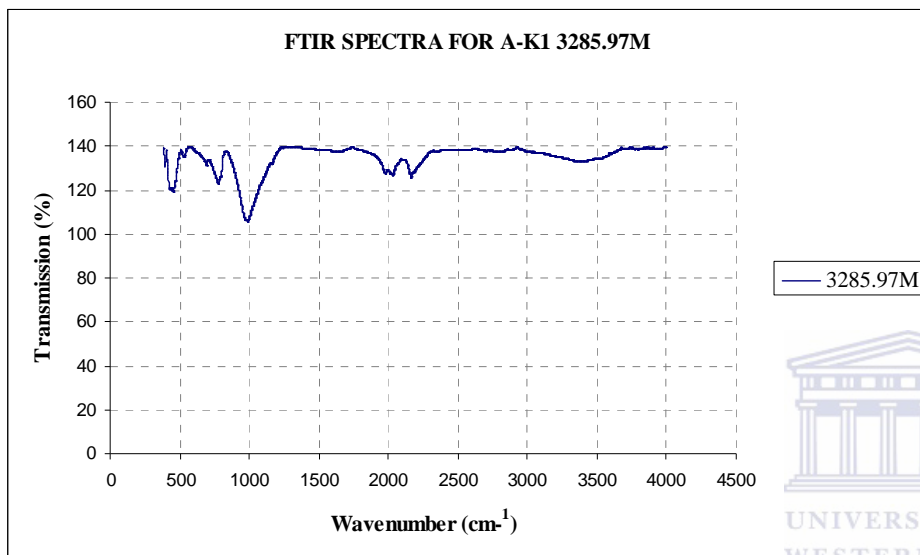
APPENDIX K (continued)



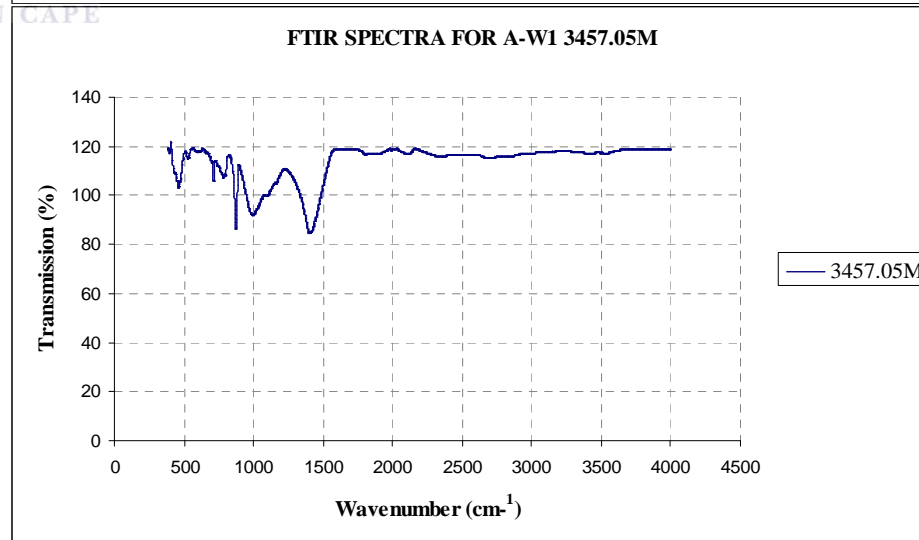
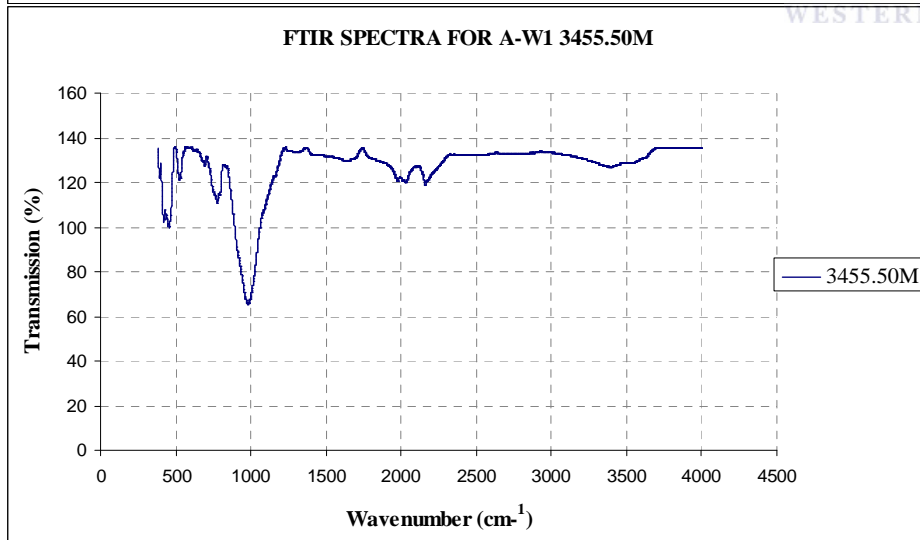
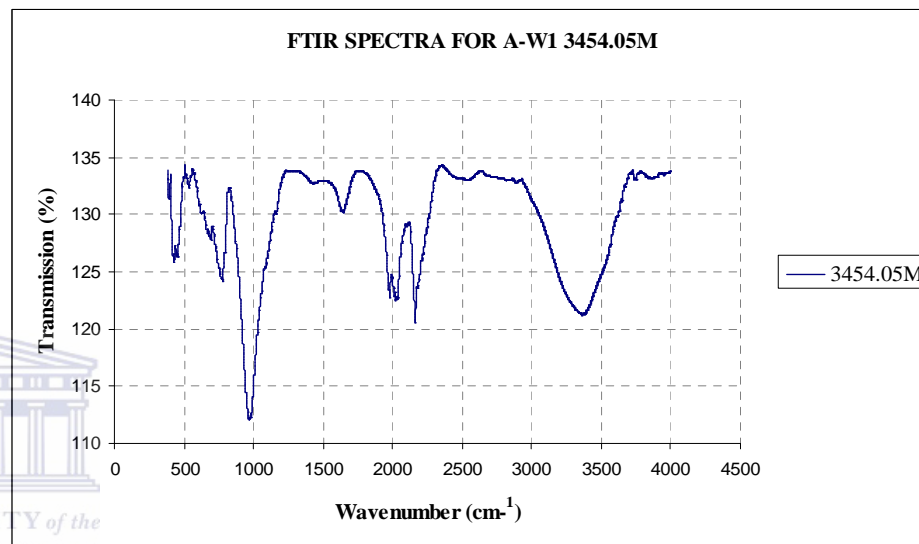
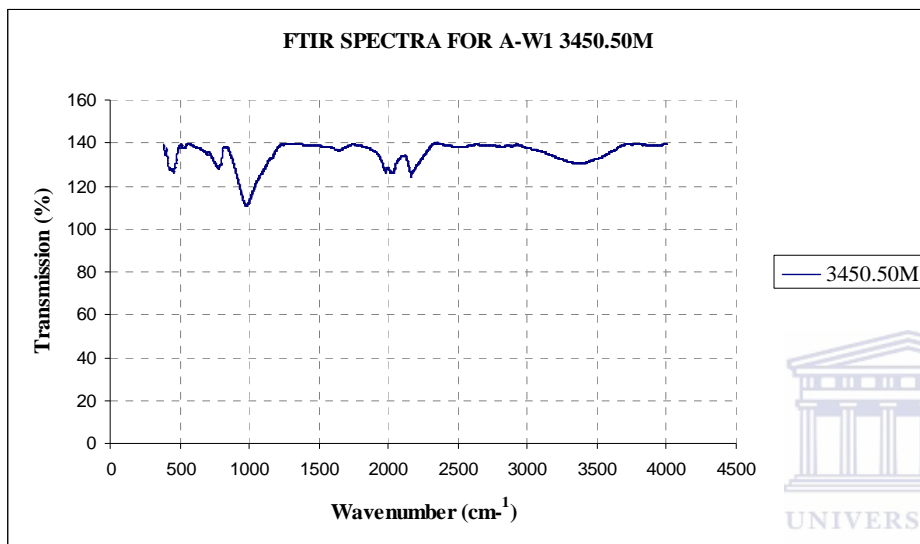
APPENDIX K (continued)



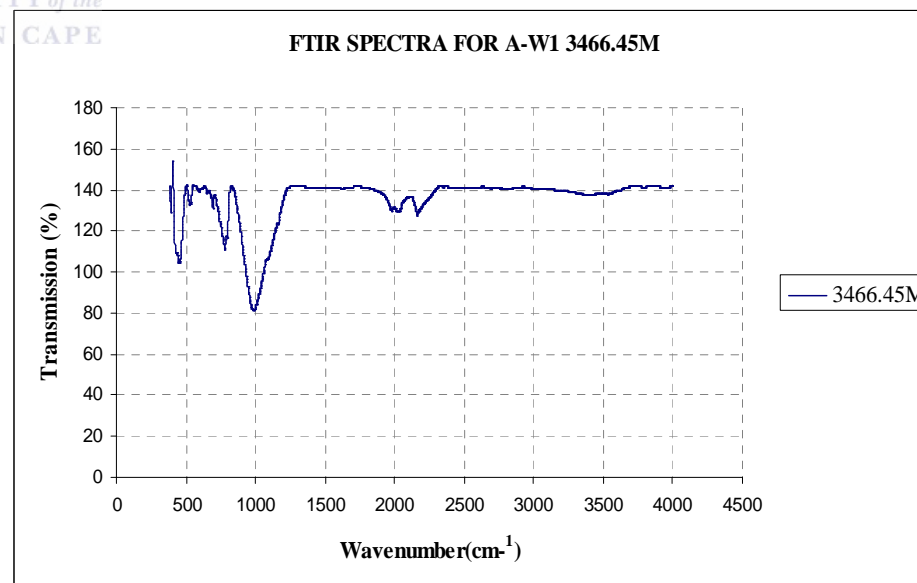
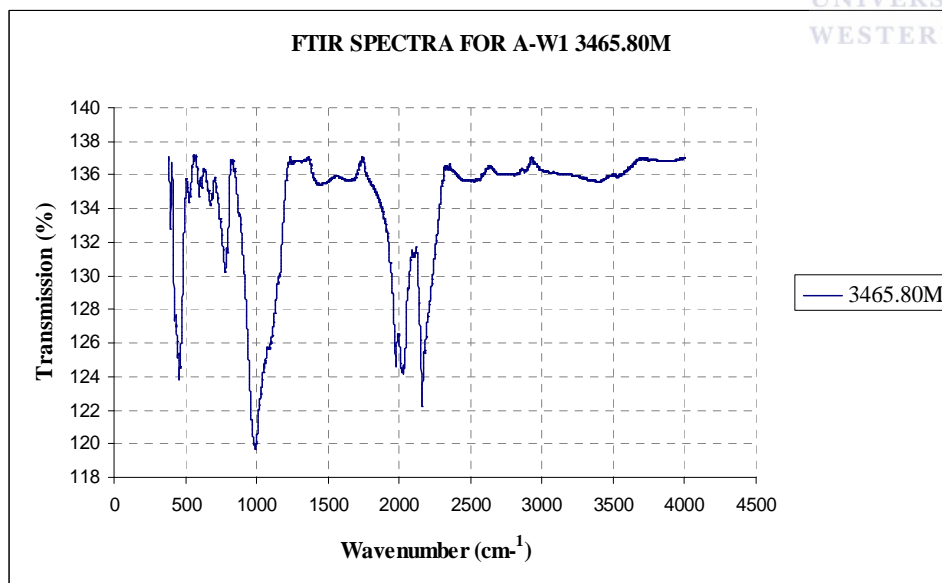
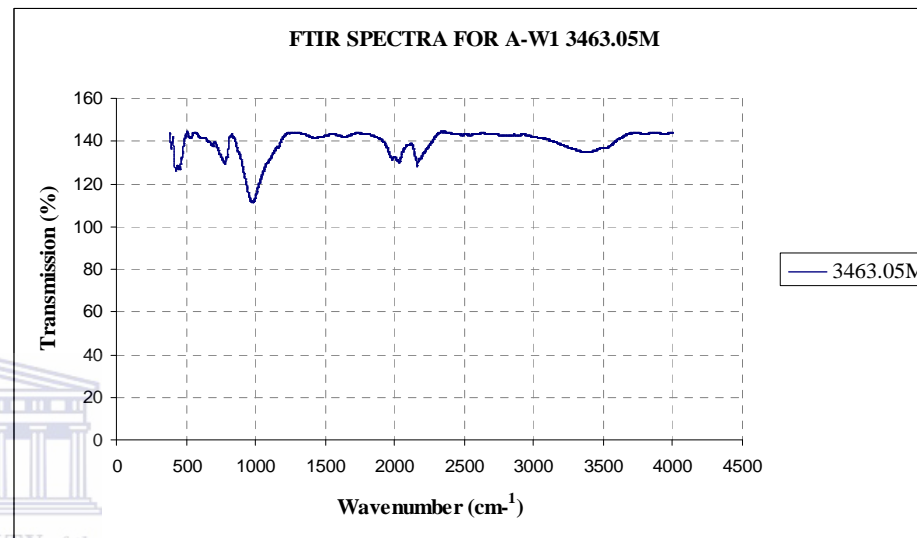
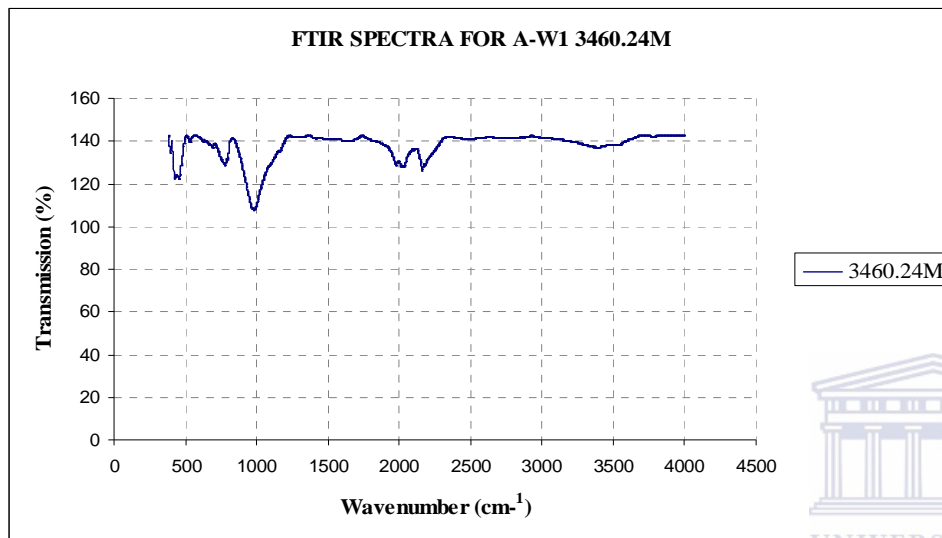
APPENDIX K (continued)



APPENDIX K (continued)



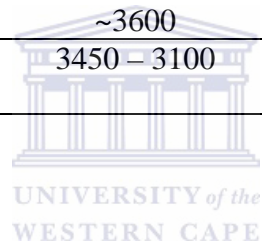
APPENDIX K (continued)



## APPENDIX L

**Table H:** showing some bands peculiar to different functional groups. (<http://www.le.ac.uk/chemistry/pdf/teachersworkshops.pdf>)

Bond	Wavenumber/cm <sup>-1</sup>	Notes
C-H	3000 – 2850	Saturated alkanes, limited value as most organic compounds contain C-H
=C-H	3100 – 3000	Unsaturated alkene or aromatic
≡C-H	3300	Terminal Alkyne
O=C-H	2800 and 2700	Aldehyde, two weak peaks
O-H	3400 – 3000	Alcohols and Phenols. If hydrogen bonding present peak will be broad 3000 – 2500 (e.g. carboxylic acids)
O-H (free)	~3600	
N-H	3450 – 3100	Amines: Primary – several peaks, Secondary – one peak, tertiary – no peaks



APPENDIX M  
X-ray Fluorescence Spectrometry (XRF) Results

A-G1 well									
Na <sub>2</sub> O/ K <sub>2</sub> O	SiO <sub>2</sub> /Al <sub>2</sub> O <sub>3</sub>	Fe <sub>2</sub> O <sub>3</sub> /K <sub>2</sub> O	Log (Na <sub>2</sub> O/ K <sub>2</sub> O)	Log (SiO <sub>2</sub> /Al <sub>2</sub> O <sub>3</sub> )	Log (Fe <sub>2</sub> O <sub>3</sub> /K <sub>2</sub> O)	CaO + Na <sub>2</sub> O	MgO/CaO	K <sub>2</sub> O/Na <sub>2</sub> O	Na <sub>2</sub> O + K <sub>2</sub> O
0.46	6.90	4.59	-0.34	0.84	0.66	2.39	1.83	2.17	4.88
0.51	7.52	6.09	-0.29	0.88	0.78	2.61	1.30	1.96	4.11
0.73	10.41	4.67	-0.14	1.02	0.67	3.93	0.39	1.38	3.40
0.13	4.23	2.10	-0.89	0.63	0.32	1.20	4.59	7.65	6.78
0.31	4.86	3.21	-0.51	0.69	0.51	1.66	3.87	3.26	5.00
0.43	6.78	4.13	-0.43	0.81	0.59	2.36	2.40	3.28	4.83
A-W1 well									
Na <sub>2</sub> O/ K <sub>2</sub> O	SiO <sub>2</sub> /Al <sub>2</sub> O <sub>3</sub>	Fe <sub>2</sub> O <sub>3</sub> /K <sub>2</sub> O	Log (Na <sub>2</sub> O/ K <sub>2</sub> O)	Log (SiO <sub>2</sub> /Al <sub>2</sub> O <sub>3</sub> )	Log (Fe <sub>2</sub> O <sub>3</sub> /K <sub>2</sub> O)	CaO + Na <sub>2</sub> O	MgO/CaO	K <sub>2</sub> O/Na <sub>2</sub> O	Na <sub>2</sub> O + K <sub>2</sub> O
1.06	6.66	11.43	0.02	0.82	1.06	2.64	2.03	0.95	3.06
1.07	6.44	17.01	0.03	0.81	1.23	4.11	0.82	0.93	2.90
1.03	7.90	15.98	0.01	0.90	1.20	4.14	0.78	0.97	3.24
1.16	6.27	15.70	0.07	0.80	1.20	2.06	3.50	0.86	2.67
5.55	8.85	63.13	0.74	0.95	1.80	38.95	0.02	0.18	1.33
1.66	6.86	20.45	0.22	0.84	1.31	19.34	0.11	0.60	2.30
1.39	7.44	17.32	0.14	0.87	1.24	3.25	1.41	0.72	2.67
0.40	4.18	6.51	-0.40	0.62	0.81	1.62	4.76	2.52	3.97
1.06	8.14	10.66	0.02	0.91	1.03	2.82	1.16	0.95	2.57
0.62	4.57	5.52	-0.21	0.66	0.74	1.91	5.02	1.62	3.78
1.50	6.73	18.37	0.07	0.82	1.16	8.08	1.96	1.03	2.85
A-K1 well									
Na <sub>2</sub> O/ K <sub>2</sub> O	SiO <sub>2</sub> /Al <sub>2</sub> O <sub>3</sub>	Fe <sub>2</sub> O <sub>3</sub> /K <sub>2</sub> O	Log (Na <sub>2</sub> O/ K <sub>2</sub> O)	Log (SiO <sub>2</sub> /Al <sub>2</sub> O <sub>3</sub> )	Log (Fe <sub>2</sub> O <sub>3</sub> /K <sub>2</sub> O)	CaO + Na <sub>2</sub> O	MgO/CaO	K <sub>2</sub> O/Na <sub>2</sub> O	Na <sub>2</sub> O + K <sub>2</sub> O
2.00	7.19	23.06	0.30	0.86	1.36	3.27	1.62	0.50	2.49
1.47	6.38	28.04	0.17	0.80	1.45	3.53	1.18	0.68	2.30
1.33	11.68	14.21	0.12	1.07	1.15	3.49	0.53	0.75	2.13
2.86	12.11	21.36	0.46	1.08	1.33	30.28	0.02	0.35	1.90
0.20	4.08	2.76	-0.70	0.61	0.44	1.71	2.33	5.00	5.42
1.53	5.60	15.26	0.18	0.75	1.18	2.76	2.53	0.66	3.02
1.73	7.72	14.44	0.24	0.89	1.16	3.09	1.79	0.58	2.95
2.78	6.44	14.78	0.44	0.81	1.17	4.65	1.57	0.36	4.54
1.16	5.47	16.92	0.07	0.74	1.23	2.28	2.87	0.86	2.70
0.25	4.22	3.69	-0.60	0.63	0.57	1.50	3.43	4.00	4.64
1.53	7.09	15.45	0.07	0.82	1.10	5.66	1.79	1.37	3.21



**APPENDIX N**  
**X-ray Fluorescence Spectrometry (XRF) Results**

<b>Trace Elements for A-G1 well</b>															
<b>Well Name</b>	<b>Depth (m)</b>	<b>As</b>	<b>Ba</b>	<b>Ce</b>	<b>Co</b>	<b>Cu</b>	<b>Nb</b>	<b>Ni</b>	<b>Pb</b>	<b>Rb</b>	<b>Sr</b>	<b>V</b>	<b>Y</b>	<b>Zn</b>	<b>Zr</b>
A-G1	3370.24	215	452	146	14	52	8	20	12	64	92	52	21	88	480
A-G1	3371.28	230	333	173	9	55	9	22	36	64	96	96	25	74	559
A-G1	3372.70	144	179	99	19	37	8	22	35	47	121	78	20	64	365
A-G1	3375.02	154	593	171	14	50	29	32	90	311	199	127	36	116	276
A-G1	3376.23	102	385	179	8	54	24	27	41	151	167	121	39	91	400
<b>Trace Elements for A-K1 well</b>															
<b>Well name</b>	<b>Depth (m)</b>	<b>As</b>	<b>Ba</b>	<b>Ce</b>	<b>Co</b>	<b>Cu</b>	<b>Nb</b>	<b>Ni</b>	<b>Pb</b>	<b>Rb</b>	<b>Sr</b>	<b>V</b>	<b>Y</b>	<b>Zn</b>	<b>Zr</b>
A-K1	3236.27	155	197	84	24	54	7	18	13	26	68	108	27	70	227
A-K1	3236.96	263	244	180	12	63	10	28	19	28	82	129	26	88	194
A-K1	3238.35	166	177	111	8	52	17	27	38	30	85	107	18	63	183
A-K1	3239.18	216	194	269	6	66	19	29	3	12	746	217	34	53	136
A-K1	3244.75	103	634	211	18	72	23	43	62	264	199	174	45	112	264
A-K1	3283.60	174	138	91	16	56	14	32	25	39	90	150	21	61	251
A-K1	3283.90	138	200	109	16	51	13	24	11	28	90	131	22	82	303
A-K1	3284.30	202	147	101	14	66	13	25	38	35	92	97	25	129	387
A-K1	3285.97	260	191	169	37	81	17	35	50	34	94	98	24	121	543
A-K1	3289.59	129	340	150	22	47	20	32	53	169	183	132	34	98	379
<b>Trace Elements for A-W1 well</b>															
<b>Well name</b>	<b>Depth (m)</b>	<b>As</b>	<b>Ba</b>	<b>Ce</b>	<b>Co</b>	<b>Cu</b>	<b>Nb</b>	<b>Ni</b>	<b>Pb</b>	<b>Rb</b>	<b>Sr</b>	<b>V</b>	<b>Y</b>	<b>Zn</b>	<b>Zr</b>
A-W1	3450.50	186	171	106	16	61	9	29	35	46	216	56	24	73	423
A-W1	3452.50	352	440	255	25	111	31	36	24	44	1179	43	43	111	425
A-W1	3454.05	328	301	168	16	80	19	30	37	44	795	156	35	70	208
A-W1	3455.50	161	96	30	16	39	1	31	16	28	80	83	31	78	706
A-W1	3457.05	253	103	520	17	74	22	12	13	14	1572	170	38	69	208
A-W1	3460.24	246	441	257	14	63	44	20	9	12	2779	168	57	58	163
A-W1	3463.05	193	159	70	19	58	14	31	14	29	148	145	25	67	222
A-W1	3465.80	164	231	206	22	65	2	38	38	125	131	175	37	101	597
A-W1	3466.05	128	1635	101	7	49	23	30	23	40	416	129	30	78	262
A-W1	3469.20	54	326	177	24	56	24	34	39	99	117	141	48	114	342